DIPLOMARBEIT

Studies on Irradiated 4H-SiC Diodes as Semiconductor Particle Detectors

zur Erlangung des akademischen Grades

Diplom-Ingenieur (Dipl.-Ing.)

im Rahmen des Studiums

Physikalische Energie- und Messtechnik

eingereicht von

Markus Göbel

Matrikelnummer: 01612969

ausgeführt am

Institut für Hochenergiephysik der Österreichischen Akademie der Wissenschaften
Atominstitut der Fakultät für Physik der Technischen Universität Wien

unter der Anleitung von

Assistant Prof. DI Dr.techn. Albert Hirtl (TU Wien / Atominstitut)
DI Dr.techn. Thomas Bergauer (ÖAW / HEPHY)

Wien, 13. Oktober 2022

(Unterschrift Verfasser) (Unterschrift Betreuer)

Die approbierte gedruckte Originalversion dieser Diplomarbeit ist an der TU Wien Bibliothek verfügbar
The approved original version of this thesis is available in print at TU Wien Bibliothek.
TU WIEN Bibliothek Your knowledge hub

ABSTRACT

Silicon Carbide (SiC) is a chemical compound containing silicon and carbon, which has been known in principle for more than hundred years. During the last decades, this material raised interest in various fields of science and technology. Power devices based on SiC are manufactured commercially by now and have applications in eco-friendly electric cars, for example. Moreover, the 4H polytype (4H-SiC) is a promising candidate for particle detector technology. The reason for the interest in this material is that it exhibits advantages over conventional semiconductors like pure silicon. The most important properties with regard to detector technology is that SiC is able to withstand high radiation and temperature environments. While being operated under these conditions, a SiC devices exhibits a significantly lower leakage current due to its wide band gap ($E_g = 3.26\,\text{eV}$ for 4H-SiC) and faster signals. In recent years, many studies have been conducted to develop detector devices based on 4H-SiC. This thesis places its emphasis on studying the performance of heavily irradiated 4H-SiC single pixel diodes with a newly designed UV-Laser setup, using the Transient Current Technique (TCT). To expose the diodes to a known equivalent fluence Φ_{eq}, the devices were irradiated in the core of the TRIGA Mark II reactor [1] of the Atominstitut of the Technische Universität Wien. The diodes were exposed to a fluence of 5×10^{14}, 1×10^{15}, 5×10^{15} and 1×10^{16} 1 MeV neutron equivalent per cm^2. After irradiation, the devices were bonded onto a readout board and tested regarding their sensor signals as well as on the increase of their leakage current. However, even for the sensor exposed to the highest fluence only a sub-µA leakage current was obtained. In agreement with the NIEL-hypothesis, the leakage current increased with exposure to radiation. To conduct the experiments on the sensor signals, up to 1100 V reverse bias voltage was applied onto the diodes. Afterwards, a 370 nm (3.35 eV per photon) Laser was used to excite charge carriers inside the active volume. The signals were recorded with a DRS4 oscilloscope [2] and analyzed with respect to the following parameters: peak maximum (V_{max}), time-over-threshold (t_{ToT}), peak area (A_{peak}) and the signal-to-noise ratio (SNR). The collected data showed a decrease of all previously mentioned parameters with an increase of the fluence to which the device was exposed. It is noteworthy, that for the highest irradiated sensor no signal could be recorded. Regarding the parameters, a charge collection efficiency (CCE) was derived. The CCE exhibited 63 %, 45.8 % and 19.6 % (least to highest irradiated detector) of the maximum number of created charge carriers at the maximum applied bias voltage of 1100 V. Compensating the loss of performance due to radiation effects is possible by applying higher reverse bias voltages. However, the full depletion of the irradiated diodes was not achieved in any irradiated detector. After to the studies with the TCT-setup, a similar series of experiments were conducted at the beam line for non-clinical research at MedAustron [3]. In this case, signals were induced with 252.7 MeV protons, depositing less energy per particle in the detector compared to the TCT-studies. In general, the data exhibited similar results. Due to uncertainties that occurred during the studies, they are considered as bare proof of concept. In conclusion, 4H-SiC sensors exposed up to fluences up to $1{\cdot}10^{15}$ $\text{n}_{eq}/\text{cm}^2$ are capable of showing sufficient performance to detect particles.

TU WIEN Bibliothek Your knowledge hub
Die approbierte gedruckte Originalversion dieser Diplomarbeit ist an der TU Wien Bibliothek verfügbar
The approved original version of this thesis is available in print at TU Wien Bibliothek.

ZUSAMMENFASSUNG

Siliziumkarbid (SiC) ist eine seit über einem Jahrhundert bekannte Verbindung aus Silizium und Kohlenstoff. In den letzten Jahrzehnten erweckte dieses Material großes Interesse in verschiedensten Bereichen der Wissenschaft und Technik. Elektrische Bauteile auf Basis von SiC werden heutzutage kommerziell hergestellt und finden bespielsweise Anwendung in umweltfreundlichen E-Autos. Weiters ist insbesondere der Polytyp 4H-SiC einer der vielversprechendsten Kandidaten für Anwendungen in der Detektortechnologie. Siliziumkarbid zeigt Vorteile gegenüber herkömmlichen Halbleitern wie Silizium. Die wichtigsten Eigenschaften in Bezug auf Detektortechnologie ist, dass SiC gegenüber Umgebungen mit hoher Strahlenbelastung und Temperatur eine hohe Widerstandsfähigkeit aufweist. Bei Anwendungen unter diesen Bedingungen zeigen SiC-Dioden neben wesentlich schnelleren Signalen einen signifikant geringeren Dunkelstrom aufgrund der großen Bandlücke ($E_g = 3.26\,\mathrm{eV}$). In den vergangen Jahren wurden zahlreiche Studien durchgeführt, um Sensoren auf Basis von 4H-SiC zu entwickeln. Kern dieser Arbeit ist eine Studie zur Funktionstüchtigkeit hochbestrahlter Single-Pixel Detektoren mittels eines neu entwickelten UV-Laser Setups, unter Verwendung der Transient Current Technique (TCT). Um die Dioden bekannten Äquivalentfluenzen Φ_{eq} auszusetzen wurden diese im Reaktorkern des TRIGA Mark II Reaktors [1] des Atominstituts der Technischen Universität Wien bestrahlt. Folglich wurden die Detektoren $5{\times}10^{14}$, $1{\times}10^{15}$, $5{\times}10^{15}$ and $1{\times}10^{16}$ 1 MeV Neutronen Äquivalent pro cm^2 ausgesetzt. Nach der Bestrahlung wurden die Sensoren auf ein Readout-Board montiert und auf ihre Signale, sowie die Zunahme des Dunkelstroms getestet. In Übereinstimmung mit der NIEL-Hypothese zeigte sich eine Zunahme des Dunkelstroms mit steigender Fluenz, welcher der Detektor ausgesetzt wurde. Selbst für den höchstbestrahlten Sensor wurden nur Ströme im sub-µA Bereich gemessen. Für die Durchführung der Experimente bezüglich der Detektorsignale wurde Hochspannung bis 1100 V in Sperrrichtung der Diode angelegt. Anschließend wurden mit einem 370 nm Laser (3.35 eV pro Photon) Ladungsträger im aktiven Volumen erzeugt. Die Aufzeichnung der Signale erfolgte mittels eines DRS4 Oszilloskops [2] und folgende Parameter wurden untersucht: Signalhöhe (V_{max}), Signaldauer (time-over-threshold) (t_{ToT}), Signalfläche (A_{peak}) sowie das Signal-zu-Rausch Verhältnis (SNR). Die gesammelten Daten zeigen für alle Parameter eine Abnahme mit steigender Fluenz, welcher die Dioden ausgesetzt wurden. Für den höchstbestrahlten Sensor konnten keine Signale aufgenommen werden. Die aus der Signal-Fläche abgeleitete Detektor Effizienz (Anteil der von der Elektrode gesammelten Ladungsträger, Charge Collection Efficiency) ergab 63 %, 45.8 % und 19.6 % (niedrigst- bis höchstbestrahlter Detektor) bei einer Spannung von 1100 V in Sperrrichtung. Eine Kompensation des Verlusts der Effizienz durch Strahlenschäden ist durch Anlegen höherer Spannungen möglich. Eine vollständige Ausbreitung der Verarmungszone konnte für keinen der bestrahlten Detektoren erreicht werden. Zusätzlich zu den TCT-Studien wurden ähnliche Experimente am Strahlrohr für nicht-klinische Forschung bei MedAustron [3] durchgeführt. Hier wurden Signale mit 252.7 MeV Protonen erzeugt, welche weniger Energie im Detektor deponierten. Im Allgemeinen wurden ähnliche Ergebnisse erzielt. Allerdings kann diese Experimentreihe durch einige Unsicherheiten nur als Studie zur prinzipiellen Machbarkeit gesehen werden. Zusammenfassend wurde gezeigt, dass SiC-Detektoren, welche einer Fluenz bis zu $1{\cdot}10^{15}\ \mathrm{n_{eq}/cm^2}$ ausgesetzt wurden, sich als ausreichend funktionstüchtig erwiesen.

TU Bibliothek WIEN Your knowledge hub
Die approbierte gedruckte Originalversion dieser Diplomarbeit ist an der TU Wien Bibliothek verfügbar
The approved original version of this thesis is available in print at TU Wien Bibliothek.

Die approbierte gedruckte Originalversion dieser Diplomarbeit ist an der TU Wien Bibliothek verfügbar
The approved original version of this thesis is available in print at TU Wien Bibliothek.
TU WIEN Bibliothek Your knowledge hub

Contents

Abstract **i**

Zusammenfassung **ii**

1 Introduction and Motivation **1**

1.1 History of Particle Detectors - A Brief Review 1

1.1.1 The Early Beginnings 1

1.1.2 Particle Detectors Based on Electronical Properties 1

1.2 Currently Used and Investigated Detector Materials 2

1.2.1 The Development of Semiconductor Detector Devices 2

1.2.2 Silicon Carbide as a Promising Candidate for Detector Purposes 2

1.3 MedAustron 3

1.3.1 Ion Cancer Treatment and the Synchotron 3

1.3.2 Hi-Precision Beam Position and Intensity Monitor for Accurate Cancer Treatment with Ions 3

2 Theoretical Background **5**

2.1 Semiconductors and their Properties 5

2.1.1 The Band Model and the Bandgap 5

2.1.2 Influencing the Fermi Level by Doping 7

2.2 Interaction of Particles and Matter 8

2.2.1 Photons 8

2.2.2 Charged Particles 10

2.3 Irradiation Damage in Crystals 12

2.3.1 Lattice Defects 12

2.3.2 The NIEL-Hypothesis 13

2.3.3 The Shockley-Read-Hall Theorem for Non-Ideal Crystal Lattices 13

3 Semiconductor Particle Detectors **15**

3.1 The Electrical Field and Potential of a pn-Junction 15

3.2 The Influence of a Bias Voltage 18

3.3 Using a Diode as a Detector 19

3.4 Detector Signals 21

3.5 The Transient Current Technique (TCT) 22

4 Silicon Carbide **25**

4.1 General Physical Properties 25

4.2 The Lattice Configurations and Their Properties 25

4.3 A Closer Look on 4H-SiC 26

5 Experimental Setup **28**
5.1 The Samples . . . 28
5.1.1 Properties of the SiC-Diodes . . . 28
5.1.2 Irradiation of the Sensors . . . 29
5.2 The Setup in the Cleanroom . . . 29
5.2.1 The Testing Box . . . 29
5.2.2 UV-LASER System . . . 31
5.2.3 Inducing Signals . . . 32
5.2.4 Readout Chain - UCSC Board and DRS4 Evaluation Board . . . 32
5.2.5 IV-Measurements . . . 34
5.3 The Beam Facility at MedAustron . . . 34
5.4 Data Analysis . . . 35

6 Results **39**
6.1 Sample Preparation and General Information . . . 39
6.2 Laser TCT-measurements . . . 39
6.2.1 Specific Experimental Parameters . . . 39
6.2.2 Non-irradiated SiC-Sensor . . . 40
6.2.3 SiC-Sensor exposed to $5 \times 10^{14}\,\mathrm{n_{eq}/cm^2}$ . . . 45
6.2.4 SiC-Sensor exposed to $1 \times 10^{15}\,\mathrm{n_{eq}/cm^2}$ . . . 50
6.2.5 SiC-Sensor exposed to $5 \times 10^{15}\,\mathrm{n_{eq}/cm^2}$ . . . 55
6.2.6 SiC-Sensor exposed to $1 \times 10^{16}\,\mathrm{n_{eq}/cm^2}$ . . . 60
6.3 Measurements at MedAustron . . . 60
6.3.1 Specific Experimental Parameters . . . 60
6.3.2 Non-irradiated SiC-Sensor . . . 61
6.3.3 SiC-Sensor exposed to $5 \times 10^{14}\,\mathrm{n_{eq}/cm^2}$ . . . 62
6.3.4 SiC-Sensor exposed to $1 \times 10^{15}\,\mathrm{n_{eq}/cm^2}$ . . . 64
6.3.5 SiC-Sensor exposed to $5 \times 10^{15}\,\mathrm{n_{eq}/cm^2}$ . . . 65

7 Discussion **67**
7.1 Laser-TCT measurements . . . 67
7.2 Measurements at MedAustron . . . 75

8 Summary and Outlook **80**
8.1 Summary . . . 80
8.2 Outlook . . . 83

Appendix **84**

A Tables and Histograms of Experimental Data (UV-Laser-TCT) **85**
A.1 Non-irradiated SiC-Sensor . . . 85
A.2 SiC-Sensor exposed to $5 \times 10^{14}\,\mathrm{n_{eq}/cm^2}$ . . . 87
A.3 SiC-Sensor exposed to $1 \times 10^{15}\,\mathrm{n_{eq}/cm^2}$ . . . 89
A.4 SiC-Sensor exposed to $5 \times 10^{15}\,\mathrm{n_{eq}/cm^2}$ . . . 91

Die approbierte gedruckte Originalversion dieser Diplomarbeit ist an der TU Wien Bibliothek verfügbar
The approved original version of this thesis is available in print at TU Wien Bibliothek.
TU WIEN Bibliothek Your knowledge hub

B Tables and Histograms of Experimental Data (MedAustron) 93

B.1 Non-irradiated SiC-Sensor . . . 93

B.2 SiC-Sensor exposed to $5 \times 10^{14}\,\mathrm{n_{eq}/cm^2}$ . . . 94

B.3 SiC-Sensor exposed to $1 \times 10^{15}\,\mathrm{n_{eq}/cm^2}$ . . . 96

B.4 SiC-Sensor exposed to $5 \times 10^{15}\,\mathrm{n_{eq}/cm^2}$ . . . 97

C Testing Report of the UV-Laser 99

D References 106

Die approbierte gedruckte Originalversion dieser Diplomarbeit ist an der TU Wien Bibliothek verfügbar
The approved original version of this thesis is available in print at TU Wien Bibliothek.
TU Bibliothek WIEN Your knowledge hub

1 Introduction and Motivation

1.1 History of Particle Detectors - A Brief Review

1.1.1 The Early Beginnings

Particle physics is a discipline which evolved strongly during the last century. The discovery of more and even smaller particles revolutionized physics and established new experimental techniques. Within every detection, new challenges had to be faced by physicists. The very first detectors were bare photographic plates which led to the discovery of radioactive decay in 1896 by accident by H. Becquerel [4]. In this case, high-energetic particles emerging from ores containing uranium left marks on the plate by energy deposition. In the following years, V. Hess achieved the proof of cosmic radiation in an accumulative measurement with an electrometer during his famous balloon flights [5]. Besides photographic plates, the newly developed scintillators also gained popularity among physicists to detect particles. With those instruments, a light flash could be seen with the naked eye as a sign of detecting a particle, e.g. used by Rutherford [6]. Another approach which used photography to detect particles were cloud chambers [7], which led to the development of the bubble chamber in 1960. In bubble chambers, penetrating particles crossed a volume of an overheated liquid, leaving behind a track with bubbles [8]. The big advantage was that a complete particle reaction could be recorded as electrical and magnetic fields were applied. The different types of particles left behind a characteristic track depending on charge, momentum and energy. This technology was still used until the 1980s in research facilities all around the world, including CERN [9]. Unfortunately, all these detectors and their signals are not capable of being analyzed autonomously which is crucial in physics nowadays. The discovery of different types of radiation and development of techniques to detect particles led to several Nobel prizes. All physicists mentioned above received this special honor for their contribution to the understanding of modern-era physics.

1.1.2 Particle Detectors Based on Electronical Properties

Since the middle of the 20$^{\text{th}}$ century, particle physics research centers are increasing the energy and rates of particles, which are involved in the experiments [9]. This raised the need for high-speed detection and analysis devices, which are capable of proving the presence of particles electronically. The first steps with this type of technology were taken by H. Geiger in 1928 by developing proportional counters [10], which were based an gas amplification. In this device, gas atoms are ionized if a particle travels through this medium and creates charge by knocking off electrons from the shell. Thus, the created charge is proportional to the deposited energy and collected by an electric field [10]. These instruments are still used as portable radiation monitoring devices. In the following years, this concept was utilized to develop the wire chamber and especially the drift chamber to achieve a multi-dimensional resolution [9, 11]. Detectors based on gas ionization are still in use today as it is possible to achieve sufficient time resolution in the pico-second range [12]. Unfortunately, the amount of energy to ionize a gas atom is relatively high compared to the band gap of any semiconductor. In the 1940s, the first ideas came up to use a crystal and the photoelectric effect to detect α and β particles [13]. Hence, particle detectors based on semiconductor technology were developed as manufacturing processes of silicon and germanium have evolved. The ability to manipulate semiconductors with dopants was key to access a new era of technology. It affected not only the read-out electronics of sensors, it even affected the sensors themselves [9]. The first detectors based on the interaction of particles and crystals had to be cooled to low temperatures to achieve a sufficient distinction between noise and signals. As soon as doping techniques were developed

Die approbierte gedruckte Originalversion dieser Diplomarbeit ist an der TU Wien Bibliothek verfügbar
The approved original version of this thesis is available in print at TU Wien Bibliothek.
TU WIEN Bibliothek Your knowledge hub

and the properties of a pn-junction were known, diode structures became the standard rapidly [9]. Since the possibility of manufacturing integrated circuits was given, also the miniaturization of detectors was achievable. From the mid 1980s on, semiconductor detectors and small drift chambers replaced nearly all bubble chambers, which were the state-of-the-art before [9]. The evolution of technology which was developed in need for detection analysis still continues today.

1.2 Currently Used and Investigated Detector Materials

1.2.1 The Development of Semiconductor Detector Devices

During the last decades, the development of processing techniques for ultra-pure semiconductors - especially silicon - showed much progress [13]. Monocrystalline silicon is available since the 1960s. Thus, silicon gained also much popularity in detector applications. The most common technique for using silicon as a particle detector is the diode, also known as *pn*-junction. Multiple different geometric shapes have been tested and investigated. This includes single diodes, multiple diodes on a sensor pad - a pixel detector with two dimensional resolution - and layers of strip detectors to measure a trajectory [13]. Yet, besides all its advantages, pure silicon has a few drawbacks. The bandgap of silicon is 1.14 eV [14], which is in the energy range of visible light. Therefore, silicon diodes must never be exposed to light by accident during operation. Also, silicon diodes are not the perfect choice to be applied in harsh environments as they do not withstand radiation very well. Silicon-based devices get damaged easily when exposed to high fluences up to 10^{15} 1 MeV neutron equivalent [15, 16]. This results in a high dark current, in which a signal gets drowned easily. A material which attracts much attention in semiconductor technology is silicon carbide. It promises to solve a few problems related to silicon [16]. Due to silicon carbide being discovered in 1885, up until now already many experiments were conducted on this material. The main property as a wide band-gap semiconductor (band gap ≈ 3 eV [17]) is known since the 1950s but got into researchers' focus for the last 30 years. The first application as a particle detector was demonstrated in 1957 by Babcock et al. [18] for α-particles and neutrons. This work was extendend by Ferber [19] in 1966, who miniaturized detectors to apply them in nuclear reactor technology. The detectors were operated at temperatures up to 700°C with a very low dark current compared to conventional sensor technology in these days [19, 20]. A very specific property of silicon carbide is polytypism; this means that silicon carbide exhibits multiple thermodynamically stable crystals structures at room temperature. Hence, this leads to the demand of additional research as the properties of each lattice configuration may differ [21]. However, the development of devices based on silicon carbide slowed down due to the lack of high purity crystalline material and processing techniques.

1.2.2 Silicon Carbide as a Promising Candidate for Detector Purposes

In the 1990s, the first tests were carried out on ultra-pure silicon carbide detector devices as the material was available in sufficient quality by then [22]. Manufacturing silicon carbide structures for the bulk is based on sublimation (Lely method) or chemical vapor deposition (CVD). Both methods show a relatively slow growth rate [23]. For growing epitaxial layers, the liquid phase epitaxy technique as well as CVD is used. An interesting approach is to grow silicon carbide hetero epitaxial layers on a silicon substrate. The substrate material is cut from silicon wafers which can be grown with larger diameters [23]. Hence, the excellent properties like a wider band gap and estimated radiation hardness over pure silicon led to intensive research on silicon carbide. Studies were conducted by many research centers (e.g. CERN) which are developing future detector materials and devices [21, 24]. In addition, experiments were performed

TU Bibliothek Your knowledge hub WIEN
Die approbierte gedruckte Originalversion dieser Diplomarbeit ist an der TU Wien Bibliothek verfügbar
The approved original version of this thesis is available in print at TU Wien Bibliothek.

to determine how the devices perform in harsh environments [16, 25]. Nowadays, the main aspect of applying silicon carbide detectors is still nuclear instrumentation with interaction of charged particles [26]. Beside reactor technology, silicon carbide got into focus for particle monitoring systems. Hence, studies on segmented diodes have been conducted to investigate devices with spatial resolution [27]. Also, diodes have already been successfully used as neutron detection devices for spectroscopy [20]. In this thesis, single pixel diodes SiC diodes will be investgated. Irradiated diodes were tested on their signal properties. Hence, in a newly developed UV-Laser-TCT (Transient Current Technique) setup, sensors were studied on their performance after being exposed to specific 1 MeV neutron equivalent fluences. The validation process of detectors not only consists of testing sensors in cleanrooms with highly controlled conditions. Tests have also been conducted at a proton synchrotron beam. For this approach of testing sensors, MedAustron [3] offers a facility for non-clinical research. This unique opportunity is adopted by many institutes in Austria including the Institute for High Energy Physics.

1.3 MedAustron

1.3.1 Ion Cancer Treatment and the Synchotron

MedAustron is a medical treatment center for cancer diseases which provides treatment based on ion therapy [3]. This particular method shows advantages over conventional radiotherapy treatments [28–30]. Charged particles deposit their energy in another way than photons do. This is the reason that the deposition shows a maximum in a specific penetration depth, depending on the material and initial energy [28, 31]. In comparison, X-rays are attenuated exponentially exposing patients to unnecessary doses of radiation in other tissue [28]. First tests with ion cancer therapy have been performed in the 1950s in the United States of America and this technology is available in central Europe since the 1990s [32]. In Austria, the decision was made to build MedAustron in 2004, to make ion cancer therapy accessible and provide a modern research center for (non-)clinical research [3]. MedAustron is located in Wiener Neustadt, Austria and owns a synchroton which is capable of delivering protons (H^+) and carbon ions (C^{6+}) to one of the four irradiation rooms [30]. At this facility, not only medical treatment is carried out. Many institutes are offered the possibility to conduct experiments with the proton beam in an irradiation room exclusively designed for non-clinical research [30]. The facility is capable of delivering 800 MeV protons or 400 MeV/u carbon ions to the irradiation rooms with rates up to 10^9 Hz [33]. Medical treatment and non-clinical research have different requirements on the particle beam; particle rates for medical purposes are a few orders of magnitude greater than for testing of detectors in high energy physics. In this case, usual rates of 10^8 to 10^9 Hz are required for medical irradiation versus 10^3 Hz for device testing [30]. In 2021, the beam line was also commissioned for particle flux settings below the originally desired values at seven specific energies [30].

1.3.2 Hi-Precision Beam Position and Intensity Monitor for Accurate Cancer Treatment with Ions

MedAustron and the Institute of High Energy Physics started the Hi-Precision Beam Position and Intensity Monitor for Accurate Cancer Treatment with Ions (HiBPM) project in April 2021 [34]. Within this partnership, a new generation of sensor technology shall be developed, which is planned to replace the currently operating detector system. The detector devices are based on the properties of silicon carbide of a specific lattice configuration. The 4H-SiC crystal is predicted to be the most applicable material for future instrumentation. In a first step, SiC single pixel diodes are studied to provide the proof of

Die approbierte gedruckte Originalversion dieser Diplomarbeit ist an der TU Wien Bibliothek verfügbar
The approved original version of this thesis is available in print at TU Wien Bibliothek.
TU Bibliothek WIEN Your knowledge hub

concept [35]. As synchrotrons are naturally harsh environments with high radiation, all detectors shall withstand this particular stress without loosing too much performance. Hence, this thesis extends the work of [35] as identical diodes have been irradiated and are subject of investigation now. In order to do so, tests with a Laser-TCT setup in the cleanroom at the Institute of High Energy Physics and at the beam line of MedAustron with low flux settings have been performed. In the future, silicon carbide strip detectors with spatial resolution and up to 128 channels shall be developed. This also includes the need for a readout chip. Hence, a prototype of a complete ultra-precise monitoring system will be provided by the HiBPM project [34].

Die approbierte gedruckte Originalversion dieser Diplomarbeit ist an der TU Wien Bibliothek verfügbar
The approved original version of this thesis is available in print at TU Wien Bibliothek.
TU WIEN Bibliothek Your knowledge hub

2 Theoretical Background

2.1 Semiconductors and their Properties

2.1.1 The Band Model and the Bandgap

To obtain the energy states E for a single atom, the quantum-mechanical model of the stationary Schrödinger equation with the Planck constant $\hbar$, the electron mass m_e has to be applied. [36] The equation is

$$\left(-\frac{\hbar^2}{2m_\mathrm{e}}\nabla^2 + V(\vec{r})\right)\psi(\vec{r}) = E\psi(\vec{r}). \tag{1}$$

and describes the wave function $\psi(\vec{r})$ of an electron in a potential $V(\vec{r})$ and can be solved analytically for the interaction of a positive (nucleus) and a negative charge (electron) only. The solution of this equation leads the eigenfunctions $\psi(\vec{r})$ with corresponding discrete eigenvalues E, which are interpreted as energy levels. [37] For single atoms with more than one electron - for example He - a few corrections have to be applied to calculate the eigenvalues observed in an experiment. The additional electron establishes an additional potential term V_el, which can be treated in several ways [38]. A common approach is solving the Schrödinger equation by numerical methods approximately.

Delocalized Electrons

For the interaction of two or more atoms, the energy levels are shifted, as it is forbidden for Fermions (as the electrons are) to exist in the same state in the same place. This property is known as the Pauli principle [37]. In the extreme outcome of this case, atoms are forming a crystal lattice. The potential term $V(\vec{r})$ exhibits a periodic property now as the nuclei are aligned in a crystal-specific configuration. Mathematically, $V(\vec{r}) = V(\vec{r} + \vec{R})$ holds, with $\vec{R}$ being the distance until the pattern repeats itself [39]. As the potential shows this behavior, one can expect this property also for the wave functions. Thus, $\psi(\vec{r}) = \psi(\vec{r} + \vec{R})$. This mainly effects the most loosely bound electrons in the outer most shells, the so called valence electrons. For many atoms in a crystal lattice, the former discrete energy levels 'smear' out and the discrete levels cannot be observed anymore. Moreover, they also depend on the momentum $\vec{p} \propto \vec{k}$ of the electron [39] and $\vec{k}$ is the wave-vector of the propagating electron. Due to the periodicity and the propagation throughout the whole crystal, the electrons (and their wave functions) even cannot be assigned to a specific atom. Hence, valence electrons are called delocalized. For inner-shell electrons the localized wave functions and discrete values are still valid. As delocalized electrons show the ability to travel across the crystal, they contribute to the electrical conduction mechanism [39].

Energy Bands

As mentioned above, the energy state of an electron also depends on its k-vector. The dependency of the energy E on $\vec{k}$ in a specific direction is called dispersion relation, leading to the energy band structure [39]. They can differ strongly from each other. For each $\vec{k}$ not only one state is possible as multiple bands exist. The lowest band for a specific k is called valence band and the higher one(s) are named conduction band(s). Only the energetically highest electrons take part in the actual conduction as they need unoccupied states in a higher energy band to transfer energy. Energy bands - of course also from different directions - may overlap which is key to distinguish between conductors, semiconductors and isolators. Conductors show overlappping bands which allows transitions without any barrier. Isolators

Die approbierte gedruckte Originalversion dieser Diplomarbeit ist an der TU Wien Bibliothek verfügbar
The approved original version of this thesis is available in print at TU Wien Bibliothek.
TU WIEN Bibliothek Your knowledge hub

and semiconductors possess a band gap E_g up to a few eV between the valence band and the conduction band. [39]. The electrical conduction properties are determined by the electron density in the conduction band. To achieve higher conductivity electrons have to be excited (thermally or by radiation) from the valence band into the conduction band. In a perfect crystal with no defects, the borders of the bands are 'sharp' values [40].

The Fermi Level E_F and the Charge Carrier Concentration

An important property to describe the crystal is the Fermi level E_F. E_F is the highest energy state which an electron can occupy at 0 K in a conductor; for semiconductors E_F is usually located inside the band gap. Certainly, the highest occupied state at 0 K is below E_F. Consequently, the valence band is completely filled while the conduction band is totally empty at 0 K. This phenomenon is described by the Fermi-Dirac statistics and its distribution function [39]

$$f_{FD}(E) = \frac{1}{\exp\left(\frac{E-E_F}{k_B T}\right) + 1}. \tag{2}$$

It describes the probability density that specific energy levels are occupied, if they actually exist [40]. The function f_{FD} itself depends on the difference $E - E_F$ and temperature T as a parameter. At E_F, the probability is $f_{FD}(E_F) = \frac{1}{2}$ by definition. The plot of the probability distribution is also shown for different T in Fig. 1b. For the perfect crystal lattice, E_F is located exactly in the center of the band gap. At 0 K f_{FD} converges to a Heaviside-like step function, which shows clearly that only states under E_F are occupied. Thus, the density n and p of electrons and holes

$$n = N_C \cdot e^{-\frac{E_C - E_F}{k_B T}}, \tag{3}$$

$$p = N_V \cdot e^{-\frac{E_F - E_V}{k_B T}} \tag{4}$$

in the conduction/valence band is determined by the location of E_F, the lower/upper edge of the conduction/valence E_C and E_V and the effective density of states in the conduction/valence band N_C and N_V, respectively [14]. They effective density of states

$$N_{C,V} = 2\left(\frac{2\pi m^*_{e,h} k_B T}{h^2}\right)^{\frac{3}{2}} \tag{5}$$

depends on the effective mass $m^*_{e,h}$ of electrons and holes [14]. Multiplying n and p leads to the mass action law for the quadratic intrinsic charge carrier concentration [14]

$$n \cdot p = n_i^2 = N_C \cdot N_V \cdot e^{\frac{-E_g}{k_B T}} \tag{6}$$

for electrons and holes in thermal equilibrium, which only depends on the band gap $E_g = E_C - E_V$. n_i is a constant material parameter in thermal equilibrium for semiconductors. As the formula shows, n_i is strongly influenced by the temperature T. In equilibrium, $n_i = n = p$ holds, as carriers are generated in electron-hole-pairs and recombine later [14]. An important relation derived from this formula is that the number of free charge carrier is $\propto T^{3/2} \exp\left(-\frac{1}{T}\right)$ [14].

Die approbierte gedruckte Originalversion dieser Diplomarbeit ist an der TU Wien Bibliothek verfügbar
The approved original version of this thesis is available in print at TU Wien Bibliothek.
TU WIEN Bibliothek Your knowledge hub

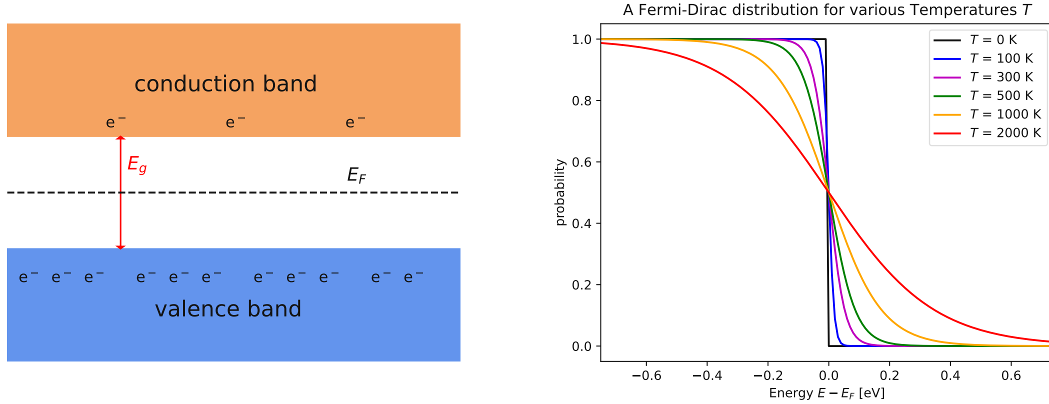

(a) The (simplified) band model. The blue (orange) block represents all bands in the valence (conduction) band.

(b) The Fermi-Dirac distribution. One can clearly see the convergence against the step function at 0 K.

Figure 1: The band model and the Fermi-Dirac-distribution

2.1.2 Influencing the Fermi Level by Doping

The location of the Fermi level can be influenced by adding 'impurities' on purpose to the crystal by doping. Depending on the dopant, additional energy levels are established inside the band gap. This reduces the excitation energy and alters the conductivity of the semiconductor [14]. Doping affects the location of the Fermi level due to the presence of additional electrons or lack of them. Adding donators (n-doping), which provide additional electrons due to owning more valence electrons, shifts the Fermi level from the center towards the conduction band. On the other hand, doping with acceptors (p-doping), adds holes (sometimes also called defect-electrons) to the valence band. This shifts the Fermi level towards the valence band due to a minor number of electrons [14]. Holes are the major charge carriers for p-doping while electrons remain the major charge carriers for n-doped materials. Now, the intrinsic electron/hole concentration cannot be derived from $n, p = n_\mathrm{i}$ anymore. Assuming that all donors (acceptors) are ionized, the difference of the Fermi-level to the conduction (valence) band is affected the following way: Assuming that $N_{D,A} \gg n_\mathrm{i}$ and every dopant contributes m additional charge carriers, the density n (p) of electrons (holes) is $n \approx m \cdot N_\mathrm{D}$ and $p \approx m \cdot N_\mathrm{A}$, respectively.

Before adding dopants, the difference between the edges to the Fermi Level is $\frac{E_\mathrm{g}}{2}$ as E_F is located in the center of the band gap. Note that these differences are not equal to the excitation energy. The location of the Fermi level just allows a conclusion about the dopant concentration. Assuming $m = 1$ and considering equation (3) and (4), the difference between the edge of the conduction (valence) and Fermi level is

$$E_\mathrm{C} - E_\mathrm{F} = k_\mathrm{B} T \ln \frac{N_\mathrm{C}}{N_\mathrm{D}}, \tag{7}$$

$$E_\mathrm{F} - E_\mathrm{V} = k_\mathrm{B} T \ln \frac{N_\mathrm{V}}{N_\mathrm{A}}. \tag{8}$$

It is now determined by the ratio of the effective density of states to the dopant concentration [14].

Doping concentration ranges for different purposes from $10^{15}\,\mathrm{cm}^{-3}$ to $10^{20}\,\mathrm{cm}^{-3}$ [14]. Highly doped material (in terms of concentration) is often denoted as n^+ or p^+. This is important in semiconductor

Die approbierte gedruckte Originalversion dieser Diplomarbeit ist an der TU Wien Bibliothek verfügbar
The approved original version of this thesis is available in print at TU Wien Bibliothek.
TU Bibliothek WIEN Your knowledge hub

technology for adjacent layers of different thickness, for example detector diodes. For elements of the fourth group of the periodic system - where silicon and carbon are located - phosphorus and boron can be used as a donor and acceptor, respectively [14]. The shift of the Fermi Level by doping is illustrated in Fig. 2.

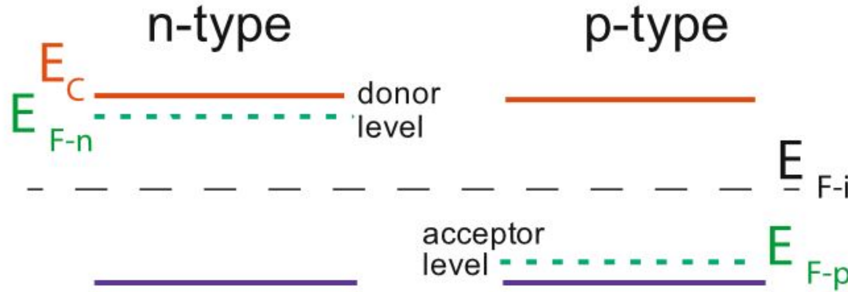

Figure 2: The influence of dopants on the Fermi Level E_F [14].

2.2 Interaction of Particles and Matter

2.2.1 Photons

If a beam of light (no matter if infrared, visible, ultra-violet or X-rays, etc.) irradiates a body, photons penetrate the layers underneath the surface and may emerge on the other side again. In between, a single photon can participate in several related effects of interaction with matter, due to which it looses energy [41, 42]. How many photons are absorbed due to any interaction can be calculated by Beer-Lamberts law. It states for the rate of the change of the intensity I in a layer of thickness $\mathrm{d}x$ that

$$\mathrm{d}I = -\mu_\mathrm{A} I \mathrm{d}x \tag{9}$$

with the linear attenuation coefficient μ_A in cm^{-1} [41]. Integrating this equatio leads to the well-known exponential decrease of the intensity

$$I(x) = I_0 \cdot e^{-\mu_\mathrm{A} x} \tag{10}$$

with increasing thickness x, which the photons travel through [41]. As multiple ways to interact with matter exist, μ_A is the sum of all attenuation coefficients from the specific effects. The likelihood of a specific interaction at an atom can be described by the atomic absorption cross section σ^abs. The attenuation coefficient is directly linked to the atomic absorption cross section (usually given in barn b, $1\,\mathrm{b} = 10^{-28}\,\mathrm{m}^2$) via $\mu_\mathrm{A} = \rho_\mathrm{a}\sigma^\mathrm{abs}$ [41]. In this case, ρ_a is the number of atoms per unit volume. To convert μ_A into the often used mass absorption coefficient μ in $\mathrm{cm}^2\,\mathrm{g}^{-1}$, one has to divide by the density ρ. This leads to the following relation with material constants and easily measurable properties only:

$$\mu = \frac{\mu_\mathrm{A}}{\rho} = \frac{1}{\rho}\frac{N}{V}\sigma^\mathrm{abs} = \frac{1}{\rho}\frac{mN_\mathrm{A}}{MV}\sigma^\mathrm{abs}. \tag{11}$$

The possibility of an interaction only depends on the energy carried by the photon. However, the intensity does not matter. The three main interaction are the photo-electric effect [43], the Compton effect [44] and pair production [45].

Die approbierte gedruckte Originalversion dieser Diplomarbeit ist an der TU Wien Bibliothek verfügbar
The approved original version of this thesis is available in print at TU Wien Bibliothek.
TU WIEN Bibliothek Your knowledge hub

The Photo-electric Effect

The photo-electric effect was first studied by A. Einstein, which resulted in his Nobel prize 1905 [43]. In this case, a photon transfers all its energy onto an electron in an atom. The photon is absorbed and the electron escapes, leaving behind an ionized atom. Therefore, at least the work function W_A must be carried by the photon. For deeper energy states, more energy ΔE than just W_A must be transferred onto the electron, as presented in Fig. 3. The remaining energy is transformed into kinetic energy of the electron. The kinetic energy is calculated via

$$E_{\text{kin}} = \hbar\omega - (W_{\text{A}} + \Delta E), \tag{12}$$

where ω describes the frequency of the photon [43]. The cross section for the photo-electrical effect has a strong dependency on the wavelength λ and charge Z of the nucleus. Experimental data show with a wavelength-dependent parameter $C(\lambda)$ that $\sigma^{\text{abs}}_{\text{P.E.}} = C(\lambda)\lambda^3 Z^4$ [46]. $C(\lambda)$ changes at the so called absoprtion-edges, if the wavelength is sufficiently small to ionize the atom by transferring its energy to a deeper shell electron [46]. This behavior can be seen in Fig. 4a.

The Compton Effect

For higher photon energies, a generalisation of the photo-electric effect by Einstein had to be developed. This was achieved by A. Compton in 1923 [44]. The Compton effect considers the scattering of the incoming photon while transferring a part of its energy onto an electron. The electron is kicked out of the shell and leaves behind an ionized atom. The process is presented in Fig. 3b. Obviously, the conservation of energy and momentum must be granted. Based on the these two relations, the remaining photon energy $E'_\gamma = \hbar\omega'$ - respectively the kinetic energy of the electron - can be calculated. A strong dependency on the scattering angle φ is found and can be written as [44].

$$E'_\gamma = \frac{E_\gamma}{1 + \frac{E_\gamma}{m_{\text{e}}c^2}(1 - \cos\varphi)}. \tag{13}$$

Pair Production

If the energy of the impinging photon increases even more, pair production occurs. The effect was predicted back in 1934 by H. Bethe [47]. In this process, the photon transforms into a pair of an electron and a positron under the influence of the electrical field of the nucleus [45]. As these particles carry mass, the rest energy is connected to them while not being in motion. The transformation into particles requires that at least the rest energy of both the electron and the positron is carried by the photon. For this effect, a threshold of 1.022 MeV exists. Thus,

$$\gamma \xrightarrow{E\, >\, 1.022\,\text{MeV}} e^- + e^+. \tag{14}$$

This threshold corresponds to two times the rest energy of 511 keV of the electron. As the positron is identical to the electron except for the charge, also the rest is equal. [45]. To conserve momentum and energy, the particles emerge with the same velocity, as they have the same mass. A scheme of the effect is shown in Fig. 3c.

Die approbierte gedruckte Originalversion dieser Diplomarbeit ist an der TU Wien Bibliothek verfügbar
The approved original version of this thesis is available in print at TU Wien Bibliothek.
TU WIEN Bibliothek Your knowledge hub

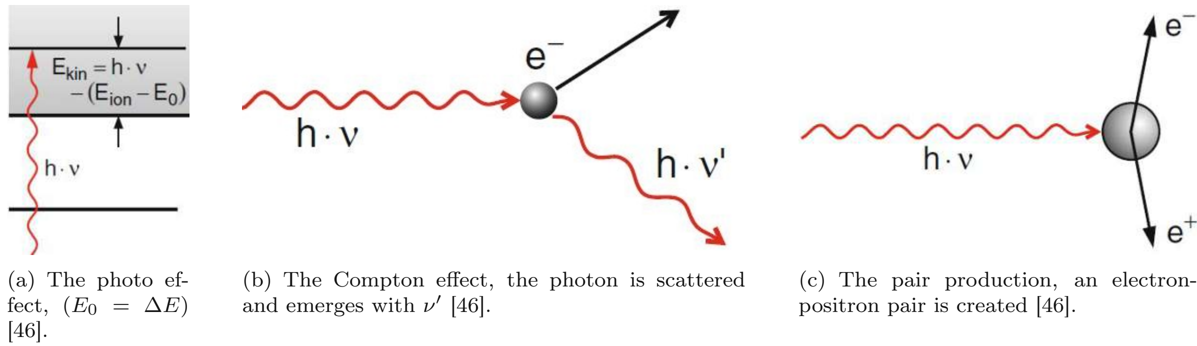

(a) The photo effect, ($E_0 = \Delta E$) [46].

(b) The Compton effect, the photon is scattered and emerges with ν' [46].

(c) The pair production, an electron-positron pair is created [46].

Figure 3: The schemes of the interaction of light and matter.

These three interactions dominate over a wide energy range from severel eV to a few MeV. The effects do not supersede each other strictly. Over a wide range, at least two interactions are possible. For a specific energy, only a possibility for each interaction can be given. Hence, it is impossible to predict which interaction will be undergone for a specific electron [41, 46]. Next to the three discussed effects, there are many more possibilities for photons to interact with matter, especially in the low-energy and high-energy range [41]. Namely, this is Rayleigh- or Thomson scattering for low-energy photons. The first of these two effects is the scattering at molecules, while the other describes scattering at free or loosely bound charges. For high energies, also nucleus-photon interaction can take place [41]. The cross sections for a few of the possible interaction are plotted in Fig. 4 against the energy of the incoming photon.

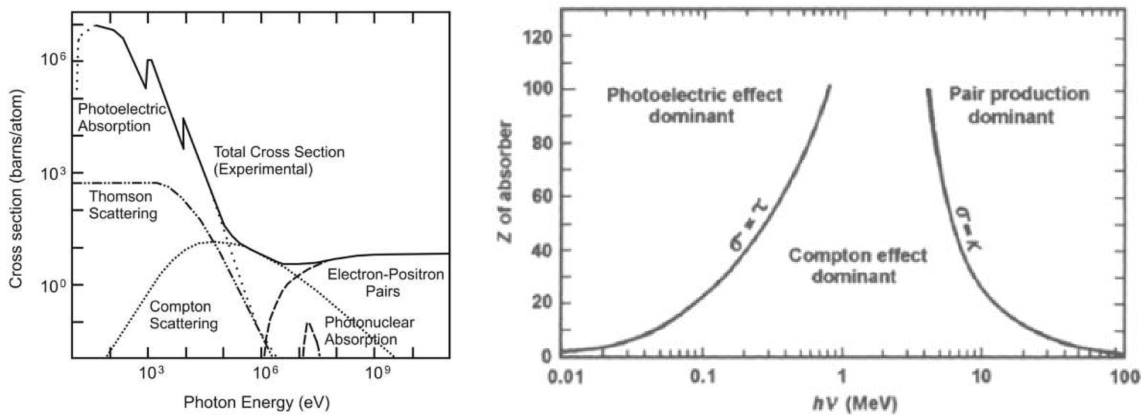

Figure 4: The cross section in dependence of the photon energy [41] and the energy regions with the dominant effect [42].

2.2.2 Charged Particles

As for neutral particles, there exist a few mechanisms how charged particles interact with matter. Again, the interactions cause energy loss of the impinging particle, which may differ significantly from particle to particle, like protons and electrons [48]. In this chapter, only 'heavy' particles like protons are considered, as they are the most common projectiles in beam lines like MedAustron [3]. Depending on their penetration depth, the particles loose their energy not at the same rate. However, an average energy loss

Die approbierte gedruckte Originalversion dieser Diplomarbeit ist an der TU Wien Bibliothek verfügbar
The approved original version of this thesis is available in print at TU Wien Bibliothek.
TU WIEN Bibliothek Your knowledge hub

per unit length $\langle \mathrm{d}E/\mathrm{d}x \rangle$ can be derived. Most generally, this property can be calculated as [48].

$$-\left\langle \frac{\mathrm{d}E}{\mathrm{d}x} \right\rangle = n \int_{T_{\min}}^{T_{\max}} T \left(\frac{\mathrm{d}\sigma_A}{\mathrm{d}T} \right) \mathrm{d}T. \tag{15}$$

In this formula, n is the density of the target material and $\frac{\mathrm{d}\sigma_A}{\mathrm{d}T}$ the differential cross section for an energy transfer T [48]. The integral represents all possible losses during a collision. If the integral is calculated with a known formula for $T_{\min}$ and the electron density n in the target, the famous Bethe-Bloch-Equation [47] can be derived, which is known since 1930. In modern forms, the equation also has correction terms and is written as [48]

$$-\left\langle \frac{\mathrm{d}E}{\mathrm{d}x} \right\rangle = K \frac{Z}{A} \rho \frac{z^2}{\beta^2} \left[\frac{1}{2} \ln \left(\frac{2m_\mathrm{e}c^2\beta^2\gamma^2 T_{\max}}{I^2} \right) - \beta^2 - \frac{\delta(\beta\gamma)}{2} - \frac{C(\beta\gamma, I)}{Z} \right]. \tag{16}$$

This formula depends on numerous parameters, which are commonly well known for the target material. T_{max} can be calculated as well, although it depends strongly on the projectile. Thus, it will not be replaced here [48]. Only K depends on non-material constants; it collects all other occurring physical constants. Hence, $K = 4\pi N_\mathrm{A} r_\mathrm{e}^2 m_\mathrm{e} c^2$. The other parameters are [48]:

Z	...	atomic number / nucleus charge in terms of e
A	...	atomic mass number
ρ	...	target density
z	...	projectile charge in terms of e
I	...	average ionization energy of the target material
β	...	velocity of the projectile in terms of c
γ	...	Lorentz factor
$T_{\max}$	...	maximum possible energy transfer

The $\delta(\beta\gamma)/2$ term is a density-correction term, which only has as an effect for very fast particles. On the other hand, the $C(\beta\gamma, I)/Z$ term is known as the shell correction which is necessary for low values of β [48]. The Bethe-Bloch-Equation possesses a minimum for each projectile-target combination. A particle with this energy shows the least ionization impact compared to other energies. These particles are called minimum ionizing particles (MIP) and are of special interest when testing a newly developed detector. As the equation depends on a few material and projectile parameters, the MIP is also material and particle specific [49]. However, the curves resulting from the Bethe-Bloch-equation for different projectiles exhibit similar shapes. Also, the energy of a MIP is quite similar for different impinging particles. Exemplary curves are presented in Fig. 5a below.

A result of this equation is the unique behavior for the stopping power $S(E)$, which is defined as the energy loss per unit length $-\frac{\mathrm{d}E}{\mathrm{d}x}$. The stopping power of a material increases with the penetration depth until it reaches a maximum [48]. After this maximum, $S(E)$ decreases nearly instantly as seen in Fig. 5b. This is based on the fact that a particle is slowed down by energy loss, which increases the energy loss even more. This can be seen in the Bethe-Bloch equation due to the β^{-2} term. The maximum is called Bragg-Peak and plays an important role in cancer treatment with ions [28, 31].
The actual penetration depth for the particles is a statistical quantity as each particle travels another way. However, the highest energy deposition takes place in a small area around the Bragg-Peak as the stopping power exhibits a maximum [48]. For the energy deposition and the number of created charge

TU Bibliothek Your knowledge hub WIEN
Die approbierte gedruckte Originalversion dieser Diplomarbeit ist an der TU Wien Bibliothek verfügbar
The approved original version of this thesis is available in print at TU Wien Bibliothek.

carriers a Landau-distribution can be obtained. The curve of a Landau-distributed value is characterized through an asymmetrical shape which has a maximum (most probable value) and a 'tail' for values higher than the most probable value. According to this distribution, the average value is higher than the most probable one [48]. It must be noted, that the stopping power only describes the loss of energy of the impinging particle. Hence, further energy transport due to secondary particles is possible [48].

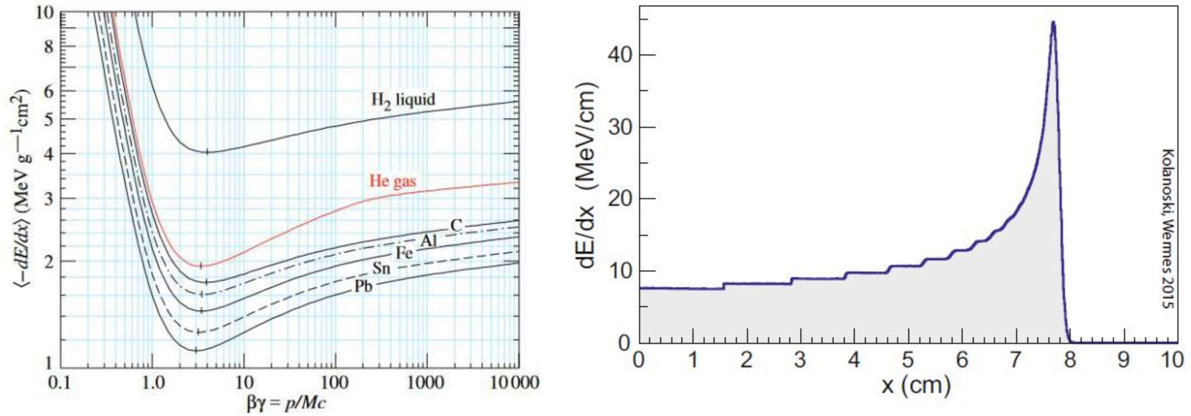

(a) The Bethe-Bloch-equation for different elements and protons [49].

(b) The Bragg Peak in $-\langle \frac{\mathrm{d}E}{\mathrm{d}x} \rangle$ of 100 MeV protons in water [48].

Figure 5: The results of interaction of charged particles and matter.

2.3 Irradiation Damage in Crystals

2.3.1 Lattice Defects

In relation to the perfect crystal lattice, every deviation from the perfect condition is considered a defect. If enough energy is transferred onto an atom, it can be knocked out of its lattice position into an interstitial site, leaving behind a vacancy [15]. This constellation of a vacancy and an interstitial atom is called a Frenkel-pair and is a point defect. To knock one atom out of its initial position, at least the displacement energy E_d must be transferred. A high E_d is a requirement for a detector in high energy physics, it indicates a high radiation hardness. Therefore, it is a crucial property for designing a detector which shall be operated reliably in environments with strong (particle) radiation fields like particle accelerators. An accumulation of point defects - a cluster - is considered a volume defect and may be caused by irradiating a crystal [15]. Any imperfection inside a crystal has influences on the properties of the crystal lattice; they affect the electrical conductivity. Therefore, they lower the quality of the detector signals. Of course there also exist line defects and borders of possible phases (interfaces and surfaces). They are caused by other reasons than radiation. These defects will not be discussed here as they should not appear in grown high purity single crystals. The interested reader is recommended to read [50].

Die approbierte gedruckte Originalversion dieser Diplomarbeit ist an der TU Wien Bibliothek verfügbar
The approved original version of this thesis is available in print at TU Wien Bibliothek.
TU WIEN Bibliothek Your knowledge hub

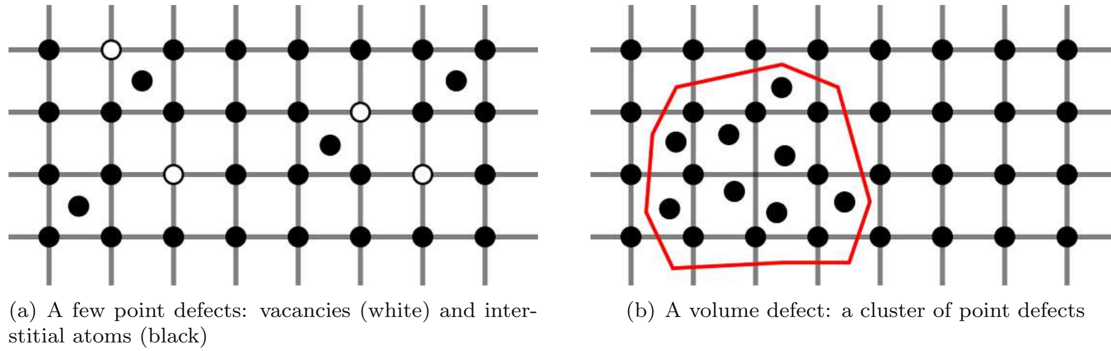

(a) A few point defects: vacancies (white) and interstitial atoms (black)

(b) A volume defect: a cluster of point defects

Figure 6: The defects in a crystal lattice caused by irradiation

2.3.2 The NIEL-Hypothesis

The so-called NIEL hypothesis (Non-Ionizing Energy Loss) is a theory, how deposited energy affects the crystal lattice [51]. Irradiation, which is basically bombardment of a body with particles, causes several defects. Therefore, NIEL describes the amount of energy transferred to the crystal, which does not lead to ionization effects. The impinging particles transfer their energy via collisions to atoms in the crystal lattice. The energy is dissipated due to two reasons: On one hand phonons are excited. On the other hand, atoms may get knocked out of their lattice positions - which is considered radiation damage. To be material-independent, the NIEL is defined in $\mathrm{MeVcm}^2/\mathrm{g}$ or as damage function D, which is a cross section in MeVmb. As a reference, 1 MeV neutron equivalent (n_{eq}) is 95 MeVmb [51]. The fraction of the energy that causes knock-offs depends on the energy of the impinging particles. The idea of the NIEL hypothesis is that the amount of radiation damage scales linearly with the total deposited energy [51]. Hence, the damage - the number of caused vacancies - is independent of the affected area and energy. A wide irradiated area due to scattering of low energy particles yields the same damage as a focused beam of high energetic projectiles. With this information, it is possible to predict radiation damage in radiation fields via NIEL scaling [51]. This allows the simulation of devices and all their affected parameters, e.g. leakage current or effective space charge, in radiation fields. The increase of the leakage current is strictly proportional to the fluence Φ. Specifically, this linear approach uses the total equivalent fluence Φ_{eq} and the damage factor α, which is a material constant, if normalized to temperature [15, 52]. According to the NIEL hypothesis, there exists a model to describe the increase of the leakage current per unit volume

$$\frac{\Delta I}{V} = \alpha \cdot \Phi_{\mathrm{eq}} \tag{17}$$

due to radiation damage [51]. The equivalent fluence Φ_{eq} corresponds to a fluence of 1 MeV neutrons. [15] The leakage current depends on several (external) factors. Hence, a standard procedure to determine α at specific temperatures and annealing time has evolved [52]. This linear property can also be used to observe annealing effects. Heating up the crystal and recording the leakage current against the reverse bias voltage (IV-measurements) shows a change of α, due to the recovering of the lattice defects [15].

2.3.3 The Shockley-Read-Hall Theorem for Non-Ideal Crystal Lattices

Real crystals possess a few defects, like impurities (non-lattice atoms), dislocated or missing atoms and grain boundaries. Even the surface or phase interfaces are technically a defect, as they break the lattice symmetry. Thus, it is necessary to consider them in the band model. Impurities and defects establish

Die approbierte gedruckte Originalversion dieser Diplomarbeit ist an der TU Wien Bibliothek verfügbar
The approved original version of this thesis is available in print at TU Wien Bibliothek.
TU Bibliothek Your knowledge hub WIEN

energy levels E_{TL} (sometimes called 'deep levels' or 'trap levels') in the forbidden zone, the band gap [14]. Hence, excited electrons or holes are possibly trapped by these states and do not contribute to the conduction mechanism. A property that describes the purity of the crystal is the lifetime

$$\tau_{\mathrm{L}} = \frac{1}{\sigma v_{\mathrm{th}} N_{\mathrm{t}}}. \tag{18}$$

of the electrons. It depends on the following parameters: σ is the charge carrier cross section, v_{th} is the thermal velocity of the carriers, while N_{t} stands for the impurity (trap) concentration [14]. Clearly, τ_{L} diverges with a lower impurity concentration according to Eq. (18).

More important than the viewpoint of being a trap, is that these levels also act as centers for generating electron-hole-pairs [14]. To quantify this effect, a statistical approach via emission and capture rates R for electrons and holes is chosen. For electrons, the emission rate from the trap level is denoted by $R_{\mathrm{e}}^{\uparrow}$, while the capture rate is $R_{\mathrm{e}}^{\downarrow}$. For holes, the emission rate from the trap level is denoted by $R_{\mathrm{h}}^{\downarrow}$, while the capture rate is $R_{\mathrm{h}}^{\uparrow}$. In thermal equilibrium, the rates from the trap level (index TL) of emission from or into the corresponding band are equal. Therefore, $R_{\mathrm{e}}^{\uparrow} = R_{\mathrm{e}}^{\downarrow} = R_{\mathrm{e}}$ and $R_{\mathrm{h}}^{\downarrow} = R_{\mathrm{h}}^{\uparrow} = R_{\mathrm{h}}$ [14]. The rates are calcuted with the fraction n_{TL} of occupied trap level states, the charge carrier cross section σ, the thermal velocity of the charge carrier v_{th} and the state density $N_{C,V}$ in the conduction and valence band by [14]

$$R_{\mathrm{e}} = n_{\mathrm{TL}} \cdot \sigma_{\mathrm{e}} \cdot v_{\mathrm{th,e}} \cdot N_{\mathrm{C}} \cdot e^{\frac{E_{\mathrm{TL}}-E_{\mathrm{C}}}{k_{\mathrm{B}}T}}, \tag{19}$$

$$R_{\mathrm{h}} = n_{\mathrm{TL}} \cdot \sigma_{\mathrm{h}} \cdot v_{\mathrm{th,h}} \cdot N_{\mathrm{V}} \cdot e^{\frac{E_{\mathrm{V}}-E_{\mathrm{TL}}}{k_{\mathrm{B}}T}}. \tag{20}$$

The involved energy levels are shown in Fig. 7. Here, the needed excitation energy is visible, being the difference of the deep level and the edge of the corresponding band.

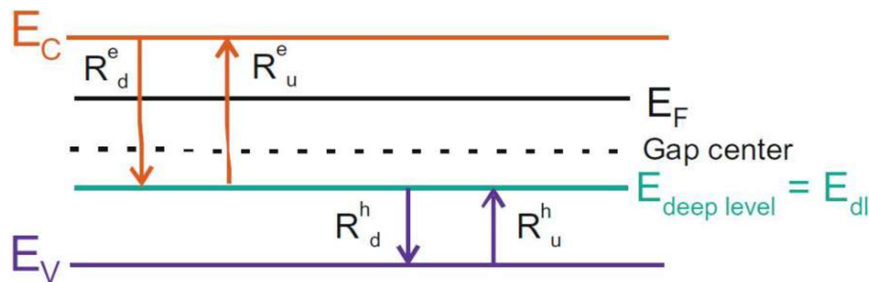

Figure 7: The participating energy levels for the Shockley-Read-Hall transitions [14].

Die approbierte gedruckte Originalversion dieser Diplomarbeit ist an der TU Wien Bibliothek verfügbar
The approved original version of this thesis is available in print at TU Wien Bibliothek.
TU WIEN Bibliothek Your knowledge hub

3 Semiconductor Particle Detectors

3.1 The Electrical Field and Potential of a pn-Junction

A pn-junction (also called a diode) consists of a connected n-doped and p-doped region. The most important property of a diode is that the Fermi level E_F is constant throughout the whole volume. This holds true, even though the concentration of major charge carriers varies in different areas. At the moment of contact, electrons and holes flow towards the pn-interface where they recombine, leaving behind positive charges from the donor atom in the n-region and vice versa [14]. This region is called depletion zone due to the lack of major charge carriers, or space charge region (SCR) because of the 'background' charge of the dopants. It is noteworthy to mention, that the n-doped region is then charged positively, while the p-doped region has a negative space charge [14]. The pn-junction before and after connecting is shown below in Fig. 8. As soon as the p-type and n-type material get into contact the valence and conduction band bend to fulfill $E_\mathrm{F} = const.$ [14].

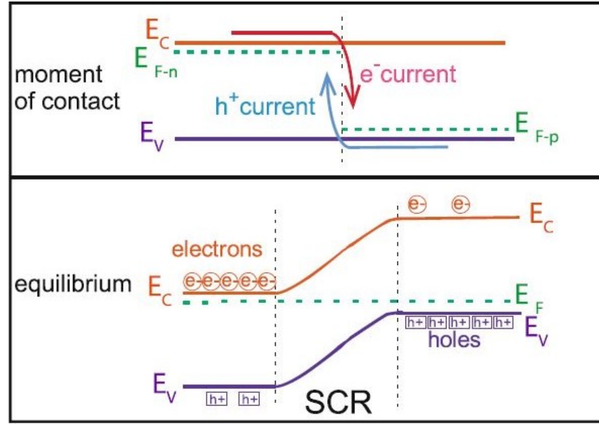

Figure 8: The pn-junction in equilibrium [14].

The shape of the resulting electrical field $\vec{E}$ as well as the potential Φ can be calculated using the Poisson-Equation. $N_\mathrm{A}, N_\mathrm{D} \gg n_\mathrm{i}$ is valid in nearly all doped semiconductors, therefore, $N_\mathrm{A,D} \mp n_\mathrm{i} \approx N_\mathrm{A,D}$.. Assuming that the dopants own one electron more/less than a crystal lattice atom, the charge density in the doped and depleted volumes are equal to the dopant concentration times the elementary charge e. With this prerequisite, $\vec{E}$ and Φ can be derived based on [14], [53] and [54]. The Poisson-equation yields

$$\nabla^2 \Phi(\vec{r}) = -\frac{\varrho(\vec{r})}{\varepsilon_0 \varepsilon_\mathrm{r}}. \tag{21}$$

For most purposes it is sufficient to consider one dimension only. In our case, the diode is considered with a simple geometry: An n-doped region attached to a p-doped region with different thickness. Hence, the Poisson equation simplifies to the following form:

$$\frac{\partial^2 \Phi(x)}{\partial x^2} = -\frac{\varrho(x)}{\varepsilon_0 \varepsilon_\mathrm{r}}. \tag{22}$$

The solution of the Poisson equation for the whole diode possesses two parts. It will be solved separately for the n-doped and p-doped region in $[-x_\mathrm{n}; 0]$ and $[0; x_\mathrm{p}]$, respectively, as they are charged differently.

Die approbierte gedruckte Originalversion dieser Diplomarbeit ist an der TU Wien Bibliothek verfügbar
The approved original version of this thesis is available in print at TU Wien Bibliothek.
TU Bibliothek WIEN Your knowledge hub

The charge density $\varrho(x)$ is

$$\varrho(-x_\mathrm{n} < x < 0) = +eN_\mathrm{D} \tag{23}$$
$$\varrho(0 < x < x_\mathrm{p}) = -eN_\mathrm{A}. \tag{24}$$

The n-type (p-type) depleted material shows the positive (negative) space charge due to 'background charge' of the dopant atoms. Contributions from non-dopants (impurities) are neglected [53, 54]. Integrating the charge density in $[-x_\mathrm{n}\,;0]$ and $[0\,;x_\mathrm{p}]$ yields the electric fields $E_{n,p}(x)$ due to Maxwell's first equation (Gauss' law). Again, only one dimension has to be considered [54], therefore,

$$\boldsymbol{\nabla}\cdot\vec{E}(\vec{r}) = \frac{\varrho(\vec{r})}{\varepsilon_0\varepsilon_\mathrm{r}} \tag{25}$$

leads to the simple relation

$$\frac{\partial E(x)}{\partial x} = \frac{\varrho(x)}{\varepsilon_0\varepsilon_\mathrm{r}}. \tag{26}$$

The electrical field between a and b is

$$E(x) = \frac{1}{\varepsilon_0\varepsilon_\mathrm{r}}\int_a^b \varrho(x)\mathrm{d}x. \tag{27}$$

As $\varrho(x)$ is constant in these intervals, a linear behaviour of $E(x)$ can be obtained. For the boundary conditions $E(-x_\mathrm{n}) = E(x_\mathrm{p}) = 0$ is chosen, which yields [54].

$$E(-x_\mathrm{n} < x < 0) = -\int_{-x_\mathrm{n}}^{0}\frac{eN_\mathrm{D}}{\varepsilon_0\varepsilon_\mathrm{r}}\mathrm{d}x = -\frac{eN_\mathrm{D}}{\varepsilon_0\varepsilon_\mathrm{r}}\cdot(x+x_\mathrm{n}) = -\frac{eN_\mathrm{D}}{\varepsilon_0\varepsilon_\mathrm{r}}\cdot x_\mathrm{n}\cdot\left(\frac{x}{x_\mathrm{n}}+1\right) \tag{28}$$
$$E(0 < x < x_\mathrm{p}) = \int_{0}^{x_\mathrm{p}}\frac{eN_\mathrm{A}}{\varepsilon_0\varepsilon_\mathrm{r}}\mathrm{d}x = \frac{eN_\mathrm{A}}{\varepsilon_0\varepsilon_\mathrm{r}}\cdot(x-x_\mathrm{p}) = \frac{eN_\mathrm{A}}{\varepsilon_0\varepsilon_\mathrm{r}}\cdot x_\mathrm{p}\cdot\left(\frac{x}{x_\mathrm{p}}-1\right) \tag{29}$$

for the electrical field. The expressions for $E(x)$ yield linear functions with the maximum electric field at $x = 0$. For charge neutrality in the whole material, $N_\mathrm{D}x_\mathrm{n} = N_\mathrm{A}x_\mathrm{p}$ must be fulfilled for all pn-junctions in thermal equilibrium [54]. The value of E_max can be obtained due to this relation. The electric potential $\Phi(x)$ can be found by integrating a second time. The electric field and the electric potential are related by $\vec{E} = -\nabla\Phi$. [53, 54] Again, only dimension must be considered, with the boundary condition $\Phi(0) = 0$ the integration leads to

$$\Phi(-x_\mathrm{n} < x < 0) = \int_{-x_\mathrm{n}}^{0}\frac{eN_\mathrm{D}}{\varepsilon_0\varepsilon_\mathrm{r}}\cdot(x+x_\mathrm{n})\mathrm{d}x = \frac{eN_\mathrm{D}}{\varepsilon_0\varepsilon_\mathrm{r}}\cdot\left(\frac{x^2}{2}+xx_\mathrm{n}\right) = \frac{eN_\mathrm{D}}{\varepsilon_0\varepsilon_\mathrm{r}}\cdot x_\mathrm{n}^2\cdot\left[\frac{1}{2}\left(\frac{x}{x_\mathrm{n}}\right)^2+\frac{x}{x_\mathrm{n}}\right] \tag{30}$$
$$\Phi(0 < x < x_\mathrm{p}) = -\int_{0}^{x_\mathrm{p}}\frac{eN_\mathrm{A}}{\varepsilon_0\varepsilon_\mathrm{r}}\cdot(x-x_\mathrm{p})\mathrm{d}x = -\frac{eN_\mathrm{A}}{\varepsilon_0\varepsilon_\mathrm{r}}\cdot\left(\frac{x^2}{2}-xx_\mathrm{p}\right) = -\frac{eN_\mathrm{A}}{\varepsilon_0\varepsilon_\mathrm{r}}\cdot x_\mathrm{p}^2\cdot\left[\frac{1}{2}\left(\frac{x}{x_\mathrm{p}}\right)^2-\frac{x}{x_\mathrm{p}}\right]. \tag{31}$$

This boundary condition ensures the continuity of the potential at the pn-interface at $x = 0$. The electrical field as well as the potential in dependency of x are shown in Fig. 9.

TU WIEN Bibliothek Your knowledge hub
Die approbierte gedruckte Originalversion dieser Diplomarbeit ist an der TU Wien Bibliothek verfügbar
The approved original version of this thesis is available in print at TU Wien Bibliothek.

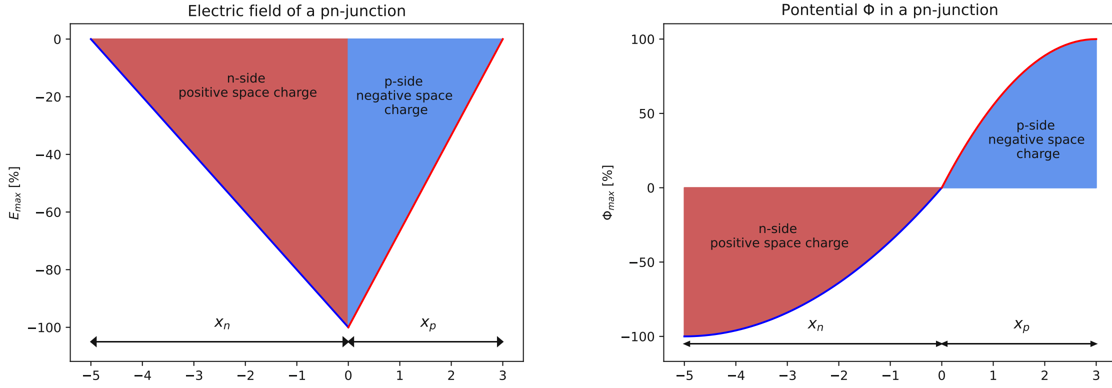

Figure 9: $E(x)$ and $\Phi(x)$ inside the diode; $x_\text{n} \neq x_\text{p}$, so Φ has no 'smooth' transition but is continuous.

The difference $\Phi(x_\text{p}) - \Phi(-x_\text{n})$ is called built-in voltage V_{bi} and represents an important parameter for designing a pn-junction. Another name of V_{bi} is diffusion voltage $V_\text{diffusion}$ [54]. This voltage is responsible for the resulting diffusion current $j_\text{diffusion}$. Thermally generated electrons/holes are attracted by this potential and drift towards the pn-interface for recombination. The diffusion voltage $V_\text{diffusion}$ yields the following [53, 54]

$$V_\text{diffusion} = \Phi(x_\text{p}) - \Phi(-x_\text{n}) = \frac{eN_\text{A}}{2\varepsilon_0\varepsilon_\text{r}} x_\text{p}^2 + \frac{eN_\text{D}}{2\varepsilon_0\varepsilon_\text{r}} x_\text{n}^2 = \frac{e}{2\varepsilon_0\varepsilon_\text{r}} \cdot (N_\text{A} x_\text{p}^2 + N_\text{D} x_\text{n}^2). \tag{32}$$

As it was mentioned before, $N_\text{D} x_\text{n} = N_\text{A} x_\text{p}$ must hold for the diode. Using the maximum electric field at $x = 0$

$$|E_\text{max}| = \frac{eN_\text{D} x_\text{n}}{\varepsilon_0\varepsilon_\text{r}} = \frac{eN_\text{A} x_\text{p}}{\varepsilon_0\varepsilon_\text{r}}, \tag{33}$$

$V_\text{diffusion}$ can be simplified with the help of the total width of the depletion zone $w = x_\text{n} + x_\text{p}$. [53, 54]. According to Eq. (32), the diffusion voltage holds

$$V_\text{diffusion} = \frac{1}{2}|E_\text{max}|(x_\text{n} + x_\text{p}) = \frac{1}{2}|E_\text{max}|w. \tag{34}$$

The approach to apply the derived equations for the purpose of using a pn-junction as a particle detector is discussed in section 3.3. An even more elegant way to calculate the diffusion voltage is the use of the difference of the Fermi levels directly. Thus, only the new Fermi level due to the concentrations of the dopant, the intrinsic material Fermi level as well as the temperature are relevant [53, 54]. The Fermi level shifts according to

$$E_{F,n} - E_{F,i} = e\Phi_n = k_\text{B}T \ln N_\text{D} - k_\text{B}T \ln n_\text{i}, \tag{35}$$

$$E_{F,i} - E_{F,p} = e\Phi_p = k_\text{B}T \ln n_\text{i} - k_\text{B}T \ln n_\text{A}. \tag{36}$$

Therefore, $V_\text{diffusion} = \Phi_p - \Phi_n$ leads to the following expression:

$$V_\text{diffusion} = \frac{k_\text{B}T}{e} \ln \frac{N_\text{D}N_\text{A}}{n_\text{i}^2}. \tag{37}$$

Die approbierte gedruckte Originalversion dieser Diplomarbeit ist an der TU Wien Bibliothek verfügbar
The approved original version of this thesis is available in print at TU Wien Bibliothek.
TU WIEN Bibliothek Your knowledge hub

3.2 The Influence of a Bias Voltage

Diodes are used in electronics for multiple purposes as they show a different behavior when being biased with external voltage. The natural equilibrium (see Fig. 10a) of thermal diffusion of charge carriers and their inhibiting effect of establishing the diffusion voltage is disturbed. Now, biasing widens (reverse bias) or narrows (forward bias) the depletion zone [54]. Mathematically, the behavior of a diode can be described with the Shockley-equation [53]

$$I = I_0 \cdot \left(\exp\left(\frac{eV_{\text{bias}}}{k_{\text{B}}T}\right) - 1 \right). \tag{38}$$

I_0 is the maximum current through the diode caused by thermal generation of electrons and holes. It leads to the so called leakage current. Additionally, the current is temperature dependent $\propto e^{-\frac{1}{T}}$. This dependency is key to improve the efficiency of a particle detector by cooling.

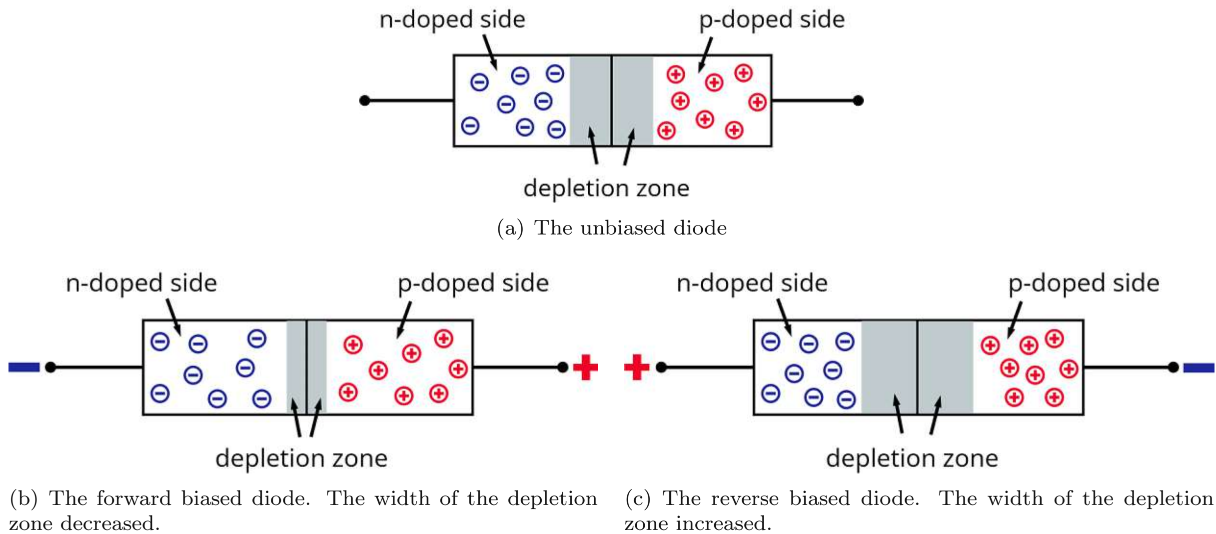

(a) The unbiased diode

(b) The forward biased diode. The width of the depletion zone decreased.

(c) The reverse biased diode. The width of the depletion zone increased.

Figure 10: The operational modes of a diode. The + and − in the figures represent the dopant atoms (+ for acceptors, − for donators) and not the space charge polarity. The polarity of the space charge is positive in the grey area for the n-type material and vice versa.

Forward Bias Mode: $V_{\text{bias}} > 0$

In forward bias mode, the positive voltage is connected to the p-type and vice versa as shown in Fig. 10b. In this case, the charge carriers are attracted by the potential on the opposite side and enter the former depletion zone. This results in a narrowing of the SCR. If the bias voltage compensates $V_{\text{diffusion}}$ charge carriers can move through the pn-junction unconstrained. The current increases exponentially the higher the bias voltage is. If V_{bias} is smaller than $V_{\text{diffusion}}$, still small reverse current is measureable due the diffusion current [53, 54].

Reverse Bias Mode: $V_{\text{bias}} < 0$

Connecting the negative potential to the p-doped side causes the opposite effect. The charge carriers are forced to move away from the pn-interface and the depletion zone increases as shown in Fig. 10c. Now, only the leakage current is present. This mode is discussed in detail in section 3.3 - applying a reverse bias voltage is the simplest way to operate a diode as a particle detector. Last but not least, there exists

Die approbierte gedruckte Originalversion dieser Diplomarbeit ist an der TU Wien Bibliothek verfügbar
The approved original version of this thesis is available in print at TU Wien Bibliothek.
TU WIEN Bibliothek Your knowledge hub

a breakdown voltage, which limits the application of a reverse bias voltage. Increasing V_{bias} over this limit results in a strong reverse current as the junction cannot withstand the strong $\vec{E}$-field [53, 54].

3.3 Using a Diode as a Detector

For the purpose of detecting ionizing radiation, diodes have to be designed carefully according to the experimental requirements. In most cases, the n-type and the p-type material are not doped equally [54]. The thickness of the doped regions usually differ significantly. For example, a p-in-n diode has a heavily doped p-type (p^+) implant on top of a n-type bulk. We choose a large n-doped volume with thickness x_{n} with a p-type layer (thickness x_{p}) on top. Thus, $x_{\mathrm{n}} \gg x_{\mathrm{p}}$, which is an important relation later. A particle impinges the material and looses energy due to collisions. This may cause the excitation of electrons into the conduction band. However, the intrinsic charge carrier concentration n_{i} must be considered. Generally, this number is much greater than the number of electron-hole-pairs generated by ionization [54]. There exist two approaches to get rid of unwanted charge carriers in the detector bulk. First, reducing temperature is a possible solution, as the intrinsic charge carrier density $n_{\mathrm{i}} \propto T^{3/2} e^{-\frac{1}{T}}$ [54]. A more convenient way is to apply a high reverse bias voltage as mentioned previously. This increases the width of the depletion zone. If the material is fully depleted, no charge carriers are present in the whole doped material. The depleted zone is named active region. Now, charge contributing to the conduction mechanism created by ionization can be detected easily. A scheme of how a semiconductor particle detector works is provided in Fig. 11. The interaction mechanism itself depends on the particle type; particles carrying charge (e.g. protons) interact in another way than neutral particles (e.g. photons) do. [54].

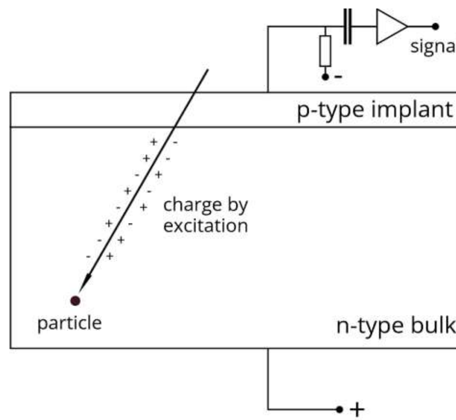

Figure 11: The basic principle of detecting a particle, which deposited energy in the (n-type) bulk. The impinging particle excites electrons into the conduction band and creates electron-hole-pairs. The induced charge is collected via the reverse bias voltage and read out by a capacitor.

To excite an electron into the conduction band, at least the energy equal to the band gap E_g must be deposited in the material during a single collision. High-energetic particles may do this multiples times by scattering. The number N_{carriers} of induced electron-hole-pairs is given approximately by the total deposited energy and the average energy $\langle E_{\mathrm{coll}} \rangle$ transferred in a collision via

$$N_{\mathrm{carriers}} = \frac{E_{\mathrm{deposited}}}{\langle E_{\mathrm{coll}} \rangle}. \tag{39}$$

TU Bibliothek Your knowledge hub WIEN
Die approbierte gedruckte Originalversion dieser Diplomarbeit ist an der TU Wien Bibliothek verfügbar
The approved original version of this thesis is available in print at TU Wien Bibliothek.

Clearly, $\langle E_{\mathrm{coll}} \rangle > E_{\mathrm{g}}$ to achieve excitation [14]. In section 3.1 equation (34) was derived and will be now specified for the operation of a diode as a particle detector. In general, in detectors one doped region possesses more volume than the other; this allows a determination of the width of the depletion zone. We arbitrarily chose $x_{\mathrm{n}} \gg x_{\mathrm{p}}$ before, which leads to the simple relation $w = x_{\mathrm{n}} + x_{\mathrm{p}} \approx x_{\mathrm{n}}$ for the total width of the depletion zone [54]. Thus, the diffusion voltage is calculated by

$$V_{\mathrm{diffusion}} = \frac{e N_{\mathrm{D}} x_{\mathrm{n}}}{2\varepsilon_0 \varepsilon_{\mathrm{r}}} (x_{\mathrm{n}} + x_{\mathrm{p}}) \approx \frac{e N_{\mathrm{D}} w^2}{2\varepsilon_0 \varepsilon_{\mathrm{r}}}. \tag{40}$$

An often used quantity to describe the dopant concentration is the resistivity ρ. The resistivity connects the dopant concentration by

$$\rho = \frac{1}{e \mu N_{\mathrm{D}}} \tag{41}$$

with the mobility μ of the major charge carrier. Hence, it is suitable to characterize the material from which the active region of a semiconductor particle detector is made of. Now, it is possible to write $V_{\mathrm{diffusion}}$ in dependency of the mobility and the resistivity via [54]

$$N_{\mathrm{D}} = \frac{1}{e \mu \rho}, \tag{42}$$

leading to the relation

$$V_{\mathrm{diffusion}} = \frac{1}{2 \mu \rho \varepsilon_0 \varepsilon_{\mathrm{r}}} w^2. \tag{43}$$

Within the equation above and the additional bias voltage V_{bias}, the width of the depletion zone is given by [54]

$$w = \sqrt{2 \varepsilon_0 \varepsilon_{\mathrm{r}} \rho \mu (V_{\mathrm{diffusion}} + V_{\mathrm{bias}})}. \tag{44}$$

If $V_{\mathrm{bias}} \gg V_{\mathrm{diffusion}}$ the diffusion voltage can be neglected and the width of the depletion zone only depends on the bias voltage [54] by

$$w = \sqrt{2 \varepsilon_0 \varepsilon_{\mathrm{r}} \rho \mu V_{\mathrm{bias}}}. \tag{45}$$

Clearly, an important point of interest is the full depletion voltage V_{FD}. At this point, the detector is fully depleted and no more charge carriers are present. Thermally generated charge carriers are swiped out of the detector volume completely [14]. In reference to V_{FD}, this mode is called over-depletion. Unfortunately, this leads to the increase of the leakage current as charge carriers are attracted by the bias voltage. It is a downside which can be reduced by cooling as low temperatures suppress the generation of free charge carriers. Using the formula above and D for the whole diode length, V_{FD} can be calculated the following way [14, 54]:

$$V_{\mathrm{FD}} = \frac{D^2}{2 \varepsilon_0 \varepsilon_{\mathrm{r}} \mu \rho}. \tag{46}$$

As soon as $V_{\mathrm{bias}} > V_{\mathrm{FD}}$, the electric field inside the diode gets an offset on the geometric borders of the

Die approbierte gedruckte Originalversion dieser Diplomarbeit ist an der TU Wien Bibliothek verfügbar
The approved original version of this thesis is available in print at TU Wien Bibliothek.
TU WIEN Bibliothek Your knowledge hub

volume. The function of $E(x)$ is the following [14]:

$$E(x) = \frac{2V_{\mathrm{FD}}}{D}\left(1 - \frac{x}{D}\right) - \frac{V_{\mathrm{bias}} - V_{\mathrm{FD}}}{D}. \tag{47}$$

This leakage current is dominated by the Shockley-Read-Hall transitions (see section 2.3.3) and the average lifetime of the charge carriers. The leakage (reverse) current current per cross-section j_{R} is

$$j_{\mathrm{R}} = e \cdot G_{\mathrm{SCR}} \cdot w = \frac{1}{2} \cdot e \cdot n_{\mathrm{i}} \cdot \sigma \cdot v_{\mathrm{th}} \cdot N_{\mathrm{t}} \cdot w \tag{48}$$

and is determined by the generation rate G_{SCR} (transmission rates $R_{\mathrm{e,h}}$) of charge in the space charge region [14]. The total leakage current is $I_{\mathrm{L}} = j_{\mathrm{R}} \cdot A$. Now, $w \propto \sqrt{V}$ and so this dependency holds also for j_{R}. Moreover, the intrinsic charge carrier concentration n_{i} also appears in j_R, establishing the known temperature dependency. If a bias voltage is applied the pn-junction acts as a capacitor with capacity C. Therefore, C depends on V_{bias} and remains constant after the bias voltage reached V_{FD}. The capacity of a plate capacitor is $\propto A/D$ and the following relation holds [14]

$$C(V_{\mathrm{bias}} \leq V_{\mathrm{FD}}) = A\sqrt{\frac{\varepsilon_0 \varepsilon_{\mathrm{r}}}{2\mu\rho V_{\mathrm{bias}}}} \tag{49}$$

$$C(V_{\mathrm{bias}} > V_{\mathrm{FD}}) = A\frac{\varepsilon_0 \varepsilon_{\mathrm{r}}}{D}. \tag{50}$$

Measuring the capacitance of the diode is also an approach to determine the full depletion voltage V_{FD}.

3.4 Detector Signals

The main principle of a semiconductor detector is collecting electric charge very fast. In the late 1930's Shockley and Ramo stated the following theorem, which extends the model of induced current by a moving charge carrier [55, 56]. In the low frequency regime, the assumption is valid, that the current is determined by the number of arriving charge carriers at an electrode. For high frequencies, this theory must be adopted. Also, the instantaneous movement of charge has an effect on the collected charge and current on the electrode [55]. To derive the equation found by Ramo [55] a few ideal conditions must be met. This involves a unit potential between the electrodes (e.g. an infinite plate capacitor) and neglect of any space charge in between. Hence, the induced charge Q and the current i depend on the instantaneous velocity of the point charge q, the so-called weighting field E_{w} and the unit potential V_{w} at the position x of q [55, 56]. The charge and the current can be written as

$$Q = -q \cdot V_{\mathrm{w}}(x) \tag{51}$$

$$i = q \cdot \vec{v}_{\mathrm{q}} \vec{E}_{\mathrm{w}}(x). \tag{52}$$

The weighting field depends on the geometry of the arrangement. For simple parallel plate capacitors - which semiconductor diode particle detectors in the first approximation are - the weighting field is $1/D$. The weighting field therefore describes the ability to induce current in the corresponding electrode. It can be calculated if the drift velocity is known [14].
The actual movement and drift velocity $\vec{v}$ of the charge carriers are determined by the actual electric field and the mobility $\mu_{\mathrm{e,h}}$ of electrons and holes [57]. The mobility is a macroscopic property, which considers all interactions. It is a convenient approach to model the movement of charge carriers in an electric field

Die approbierte gedruckte Originalversion dieser Diplomarbeit ist an der TU Wien Bibliothek verfügbar
The approved original version of this thesis is available in print at TU Wien Bibliothek.
TU WIEN Bibliothek Your knowledge hub

$\vec{E}$ [57]. This concept yields:

$$\vec{v}_\mathrm{e} = \mu_\mathrm{e}\vec{E} \tag{53}$$
$$\vec{v}_\mathrm{h} = \mu_\mathrm{h}\vec{E}. \tag{54}$$

An applicable approach to describe the drift movement is the Drude model [58]. Within this model, the mobilities of charge carriers can be calculated using only a single parameter: the relaxation time τ. All interactions (mainly collisions and change of momentum) are taken into account and an effective value is derived, which results in τ. The relaxation time itself depends on multiple contributions and they in turn depend on the temperature. Hence, a differential equation can be constructed to model the drift velocity [57]

$$m_\mathrm{eff}\left(\dot{\vec{v}}_\mathrm{D} + \frac{v_\mathrm{D}}{\tau}\right) = q\vec{E}. \tag{55}$$

For stable conditions, it is acceptable to consider that the drift velocity is constant. According to this assumption, the rate of change $\dot{\vec{v}}_\mathrm{D} = 0$ and the equation (55) simplifies to [57]

$$m_\mathrm{eff}\frac{v_\mathrm{D}}{\tau} = qE. \tag{56}$$

Isolating $v_{\mathrm{D;e,h}}$ in equation (56) leads directly to the term for the mobility

$$\mu_\mathrm{e,h} = \frac{q\tau}{m_\mathrm{eff}^\mathrm{e,h}}. \tag{57}$$

Thus, the simple relation $v_\mathrm{D} = \mu E$ follows for the drift velocity. As long as the charge carriers are drifting towards the electrodes, a signal can be obtained. Depending on the lateral position where the charge is created, the duration of the signal is determined. The signal induced from a single carrier stops immediately after it reaches the electrode. In the case of an impinging particle, charge is created along its path throughout the material. For the reason of simplicity, the projectile moves through the total active volume of thickness D and excites N charges along its path uniformly [57]. Therefore, the total line charge is $\pm Ne$ and each carrier has a different drift distance towards the electrode. This results in linear decreasing current

$$i(t) = Ne\frac{v_\mathrm{D}}{D}\left(1 - \frac{v_\mathrm{D}}{D}\cdot t\right) \qquad 0 < t < \frac{D}{v_\mathrm{D}}. \tag{58}$$

depending on the length D of the depletion zone and the drift velocity vD, after the first carrier arrived at the electrode [57].

3.5 The Transient Current Technique (TCT)

A very reliable method to study the properities of specific sensors is the so-called Transient Current Technique (TCT). TCT setups use ultra-fast pulsed Laser-systems and wide band oscilloscopes. The Laser simulates a particle impinging the detector bulk and creates charge by ionization [14]. The charge drifts towards the electrodes where it gets collected. Both carriers contribute to the signal due to their

Die approbierte gedruckte Originalversion dieser Diplomarbeit ist an der TU Wien Bibliothek verfügbar
The approved original version of this thesis is available in print at TU Wien Bibliothek.
TU WIEN Bibliothek Your knowledge hub

drift velocities and the weighting field [14]

$$I_{\mathrm{e,h}}(t) = -N_{\mathrm{e,h}}\vec{E}_{\mathrm{w}}\vec{v}_{\mathrm{e,h}}(t). \tag{59}$$

In total, the current $I(t) = I_{\mathrm{e}}(t) + I_{\mathrm{h}}(t)$ is recorded. For simple diodes $E_{\mathrm{w}} = \frac{1}{D}$ and in all cases $v = \mu E$ holds, which leads to

$$I(t) = -\frac{N_{\mathrm{e}}(0)\mu_{\mathrm{e}}E(\vec{r}(t)) + N_{\mathrm{h}}(0)\mu_{\mathrm{h}}E(\vec{r}(t))}{D} \tag{60}$$

for the signal current [14]. It must be noted, that the electric field depends on the position of the carriers, which is time dependent. Depending on the surface which is chosen to be exposed to the Laser beam, the TCT-experiment is named top-TCT or edge-TCT. The energy of the photons is below the displacement energy of the bulk atoms and creates no further damage inside the crystal [59]. The signal shape can differ strongly on the position where the charge was induced. Hence, it is possible to conduct research about the properties of electrons or holes specifically. This is done by creating charge close to a p-type (n-type) implant for studies about electrons (holes). The opposite charge carriers recombine instantly after creation and do not contribute to a signal [13].

With TCT the full depletion voltage can be determined easily using holes as shown in Fig 12. Holes are chosen, as they have minor mobility than electrons and exhibit longer signals [14]. To measure V_{FD}, the bias voltage is raised stepwise, increasing the depletion zone. Also, the electric field covers a bigger volume the higher V_{bais} is. As long as the diode is not fully depleted, $\vec{E} \neq 0$ only in the SCR. The Laser is injected into the backside, which is not contacted by the depletion zone at $V_{\mathrm{bias}} = 0$. Below V_{FD}, holes must diffuse through the non-depleted region until they reach the depletion zone and are attracted by the electrical field [14]. Due to the diffusion, the carriers arrive little by little. The increase seen in 12 is caused by the weighting field, as fast moving electrons induce a current depending on E_{W} [14]. For $V_{\mathrm{bias}} > V_{\mathrm{FD}}$ the carriers are attracted by $\vec{E}$ which is greater than 0 at the electrodes. Now, the linear decrease of the current - see Eq. (58) - can be obtained. As soon the current shows a maximum, V_{FD} is reached. Another important field, in which TCT is used extensively, is the investigation of previously irradiated sensors [60]. An aspect of interest here is the charge collection efficiency; for this measurement the integrated current ($Q = \int I(t)\mathrm{d}t$) is measured and compared to an unirradiated reference sample [14].

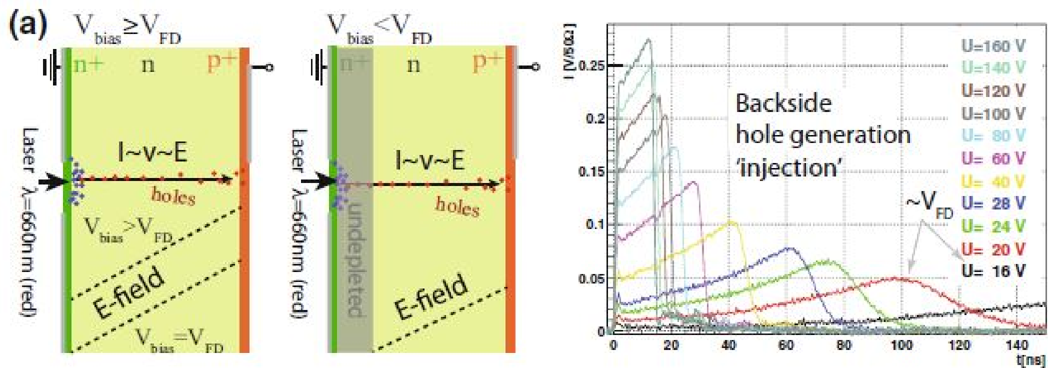

Figure 12: Determination of V_{FD} in a Si-detector using holes. The Laser is injected into the n-type material and holes drift towards the p-type region. V_{FD} is between 10 V and 20 V as a maximum appears here for the first time [13].

TU WIEN Bibliothek Your knowledge hub
Die approbierte gedruckte Originalversion dieser Diplomarbeit ist an der TU Wien Bibliothek verfügbar
The approved original version of this thesis is available in print at TU Wien Bibliothek.

The transient current technique gained huge popularity due its relative simple setup combined with a large number of approaches to study detectors. In recent years, UV-Lasers have been accessible and TCT measurements where applicable for studies on wide band gap semiconductor devices as silicon carbide [14]. This method has big advantages over radioactive sources like Am-241 (alpha source) or Fe-55 (beta source). Radioactive sources eject particles statistically in every direction with a specific energy, depending on their decay scheme. In comparison, TCT experiments can be repeated easily under the exact same conditions as the Laser driver provides full control over the operation. Even pile-up effects can be avoided on purpose. Most Laser drivers offer the possibility to send trigger signals to other devices like oscilloscopes. For a perfect alignment, the repetition rate can be set in a way to achieve sufficient data collection with clear peaks in defined intervals [14].

TU WIEN Bibliothek Your knowledge hub
Die approbierte gedruckte Originalversion dieser Diplomarbeit ist an der TU Wien Bibliothek verfügbar
The approved original version of this thesis is available in print at TU Wien Bibliothek.

4 Silicon Carbide

4.1 General Physical Properties

Silicon carbide consists of a silicon atom and a carbon atom per formula unit and is denoted as SiC therefore [17].. Both atoms are located in the fourth main group of the periodic system and own four valence electrons. These elements differ in electronegativity, which causes a slightly positive charged area around the silicon atoms. Measurements of the composition of the binding mechanism yield a small contribution of 12 % ionic bonding [17]. In solid state, polytypism occurs: silicon carbide forms different crystal lattices, depending on their stacking sequence of the silicon-carbon-pairs. In most studies, four to five polytypes are stated as thermodynamically stable and are considered as the basic crystal structures [17, 24]. Silicon carbide is a semiconductor with a large band gap and a high electron saturation velocity [23]. Moreover, it shows a high thermal conductivity and high displacement energy for lattice atoms [21]. Additionally, a high electric breakdown field of a couple of MeV cm^{-1} indicates a hardness against high bias voltages [61]. This mix of properties makes this material an interesting and promising candidate for detector devices. According to that, many studies about silicon carbide itself, the polytypes and measuring its properties have been conducted recently.

4.2 The Lattice Configurations and Their Properties

The most important polytypes are 3C-SiC, 4H-SiC and 6H-SiC. C and H stand for cubic and hexagonal symmetry, respectively [23]. In literature, cubic SiC is also denoted as β-SiC and hexagonal configurations as α-SiC [62]. There also exists a 2H, 15R (rhombohedral) and a few other configurations [17, 23, 24] which will not be discussed here. Pure single crystals show different electrical properties, which will be presented below [63]. The cubic configuration repeats itself every three layers as it is denoted by the 3 in 3C. Therefore, 3C-SiC owns a simple ABC stacking sequence. More important for detector applications are the 4H-SiC and 6H-SiC polytype, especially 4H [21, 63]. In a hexagonal lattice, the silicon and carbon atoms are forming tetrahedrons with a carbon atom in the center surrounded by four silicon atoms in the corners of the tetrahedron. Hence, in the next layer the silicon atom has four carbon neighbors in the same structure of a tetrahedron. The result are alternating layers of silicon and carbon. The atom in the next layer has two possible positions; in the same location as the atom underneath the atom or one position shifted. The number in front of the H represent the number of layers after the structure repeats itself. The 4H-SiC and 6H-SiC polytype only differ by the orientation of the next tetrahedral center which result in another stacking sequence. For 4H-SiC, this sequence is ABCB and ABCACB for 6H-SiC. [23]. The projections of the lattices are shown in Fig. 13.

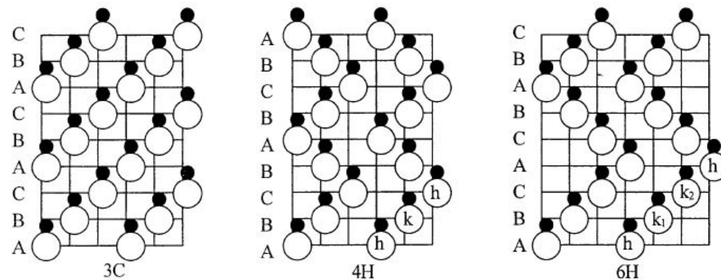

Figure 13: The three main polytypes of SiC. Silicon atoms are shown in white, while carbon atoms are black. The layers are denoted by A, B and C [23].

Die approbierte gedruckte Originalversion dieser Diplomarbeit ist an der TU Wien Bibliothek verfügbar
The approved original version of this thesis is available in print at TU Wien Bibliothek.
TU Bibliothek WIEN Your knowledge hub

Depending on their crystal structure, the polytypes also differ in their electronic properties like the band gap. While E_g is 2.39 eV for 3C-SiC, [61] it is 3.26 eV for the 4H lattice [61]. For every discussed kind of crystal structures, the electron saturation velocity is $2 \cdot 10^7\,\mathrm{cm\,s^{-1}}$ [23]. Coutinho et al. [61] compare in a review article the most important properties for these polytypes which are shown in Table 1.

Property	symbol	unit	3C-SiC	4H-SiC	6H-SiC
band gap	E_g	eV	2.39	3.26	3.03
electron mobilties	$\mu_{\mathrm{e},\parallel}$	$\mathrm{cm^2/(Vs)}$	750	800	97
	$\mu_{\mathrm{e},\perp}$	$\mathrm{cm^2/(Vs)}$	750	880	360
hole mobilty	μ_h	$\mathrm{cm^2/(Vs)}$	40	115	90
Breakdown field	E_B	MV/cm	~ 4	~ 3	

Table 1: The most important properties of the 3C-, 4H- and 6H-SiC polytype [61].

4.3 A Closer Look on 4H-SiC

4H-SiC is the most promising candidate for future application as a detector in high energy physics. Although 4H-SiC was commercially available three years later then 6H-SiC [24], it is now mainly used in SiC devices. The extensive reserach on 4H-SiC is based on the fact, that the electron mobility is about one order of magnitude higher than in 6H-SiC [61]. A lot of effort has been put into studies regarding the material properties and understanding its fundamentals. The 4H stacking sequence is ABCB along the c-axis (parallel to the z-axis) and shown in Fig. 14a, with carbon atoms in black and grey, while silicon atoms are drawn in light and darker turquoise. The third layer is shifted compared to the first layer, which results in the 4H configuration. Otherwise, it would have been the simplest lattice, namely 2H. In other words, the bonds in the unit cell of the 4H lattice are half cubic bonds and half hexagonal bonds [24]. The fourth layer is similar to the second one again. The unit cell, which is the geometric difference between the polytypes, have other lattice constants along the c-axis while the inter atomic distance remains equal. The distance between the Si and C atoms a=3.0817 Å while the length of the unit cell c = 10.0791 Å [64].

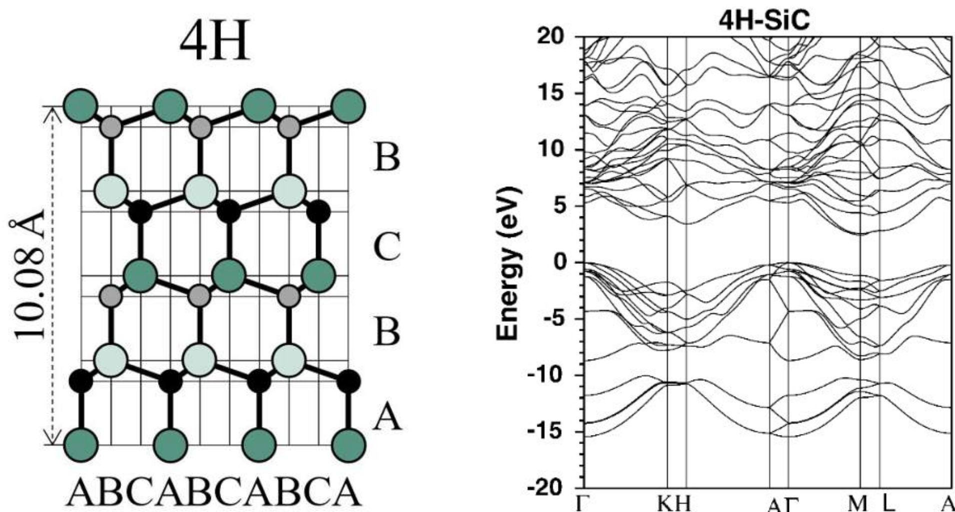

(a) The spatial configuration [65]. The x-axis shows the projection of the hexagonal lattice

(b) The electronic configuration [64]. The x-axis shows important points of the Brillouin zone.

Figure 14: The geometric and band structure properties of 4H-SiC.

Die approbierte gedruckte Originalversion dieser Diplomarbeit ist an der TU Wien Bibliothek verfügbar
The approved original version of this thesis is available in print at TU Wien Bibliothek.
TU WIEN Bibliothek Your knowledge hub

As it was mentioned before, 4H-SiC has the broadest band gap among the polytypes and is an indirect semiconductor. Thus, the location of the valence band maximum and the minimum of the conduction band are not located on the same k-vector in the first Brillouin zone. The Brillouin zone identifies the smallest $\vec{k}$-vectors in each possible direction [39]. According to [64], 192 k-vectors are possbile. The transition from the valence band into conduction band takes place via the points Γ-M with a change of $\vec{k}$ [64, 66] as shown in Fig. 14b. Many calculations have been performed on the band structure; by now, the theoretical results and experimental values for the band gap of 3.26 eV agree well with each other [64, 66]. Examining the band gap is not the only energetic property where many experiments have been conducted. An important property for particle detectors is the amount of energy, which is needed to create an electron-hole-pair. In 2013 Chaudhuri et al. [67] reported a value of 7.28 eV for 4H-SiC specifically, which was found experimentally. Another important property is the displacement energy. It describes the energy to knock an atom out of is lattice position. As 4H-SiC consists of both silicon and carbon atoms, the displacement energy differs for each species [68]. For the carbon atom the displacement energy is 20 eV while it is 35 eV for silicon atoms [68]. For p-type 4H-SiC, a theoretical study exhibited an anisotropic hole drift [69]. This study claims a linear dependence on the electrical field for the drift parallel to the c-axis. On the other hand, for movement perpendicular to the c-axis a non-linear dependency was calculated [69].

In recent years, the techniques to grow 4H-SiC have evolved. SiC growth processes need high temperature environments and are still challenging procedures nowadays [70]. By 1996, 4H-SiC has been available in bulk form, although the purity was relatively poor [24]. Wafers comparable to silicon processing technology were only accessible up to a thickness of 500 µm [21]. High quality 4H-SiC can be produced by growing epitaxial layers on top of a bulk, while the thickness of this layer was limited to around 50 µm [21]. The best-quality 4H-SiC can be produced with growing this epitaxial layer on a 4°(in respect to the perpendicular plane of the wafer) cut silicon bulk. The tilted angle has the big advantage that only specific sites are possible to be bonded on [21]. This method increases the purity significantly. The processes themselves are mostly based on chemical vapor deposition (CVD) techniques with low grow rates around 1 µm/h. In comparison, the growth rate is in the mm/h range for the bulk [23, 70].

TU WIEN Bibliothek Your knowledge hub
Die approbierte gedruckte Originalversion dieser Diplomarbeit ist an der TU Wien Bibliothek verfügbar
The approved original version of this thesis is available in print at TU Wien Bibliothek.

5 Experimental Setup

Experiments were conducted at two different locations with the same set of irradiated SiC diodes. First, UV-Laser-TCT studies were carried out in the clean room of the Institute for High Energy Physiscs. Secondly, a similar study with protons was conducted at MedAustron [3]. In both series of series of experiments, nearly the same instruments were used. In the following section, the setup and method of the data analysis will be discussed.

5.1 The Samples

5.1.1 Properties of the SiC-Diodes

The silicon carbide diodes are provided by CNM (Centro Nacional de Microelectrónica, Barcelona, Spain) [71] for research purposes. The samples were manufactured during production run 8435 and run 13575. However, the diodes originating from these runs show identical properties. The p-on-n diodes have a 45 µm active epitaxial layer of n-doped SiC, with a heavily doped p^+ SiC layer on top. The resistivity of the active layer is 20 Ω cm. Additionally, a protective metallization layer made of Ti, W and Al as well a passivation layer (SiO_2 + Si_3N_4) is located on the surface. The base area of the active region of the diode is 3 mm × 3 mm and has no segmentation for spatial resolution purposes. The total width is 4.4 mm × 4.4 mm, the dimensions are shown in Fig. 15 as well as in Fig. 16. The cross section of the diode (Fig. 16 - taken from Rafí et al. [27, 72]) corresponds to a nearly identical diode with a segmentation of the p-type implant. This design is not valid for the diodes investigated in this thesis, as diodes originating from run 8435 and run 13575 have a continuous p-type implant. Also, the authors discuss the manufacturing process of the diodes in [72] in detail. The epitaxial layer of n-type 4H-SiC was grown on a 4H-SiC bulk which result in a total thickness of approximately 500 µm. In a previous Master's thesis, the full-depletion voltage of this diode was determined to be 296 V [73].

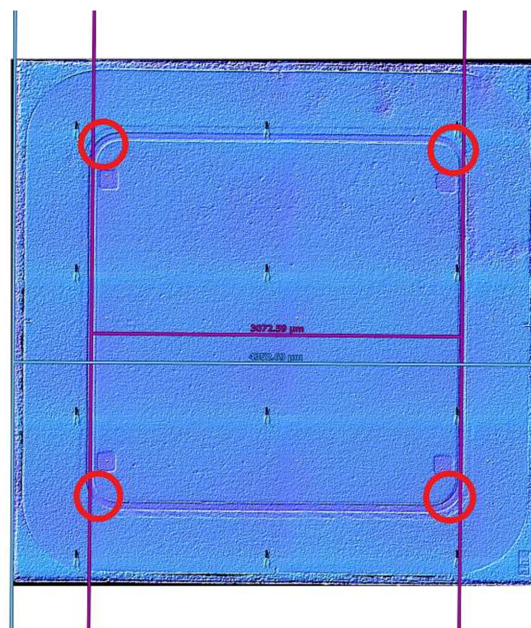

Figure 15: The CNM diode seen from above in a microscope. The active region is 3 mm×3 mm. The red circles indicate the spots the Laser was focused onto. The highest signals were achieved here.

Die approbierte gedruckte Originalversion dieser Diplomarbeit ist an der TU Wien Bibliothek verfügbar
The approved original version of this thesis is available in print at TU Wien Bibliothek.
TU Bibliothek WIEN Your knowledge hub

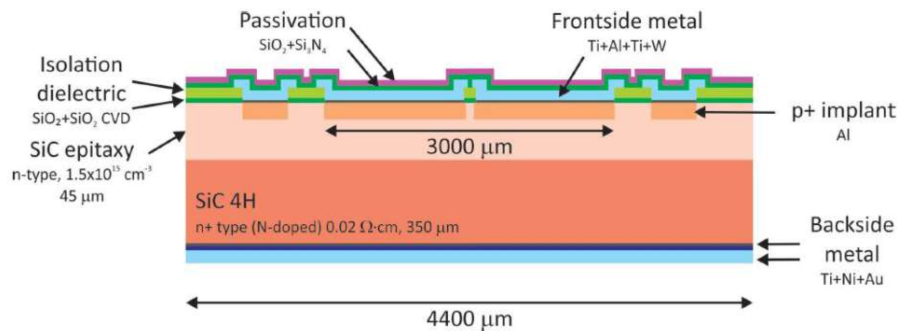

Figure 16: The cross section of the 4H-SiC diode provided by CNM [72]. The sensor which were evaluated in this work are not segmented and have a connected p^+ implant.

5.1.2 Irradiation of the Sensors

For this study, only the samples from production run 13575 were exposed to neutrons inside the reactor core at the Atominstitut of the Technical University of Vienna. The institute owns a 250 kW TRIGA Mark II reactor [1] for research purposes. As most research reactors, also this facility is built in a swimming-pool design. [74] The reactor core consists of roughly 3 kg enriched uranium with a 19.8 % amount of the fissionable isotope ^{235}U. Beside the continuous mode, the reactor can operate in a pulsed mode with a maxmimum of 250 MW for approximately 40 ms [1]. A negative temperature coefficient regarding the reactivity, slows down the chain reaction rapidly [75]. The research facility is equipped with a few beam tubes; the beam lines extract thermal, epithermal and fast neutrons. A previous thesis by P. Salajka [76] determined the factor, which is necessary to reduce the neutron energy spectrum to a monoenergetic equivalent flux. This allows to calculate the the necessary irradiation time to expose samples to a specific equivalent fluences [76]. As reference energy, the high energy physics standard of 1 MeV neutrons was used. The irradiation took place in advance of this thesis. The irradiated samples were stored at $-20°$C in a refrigerator at the Institute of High Energy Physics.

5.2 The Setup in the Cleanroom

5.2.1 The Testing Box

The testing environment is a shielded aluminum box with a home made experimental testing stage inside. As the box is a made out of metal, it also acts as a Faraday cage and shields the components from outside electro-magnetic fields. The whole setup is shown in Fig. 17, numbers 1 to 7 mark the instruments involved in the measurements. These components are:

1. Laser Head for the 370 nm UV-Laser [77]
2. Laser Driver PiLas DX [77]
3. High voltage supply / Source Source Measuring Unit SMU (Keithley 2470 Sourcemeter) [78]
4. Power supply for the TEC-controller and the LGAD board with the read-out electronics
5. Laser optics [79, 80]
6. Testing stage with the 'cold chuck'
7. DRS4 oscilloscope for analyzing the signal channel [2]

Die approbierte gedruckte Originalversion dieser Diplomarbeit ist an der TU Wien Bibliothek verfügbar
The approved original version of this thesis is available in print at TU Wien Bibliothek.
TU WIEN Bibliothek Your knowledge hub

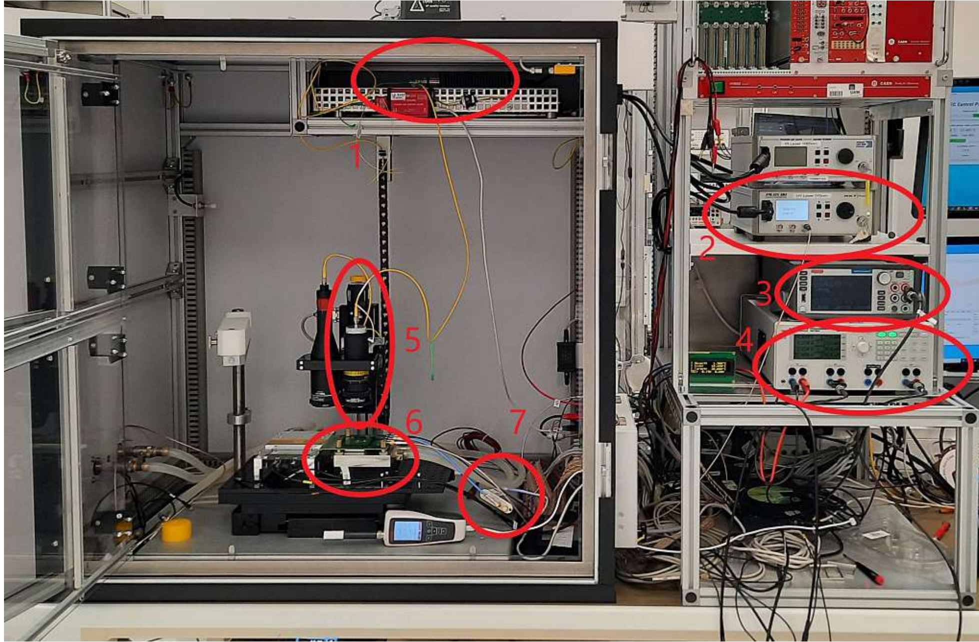

Figure 17: The Laser-TCT setup in the clean room, the numbers refer to the list in the text.

To ensure stable testing conditions, a few parameters must be held at constant values. First, detectors should be tested over a wide temperature range. Thus, a two-stage cooling and heating system is installed. The so called 'cold-chuck' reaches temperatures down to −30 °C and up to +50 °C. To achieve this, the later described sensor board is mounted onto an aluminum block, which is cooled/heated by a Peltier element (CP1.4-127-06L-RTV by Laird Technologies). Controlling the Peltier element is achieved by a Meerstetter 1090 TEC controller [81]. The emitted heat is transferred away by a cooling fluid system (Huber Ministat 240) [82] to the outside of the box. During cooling a device, also the humidity must be considered, there is no vacuum inside this environment. Spontaneous icing due to condensing water on the surface of the cold chuck, or even worse on the detector board, must be strictly avoided. This can cause severe damage or even destruction by unwanted electrical contacts. To lower the dewpoint of the air, the humidity inside the box must be reduced. In order to do so, dry air with a dewpoint of −60 °C is blown into the box. Within one minute the system is capable of injecting 200 L into the environment. The box is also equipped with two Laser units (PiL106-FC with $\lambda = 1060$ nm and PiL037-FC with $\lambda = 370$ nm, both from NKT Photonics) [77] which are also located inside the box. The used Laser system is described in detail below. Additionally, the Laser heads are placed on a shielded and covered shelf to avoid any breakout of radiation. Laser fibers guide the light outside from this shelf into the Laser optics and focus them onto the testing stage. Monitoring the Laser intensity is possible due to a Thorlabs PM 100 powermeter [83]. To ensure proper positioning of the Laser beam, the testing stage is mounted on a table, which is adjustable in the xy-plane. Vertical movements in z-direction are provided by moving the Laser optics up and down instead of the table. Cables are either brought into chamber via connector plugs on the outside of the box, or passed through a sidegate. Wherever it is possible, shielded cables are used to avoid any disturbing signals originating from electronics outside the testing box. All control units (Laser drivers) and the power supply for the devices (voltage and current supply, the Lasers and the TEC controller) are located in a rack next to the box. Necessary for powering the detector board are high voltage (up to ±1 kV) for biasing the detector and low voltage for the onboard electronics (+2.25 V, ≈ 16 mA). In addition, the second stage of the cooling system (the TEC controller and the Peltier element

Die approbierte gedruckte Originalversion dieser Diplomarbeit ist an der TU Wien Bibliothek verfügbar
The approved original version of this thesis is available in print at TU Wien Bibliothek.
TU Bibliothek WIEN Your knowledge hub

in series) needs a voltage supply of 24 V and uses up to 4 A. Controlling software for all components were mostly developed by HEPHY on a LabView and Python3 basis. A scheme how all units and instruments interact with each other or the control software is presented in Fig. 18.

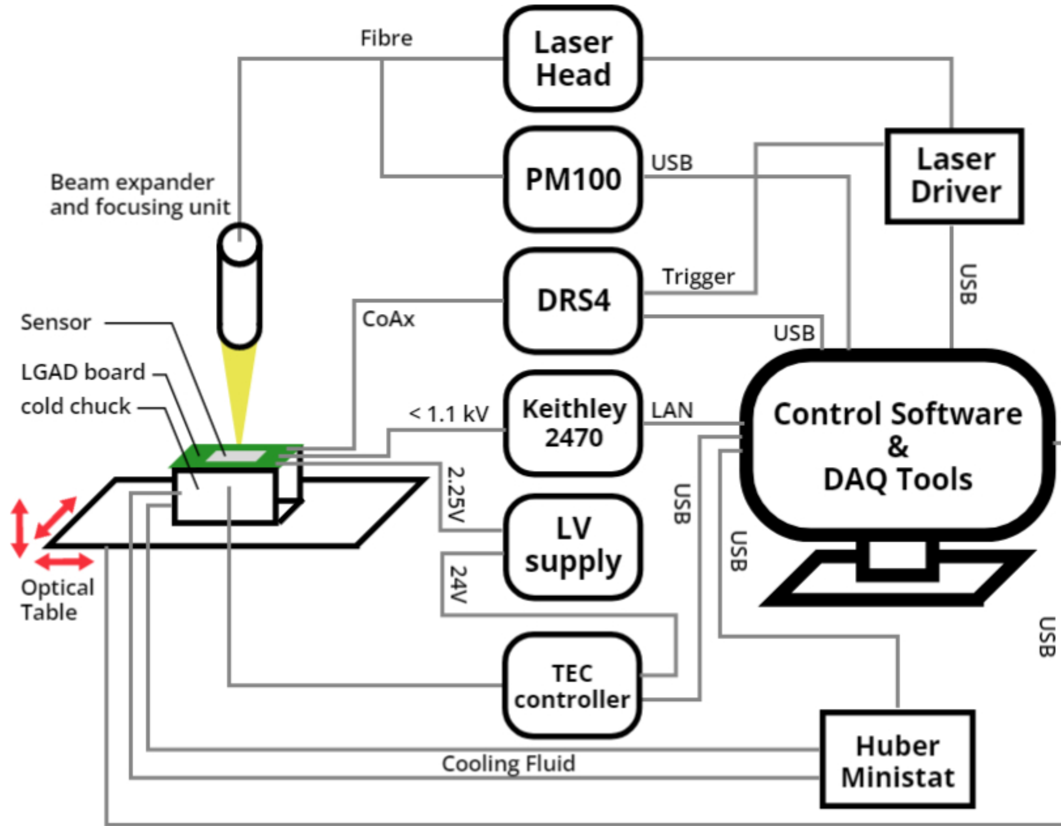

Figure 18: A simplified scheme of the Laser-TCT setup.

5.2.2 UV-LASER System

The excitation energy for the electrons in the semiconductor is provided by an UV-Laser system. The PiLas Picosecond Pulsed Diode Laser by NKT Photonics with a wave-length of 370 nm (PiL037-FC) [77] is installed in this setup. This wavelength is equal to a photon energy of 3.35 eV. The spectral width (full width at maximum) is 1.1 nm. As the Laser operates in a pulsed mode, there exists a maximum repetition rate of 40 MHz. The maximum power of a Laser pulse is 150 mW, while the average power at the maximum repetition is 330 µW. The presented values were measured at the internal 'tune value' of 30. The tune value describes the internal attenuation and 30 is the default value for a rate of 40 MHz. [77] However, for these experiments, only rates in the kHz and below are used. Taking the average power P_{avg}, the photon energy E_γ and the maximum repetition rate r_{max} into account, one can calculate the total energy per Laser pulse

$$E_{\mathrm{pulse}} = \frac{P_{\mathrm{avg}}}{r_{\mathrm{max}}} \approx 51.5\,\mathrm{MeV} \tag{61}$$

as well as the number of released photons

$$n_{\mathrm{photons}} = \frac{E_{\mathrm{pulse}}}{E_\gamma} \approx 1.54 \times 10^7. \tag{62}$$

Die approbierte gedruckte Originalversion dieser Diplomarbeit ist an der TU Wien Bibliothek verfügbar
The approved original version of this thesis is available in print at TU Wien Bibliothek.
TU WIEN Bibliothek Your knowledge hub

The calculation corresponds to the values given above. A Laser pulse lasts typically 150 ps - 300 ps and depends on the Laser settings. The manufacturer states that the jitter RMS value of the pulse width is 3 ps. The FWHM value of the pulse duration is known to be 44 ps [77]. The testing report of the manufacturer with all parameters is enclosed in Appendix C. The Laser is focused onto the testing stage via two more devices. At first, a beam expander by Edmund Optics [79] widens the Laser beam by the factor 20. Directly behind the widened Laser beam a coated plano-convex lense (focal lenght 100 mm) by Thorlabs [80] narrows it again. Within this setup, the Laser is shined on the smallest possible spot on the detector surface.

5.2.3 Inducing Signals

The generation of signals inside the detector was optimized due to the properties of the involved instruments. As the DRS4 evaluation board showed a maximum recording rate of approximately 500 events per second the repetition rate f_{rep} was set to 500 Hz. A big advantage of the Laser driver unit is that it is capable of sending a trigger pulse to other instruments. Therefore, the outgoing trigger pulse was sent to the DRS4 oscilloscope. This setup ensured that at least one signal peak per event was recorded. To create a signal, the Laser was focused onto the small slit between the passivation layers. These areas are indicated in Fig. 15 with red circles. This area is the only way to hit the active SiC volume without loosing too much intensity in layer above. The absorbed intensity of the laser beam is determined by Beer-Lambert's law. Thus, the law states the intensity of the Laser beam decreases exponentially inside a material. This laws depends on the attenuation coefficient μ_{A} and the thickness d of the material. The intensity is attenuated by

$$\frac{I_{\mathrm{deposited}}}{I_0} = 1 - e^{-\mu_{\mathrm{A}} d}, \tag{63}$$

this also holds for the Laser power, as the intensity is power per area. Thus, the estimated number of electron-hole-pairs can be derived. Assuming that one photon is able to create one electron-hole-pair, the number of the released photons - see Eq. (62) - times the attenuation is equal to the number of created electron-hole-pairs.

5.2.4 Readout Chain - UCSC Board and DRS4 Evaluation Board

The readout of the sensor in the cleanroom was based on two devices. At first, the diodes are bonded onto a readout board which is distributed by the University of California Santa Cruz (UCSC) [84]. This board is widely known as UCSC-board or just as LGAD-board (LGAD stands for Low Gain Avalanche Diode). It offers an analogue low noise amplification of bare detector signals, even in noisy environments [85]. For this work, a single channel readout board was used. The UCSC board is based on a transistor, which is sensitive to charge deposited on a coupling capacitor [86]. The diodes are bonded adhesively onto the bonding pad and connected to other side of the capacitor. The circuit acts like an inverting transimpendance amplifier, which can be described in the simplest way according to Ohm's law. An incoming current I_{in} gets converted into a voltage signal V_{put} and can be probed by an oscilloscope afterwards. The transimpedance Z_{trans} connects the properties by

$$U_{\mathrm{out}} = I_{\mathrm{in}} \cdot Z_{\mathrm{trans}}. \tag{64}$$

TU Bibliothek WIEN Your knowledge hub
Die approbierte gedruckte Originalversion dieser Diplomarbeit ist an der TU Wien Bibliothek verfügbar
The approved original version of this thesis is available in print at TU Wien Bibliothek.

For the configuration of the board used in this setup, the transimpedance Z is $470\,\Omega$. The bandwidth to transmitting signals in this configuration of the board is approximately 2 GHz [85]. The UCSC board is validated by various institutions including CERN [86] and has many applications in high energy physics. It owns four inputs and one output channel; the first input is the high voltage supply to bias the sensor bonded onto the board. The second one powers the amplifying circuit itself with 2.25 V and 15 to 17 mA. Moreover, there exist another two inputs for testing the impedance and for calibration of the board. The only output is the one where the oscilloscope can be connected for data acquisition purposes [86].

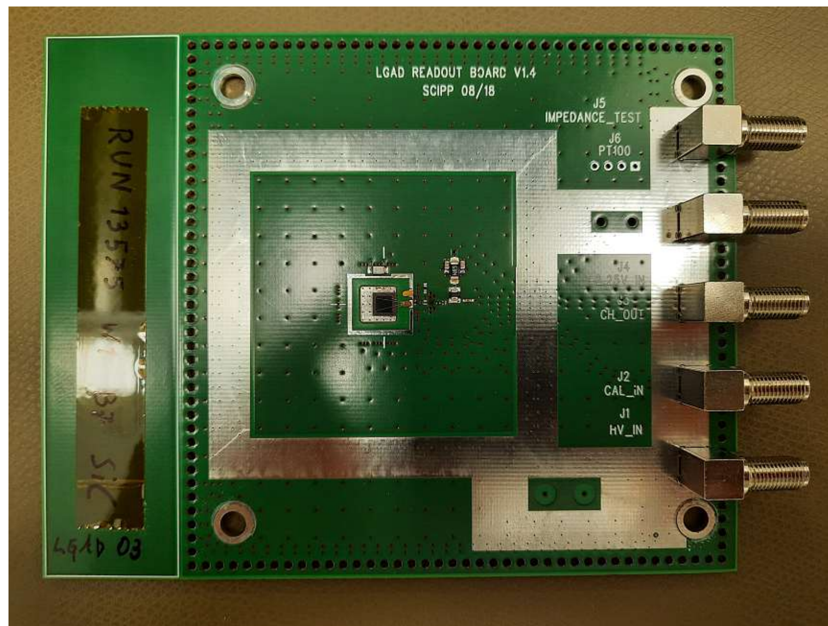

Figure 19: The UCSC-Board with a bonded 4H-SiC diode on the sensor pad. The connectors on the right side are: impedance test, low voltage in, channel out, calibration in and high voltage in (top from bottom).

The second instrument in the readout chain is the so-called DRS4 chip. Additionally, the exclusively for this chip designed evaluation board is also installed in this setup [87]. The DRS4 chip is distributed by the technology transfer program by the Paul Scherrer Institute (PSI), Switzerland [2]. In combination with the evaluation board it offers a simple and relatively cheap low-noise alternative to other oscilloscopes. The accuracy of the digitization is determined to an effective number of 11.5 bits [2]. DRS stands for Domino Ring Sampler and describes the technology of this device. The so called domino wave is the continuous storage of samples until the wave is stopped by setting a flag to 'high'. No cells are overwritten until every cell was shifted into the readout register [88]. The DRS4 chip is based on a switched capacitor array (SCA) with 1024 capacitors (storage cells) for each of the eight channels [88]. For the readout, a shift register is used, which is clocked at 33 MHz, regarding to a readout time of roughly 30 ns per cell. This leads to a dead time of approximately 31 µs. Sampling rates are adjustable between 700 MHz ($\Delta t \approx$ 1.43 ns) and 5.12 GHz ($\Delta t \approx$ 195 ps) [88]. Details on the electronics of the DRS4 chips are accessible in [88].

The most convenient way to use this device is the DSR4 evaluation board. It is responsible for the digitization and possesses interfaces to interact with this chip [89]. The evaluation board is designed in a way that it can be used as a digital four-channel oscilloscope. It must be noted that the maximum peak-to-peak voltage for each channel is just 1 V [89]. Powering this device is secured by an USB plug.

TU WIEN Bibliothek Your knowledge hub
Die approbierte gedruckte Originalversion dieser Diplomarbeit ist an der TU Wien Bibliothek verfügbar
The approved original version of this thesis is available in print at TU Wien Bibliothek.

This interface of the board is also used to send digitized data to some analysis software. Triggering the oscilloscope is possible in two ways; either a self triggering mode, using an internal channel or connecting th board to an external trigger pulse [89]. The PSI also distributes a simple oscilloscope software which displays the recorded samples and saves them to a binary (`.dat`) or in a better formatted `.xml` file [89]. The Institute of High Energy Physics extended this software to provide interfaces to other instruments. These devices are mainly installed at the Laser-TCT setup; In the case of this thesis, especially the interface to the sourcemeter and optical table was used.

(a) The front plane of the DRS4 evaluation board. It provides the USB port for power supply as well as data transfer, trigger in-/outputs and clock in-outputs.

(b) The back plane of the DRS4 evaluation board. Here the signal is fed in into channel 1 to 4. In this case, two channels are terminated with 50 Ω.

Figure 20: The DRS4 evaluation board seen from the front and back with all connectors.

5.2.5 IV-Measurements

The high voltage supply (Keithley 2470 Sourcemeter [78]) does not only provide the bias voltage, it also acts as a sourcemeter. The used model is capable of applying a maximum of ±1100 V, while measuring currents is possible in the range from a few pA to 1 A. Controlling the sourcemeter was achieved by a local network interface and is based on a Python3 script. The software provides full control of the unit and logging of the data, especially voltage and current. Measuring the current was achieved by averaging a specific number of samples to obtain one data point. The ramping rates for IV measurements to raise the voltage is usually relatively slow (1 V per 5 to 10 s). This allows to establish quasi-equilibrium states before increasing the bias voltage again.

5.3 The Beam Facility at MedAustron

In a second series of experiments, the diodes were tested in a particle beam environment at MedAustron [3]. Beside the medical purpose, also non-medical research is conducted. For this thesis, only the proton low flux setting was used [30]. In these setting, particle rates in the kHz, 100 kHz and MHz range are commissioned for seven specific proton energies between 62.4 MeV and 252.7 MeV [30]. To test the devices, a similar setup was designed like at the cleanroom at the Institute of High Energy Physics. The main difference is that the edge of the sensor was exposed to the proton beam, instead of the top surface. Unfortunately, an aluminum protection cover is soldered onto the UCSC-board where the particles have to travel through. The bias supply as well as powering the readout board was granted by the previously described instruments. Data acquisition was achieved by the DRS4 oscilloscope as

Die approbierte gedruckte Originalversion dieser Diplomarbeit ist an der TU Wien Bibliothek verfügbar
The approved original version of this thesis is available in print at TU Wien Bibliothek.
TU WIEN Bibliothek Your knowledge hub

well as a Rhode&Schwarz RTP oscilloscope [90] in parallel. The scheme of the setup presented in Fig. 18 is also valid for these experiments, except for the signal splitting. The setup itself is shown in Fig. 21a,b. The black planes in the left picture are two scintillators, which were used as beam monitor if flux is present. Hence, this data was not collected for this series of experiments. The red arrow in the right picture indicates the beam direction. The slightly present green Laser traces were used to achieve a proper positioning of the detector in the beam. Clearly, for the actual measurement these Lasers were switched off.

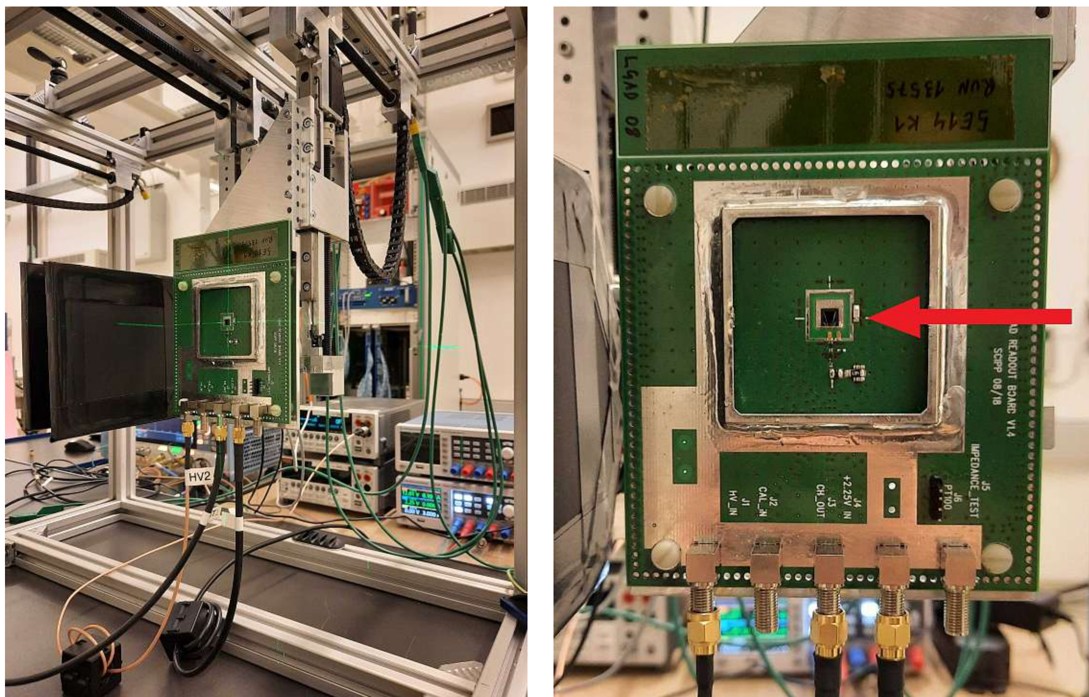

(a) The whole setup at MedAustron with all control units and additional instruments.

(b) The UCSC board in the setup with the protection cover.

Figure 21: The setup in the irradiation room for non-clinical research at MedAustron

5.4 Data Analysis

The channel-out of the UCSC readout board is connected to a DRS4 evaluation board [2] or the RTP oscilloscope [90]. The data are saved and analyzed afterwards. For this purpose, a homemade peak analysis software was developed on the basis of Python3. It is designed to investigate the events containing the peak data. The software characterizes each peak with the following parameters:

Parameter	Symbol	Unit	Physical meaning
peak maximum	V_{max}	V	the highest sample recorded by the oscilloscope
peak area	A_{peak}	Vs	calculated by numerical trapezoid integration, proportional to the created charge
time over threshold	t_{ToT}	s	the length of the signal
signal to noise ratio	SNR	dB	the intensity of the signal compared to the noise

Table 2: The four quantities to describe the signal peak.

Die approbierte gedruckte Originalversion dieser Diplomarbeit ist an der TU Wien Bibliothek verfügbar
The approved original version of this thesis is available in print at TU Wien Bibliothek.
TU Bibliothek WIEN Your knowledge hub

To obtain these values, not only the peak itself is recorded; instead, samples before and after the peak are saved additionally. The number of noise samples is at least two (in the case of silicon carbide and the DRS4 oscilloscope three) orders of magnitude greater than the number of peak samples. From all these samples, the mean μ and the standard deviation σ is calculated. As the number of noise samples is much higher than the number of peak samples, the influence on μ and σ of these few signal samples are neglected. Thus, μ can be considered as 'ground level' and σ as noise RMS (root mean square) value. Afterwards, this calculated mean is subtracted from every sample, this ensures that the mean of all samples is 0. If a sample has a greater difference then a specified number of σ from μ, this sample is considered a signal sample. The whole peak are all consecutive signal samples, if the condition of a minimal peak length is met. There exist two approaches to detect peaks. The first one is to apply a fixed value for the threshold. The second method is known as constant fraction discrimination (CFD). In this case, the highest sample is found first and the given fraction calculated as threshold. The parameter for the minimal peak length shall remove any noise signals originating from non-particle-impingement induced charge. This is important for the DRS4 oscilloscope data specifically. While the peak maximum as well as the time-over-threshold are found easily, the other properties need boundary conditions to be determined. Hence, the peak area is calculated by numerical integration of the voltage samples over a specific time interval. This interval is not only the time-over-threshold. For this purpose, there exist a parameter for the time interval of additionally considered samples before and after the first and last sample of the time-over-threshold interval. The idea is to try to consider all the remaining samples, which belong to the peak but stayed below the threshold. The area between the noise samples will average to zero and just the peak area remains. The signal to noise ratio SNR needs further data analysis: it is calculated from the RMS values of the signal and the noise samples via

$$SNR = 20 \cdot \log\left(\frac{V_{\mathrm{RMS,signal}}}{V_{\mathrm{RMS,noise}}}\right). \tag{65}$$

RMS values of discrete values are calculated by the equation

$$RMS_{\mathrm{k}} = \sqrt{\frac{1}{n_{\mathrm{k}}}\sum_{i=1}^{n_{\mathrm{k}}} x_{\mathrm{k}}^2}. \tag{66}$$

In this case, k can either be the signal (the peak) or noise and n_{k} represents the number of corresponding samples of the signal or noise, respectively. All parameters except the SNR are drawn in Fig. 22. The peak itself (green line) is a typical signal of a non-irradiated silicon carbide detector, operated at ambient conditions. As readout device, the DRS4 oscilloscope was used. The black dots mark the first and last sample, which are considered as part of the peak. All other peak samples are indicated as small red dots on the green signal line. This can be also seen as these points lay underneath the red line, which represent the threshold for being considered as a peak sample. Only these samples below the threshold contribute to the peak RMS value. The peak area is calculated between the samples named analysis borders and marked as green dots. The yellow line indicates the constant fraction discrimination threshold. This method is used to characterize the rising time of a peak. It allows a comparisson of peaks of different maxima which may be originating from different detectors. In Fig. 22, the CFD threshold is drawn at 25 % of the peak maximum. The CFD threshold can only be calculated, once the whole event data was analyzed.

TU Bibliothek WIEN Your knowledge hub
Die approbierte gedruckte Originalversion dieser Diplomarbeit ist an der TU Wien Bibliothek verfügbar
The approved original version of this thesis is available in print at TU Wien Bibliothek.

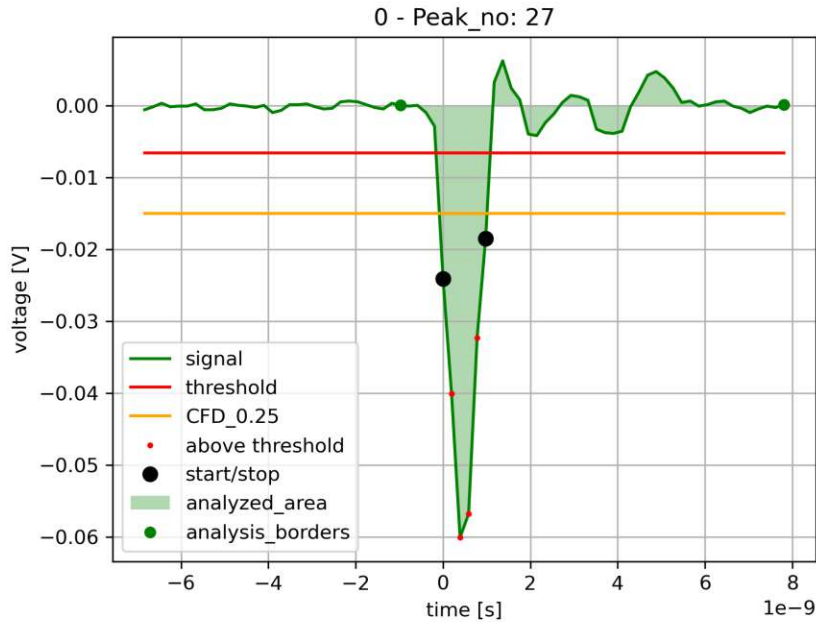

Figure 22: An example peak of an non-irradiated SiC detector. All relevant parameters for the analysis are marked for better understanding.

In order to obtain reliable results, the software generates statistics for all mentioned parameters. Typically, 10^4 to 10^6 events are recorded. The software provides the derived parameters for each peak as well as the mean and the standard deviation for each parameter. Moreover, the collected data are clustered (and saved in a file) in a histogram format (lower bound, upper bound, relative abundancy per data bin) in a `.csv`-file. Also, all plots are provided. To achieve a higher precision, the resulting data can be fitted with a Gaussian distribution. Within this approach, contributions originating from noise is minimized and best values for the distribution of the real signals are calculated. In the example histograms in Fig. 23a-d, the directly measured values are nearly equal to the means obtained after the fit. The biggest effect of the fit is the narrowing of the standard deviation. Hence, the standard deviation may be reduced to a third of the directly observed value, like in Fig. 23c. The directly measured mean and standard deviation is $(4.250 \pm 0.381) \times 10^{-11}$ Vs, while it is $(4.307 \pm 0.131) \times 10^{-11}$ Vs after fitting. Fitting the histograms has limitations to obtain reliable values; especially for the time-over-threshold in combination with broad bin widths. This parameter exhibits the majority of the values in the range of the lower limit. This may lead to 'bad' fitting parameters like standard deviations greater than the mean. This would mean that negative values for this parameter are observable, according to the fit. However, only parameters >0 are valid in this work. By now, data files originating from the DRS4 oscilloscope and RTP oscilloscope [90] by Rhode&Schwarz can be analyzed. Other data sources can be implemented easily, as long as the format is known and parsed correctly into the analysis software.

Die approbierte gedruckte Originalversion dieser Diplomarbeit ist an der TU Wien Bibliothek verfügbar
The approved original version of this thesis is available in print at TU Wien Bibliothek.
TU WIEN Bibliothek Your knowledge hub

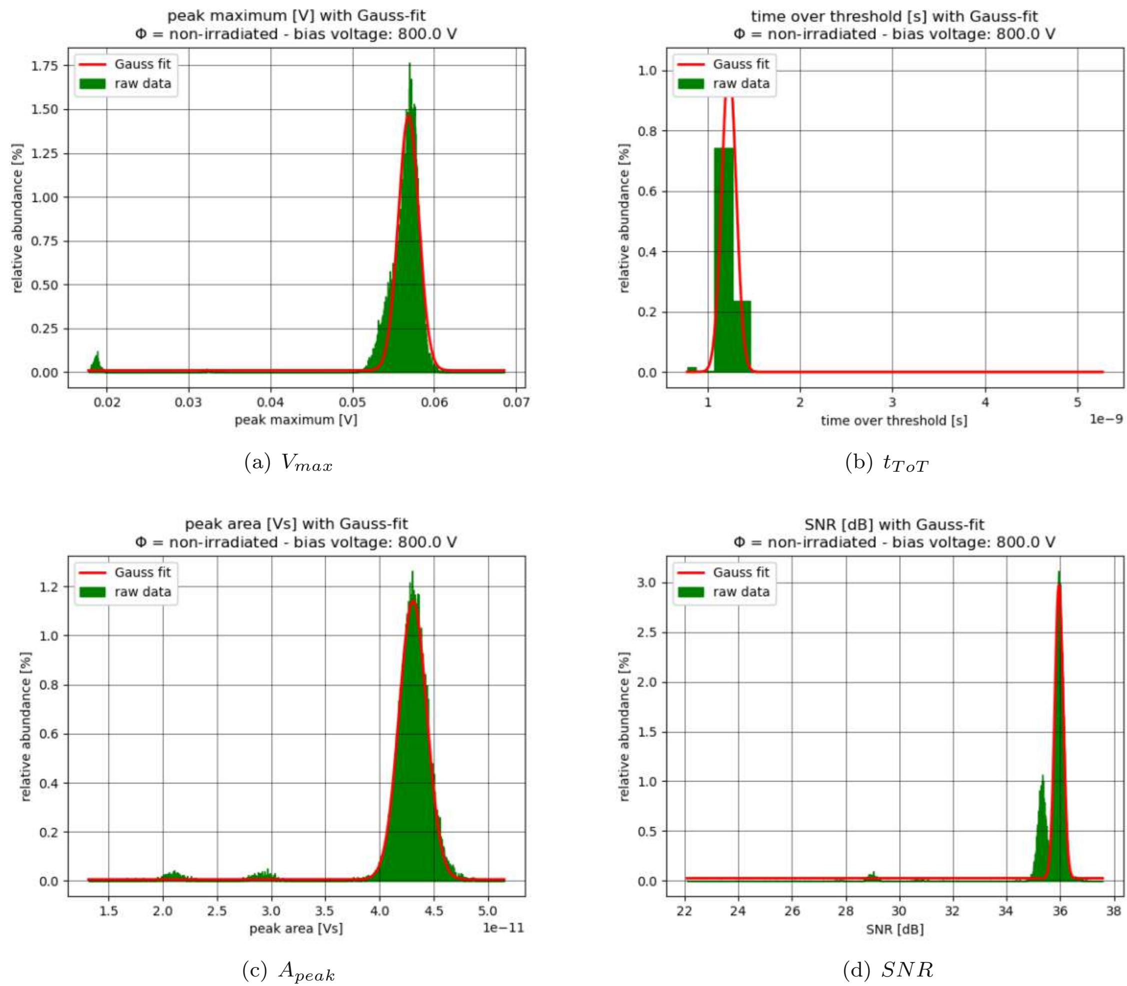

(a) V_{max} (b) t_{ToT}

(c) A_{peak} (d) SNR

Figure 23: Example data (non-irradiated sample, reverse bias 800 V) plotted in a histogram with the corresponding fit. The noise peaks are 'excluded' due to the fitting.

Die approbierte gedruckte Originalversion dieser Diplomarbeit ist an der TU Wien Bibliothek verfügbar
The approved original version of this thesis is available in print at TU Wien Bibliothek.
TU Bibliothek Your knowledge hub WIEN

6 Results

6.1 Sample Preparation and General Information

Radiation damage was achieved be exposing the samples to fluences (1 MeV neutron equivalent per cm^2) at the TRIGA Mark II Reactor core. The irradiation took place before the work on this thesis started. Following fluences were achieved by specific irradiation times:

Fluence [n_{eq}/cm^2]	**Irradiation Time**
5×10^{14}	18 min
1×10^{15}	36 min
5×10^{15}	3 h
1×10^{16}	6 h

The detectors were studied at room temperature in two similar experiment series. First, in the cleanroom with the Laser-TCT setup and at the beam facility at MedAustron with protons, secdondly. After determining the parameters described in section 5.4, a fit of the resulting histogram was performed with a Gaussian distribution for each parameter to obtain more precise values. This fit is sufficient as all involved instruments show a statistical uncertainty (e.g. noise, Laser intensity, etc.). On the other hand, for the measurements at MedAustron, the fit was not performed as the parameters follow a Landau-distribution. At the time the data was analyzed, the analysis software was not capable of performing Landau fits on data sets. Hence, only average values are presented. The exact values for each parameter of the direct measurement and after the fitting are presented in the Appendix A (TCT) and B (MedAustron). Also, additional histograms are enclosed in these sections. In the following chapter, the index d indicates a directly measured value, while f stands for a parameter derived after the fitting. The same experiments were performed with a non-irradiated sample as reference. While not being under investigation, the detectors were stored in a refrigerator at -20°C to suppress annealing effects. To avoid icing due to humidity and possible damage, the detectors were heated up under a dry atmosphere until they reached room temperature.

6.2 Laser TCT-measurements

6.2.1 Specific Experimental Parameters

The Laser-TCT measurements were performed in a cleanroom at the Institute of High Energy Physics. This series of experiment included two measurements each; recording the leakage current (in the return channel of the high voltage supply), as well as recording the signal peaks themselves as voltage samples. For the leakage current, 100 single measurements were taken at each voltage. Afterwards, they were averaged, resulting in the data point for this voltage. Increasing the bias voltage was done as soon as the averaging was performed. To avoid unwanted effects due to voltage increase, the measurements were taken 10 s after the increase. The actual peak data was collected with the DRS4 oscilloscope at its highest sampling rate of 5.12 GS/s. The data sets were recorded for bias voltages ranging from 50 V to 1100 V while increasing the voltage in steps of 50 V. 25 000 events were recorded per bias voltage with a repetition rate of 500 Hz and no attenuation of the Laser beam. No attenuation was achieved by setting the parameter 'tune value' of the Laser driver to 0. The Laser delivered an average power of 6.25 nW in this configuration. For the specific wave length $\lambda = 370\,\text{nm}$ an attenuation coefficient of $\mu_A \approx 42.25\,\text{cm}^{-1}$ [91] was reported in 1998 for silicon carbide. Taking this parameter, the active thickness

TU Bibliothek Your knowledge hub WIEN
Die approbierte gedruckte Originalversion dieser Diplomarbeit ist an der TU Wien Bibliothek verfügbar
The approved original version of this thesis is available in print at TU Wien Bibliothek.

and Beer-Lambert's law the beam was attenuated by roughly 17.31%. In terms of energy, an amount of 13.4 MeV was deposited in the material. Within this setup, about 4×10^6 electron-hole pairs were created within a Laser pulse. The experiments were conducted out at room temperature on the cold chuck which regulated the temperature to +20°C.

6.2.2 Non-irradiated SiC-Sensor

Leakage current

The leakage current of the non-irradiated detector stays below 4.5 nA for the bias range up to 500 V. From 0 V to 300 V to curves shows a smaller increase than above 300 V, which is about the full depletion voltage. The plot of this data is presented in Fig. 24.

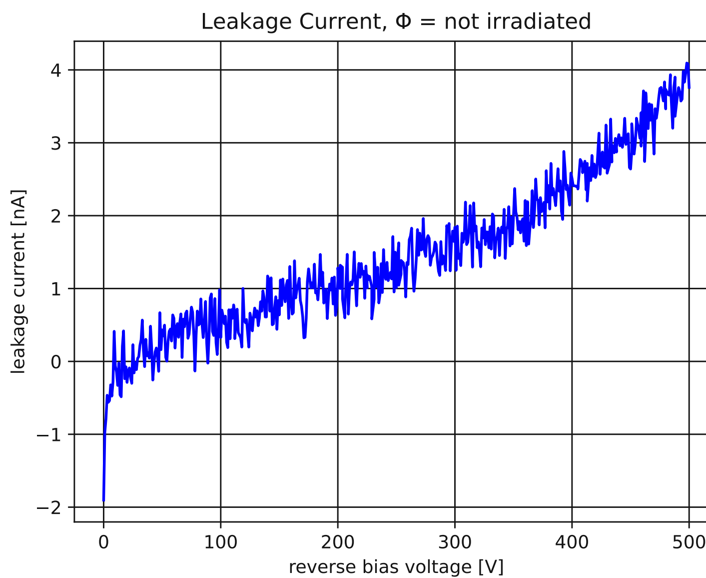

Figure 24: The leakage current up to 500 V for the non-irradiated sensor.

Peak maximum

The two Figs. 25a,b show the development of the peak maximum with increasing bias voltage up to 1100 V. Both plots of the average peak maximum before and after the fitting show an continuous increase. Hence, the maximum observed mean peak height after the fitting is $\mu_\mathrm{f} = 58.742$ mV (direct measurement $\mu_\mathrm{d} = 57.536$ mV) at 1100 V bias voltage with a standard deviation of $\sigma_\mathrm{f} = 1.22$ mV ($\sigma_\mathrm{d} = 5.357$ V). The smallest peak maximum value is linked to the 50 V bias voltage and $\mu_\mathrm{f} = 17.414$ mV ($\mu_\mathrm{d} = 18.102$ mV) with a standard deviation $\sigma_\mathrm{f} = 0.57$ mV ($\sigma_\mathrm{d} = 5.304$ mV). The maximum is therefore roughly three times larger than the minimum. The absolute difference of the mean peak maximum between two adjacent data point decreases the higher the bias voltage is until the curve develops nearly linearly above 600 V. Additionally, Fig. 25c,d show plots of the measured peak maxima at 300 V and 1000 V. The peak around 18 mV is a noise peak caused by the DRS4 evaluation board.

Die approbierte gedruckte Originalversion dieser Diplomarbeit ist an der TU Wien Bibliothek verfügbar
The approved original version of this thesis is available in print at TU Wien Bibliothek.
TU WIEN Bibliothek Your knowledge hub

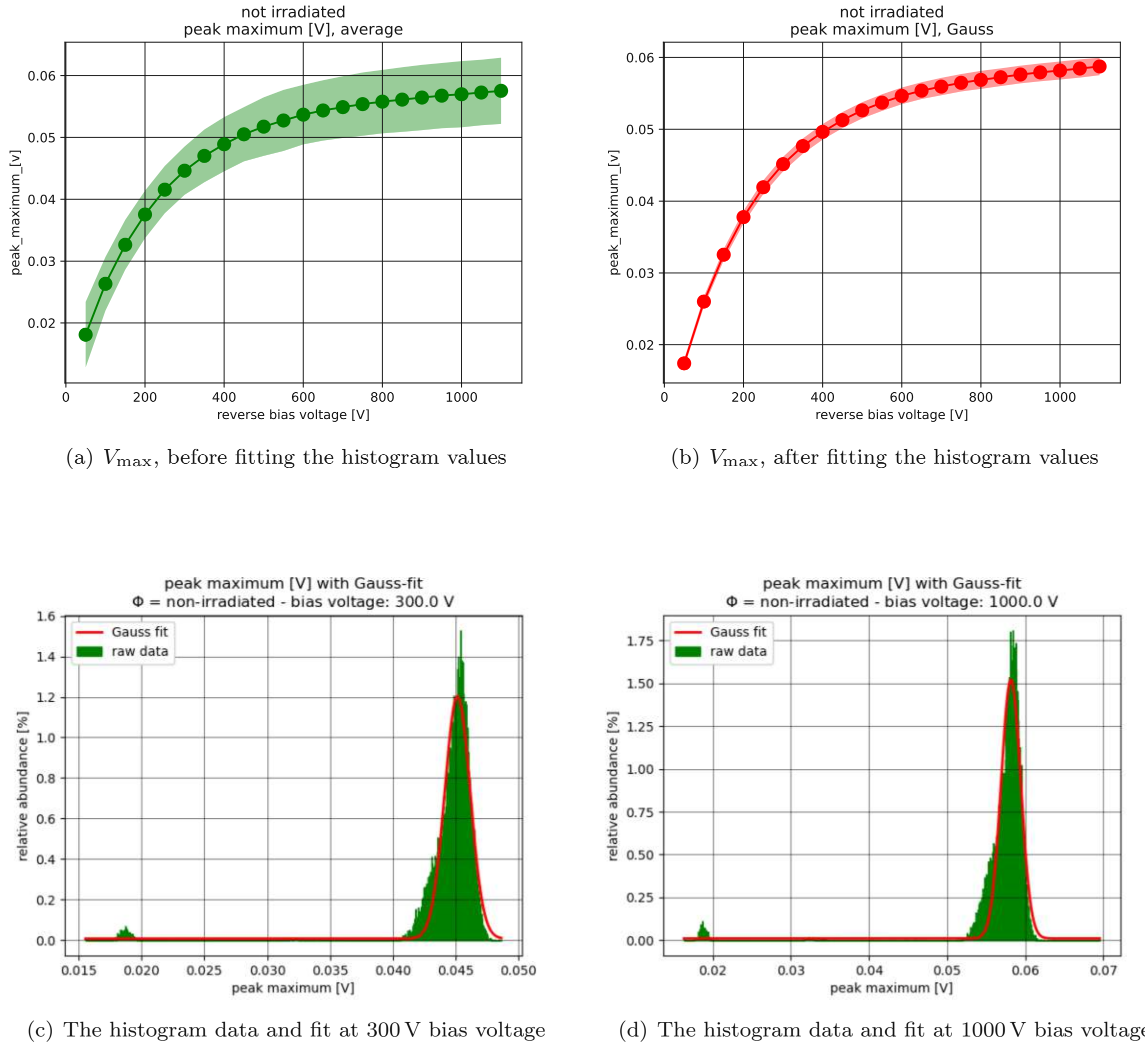

(a) V_{max}, before fitting the histogram values

(b) V_{max}, after fitting the histogram values

(c) The histogram data and fit at 300 V bias voltage

(d) The histogram data and fit at 1000 V bias voltage

Figure 25: The mean and standard deviation of V_{max} for the non-irradiated sensor before and after fitting.

Time-over-threshold

As the minimal number of samples which a signal must contain is set arbitrarily to four, the minimal t_{ToT} is 0.78 ns, considering the sampling rate of the DRS4 oscilloscope. From 50 V to 300 V the time-over-threshold increases in both plots in Fig. 26a,b, which represent the directly observed values as well the means after the fitting. The values of μ_{f} increase from 1.203 ns to 1.292 ns (μ_{d} from 1.91 ns to 1.293 ns) with a decreasing rate of change. Respectively, the standard deviations σ_{f} are 0.089 ns and 0.106 ns for 50 and 300 V (for σ_{d} they are 0.126 ns and 0.165 ns). The measured maximum appears at 300 V, after which the values start to decrease again. At a bias of 1000 V (1050 V for the direct measurement) t_{ToT} is smaller than the value of the lowest bias voltage. The measured minimum at the highest bias is $\mu_{\mathrm{f}} = 1.191$ ns ($\mu_{\mathrm{d}} = 1.179$ mV) with a standard deviation $\sigma_{\mathrm{f}} = 0.082$ mV ($\sigma_{\mathrm{d}} = 0.117$ mV). Fig. 26a,b present the plots of the average values, respectively the mean, and the standard deviation before and after the fitting. Next to this, 26c,d show the histogram data at the exemplary bias voltage of 300 V and 1000 V. The discrete values lead to a minor number of bins which are clearly present in these plots.

Die approbierte gedruckte Originalversion dieser Diplomarbeit ist an der TU Wien Bibliothek verfügbar
The approved original version of this thesis is available in print at TU Wien Bibliothek.
TU WIEN Bibliothek Your knowledge hub

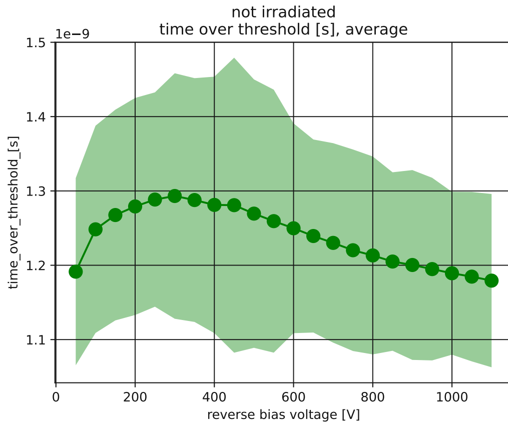

(a) t_{ToT}, before fitting the histogram values

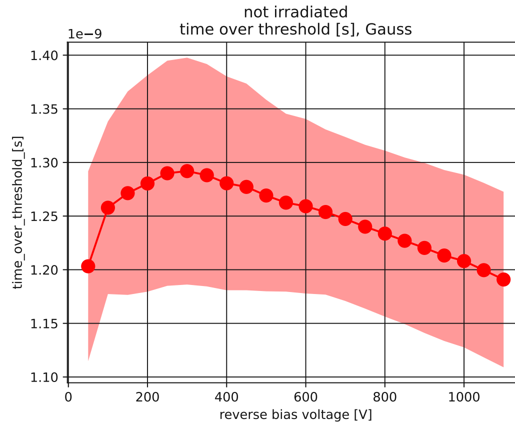

(b) t_{ToT}, after fitting the histogram values

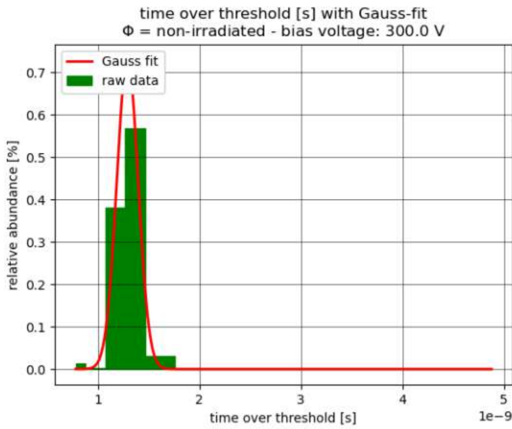

(c) The histogram data and fit at 300 V bias voltage

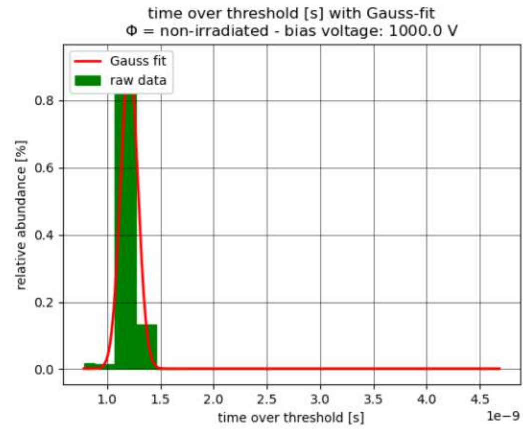

(d) The histogram data and fit at 1000 V bias voltage

Figure 26: a,b) t_{ToT} plotted against the bias voltage, c,d) exemplary histogram data

Peak area

The curve of the peak area increases with an increasing bias voltage. This parameter exhibits a saturation behavior in both data rows of the direct measurement and after the fit. The plots are presented in Fig. 27a,b and refer to the observed average and standard deviation values before and after fitting. The minimal average peak area is located at the lowest bias voltage. Therefore $\mu_{\mathrm{f}} = 1.793{\times}10^{-11}$ Vs ($\mu_{\mathrm{d}} = 1.816{\times}10^{-11}$ Vs) with a standard deviation $\sigma_{\mathrm{f}} = 0.094{\times}10^{-11}$ Vs ($\sigma_{\mathrm{d}} = 0.185{\times}10^{-11}$ Vs). The saturation effect occurs at a mean peak area of $\mu_{\mathrm{f}} \approx 4.31{\times}10^{-11}$ Vs ($\mu_{\mathrm{d}} \approx 4.25{\times}10^{-11}$ Vs) when applying a bias voltage of 600 V or higher. Moreover, the standard deviation saturates at $\sigma_{\mathrm{f}} < 0.131\ {\times}10^{-11}$ Vs as well. For the directly measured values, σ_{d} also saturates at value smaller than $0.386\ {\times}10^{-11}$ Vs. In addition, the histogram with the corresponding fits are shown in Fig. 27c,d for 300 V and 1000 V bias voltage. The curve of the fit is well-aligned within the shape of the histogram, this holds for all derived histograms.

Die approbierte gedruckte Originalversion dieser Diplomarbeit ist an der TU Wien Bibliothek verfügbar
The approved original version of this thesis is available in print at TU Wien Bibliothek.
TU WIEN Bibliothek Your knowledge hub

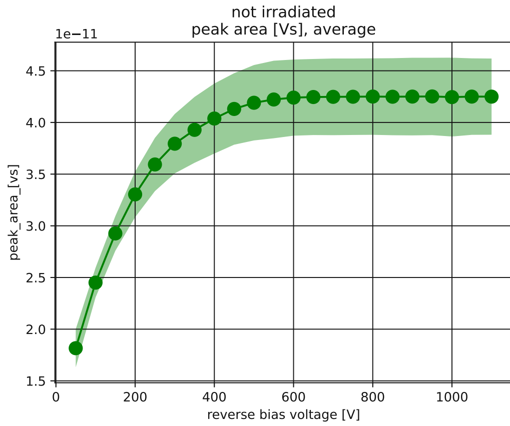

(a) A_{peak}, before fitting the histogram values

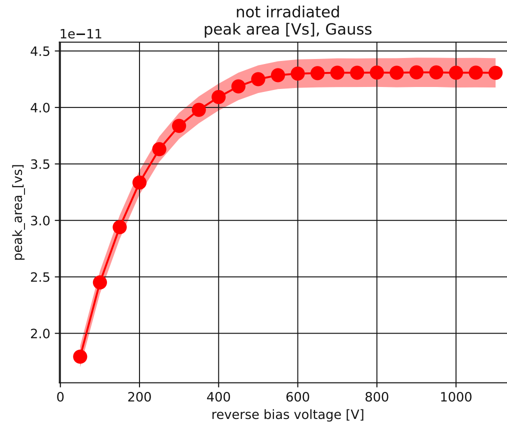

(b) A_{peak}, after fitting the histogram values

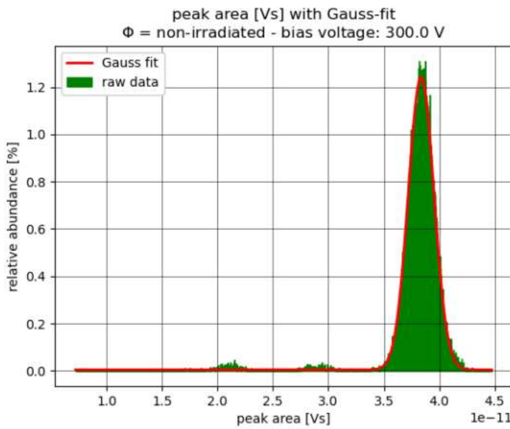

(c) The histogram data and fit at 300 V bias voltage

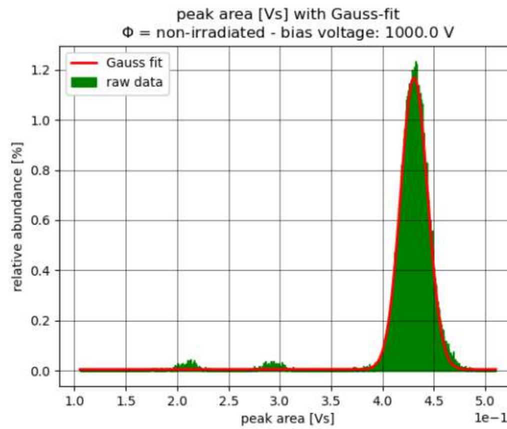

(d) The histogram data and fit at 1000 V bias voltage

Figure 27: a,b) A_{peak} plotted against the bias voltage, c,d) exemplary histogram data

Signal-to-Noise ratio

The last of the four parameters to characterize the sensor at different bias voltages is the signal-to-noise ratio SNR. The corresponding plots of the parameter over the whole bias voltage range are presented in Fig. 28a,b. The curve shows a plateau between 400 V and 650 V bias voltage with a SNR of $\mu_{\mathrm{f}} \approx 36.1$ dB ($\mu_{\mathrm{d}} \approx 36.0$ dB) with a maximum of $\mu_{\mathrm{f}} = 36.23$ dB ($\mu_{\mathrm{d}} = 36.16$ dB) at 450 V. Before reaching this plateau, the signal-to-noise ration increases. Afterwards, it decreases again if a bias voltage of 700 V or higher is applied. However, the difference between the maximum and the minimum of each side is different, showing a smaller difference for higher bias voltages. Hence, Fig. 28c,d show the resulting histogram of the measurement at 300 V and 1000 V. Both plots exhibit a double peak, leading to a fit which does not follow the histogram shape. This is caused by the minor number of peak samples and discussed in detail in chapter 7. For the diagram referring to 300 V the first peak is located at 35.5 dB while the second one is at 36.2 dB. The other plot show the peaks at 35 dB and 35.5 dB respectively. Above 700 V bias voltage the fitting algorithm 'catches' the dominant one of the two peak. This is indicated as the standard deviation drops.

Die approbierte gedruckte Originalversion dieser Diplomarbeit ist an der TU Wien Bibliothek verfügbar
The approved original version of this thesis is available in print at TU Wien Bibliothek.
TU WIEN Bibliothek Your knowledge hub

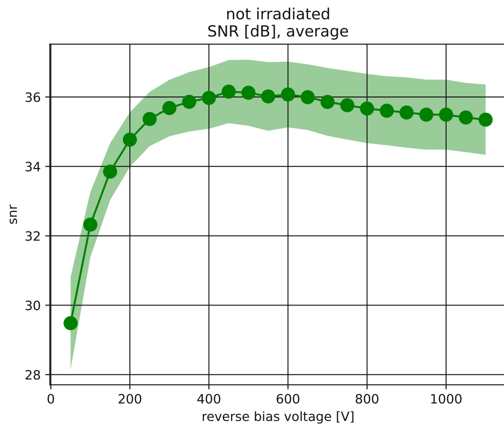

(a) SNR, before fitting the histogram values

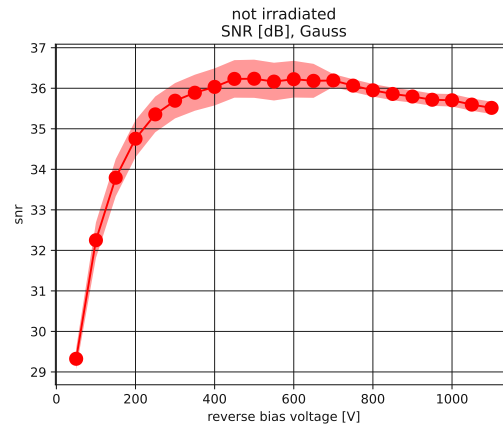

(b) SNR, after fitting the histogram values

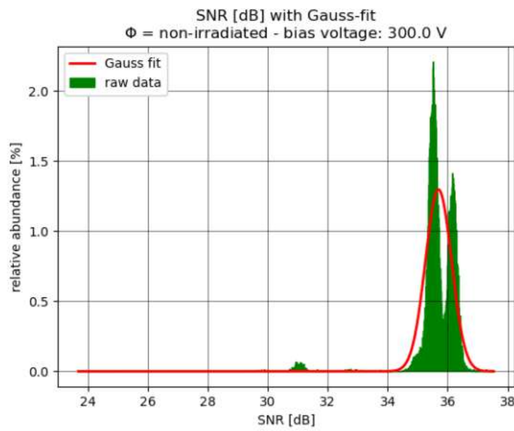

(c) The histogram data and fit at 300 V bias voltage

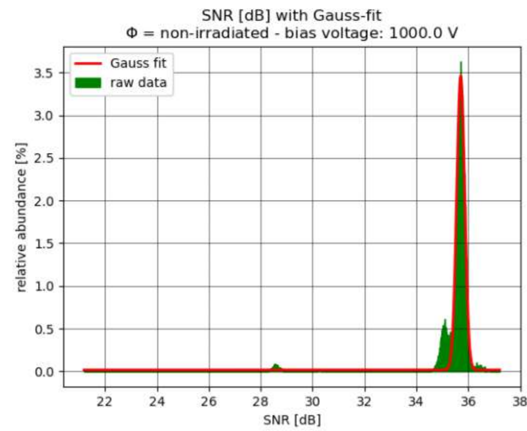

(d) The histogram data and fit at 1000 V bias voltage

Figure 28: a,b) SNR plotted against the bias voltage, c,d) exemplary histogram data

Die approbierte gedruckte Originalversion dieser Diplomarbeit ist an der TU Wien Bibliothek verfügbar
The approved original version of this thesis is available in print at TU Wien Bibliothek.
TU WIEN Bibliothek Your knowledge hub

6.2.3 SiC-Sensor exposed to 5×10^{14} $\mathbf{n_{eq}/cm^2}$

Leakage current

The trend is an increase of the leakage current with an increasing bias voltage. At the highest bias voltages the current stayed below 4 nA. The increase trend is nearly constant in the whole observed bias voltage range. The recorded IV-curve is shown in Fig. 29.

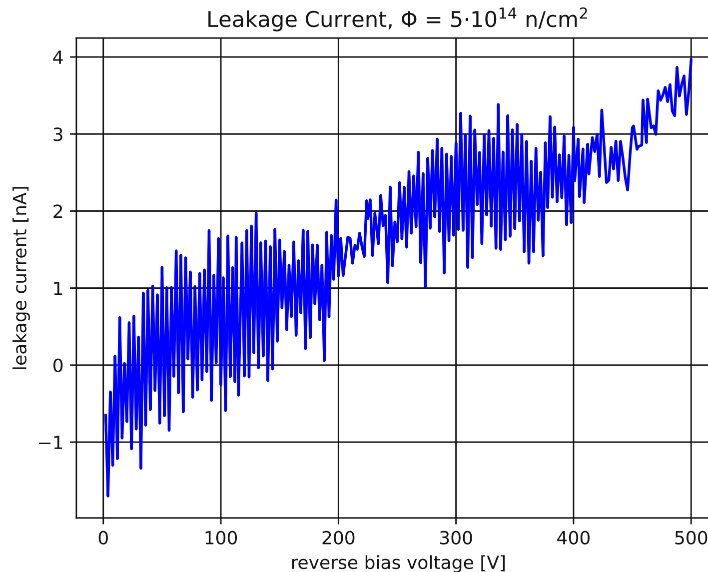

Figure 29: The leakage current up to 500 V for the sensor exposed 5×10^{14} n$_{eq}$/cm^2.

Peak maximum

At first the peak maximum was investigated, the mean of this parameter shows an increase over the whole range of bias voltages. This holds for both the directly observed values as well as for the fit parameters. Thus, Fig. 30a,b show V_{max} versus the bias voltage before and after fitting. The minimum of μ_{f} is located at the lowest bias voltage of 50 V and is 8.713 mV ($\mu_{\mathrm{d}} = 9.907$ mV). The corresponding standard deviation σ_{f} is 0.487 mV ($\sigma_{\mathrm{d}} = 7.114$ mV). The increase of the average peak maximum comes hand in hand with an increase of the bias voltage. Above a bias voltage of 400 V, the peak maximum progresses nearly linear. Therefore, the maximum is linked to the maximum bias voltage of 1100 V with $\mu_{\mathrm{f}} = 37.427$ mV ($\mu_{\mathrm{d}} = 37.242$ mV). The standard deviation σ_{f} of the maximum is 1.060 mV ($\sigma_{\mathrm{d}} = 3.833$ mV). In Fig. 30c,d the histograms of the peak maximum values at 300 V and 1000 V are presented. The visible peak at 18 mV is a noise signal caused by the DRS4 evaluation board.

Die approbierte gedruckte Originalversion dieser Diplomarbeit ist an der TU Wien Bibliothek verfügbar
The approved original version of this thesis is available in print at TU Wien Bibliothek.
TU WIEN Bibliothek Your knowledge hub

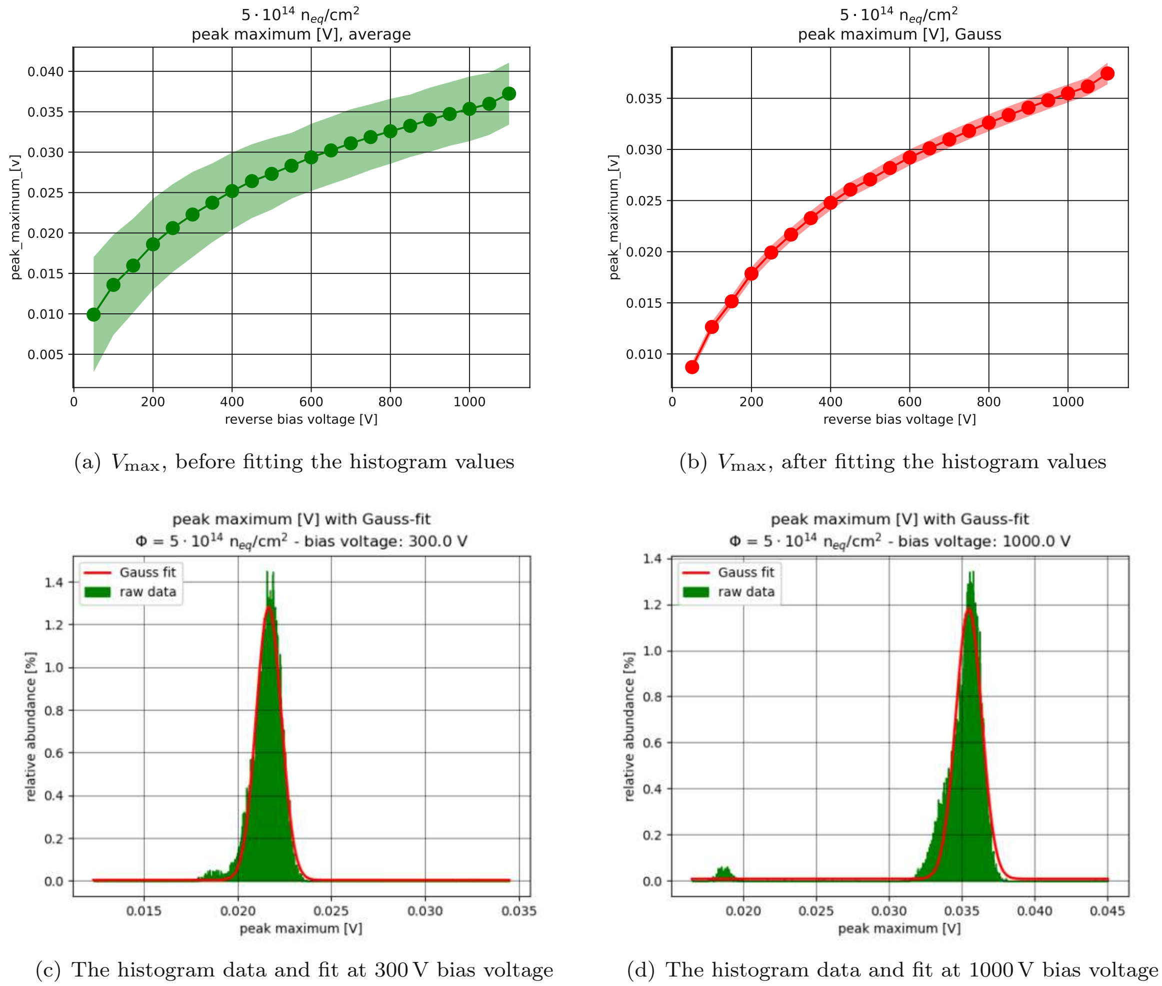

(a) $V_{\max}$, before fitting the histogram values

(b) $V_{\max}$, after fitting the histogram values

(c) The histogram data and fit at 300 V bias voltage

(d) The histogram data and fit at 1000 V bias voltage

Figure 30: a,b) $V_{\max}$ plotted against the bias voltage, c,d) exemplary histogram data

Time over threshold

Due to the setting in the analysis software, a minimal peak length of four voltage samples is required. This is resulting in a minimal t_{ToT} of 0.78 ns, after taking the sampling rate of the DRS4 oscilloscope into account. Generally, for this sensor, the time-over-threshold average values increase with an increasing bias voltage. This can be seen in the plots of the directly measured average values as well in the curve after the fit in Fig. 31a,b. The shortest signal occurs at 50 V bias voltage with $\mu_{\mathrm{d}} = 0.822$ ns with a standard deviation $\sigma_{\mathrm{d}} = 0.128$ ns. The mean $\mu_{\mathrm{f}} = 0.412$ which is observed after the fitting cannot be considered as reliable as it is smaller than the minimal time-over-threshold. All other points in the curve after the fitting are lying within $\mu_{\mathrm{d}} \pm \sigma_{\mathrm{d}}$ indicating reliability. The maximum is reached at the highest applied bias voltage and $\mu_{\mathrm{d}} = 1.133$ ($\mu_{\mathrm{f}} = 1.122$ ns) with $\sigma_{\mathrm{d}} = 0.120$ ns ($\sigma_{\mathrm{f}} = 0.080$ ns). Also, at first the increases are greater from 50 V to 400 V until the curves behaves like a linear function until 1100 V. Examplary histogram of the time-over-threshold are presented in Fig. 31c,d. The values are concentrated in a few bin as this parameter exhibits only discrete values in a small range.

Die approbierte gedruckte Originalversion dieser Diplomarbeit ist an der TU Wien Bibliothek verfügbar
The approved original version of this thesis is available in print at TU Wien Bibliothek.
TU WIEN Bibliothek Your knowledge hub

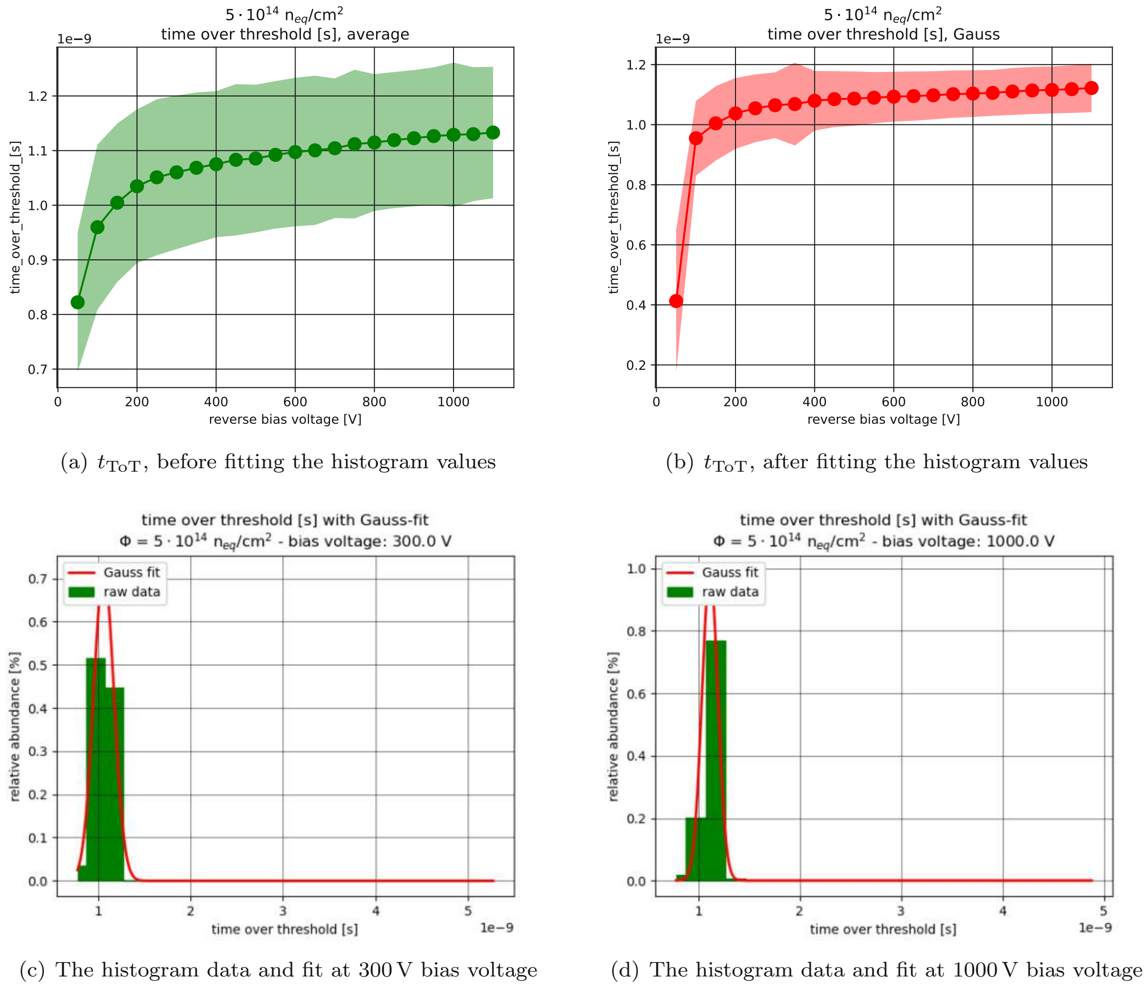

(a) t_{ToT}, before fitting the histogram values

(b) t_{ToT}, after fitting the histogram values

(c) The histogram data and fit at 300 V bias voltage

(d) The histogram data and fit at 1000 V bias voltage

Figure 31: a,b) t_{ToT} plotted against the bias voltage, c,d) exemplary histogram data

Peak area

The average peak area increases with increasing bias voltage. No saturation effect is observable for a bias voltage up to 1100 V. Both plots of the directly observed values as well as the ones after the fitting are presented in Fig. 32a,b. Fitting the data of the direct measurement yields a first value of $\mu_{\mathrm{f}} = 7.01\times10^{-12}$ Vs (while $\mu_{\mathrm{d}} = 7.70\times10^{-12}$ Vs) at 50 V bias voltage with a standard deviation $\sigma_{\mathrm{f}} = 8.8\times10^{-13}$ Vs ($\sigma_{\mathrm{d}} = 3.71\times10^{-12}$ Vs). Above a bias voltage of 400 V, the curve follows in both cases a linear-like shape. On the other side of the voltage ramp at 1100 V, the average peak area is nearly four times larger. The corresponding value are $\mu_{\mathrm{f}} = 2.716\times10^{-11}$ Vs ($\mu_{\mathrm{d}} = 2.707\times10^{-11}$ Vs) and for the standard deviation $\sigma_{\mathrm{f}} = 1.12\times10^{-12}$ Vs ($\sigma_{\mathrm{d}} = 1.58\times10^{-12}$ Vs). The alignment of the fit within the shape of histogram is visible in Fig. 32c,d. Here are two histograms are presented from measurements at 300 V and 1000 V bias voltage.

Die approbierte gedruckte Originalversion dieser Diplomarbeit ist an der TU Wien Bibliothek verfügbar
The approved original version of this thesis is available in print at TU Wien Bibliothek.
TU Bibliothek WIEN Your knowledge hub

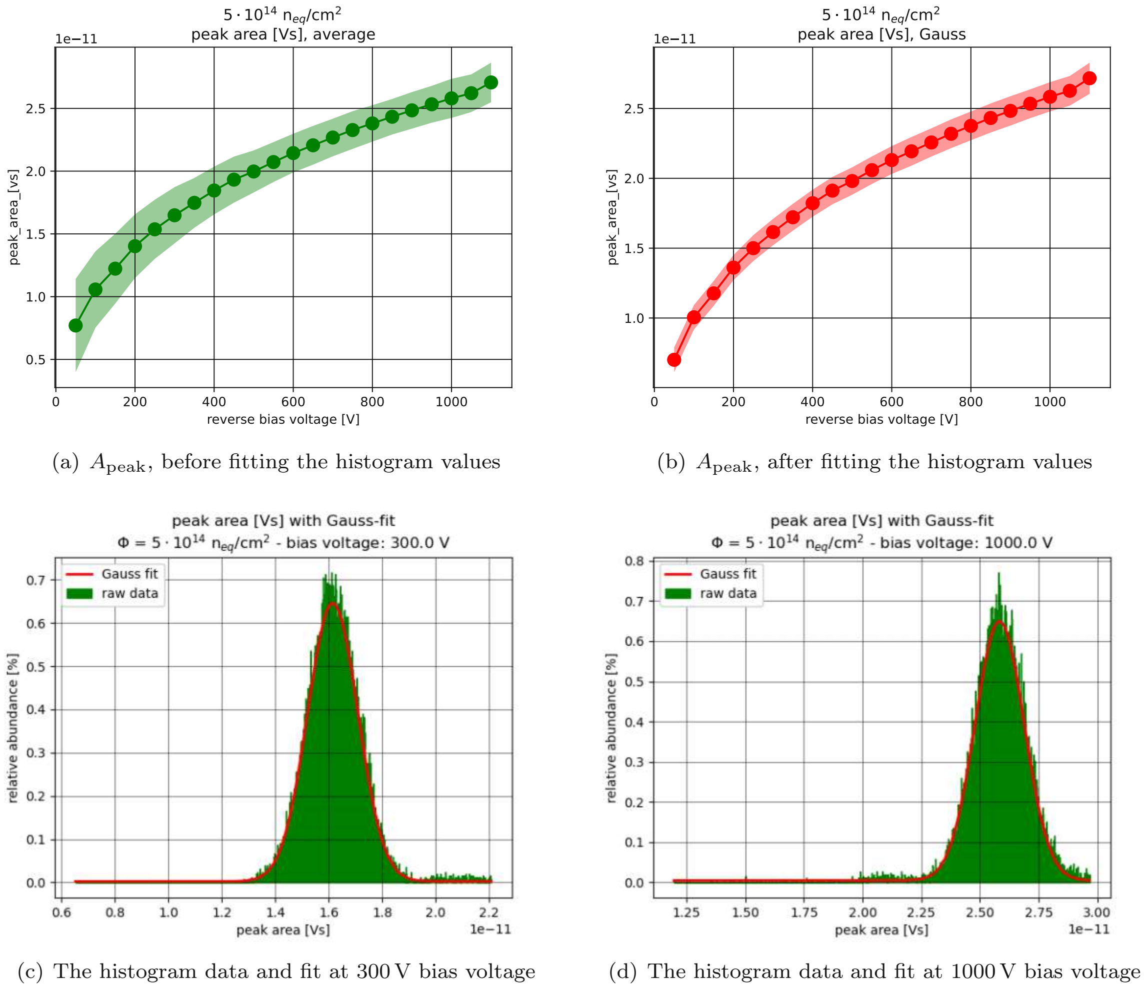

(a) A_{peak}, before fitting the histogram values

(b) A_{peak}, after fitting the histogram values

(c) The histogram data and fit at 300 V bias voltage

(d) The histogram data and fit at 1000 V bias voltage

Figure 32: a,b) A_{peak} plotted against the bias voltage, c,d) exemplary histogram data

Signal-to-noise ratio

At last the signal-to-noise ratio SNR was investigated. Generally, the SNR exhibit greater values the higher the bias voltage is. The correspnoding curves are presented in Fig. 33a,b. The minimum of the mean according to the fit is $\mu_{\text{f}} = 24.50\,\text{dB}$ ($\mu_{\text{d}} = 24.92\,\text{dB}$) at 50 V bias voltage with a standard deviation $\sigma_{\text{f}} = 0.45\,\text{dB}$ ($\sigma_{\text{d}} = 2.31\,\text{dB}$). Both plots exhibit a greater increase for adjacent data points in the lower bias voltage region. From 400 V bias voltage upwards, the plots behave linear-like. The highest mean value of the SNR $\mu_{\text{f}} = 33.88\,\text{dB}$ ($\mu_{\text{d}} = 34.00$) is observed at the highest applied voltage of 1100 V; the standard deviation is $\sigma_{\text{f}} = 0.20\,\text{dB}$ ($\sigma_{\text{d}} = 0.76\,\text{dB}$). The other two plots in Fig. 33c,d show exemplarily the distribution of this parameter at 300 V and 1000 V bias voltage. Most noticable, the plots show a double peak, closely located at each other Hence, the fit does not follow the given shape. This structure is caused by the low sample rate of the DRS4, resulting in small number of samples. It is discussed in chapter 7 particularly. The first plot show the peaks at 30.5 dB and 31 dB. On the other hand, for the second plot these peaks are located at 33.7 dB and 34.3 dB respectively. The standard deviations of the average values derived from fitting are much smaller above 700 V bias voltage than below. In this case, the fitting algorithm is able to find the dominant one of the peaks.

Die approbierte gedruckte Originalversion dieser Diplomarbeit ist an der TU Wien Bibliothek verfügbar
The approved original version of this thesis is available in print at TU Wien Bibliothek.
TU WIEN Bibliothek Your knowledge hub

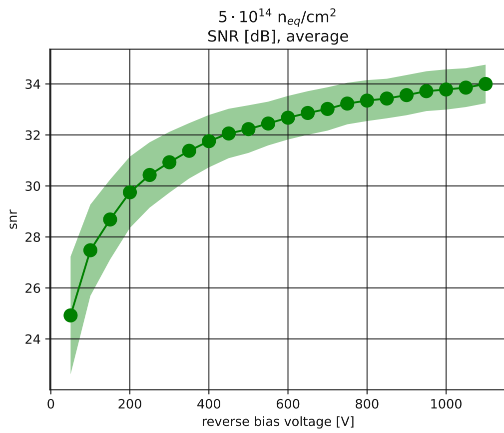

(a) SNR, before fitting the histogram values

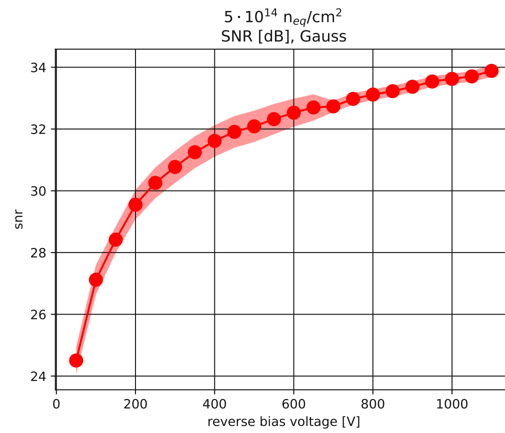

(b) SNR, after fitting the histogram values

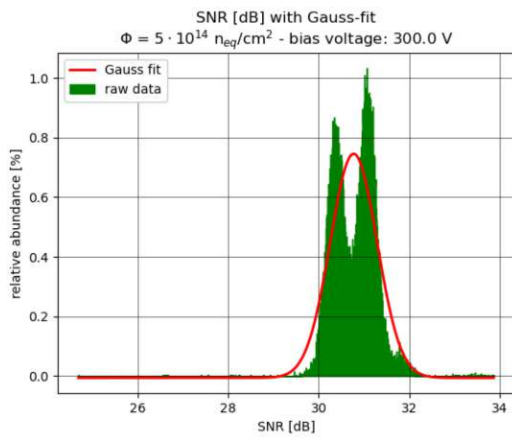

(c) The histogram data and fit at 300 V bias voltage

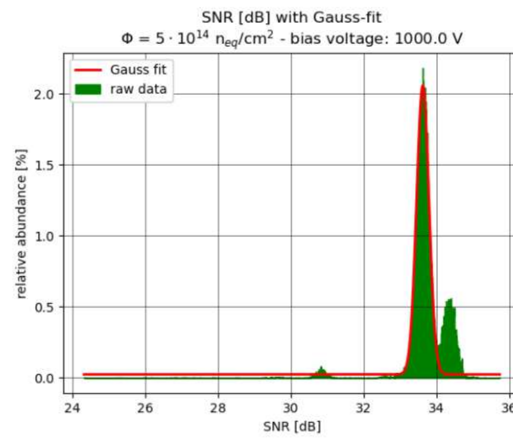

(d) The histogram data and fit at 1000 V bias voltage

Figure 33: a,b) SNR plotted against the bias voltage, c,d) exemplary histogram data

Die approbierte gedruckte Originalversion dieser Diplomarbeit ist an der TU Wien Bibliothek verfügbar
The approved original version of this thesis is available in print at TU Wien Bibliothek.
TU Bibliothek Your knowledge hub WIEN

6.2.4 SiC-Sensor exposed to 1×10^{15} n_{eq}/cm^2

This sensor only yields detectable sensor signals above 100 V bias voltage. Hence, no signals could be recorded for a bias voltage of 50 V and no characteristic parameter were derived. Therefore, all data and plots presented in this section do not show this first measurement.

Leakage current

The general trend of the leakage current is an increase of the current with incresing bias voltage. This curve show two area with different trends below and above 400 V. Below 400 V, the curve shows an increase until exhibits an saturation-like behavior; above 400 V the current increases again in nearly linear trend, staying below 8 nA, see Fig. 34.

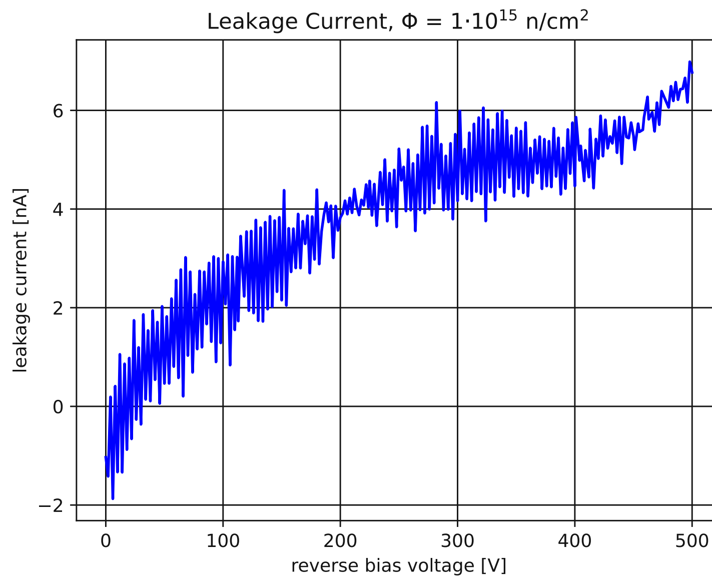

Figure 34: The leakage current up to 500 V for the sensor exposed 1×10^{15} n_{eq}/cm^2.

Peak maximum

Both the fitting and directly obtained values show that the measured values increase. The plots for this parameter before and after the fitting are shown in Fig. 35a,b. The minimum of the average peak height is located at the lowest bias voltage of 100 V with a value of $\mu_f = 8.499$ mV ($\mu_d = 9.973$ mV) with a standard deviation $\sigma_f = 0.514$ mV ($\sigma_d = 7.482$ mV). Above 300 V bias voltage, the growth is nearly linear. As it increases throughout the whole bias voltage range, the last measurement shows the highest average peak maximum with $\mu_f = 26.411$ mV ($\mu_d = 0.803$ mV). At this point, the standard deviation is $\sigma_f = 0.803$ mV ($\sigma_d = 5.551$ mV). Hence, the maximum is nearly four times as high as the least value. Also two exemplary histograms are shown in Fig. 35c,d. They present the distribution of the peak area values at 300 V and 1000 V bias voltage. Thus, also the fit of these histograms are shown. In both histograms an additional peak appears around 18 mV which is known as a noise peak.

Die approbierte gedruckte Originalversion dieser Diplomarbeit ist an der TU Wien Bibliothek verfügbar
The approved original version of this thesis is available in print at TU Wien Bibliothek.
TU WIEN Bibliothek Your knowledge hub

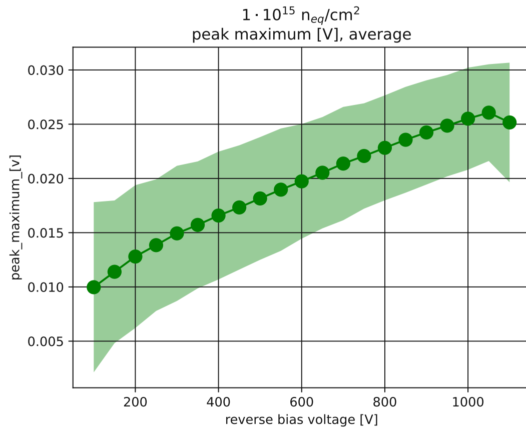

(a) $V_{\max}$, before fitting the histogram values

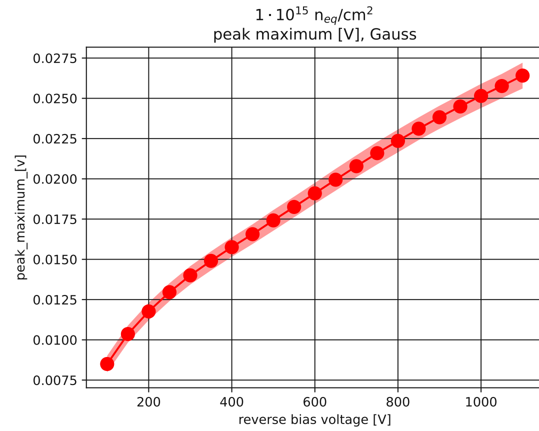

(b) $V_{\max}$, after fitting the histogram values

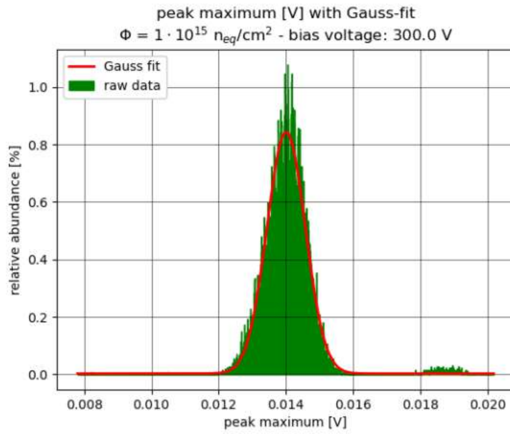

(c) The histogram data and fit at 300 V bias voltage

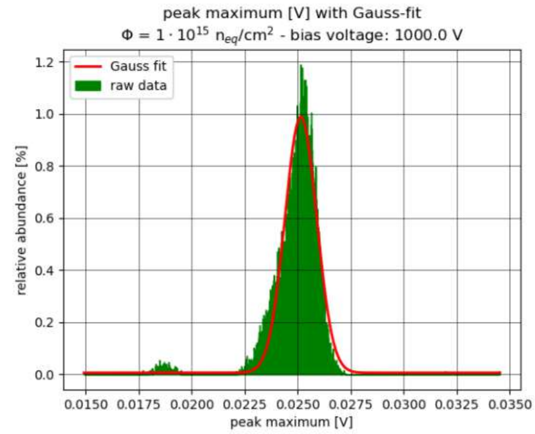

(d) The histogram data and fit at 1000 V bias voltage

Figure 35: a,b) $V_{\max}$ plotted against the bias voltage, c,d) exemplary histogram data

Time over threshold

A signal is only considered as a peak if it contains at least four voltage samples above the threshold. Again, this leads to a minimal t_{ToT} of 0.78 ns. The curve for both the directly measured time-over-threshold as well as their values after the fit are presented in Fig. 36a,b. The first mean value of this parameter at a bias voltage of 100 V is slightly greater this limit with $\mu_{\mathrm{f,d}} = 0.795\,\mathrm{ns}$ (the standard deviation is $\sigma_{\mathrm{f,d}}$ 0.115 ns). These two values hold for both the direct measurement and after the fit. For the next bias voltage of 150 V, only the directly measured mean ($\mu_{\mathrm{d}} \pm \sigma_{\mathrm{d}} = 0.821 \pm 0.114\,\mathrm{ns}$) can be considered as reliable. The value which is derived from fitting ($\mu_{\mathrm{f}} = 0.409\,\mathrm{ns}$) is below the limit of 0.78 ns and is neglected for further analysis. With increasing voltage also the time-over-threshold increases up to to 1050 V bias voltage, from 300 V on nearly linearly. In the data of the direct measurement, the curve reaches a maximum value of $\mu_{\mathrm{d}} = 1.053\,\mathrm{ns}$ ($\mu_{\mathrm{f}} = 1.056\,\mathrm{ns}$). The standard deviation at this bias voltage is $\sigma_{\mathrm{d}} = 0.140\,\mathrm{ns}$ ($\sigma_{\mathrm{f}} = 0.110\,\mathrm{ns}$). The next value, which refers to 1100 V, is slightly smaller with $\mu_{\mathrm{d}} = 1.042\,\mathrm{ns}$ ($\mu_{\mathrm{f}} = 1.048\,\mathrm{ns}$) and $\sigma_{\mathrm{d}} = 0.141\,\mathrm{ns}$ ($\sigma_{\mathrm{f}} = 0.122\,\mathrm{ns}$). The distribution of the values of the time-over-threshold is shown in Fig. Fig. 36c,d with the corresponding fit. The small values are concentrated in a few bins according to the number of signal samples.

Die approbierte gedruckte Originalversion dieser Diplomarbeit ist an der TU Wien Bibliothek verfügbar
The approved original version of this thesis is available in print at TU Wien Bibliothek.
TU WIEN Bibliothek Your knowledge hub

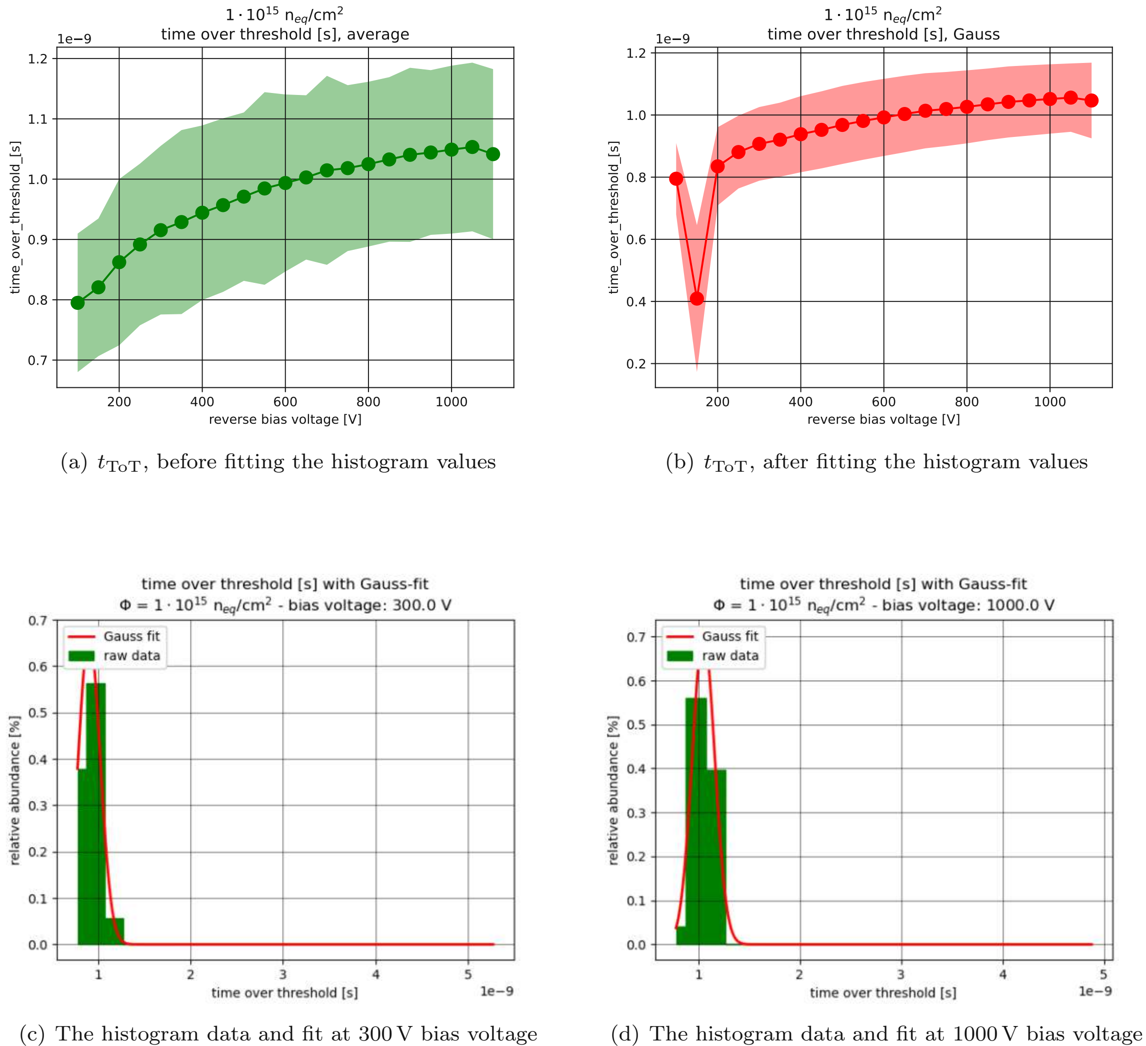

(a) t_{ToT}, before fitting the histogram values

(b) t_{ToT}, after fitting the histogram values

(c) The histogram data and fit at 300 V bias voltage

(d) The histogram data and fit at 1000 V bias voltage

Figure 36: a,b) t_{ToT} plotted against the bias voltage, c,d) exemplary histogram data

Peak area

As third parameter, the average peak area A_{peak} was investigated. For this parameter, also an increase can be seen for the whole bias voltage interval. It can be seen in the curves for the directly measured average peak area as well as in curve after the fit, which are plotted in Fig. 37a,b. The minimal mean value at 100 V is $\mu_{\mathrm{f}} = 6.37{\times}10^{-12}$ Vs ($\mu_{\mathrm{d}} = 7.25{\times}10^{-12}$ Vs) with a standard deviation $\sigma_{\mathrm{f}} = 8.8{\times}10^{-13}$ Vs ($\sigma_{\mathrm{d}} = 4.15{\times}10^{-11}$ Vs). The absolute values of the increase are greater until a bias voltage of 300 V. From here on, the increase is nearly linearly. The maximum average peak area is obtained at different bias voltages; for the direct measurement the maximum appears at 1050 V with $\mu_{\mathrm{d}} = 1.950{\times}10^{-11}$ Vs and $\sigma_{\mathrm{d}} = 1.75{\times}10^{-12}$ Vs. The mean of this parameter drops at 1100 V to $\mu_{\mathrm{d}} = 1.878{\times}10^{-11}$ Vs ($\sigma_{\mathrm{d}} = 2.90{\times}10^{-12}$ Vs). In the data after the fit, the maximum is located at 1100 V bias voltage and $\mu_{\mathrm{f}} = 1.976{\times}10^{-11}$ V with a standard deviation $\sigma_{\mathrm{f}} = 1.26{\times}10^{-12}$. At 1050 V μ_{f} is smaller than at 1100 V with $\mu_{\mathrm{f}} = 1.932{\times}10^{-11}$ Vs ($\sigma_{\mathrm{f}} = 9.9{\times}10^{-13}$ Vs). The fit of the histograms are shown Fig. 37c,d for the bias voltages of 300 V and 1000 V. The Gaussian distribution follows the shape of the histogram as seen below.

Die approbierte gedruckte Originalversion dieser Diplomarbeit ist an der TU Wien Bibliothek verfügbar
The approved original version of this thesis is available in print at TU Wien Bibliothek.
TU WIEN Bibliothek Your knowledge hub

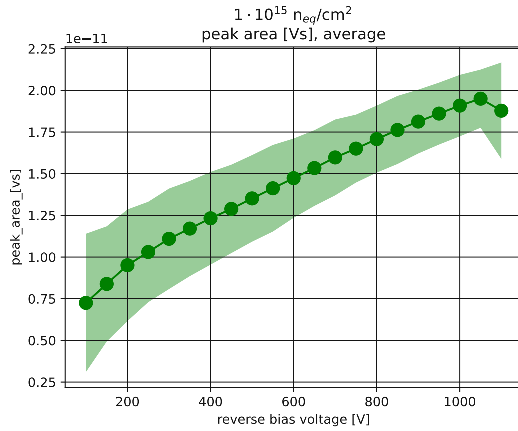

(a) A_{peak}, before fitting the histogram values

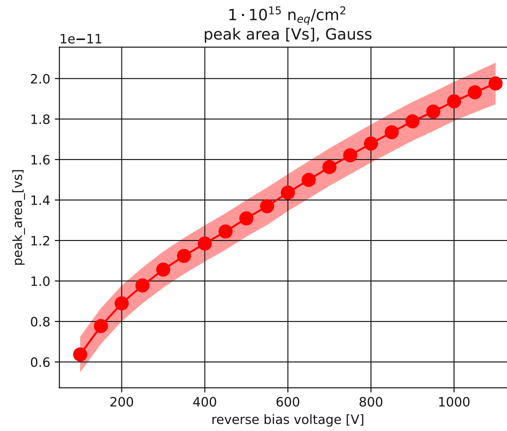

(b) A_{peak}, after fitting the histogram values

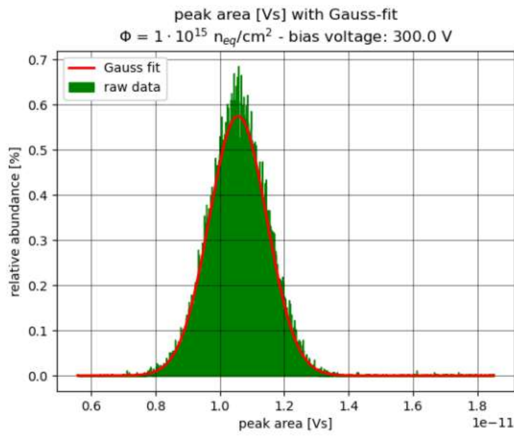

(c) The histogram data and fit at 300 V bias voltage

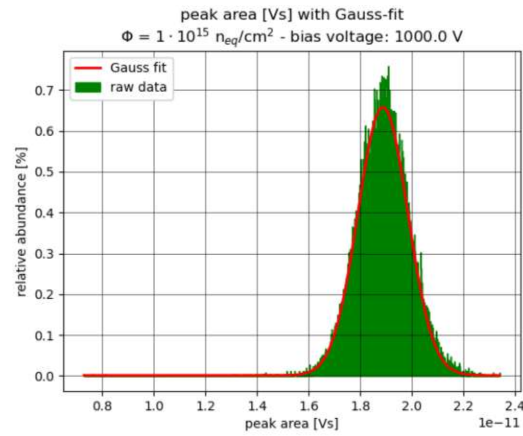

(d) The histogram data and fit at 1000 V bias voltage

Figure 37: a,b) A_{peak} plotted against the bias voltage, c,d) exemplary histogram data

Signal-to-noise ratio

At last the average signal-to-noise ratio SNR is derived. Both the directly measured means and the average parameter after the fitting are presented in Fig. 38a,b. Starting with the minimum mean value of $\mu_{\text{f}} = 24.22\,\text{dB}$ ($\mu_{\text{d}} = 24.73\,\text{dB}$) with a standard deviation $\sigma_{\text{f}} = 0.40\,\text{dB}$ ($\sigma_{\text{d}} = 2.59\,\text{dB}$) at 100 V bias voltage the SNR increases with higher bias voltages. The maximum is located at 1050 V for directly measured values and at 1100 V bias voltage for the fitted data. In numbers, the maximum of the direct measurement is $\mu_{\text{d}} = 31.99\,\text{dB}$ ($\sigma_{\text{d}} = 0.96\,\text{dB}$) and decreases to $\mu_{\text{d}} = 31.70\,\text{dB}$ ($\sigma_{\text{d}} = 1.45\,\text{dB}$) at 1100 V bias voltage. On the other hand, the maximum of the average SNR after the fit $\mu_{\text{f}} = 32.06\,\text{dB}$ ($\sigma_{\text{f}} = 0.57\,\text{dB}$). Right before at 1050 V bias voltage $\mu_{\text{f}} = 31.91\,\text{dB}$ (with $\sigma_{\text{f}} = 0.52\,\text{dB}$). The histograms of the distribution of the SNR in 38c,d for 300 V and 1000 V bias voltage exhibit double peaks. Thus, the fit is not aligned with the shape of the histogram. The double peaks are caused by the small number of signal samples, due to the low DRS4 sampling rate. An explanation is given in chapter 7. This double peak behavior is present for all bias voltages. The plot regarding the 300 V bias voltage show the peaks at 27.5 dB and 28.5 dB. The second one show them 31.2 dB and 32.0 dB. Moreover, the fitting algorithm is not capable of detecting the dominant peak in histograms regarding to bias voltages higher than 200 V.

Die approbierte gedruckte Originalversion dieser Diplomarbeit ist an der TU Wien Bibliothek verfügbar
The approved original version of this thesis is available in print at TU Wien Bibliothek.
TU Bibliothek WIEN Your knowledge hub

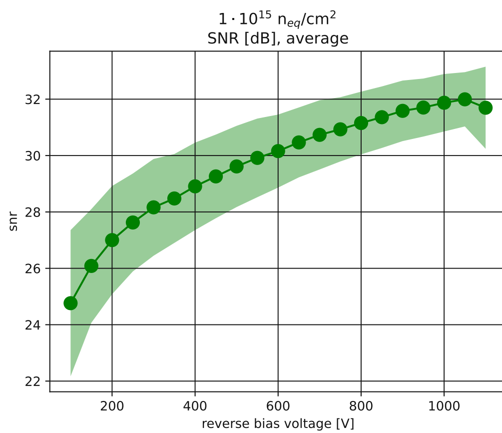

(a) SNR, before fitting the histogram values

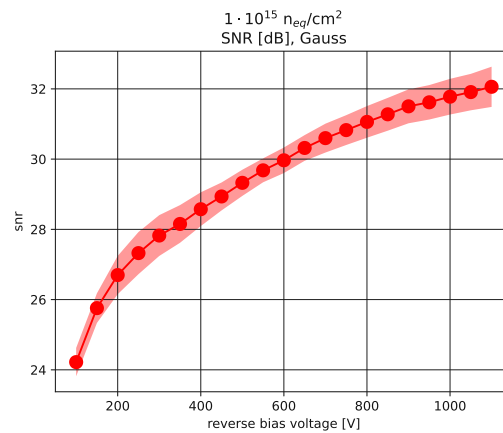

(b) SNR, after fitting the histogram values

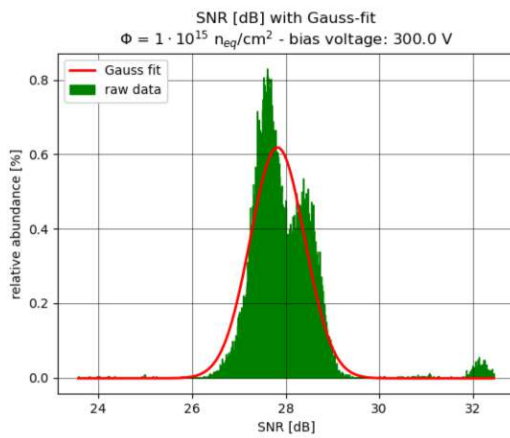

(c) The histogram data and fit at 300 V bias voltage

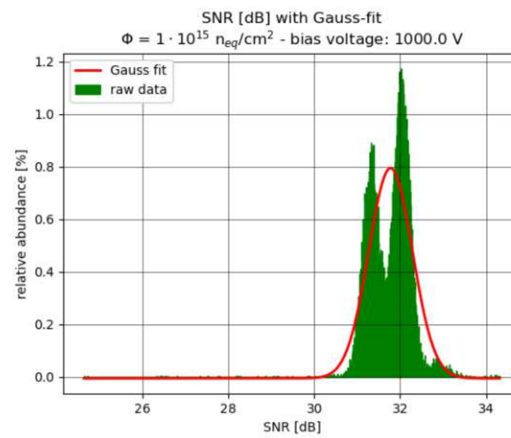

(d) The histogram data and fit at 1000 V bias voltage

Figure 38: a,b) SNR plotted against the bias voltage, c,d) exemplary histogram data

Die approbierte gedruckte Originalversion dieser Diplomarbeit ist an der TU Wien Bibliothek verfügbar
The approved original version of this thesis is available in print at TU Wien Bibliothek.
TU WIEN Bibliothek Your knowledge hub

6.2.5 SiC-Sensor exposed to 5×10^{15} n_{eq}/cm^2

Signals could be reliably detected with a high bias voltages only. Hence, at least 350 V had to be applied to observe signals, no data could be collected below. Thus, any plot about the characteristic parameters in the following section do not contain data points below 350 V bias voltage.

Leakage current

The trend of the leakage current is an increase with increasing bias voltage. Below 400 V, the curve shows an increase until it exhibits a saturation-like behavior. Above 400 V the leakage current increases again. For the bias voltage range of 500 V, the leakage current stayed below 11 nA. The IV-curve is presented in Fig. 39.

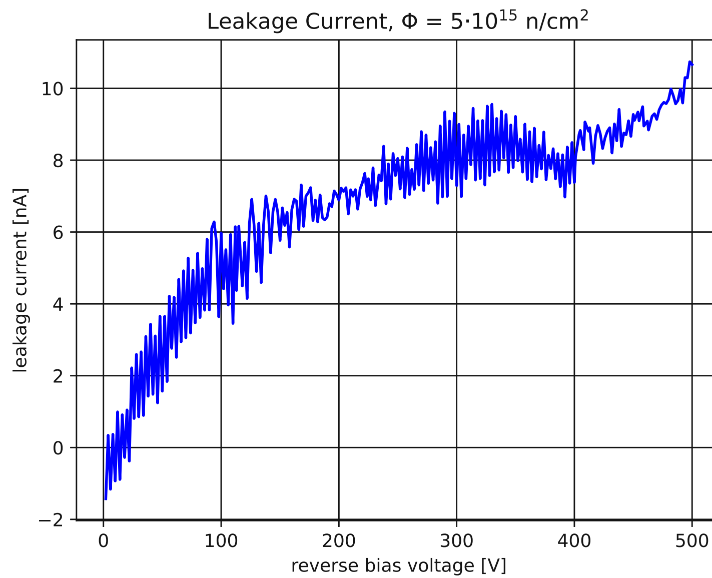

Figure 39: The leakage current up to 500 V for the sensor exposed 5×10^{15} n_{eq}/cm^2.

Peak maximum

The V_{max} shows an increase over the whole range of the bias voltage. A plot of the curve are shown in Fig. 40a,b for the directly measured parameter and the parameters after the fit. The first mean at 350 V bias voltage is $\mu_f = 6.059$ mV ($\mu_d = 8.331$ mV) with a standard deviation $\sigma_f = 0.466$ mV ($\sigma_d = 9.521$ mV). This value grows nearly linearly above 400 V bias voltage until it reaches the maximum value of 1100 V in both data sets. The highest mean of V_{max} is located here with $\mu_f = 11.961$ mV ($\mu_d = 13.011$ mV) and a standard deviation $\sigma_f = 0.585$ mV ($\sigma_d = 6.648$ mV). In the other two plots in Fig. 40c,d, the distribution of the values are shown including the fit. The refer to a bias voltage of 500 V and 1000 V. In both plots appears an additional peak around 18 mV which is caused by noise.

Die approbierte gedruckte Originalversion dieser Diplomarbeit ist an der TU Wien Bibliothek verfügbar
The approved original version of this thesis is available in print at TU Wien Bibliothek.
TU WIEN Bibliothek Your knowledge hub

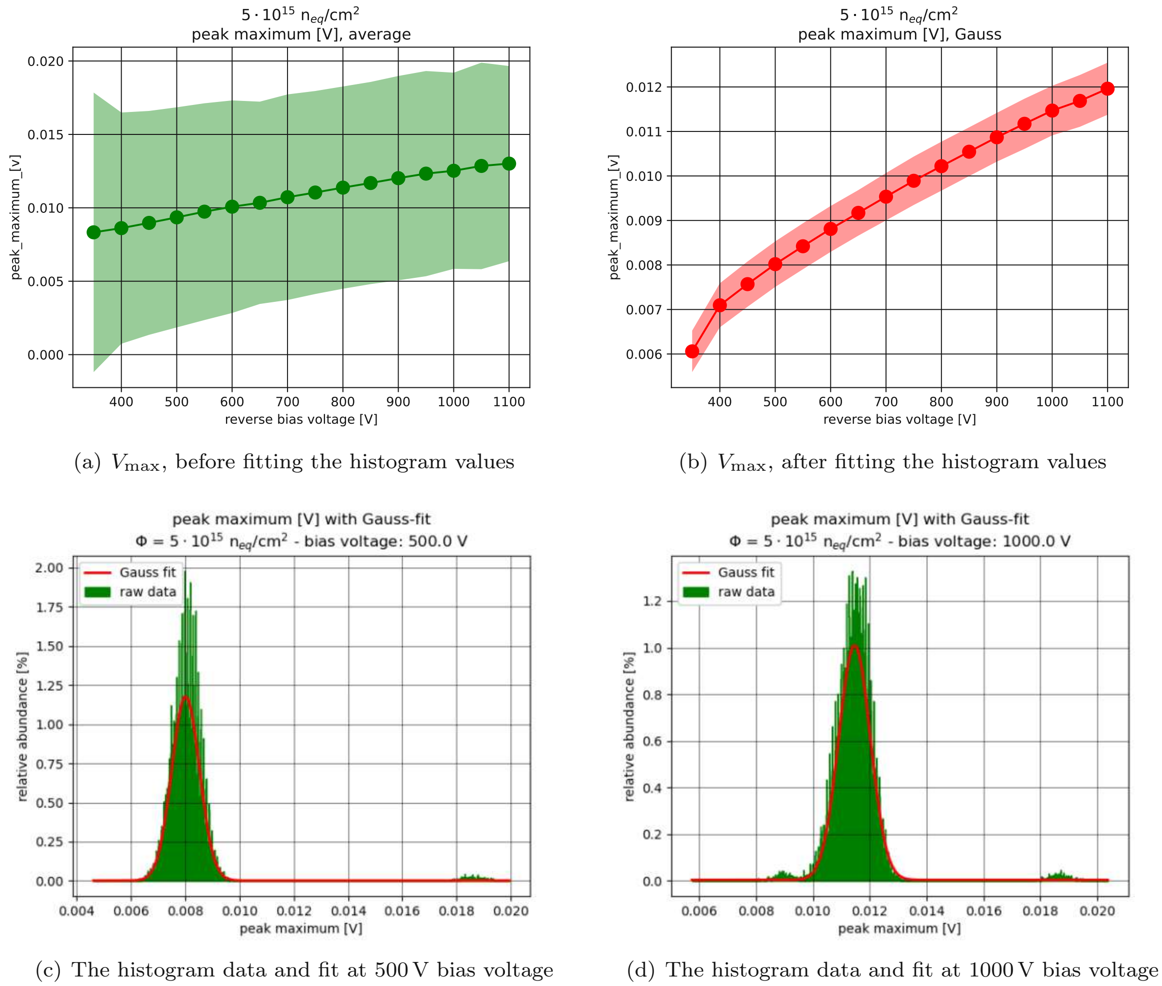

(a) $V_{\max}$, before fitting the histogram values

(b) $V_{\max}$, after fitting the histogram values

(c) The histogram data and fit at 500 V bias voltage

(d) The histogram data and fit at 1000 V bias voltage

Figure 40: a,b) $V_{\max}$ plotted against the bias voltage, c,d) exemplary histogram data

Time over threshold

For this parameter exists a lower boundary due to the analysis software. In this case, a peak consists at least of three voltage samples. This length refers to a minimal signal length of 0.59 ns. As this boundary exist, only the directly measured value is reliable for the lowest bias voltage of 350 V - the value after the fit is an outlier. The plots are shown in Fig. 41a,b. The directly measured mean value is $\mu_{\mathrm{d}} = 0.627$ ns ($\mu_{\mathrm{f}} = 0.451$ ns) with a standard deviation $\sigma_{\mathrm{f}} = 0.168$ ns. In general, this parameter increases in both the directly measured curve as well as the parameters after the fitting. They exhibit a nearly-linear behavior. The maximum value for the time-over-threshold is $\mu_{\mathrm{f,d}} = 0.802$ ns for the maximum applied bias voltage of 1100 V. The corresponding standard deviation $\sigma_{\mathrm{f,d}} = 0.110$ ns. These two values appear in both data series. Next to the plots of the SNR against the bias voltage, Fig. 41c,d show the distribution of this parameter including the corresponding fit. The values are concentrated in less bins in both plots.

Die approbierte gedruckte Originalversion dieser Diplomarbeit ist an der TU Wien Bibliothek verfügbar
The approved original version of this thesis is available in print at TU Wien Bibliothek.
TU WIEN Bibliothek Your knowledge hub

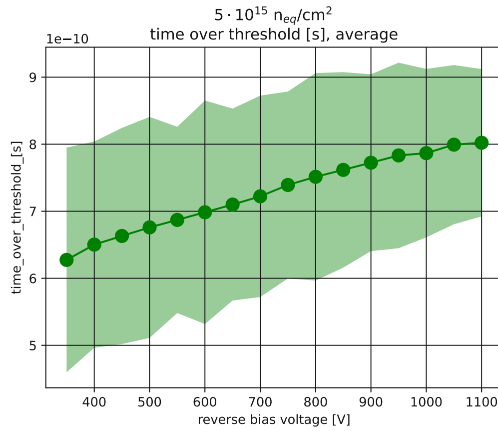

(a) t_{ToT}, before fitting the histogram values

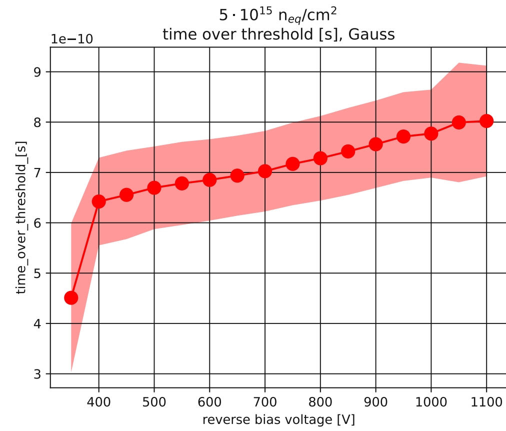

(b) t_{ToT}, after fitting the histogram values

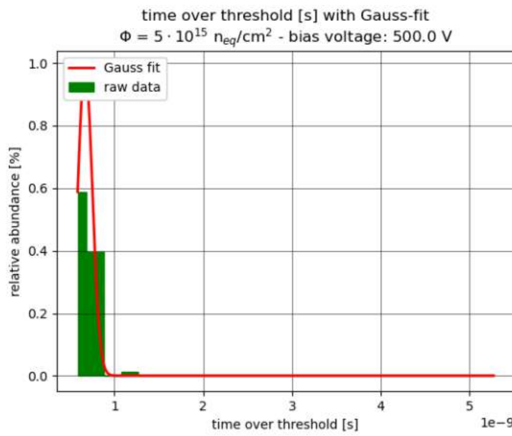

(c) The histogram data and fit at 500 V bias voltage

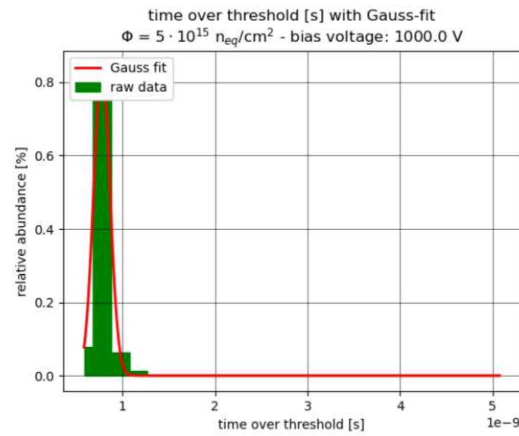

(d) The histogram data and fit at 1000 V bias voltage

Figure 41: a,b) t_{ToT} plotted against the bias voltage, c,d) exemplary histogram data

Peak area

Once again, an increase of the means is obtainable for increasing bias voltages. The corresponding curves of the parameter before and after the fit are presented in Fig. 42a,b. The minimum is located at the lowest bias voltage of 350 V; after the fit a value of $\mu_{\mathrm{f}} = 4.45{\times}10^{-12}$ Vs ($\mu_{\mathrm{d}} = 5.39{\times}10^{-12}$ Vs) with a standard deviation $\sigma_{\mathrm{f}} = 8.9{\times}10^{-13}$ Vs ($\sigma_{\mathrm{d}} = 5.09{\times}10^{-12}$ Vs) is derived. The average peak area increases nearly linearly from 400 V to 1000 V until a trend-braking 'outlier' appears in the graph after the fitting at 1050 V bias voltage. However, the maximum mean value is in both cases located at the highest bias applied bias voltage. Therefore, $\mu_{\mathrm{f}} = 7.79{\times}10^{-12}$ Vs ($\mu_{\mathrm{d}} = 8.46{\times}10^{-12}$ Vs), the standard deviation $\sigma_{\mathrm{f}} = 8.7\ {\times}10^{-13}$ Vs ($\sigma_{\mathrm{d}} = 3.59{\times}10^{-12}$ Vs). The histograms for 500 V and 1000 V bias voltage are presented in Fig. 42c,d exemplarily. The fitted Gaussian distribution follows the shape of the histogram in both plots.

Die approbierte gedruckte Originalversion dieser Diplomarbeit ist an der TU Wien Bibliothek verfügbar
The approved original version of this thesis is available in print at TU Wien Bibliothek.
TU Bibliothek WIEN Your knowledge hub

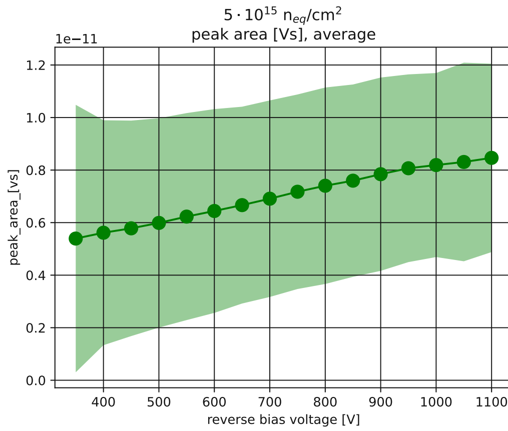

(a) A_{peak}, before fitting the histogram values

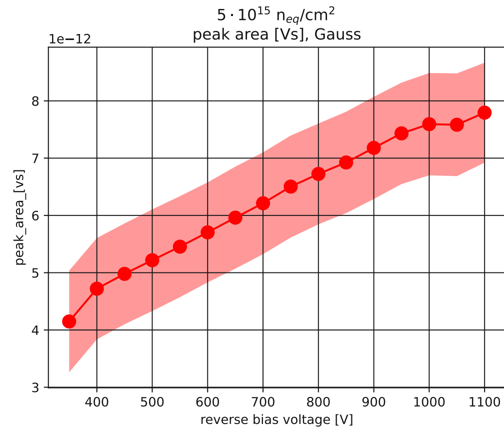

(b) A_{peak}, after fitting the histogram values

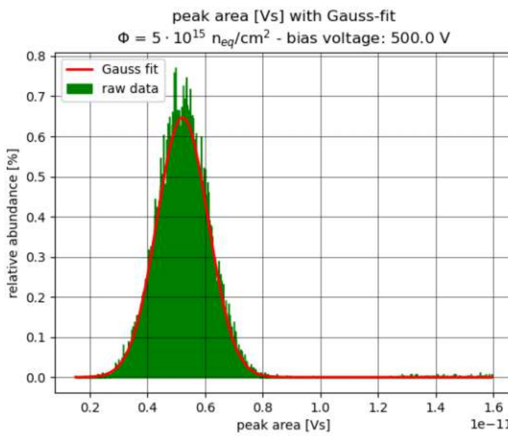

(c) The histogram data and fit at 500 V bias voltage

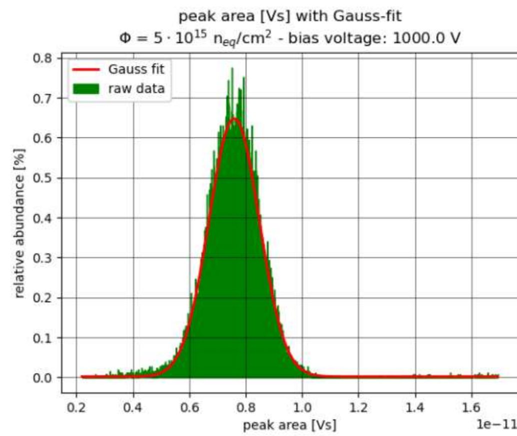

(d) The histogram data and fit at 1000 V bias voltage

Figure 42: a,b) A_{peak} plotted against the bias voltage, c,d) exemplary histogram data

Signal-to-noise ratio

The last parameter is the average SNR. Like the other parameters, also this one increases the higher the bias voltage is. Both the data from direct measurement as well as the means after the fits are shown in Fig. 43a,b. The minimum is located at the lowest bias voltage of 350 V and $\mu_{\text{f}} = 22.37\,\text{dB}$ ($\mu_{\text{d}} = 23.34$). The corresponding standard deviation $\sigma_{\text{f}} = 0.54\,\text{dB}$ ($\sigma_{\text{d}} = 3.598\,\text{dB}$). After increasing nearly linearly up to 1000 V the data show an 'trend-breaking outlier' at 1050 V in the curve after the fitting. Nevertheless the maximum SNR appears with the highest bias voltage at 1100 V in both data sets. The maximum SNR is $\mu_{\text{f}} = 26.69\,\text{dB}$ ($\mu_{\text{d}} = 27.01\,\text{dB}$) with a standard deviation of 0.34 dB ($\sigma_{\text{d}} = 1.90\,\text{dB}$). The fit of the histograms exhibit a shape-following Gaussian distribution. For this case, Fig. 43c,d show exemplary histograms with their fit. In these data, no double peaks were recorded.

Die approbierte gedruckte Originalversion dieser Diplomarbeit ist an der TU Wien Bibliothek verfügbar
The approved original version of this thesis is available in print at TU Wien Bibliothek.
TU WIEN Bibliothek Your knowledge hub

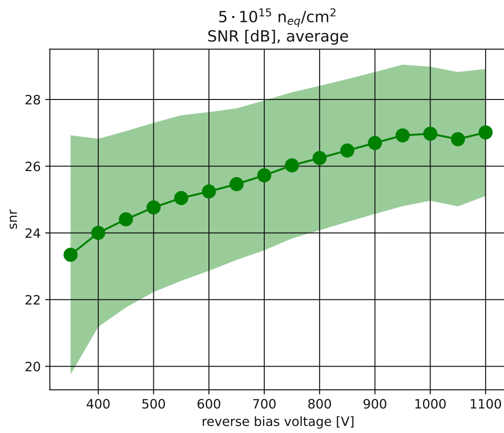

(a) SNR, before fitting the histogram values

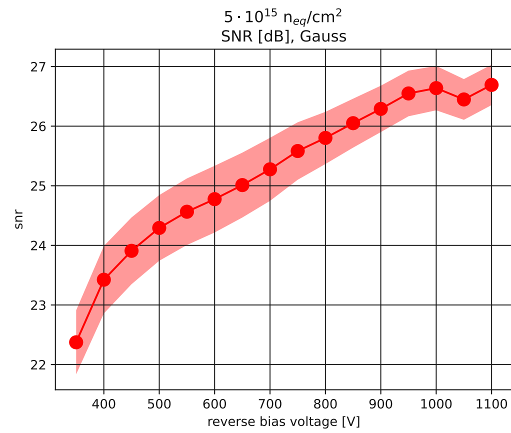

(b) SNR, after fitting the histogram values

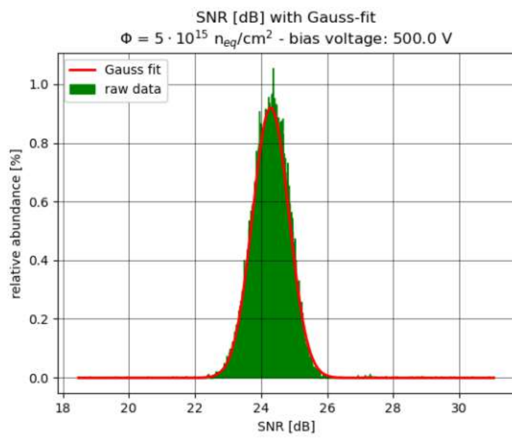

(c) The histogram data and fit at 500 V bias voltage

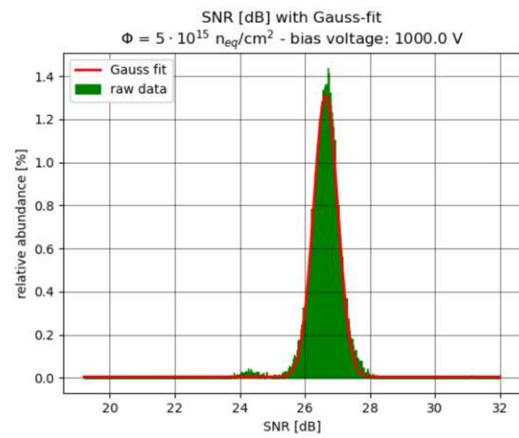

(d) The histogram data and fit at 1000 V bias voltage

Figure 43: a,b) SNR plotted against the bias voltage, c,d) exemplary histogram data

Die approbierte gedruckte Originalversion dieser Diplomarbeit ist an der TU Wien Bibliothek verfügbar
The approved original version of this thesis is available in print at TU Wien Bibliothek.
TU WIEN Bibliothek Your knowledge hub

6.2.6 SiC-Sensor exposed to 1×10^{16} $\mathbf{n_{eq}/cm^2}$

For this sensor, no signal could be recorded for any bias voltage. Thus, all efforts to achieve a detectable signal - like varying the Laser injection position of applying a very high bias voltage - showed no effect. Only a IV-curve could be taken. The general trend is an increase of the leakage current with the bias voltage. Between 80 V and 130 V the curve reaches a plateau-like area until it starts to increase again. The leakage current stays below 14 nA.

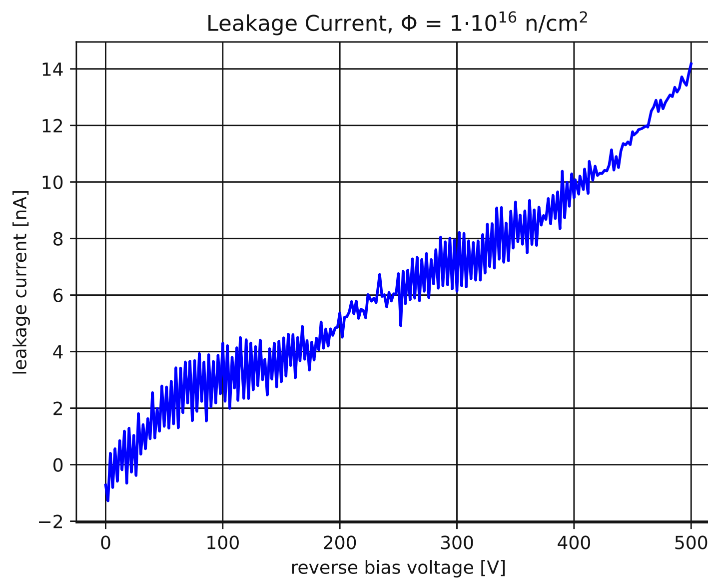

Figure 44: The leakage current up to 500 V for the sensor exposed 1×10^{16} n_{eq}/cm^2.

6.3 Measurements at MedAustron

6.3.1 Specific Experimental Parameters

At MedAustron a similar series of experiments was conducted as in the cleanroom of the Institute of High Energy Physics. As projectiles 252.2 MeV protons were used. According to the Bethe-Bloch-equation and the resulting value for the stopping power, 1.4 MeV were deposited in the Material on average. The calculation uses the band-gap energy as average excitation energy I. For this series of experiments, the low flux setting for this energy was used. As it was commissioned in 2022, the particle rate was approximately 3×10^3 per second and the intentisty of the beam was concentrated on roughly 6 mm×7.5 mm (FWHM values) [30]. For data acquisition the DRS4 oscilloscope was only capable of self-triggering onto the signal of the reference sensor. Hence, the RTP oscilloscope by Rhode&Schwarz [90] was used to record the signal peaks This device has a sampling rate of 10 GS/s. The setup of this experiments has an uncommon signal transfer line: The channel output of the UCSC board is connected to both oscilloscope by a T-piece. This results in a splitting of the signal where each oscilloscope only receives half the signal power. To calculate the real incoming signal voltage samples, the ratio of the amplitudes with and and without splitting has been determined in advance. This factor was applied during analysis on the measured values from the split setup. In addition, exemplary histograms of the collected data are shown (Fig. 68-71) next to the tables. For the detector exposed to 1×10^{16} n_{eq}/cm^2 no data could be acquitted.

Die approbierte gedruckte Originalversion dieser Diplomarbeit ist an der TU Wien Bibliothek verfügbar
The approved original version of this thesis is available in print at TU Wien Bibliothek.
TU WIEN Bibliothek Your knowledge hub

6.3.2 Non-irradiated SiC-Sensor

For this sensor also each parameter was determined.Thus, the plots of the parameters versus the bias voltage are shown in Fig. 45. First, the average peak height V_{max}, shows an increasing trend with increasing bias voltage. The minimum is located at the lowest bias voltage at 50 V with a value of 5.575 mV (standard deviation 4.572 mV). According to this trend, the maximum is on the upper end of the voltage ramp at 1050 V bias voltage with $\mu = 7.697$ mV ($\sigma = 9.025$ mV). However, a the highest bias applied voltage (1100 V) μ is 0.2 mV smaller with a 1 mV smaller standard deviation. The average time-over-threshold shows values in the range of 4.836 ns (minimum) at 50 V bias voltage to 8.342 ns (maximum) at 450 V. The corresponding standard deviations are 4.482 ns and 5.951 ns respectively. There is no clear trend visible in the data. It shows higher and lower points from 450 V to 800 V from which on the t_{ToT} decreases again. Only at 1100 V the time-over threshold is higher than at 1050 V bias voltage before. The average peak area show a saturation at approximately 2.55×10^{-11} Vs for a bias voltage of 350 V and higher. Until then, the average peak area increases steadily. Last but not least the average signal-to-noise ratio was determined. This parameter increases from 13.092 dB at 50 V bias voltage until it also shows a saturation-like behavior. Hence, from 500 V bias voltage on, the SNR values are roughly 14.1 dB. Next to this, the histograms of the distribution of the parameter values at 1000 V bias voltage are presented in Fig. 46. Each histogram shows an asymmetrical shape. The majority of the values are greater than the most probable value. Hence, the average value is greater than the most probable value as well. The histogram of the peak area exhibits a double peak, while all other plots just show one local maximum. Nevertheless, the Landau distribution is indicated in every diagram.

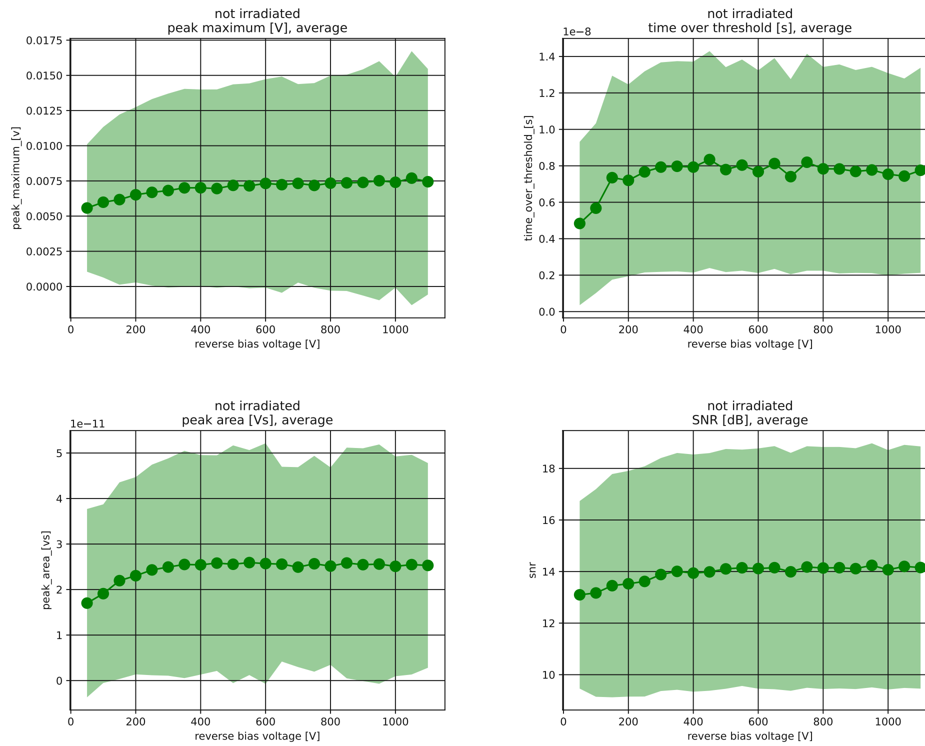

Figure 45: The mean and the standard deviation of V_{max}, t_{ToT}, A_{peak} and SNR for the reference silicon carbide sensor

Die approbierte gedruckte Originalversion dieser Diplomarbeit ist an der TU Wien Bibliothek verfügbar
The approved original version of this thesis is available in print at TU Wien Bibliothek.
TU WIEN Bibliothek Your knowledge hub

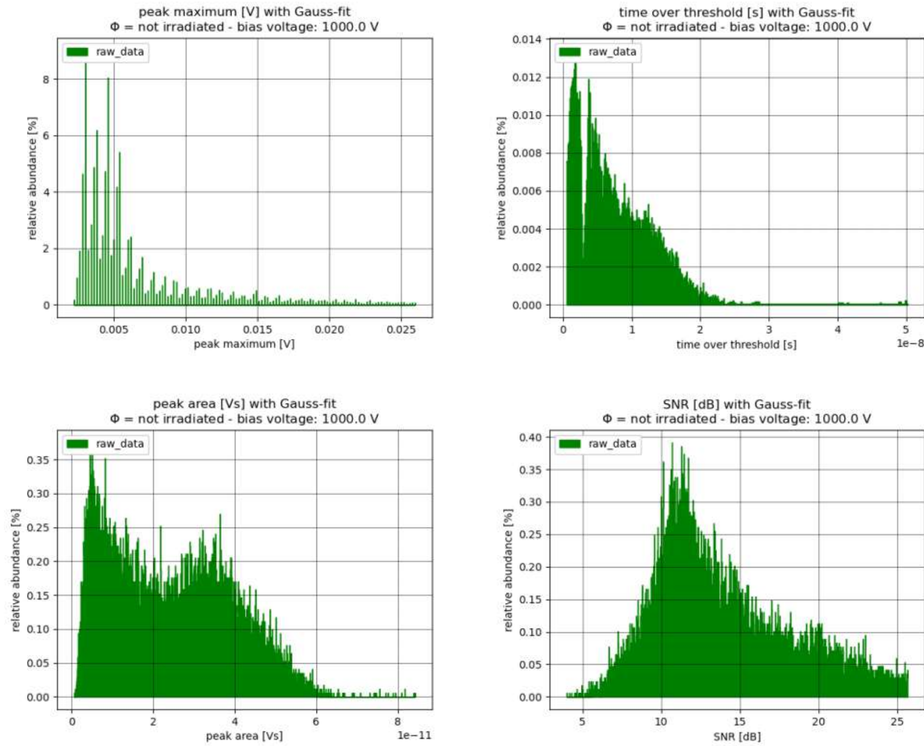

Figure 46: Exemplary histograms of all parameter distributions at 1000 V bias voltage

6.3.3 SiC-Sensor exposed to $5 \times 10^{14}\ \mathbf{n_{eq}/cm^2}$

The four parameters have also been derived for the diode which was exposed to $5\times10^{14}\ \mathrm{n_{eq}/cm^2}$. All plots of the parameters are shown in Fig. 47. The average peak height shows an increasing trend from 100 V to 1100 V bias voltage. The very first data point at 50 V is considered as an outlier. The minimum average peak height is 3.468 mV (standard deviation 2.351 mV) at 100 V and the maximum 4.584 mV (standard deviation 4.116 mV) at 1050 V bias voltage. At the highest bias voltage (1100 V), the mean is 1 mV smaller but exhibits a larger standard deviation. The average time-over-threshold data shows varying values with no clear trend. The minimum is located at the lowest bias voltage (50 V) and is 0.775 ns, with a standard deviation of 0.515 ns. The values of this parameter increase until 500 V, after it drops by half a nanosecond. For bias voltages higher than 500 V the parameter changes to lower and higher values 'randomly'. The maximum is obtained at 900 V with 2.218 ns (σ = 2.712 ns). In general, all data points are lying within the standard deviation of the value before and after. The trend of the average peak is an increase throughout the whole bias voltage range. The smallest average peak is 2.021×10^{-12} Vs (standard deviation 2.151×10^{-12} Vs) at 100 V bias voltage. At 50 V A_{peak} is 0.08×10^{-12} Vs higher. The maximum of the average peak area is located at 900 V with $\mu = 3.962\times10^{-12}$ Vs. Hence, for a bias voltage higher than 900 V the average peak area is always greater than 3.8×10^{-12} Vs with σ at least 4.7×10^{-12} Vs. The average signal-to-noise ratio shows varying values as well with a minimum of 14.812 dB (standard deviation 2.625 dB) at 100 V bias voltage. The maximum is 16.025 dB (σ = 3.466 dB) at 600 V. Additionally, Fig. 48 presents the histograms of the distribution of the parameters at 1000 V bias voltage. In each plot, the Landau distribution is indicated. The values for t_{ToT} show a double peak and with a narrow width. Again, the average values are greater than the most probable values.

Die approbierte gedruckte Originalversion dieser Diplomarbeit ist an der TU Wien Bibliothek verfügbar
The approved original version of this thesis is available in print at TU Wien Bibliothek.
TU WIEN Bibliothek Your knowledge hub

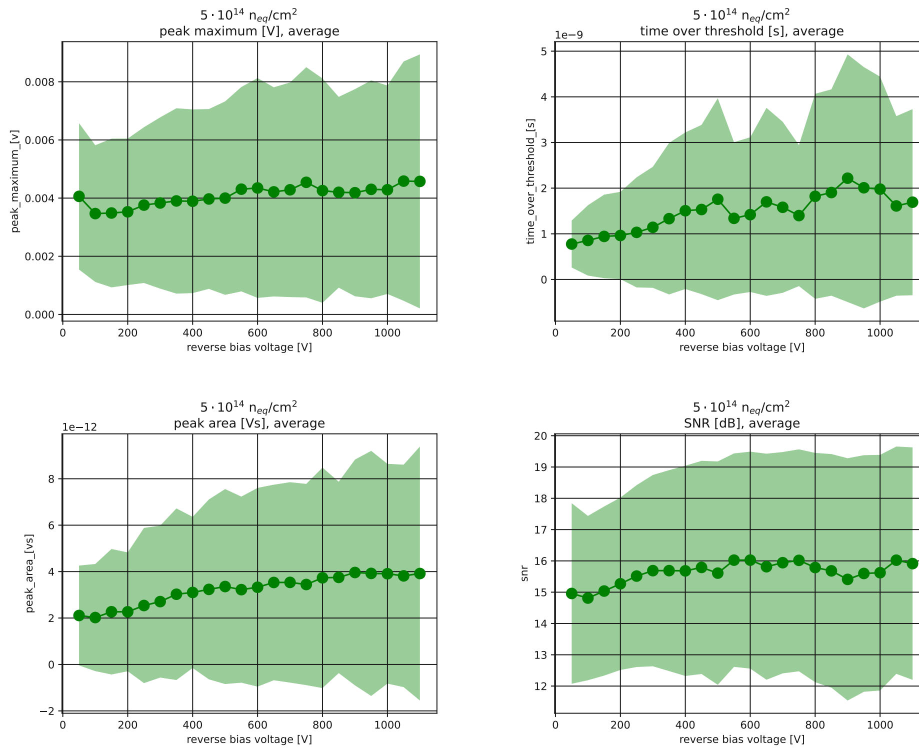

Figure 47: The mean and the standard deviation of V_{max}, t_{ToT}, A_{peak} and SNR for the silicon carbide sensor exposed to 5×10^{14} $\text{n}_{\text{eq}}/\text{cm}^2$

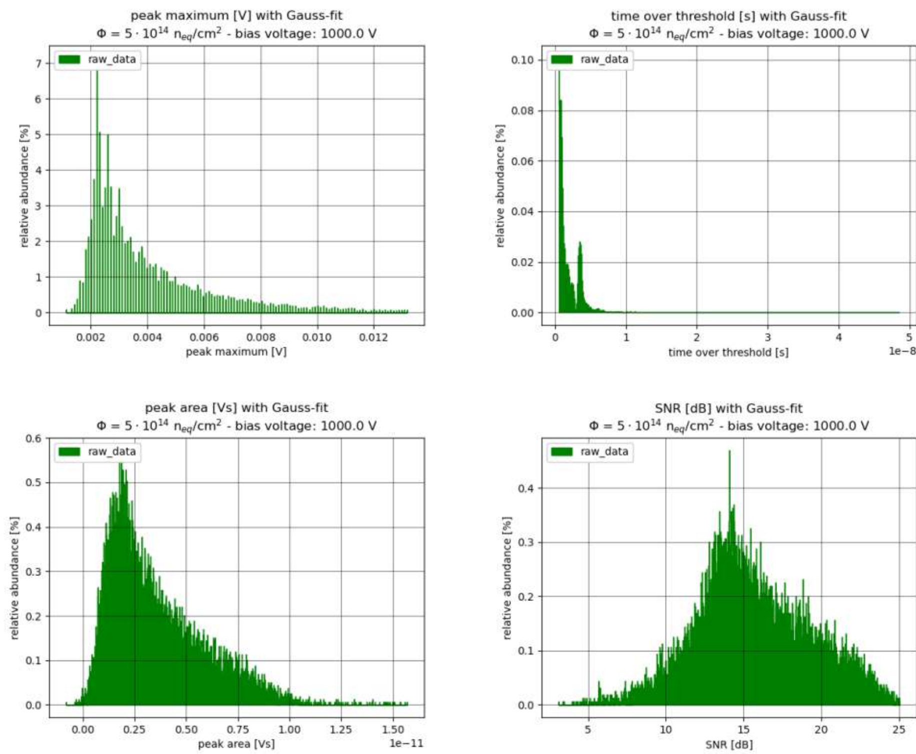

Figure 48: Exemplary histograms of all parameter distributions at 1000 V bias voltage

Die approbierte gedruckte Originalversion dieser Diplomarbeit ist an der TU Wien Bibliothek verfügbar
The approved original version of this thesis is available in print at TU Wien Bibliothek.
TU Bibliothek, Your knowledge hub, WIEN

6.3.4 SiC-Sensor exposed to 1×10^{15} $\mathbf{n_{eq}/cm^2}$

The analysis of the sensor signals yield the four parameters as well. All plots of the parameters versus the bias voltage are shown in Fig. 49. However, no values could be derived at 50 V bias voltage. For the average peak height $V_{\max}$ an increasing trend is obtainable: The minimum is located at 100 V bias voltage with a value of 3.504 mV (σ = 2.408 mV), while the maximum is linked to the highest bias voltage of 1100 V with 4.350 mV (σ = 3.869 mV). A similar trend is visible for the time-over-threshold t_{ToT}. The lower the bias voltage is, the shorter is the signal. The minimum corresponds to the lowest bias voltage with a measurable signal with a value of 0.768 ns (standard deviation 0.757 ns). The maximum is located at 900 V bias voltage (μ = 1.432 ns, σ = 2.098 ns) with being nearly equally high at 1050 V and 1100 V (μ = 1.430 ns and μ = 1.415 ns respectively). The average peak area exhibits the increasing trend as well. Starting with a value of 1.593×10^{-12} Vs at 100 V bias voltage, this parameter grows until it reaches the maximum of 3.167×10^{-12} Vs at 1050 V bias voltage. At 1100 V A_{peak} is 3.123×10^{-12} Vs. The standard deviations according to the minimum and maximum are 1.770×10^{-12} Vs and 3.167×10^{-12} Vs. At last the signal-to-noise ratio was determined. Beginning with a trend-breaking outlier at 100 V bias voltage the SNR increases until it exhibits a saturation-like behavior. The minimum is located at 150 V with 15.368 dB (standard deviation 2.612 dB) and saturates a approximately 16.05 dB ($\pm$ 0.05 dB) for bias voltages of 500 V and higher. Moreover, the histograms in Fig. 50 present the distribution of the parameters at 1000 V bias voltage. The plots of $V_{\max}$ and A_{peak} indicate the Landau distribution and it can be assumed for the other two plots as well. The t_{ToT} shows a narrow distribution with two distinct peaks. For all data sets the most probable value is smaller than the mean value.

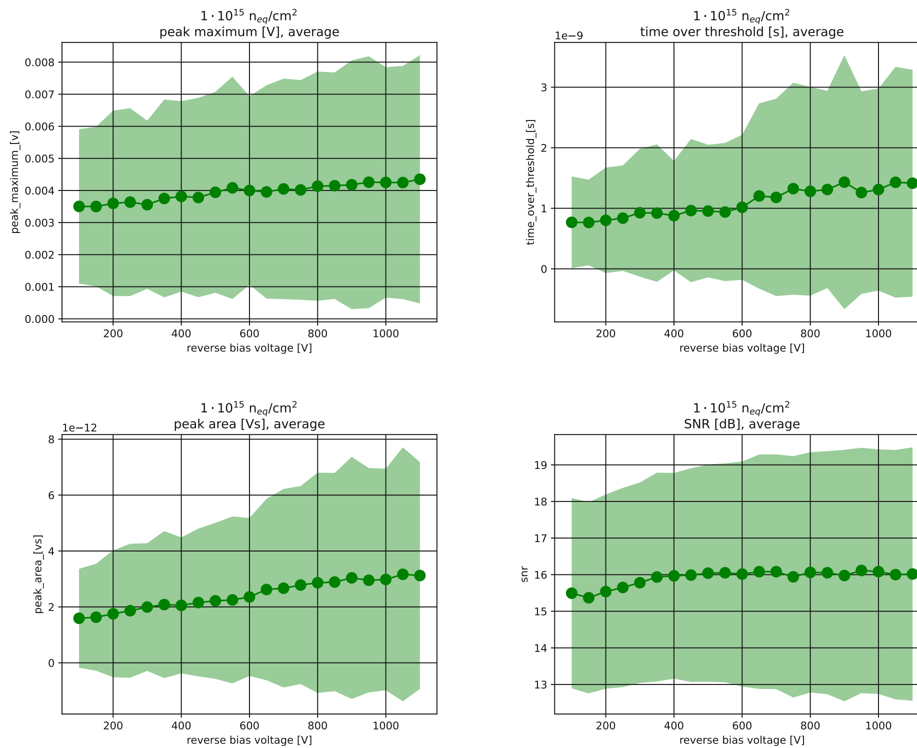

Figure 49: The mean and the standard deviation of $V_{\max}$, t_{ToT}, A_{peak} and SNR for the silicon carbide sensor exposed to 1×10^{15} $\mathrm{n_{eq}/cm^2}$

Die approbierte gedruckte Originalversion dieser Diplomarbeit ist an der TU Wien Bibliothek verfügbar
The approved original version of this thesis is available in print at TU Wien Bibliothek.
TU WIEN Bibliothek Your knowledge hub

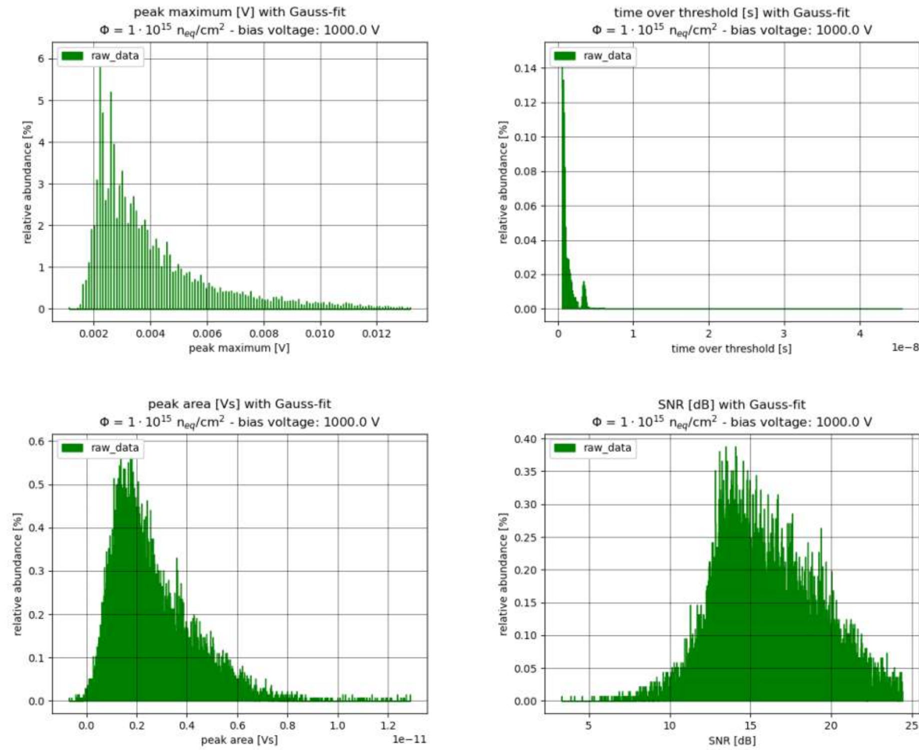

Figure 50: Exemplary histograms of all parameter distributions at 1000 V bias voltage

6.3.5 SiC-Sensor exposed to $5 \times 10^{15}\ \mathbf{n_{eq}/cm^2}$

The last diode only exhibited signals for 300 V bias voltage and higher. Unfortunately, no data was acquitted for bias voltage above 800 V as well. The plots for each parameter is presented in Fig. 51. The data for the average peak maximum $V_{\max}$ show values between 4 mV and 6 mV, with a minimum of 4.422 mV and maximum of 5.643 mV. The standard deviations for the minimum and maximum are 4.609 mV (800 V bias voltage) and 3.855 mV (350 V bias voltage) respectively. Moreover, the standard deviations of all values show that all other data points are located within $\mu + \sigma$. The average time-over-threshold t_{ToT} exhibits values of approximately 1 ns. The minimum t_{ToT} of 0.910 ns ($\sigma = 1.088$ ns) corresponds to a bias voltage of 850 V while the maximum is 1.175 ns (500 V, $\sigma = 1.790$ ns). The average peak area A_{peak} yields values in the range of 2.111×10^{-12} Vs (minimum) and 2.734×10^{-12} Vs (maximum). These data points are located at 750 V and 400 V bias voltage, the standard deviations are 2.811×10^{-12} Vs and 2.372×10^{-12} Vs respectively. Only the signal-to-noise ratio SNR show a visible decreasing trend. Starting with a value of 17.142 dB near the maximum of 17.258 dB at 350 V bias voltage (standard deviation of the maximum 3.423 dB) the parameter decreases until it reaches the minimum. As before, the minimum is not the last derived value. It occurs at 800 V bias voltage with 15.673 dB and standard deviation of 3.070 dB. Exemplary histograms are shown in Fig. 52 which refer to the data set at 700 V bias voltage. The plots show a Landau-like distribution for all parameters except the time-over-threshold. In this diagram, two peaks appear with a dominant one at small values and the other one at higher ones. In general, the mean values are greater than the most probable ones.

Die approbierte gedruckte Originalversion dieser Diplomarbeit ist an der TU Wien Bibliothek verfügbar
The approved original version of this thesis is available in print at TU Wien Bibliothek.
TU WIEN Bibliothek Your knowledge hub

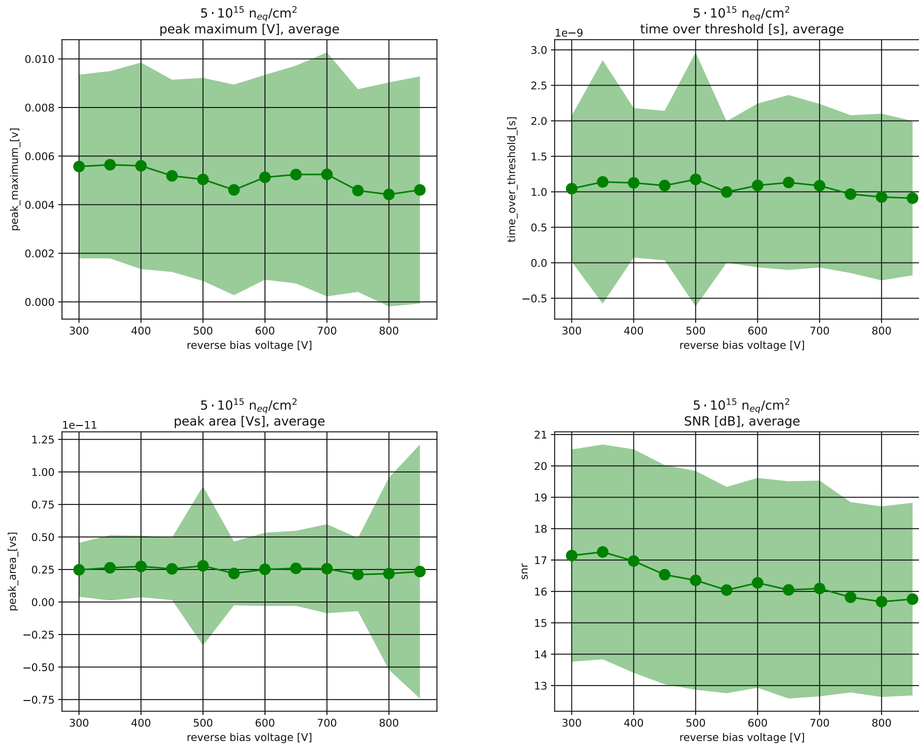

Figure 51: The mean and the standard deviation of V_{max}, t_{ToT}, A_{peak} and SNR for the silicon carbide sensor exposed to 5×10^{15} $\text{n}_{\text{eq}}/\text{cm}^2$

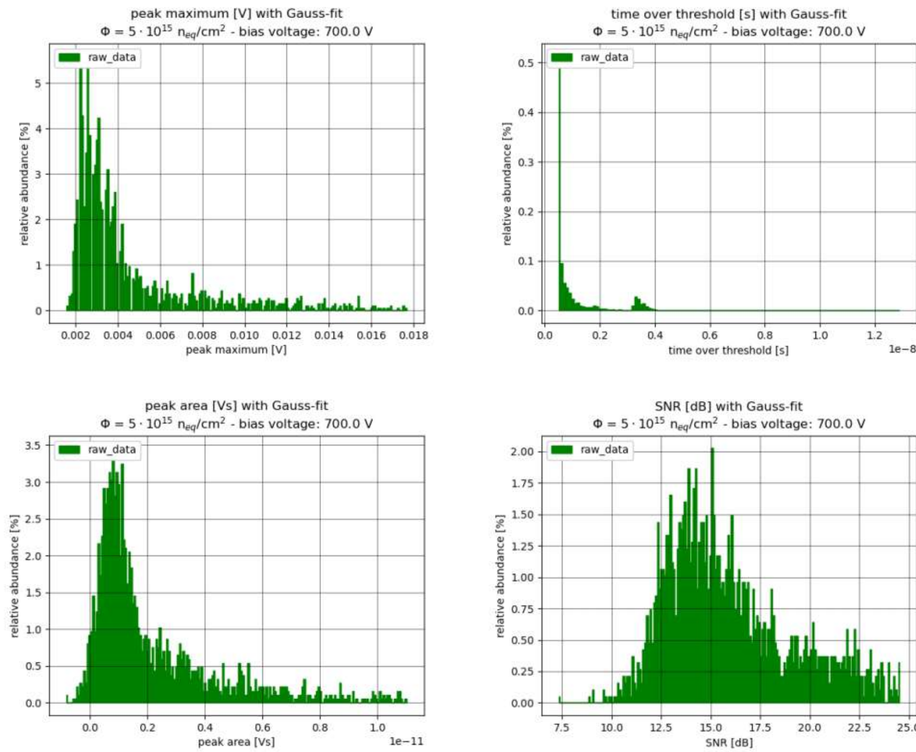

Figure 52: Exemplary histograms of all parameter distributions at 700 V bias voltage

Die approbierte gedruckte Originalversion dieser Diplomarbeit ist an der TU Wien Bibliothek verfügbar
The approved original version of this thesis is available in print at TU Wien Bibliothek.
TU WIEN Bibliothek Your knowledge hub

7 Discussion

The investigation of differently irradiated 4H-SiC sensors led to many interesting results. Irradiation with neutrons in the TRIGA Mark II reactor core at the Atominstitut of the Vienna Technical University damaged the crystal structure in a controlled way. Hence, simulating aging effects, as well as the stages of the lifecycle of this sensor due a particle beam, was achieved. The samples were exposed to different fluences each ranging from 5×10^{14} to 1×10^{16} 1 MeV neutron equivalent per cm^2. In this chapter, the following notation for the diodes will be used. The non-irradiated sample #0 acts as reference sample for the samples #1 to #4.

sample	fluence [n_{eq}/cm^2]	irradiation time
#0	-	-
#1	5×10^{14}	18 min
#2	1×10^{15}	36 min
#3	5×10^{15}	3 h
#4	1×10^{16}	6 h

Table 3: The notation for the samples in this chapter.

Fitting exhibited more precise parameters than just calculating means and standard deviation. While the means after the fit do not differ much from the directly evaluated means, the standard deviations decrease significantly. While fitting is a pure mathematical method, it works well for dominant peaks in the plotted histograms. Any peaks resulting from noise signals are nearly neglected by the fitting algorithm. Noise has a greater influence onto the directly obtained mean and a even greater one onto the standard deviation. It must be considered, that fitting only works reliably for data sets with a great range of quasi-continuous values. Thus, the plots for the peak maximum, the peak area and the signal-to-noise ratio show the comparison of the mean μ_f and standard deviations σ_f. On the other hand, the time-over-threshold has only discrete values due to the minor number of samples in a peak, which is justified by the sampling rate of the DRS4 oscilloscope. The comparison of the means of the time-over-threshold is the only plot presenting directly observed means μ_d and standard deviations σ_d. For better inter-comparability, all plots were generated using the same colors for the same samples.

7.1 Laser-TCT measurements

Leakage current

The comparison of the leakage current yields expectable results. As one would assume according to the NIEL-hypothesis, the leakage current increases with the fluence the sensor was exposed to. Thus, more damage inside the crystal was caused. It establishes inter-band-gap energy levels, which act as intermediate stages for the excitation into the conduction band. Next to this, they are generation centers for electron-hole-pairs. If an electron is trapped in these states, it is not necessary that a photon has to carry at least E_g excite the electron into the conduction band. The following, a plot with the comparison of all IV-curves is presented in Fig. 53 below. For each sample, a similar behavior is obtained. The trend of the leakage current is an increase, until it reaches a plateau-like area around 400 V. For the range over 400 V, the current starts to increase again. Interestingly, there is nearly no difference in the progress of the graph of sample #0 and #1. Both IV-curves remain on the same level, indicating that fluences up to 5×10^{14} n_{eq}/cm^2 do not have a major impact on the leakage current. The maximum observed current for these samples is around 4 nA. The next data set (#2) has a maximum located above 6 nA and #3

Die approbierte gedruckte Originalversion dieser Diplomarbeit ist an der TU Wien Bibliothek verfügbar
The approved original version of this thesis is available in print at TU Wien Bibliothek.
TU WIEN Bibliothek Your knowledge hub

below 11 nA. Only the curve of #4 shows a difference to the other plots. It does not follow the trend of exhibiting higher currents in the low bias regime. However, above 350 V bias voltage, this sample yields the highest current of the investigated sensors. Moreover, the plateau-like area is already reached around 100 V bias voltage. It is not as present as for sample #0 to #3 but the curve rises to ≈ 14 nA at 500 V. Compared to values of pure silicon detectors - which were exposed to similar fluences - the leakage current of irradiated 4H-SiC sensors is about two to three orders of magnitudes smaller [15].

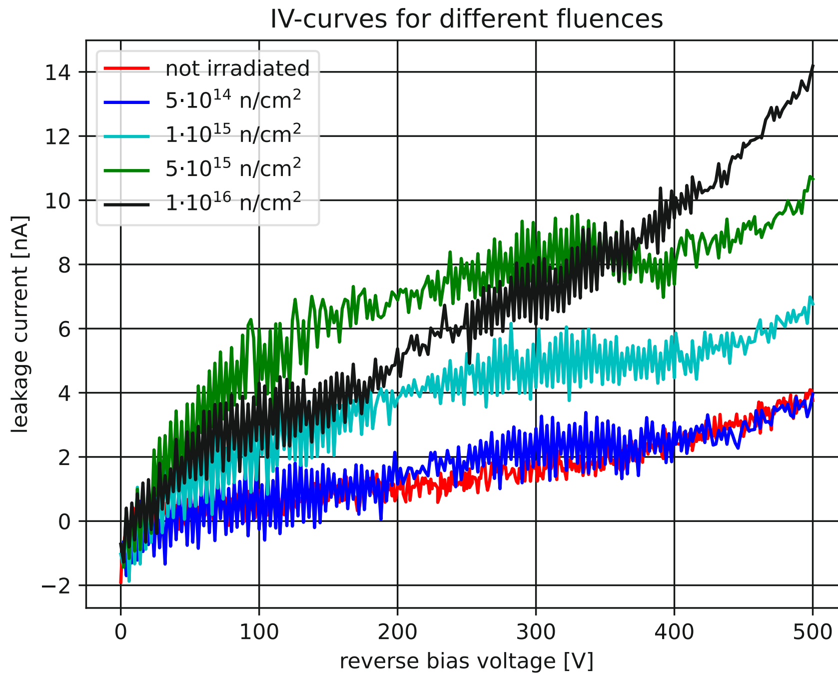

Figure 53: The comparison of the IV-curves of all samples.

Peak maximum

The first parameter derived from the peak analysis is the average peak maximum V_{max}. For comparing this parameter, the mean and the standard deviation after the fit are used. Thus, Fig. 54a shows the plots for all samples, which yield measurable average peak maxima. A comparison of the distribution of the measured peak maximum data is presented in Fig. 54b,c. Expectantly, the higher the fluence is, which the sensor was exposed to, the lower the average signal maxima are. Also, there are no intersections of two curves; meaning that for every bias voltage the lower irradiated sensor had the higher signal. Also, the shape of the of the curve differ strongly from the reference sample #0. The non-irradiated sample shows a strong increase of the average peak maximum, until the step-wise increase is nearly constant above 600 V bias voltage. In comparison, this behavior also appears for sample #1 but starts already around 400 V. Sample #2 is nearly linear-like in the whole bias voltage range. However, no signal was obtained for 50 V bias here. Bias voltage where no data could be derived also appears in sample #3. In this case, signals were only recorded for 350 V bias voltage and higher. Clearly, all samples possess their maximum of the average peak maximum at 1100 V. In terms of numbers, the reference sample #0 has the highest maximum of just below 60 mV. The maximum of sample #1 is located at roughly 37 mV, which is about 20 mV smaller, or 65 % of the reference sample respectively. For sample #2, the difference at 1100 V is 31 mV, which is less than half (45 %) the signal of #0. Expectantly, the highest irradiated

Die approbierte gedruckte Originalversion dieser Diplomarbeit ist an der TU Wien Bibliothek verfügbar
The approved original version of this thesis is available in print at TU Wien Bibliothek.
TU Bibliothek WIEN Your knowledge hub

sample #3 shows the greatest difference (46 mV), which is only 23 % compared to the reference. At 500 V bias voltage, the differences to the average peak maximum are approximately 26 mV, 36 mV and 46 mV for the sensors #1, #2 and #3 respectively. These differences refer to 52 %, 33 % and 15 % of the average peak maximum of sample #0. Below 350 V, no detectable signal was recorded for #3. As a result, differences and relative shares could only be derived for sample #1 and #2. One more exemplary point to calculate differences and relative shares is 200 V bias voltage. The difference of the average peak maximum of sample #1 to the reference is approximately 20 mV, while it is nearly 25 mV for sample #2. In terms of relative shares, these values correspond to 47 % and 34 % respectively. The histograms refer to a bias voltage of 500 V and 1000 V. All histograms show a similar Gaussian-like shape with different locations of the peak. Expectantly, the longer the sensor was irradiated, the smaller is the value of the center of the corresponding peak. Altering the bias voltage shifts the location of the peak to a higher value. However, the less the sample was irradiated, the more asymmetrical the shape is. This may be caused by the low number of samples, as the 'real' maximum is not recorded. At 18 mV appears a peak caused which is caused by noise in all data series.

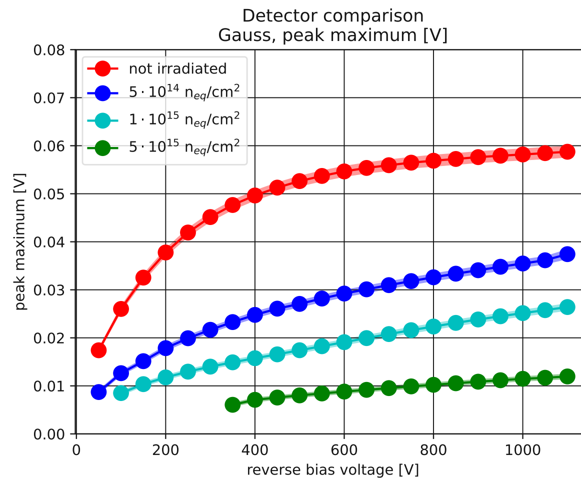

(a) The comparison of the means and standard deviations of the peak maximum V_{max} after being fitted with a Gaussian distribution.

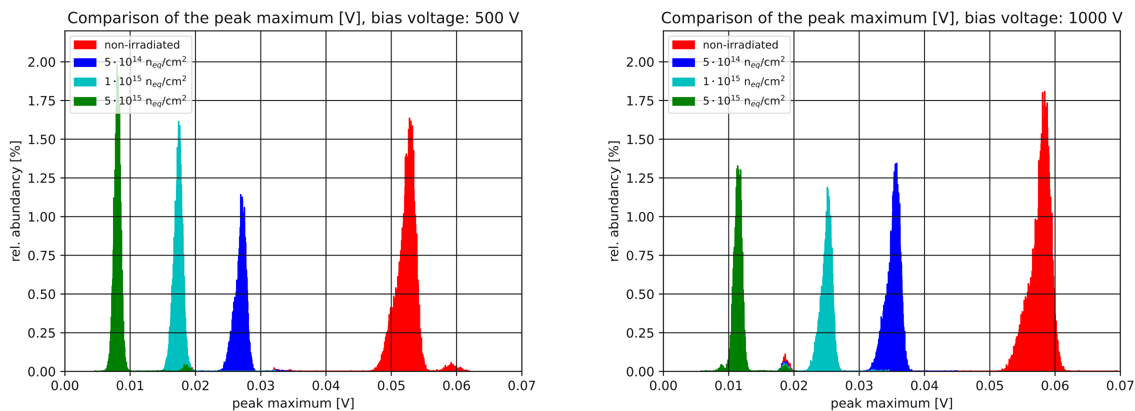

(b) The comparison of the histograms of each detector at 500 V bias voltage.

(c) The comparison of the histograms of each detector at 1000 V bias voltage.

Figure 54: The comparison of the data of the average peak maximum.

TU Bibliothek WIEN Your knowledge hub
Die approbierte gedruckte Originalversion dieser Diplomarbeit ist an der TU Wien Bibliothek verfügbar
The approved original version of this thesis is available in print at TU Wien Bibliothek.

Time-over-threshold

In comparison to the average peak maximum, where each sample showed a similar behavior, the average time-over-threshold exhibits a totally different plot. The plot regarding the comparison of the average time-over-threshold t_{ToT} is presented in Fig. 55a below. In addition, Fig. 55b,c show the distribution of the measured values at 500 V and 1000 V bias voltage. The time-over-threshold is the only parameter which has a lower boundary, according to the sampling rate of the DRS4 oscilloscope. This limitation is based on the fact that a minimal number of voltage samples, of which a peak must consist, is required by the analysis software. It must be considered, that for t_{ToT} only discrete values are possible. It is calculated as the number of peak samples times the inverse of the sampling rate. The other parameters exhibit a quasi-continuous behavior due to the analog-digital converter of the oscilloscope. Hence, the binning in the histogram is based on the number of occurrences of the discrete values. Thus, a higher calculated mean indicates a higher number of peaks with a higher number of voltage samples. Most noticeable, the reference sample possesses a maximum while all other samples just show a continuing increase as general trend. The result of the decrease of t_{ToT} is that at high bias voltages the values have the smallest differences and highest relative shares. Sample #1 shows only 46 ps difference fot the average t_{ToT} to the reference sample at a bias voltage of 1100 V. This difference is linked to a relative share of 96 % of the value of the reference sample. Also, for sample #2 the difference is about 130 ps, which leads to a relative share of 89 %. Sample #3 exhibits a difference of nearly 380 ps, it still corresponds to 68 %. As it was indicated before by the general trend, the differences increase the lower the bias voltage is. At 600 V, the differences are 164 ps, 280 ps and 552 ps for sample #1 to #3 respectively. In terms of the relative share, the values are approximately 87 %, 78 % and 56 % - which is roughly 10 % less than at the highest applied bias voltage. The longest measured average time-over threshold appears at 300 V bias voltage, which is close to the full depletion voltage (296 V according to [73]). At this point, the differences are 230 ps, 380 ps for sample #1 and #2 which refer to 82,% and 71 % relative share. For sample #3 no signal could be detected reliably.

At V_{FD}, the depletion zone covers the whole active diode volume the first time. The induced charge does not get drowned in the free charge carriers outside the space charge region anymore. If the bias voltage is higher than V_{FD}, the charge carriers are attracted by the stronger $\vec{E}$-field and get pulled towards the electrodes faster. This results in a shorter signal. The irradiated diodes do not show a behavior like the reference sample. The signal duration of irradiated samples grows throughout the whole applied bias range. This indicates a smaller life time of the electrons, before a recombination or being trapped in an intergap state. Those are established by lattice defects - caused by the irradiation with neutrons. To achieve higher values for t_{ToT} for an irradiated sample than for the reference diode, the bias voltage has to be sufficiently high. This is based on the fact that at the end of the examined voltage ramp a possible plateau can be presumed for #0. Sample #1 and #2 exhibit smaller differences the higher the bias voltage is and seem to increase further. However, only an assumption can be made in this thesis. The discrete value behavior of this parameter (number of samples) is obtainable in these plots. In this case, the first bin refers to three samples, which is just seen in the data of #3. At 500 V bias voltage, the majority of the measured values are concentrated in different bins for each detector. Increasing the voltage leads to a narrowing of the maxima of the histograms. Thus, this can also be observed in the development of the average time-over-threshold plots versus the bias voltage. sample #0 and #1 exhibit a nearly similar histogram for 1000 V bias voltage. The most significant difference is that #0 shows a higher value in the bin with the most samples compared to #1. The other two samples are distinguishable as their maxima are located in different bins.

Die approbierte gedruckte Originalversion dieser Diplomarbeit ist an der TU Wien Bibliothek verfügbar
The approved original version of this thesis is available in print at TU Wien Bibliothek.
TU Bibliothek WIEN Your knowledge hub

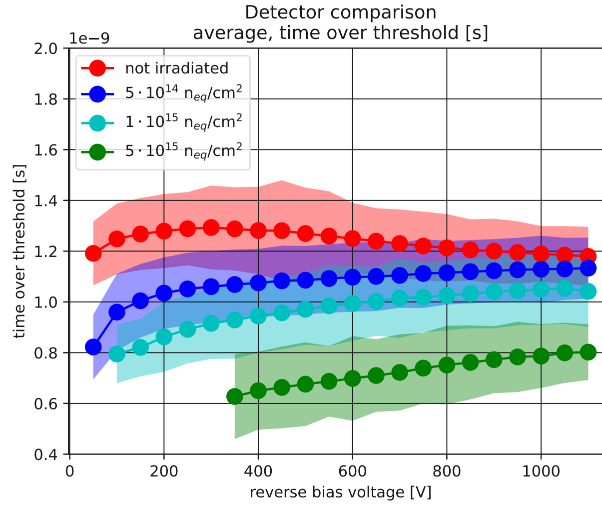

(a) The comparison of the means and standard deviations of the time-over-threshold t_{ToT} after being fitted with a Gaussian distribution.

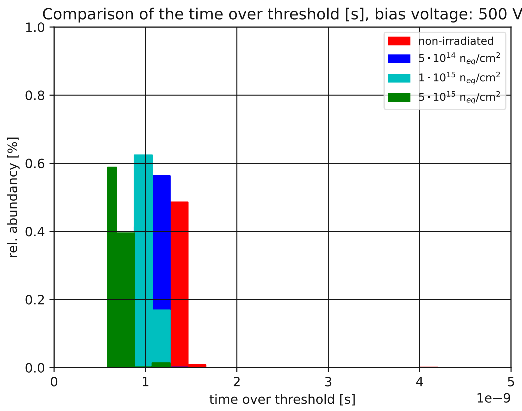

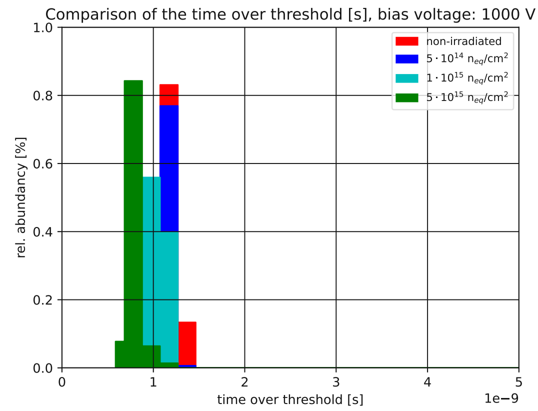

(b) The comparison of the histograms of each detector at 500 V bias voltage.

(c) The comparison of the histograms of each detector at 1000 V bias voltage.

Figure 55: The comparison of the data of the average peak maximum.

Peak area and Charge Collection Efficiency

The next parameter is the average peak area A_{peak}, which shows another time a totally different dependency on the bias voltage if compared to the average time-over-threshold and average peak maximum. Mathematically, the peak area was calculated as the numerical integral of the voltage samples during the start and stop sample. The permanently increasing V_{max} and the at first increasing and afterwards decreasing t_{ToT} are brought together. The peak area is directly linked to the excited charge (via the transimpedance Z of the readout board) in the detector, respectively the collected charge at the electrodes. The comparison of the plots of the average peak area is presented in Fig. 56a. Next to development, a comparison of the resulting histograms at 500 V and 1000 V are shown in Fig. 56b,c. Non-irradiated detectors show a saturation behavior for A_{peak}. For the reference diode, the saturation effect appears above 600 V bias voltage. Irradiated samples do not exhibit this property. The saturation can be understood as all charge carriers reach the electrodes, before they recombine or be trapped in intergap-states. In other words, the average lifetime of the carriers is longer than their drift time inside the detector. This does

Die approbierte gedruckte Originalversion dieser Diplomarbeit ist an der TU Wien Bibliothek verfügbar
The approved original version of this thesis is available in print at TU Wien Bibliothek.
TU WIEN Bibliothek Your knowledge hub

not hold for highly irradiated detectors, as the number of crystal defects is much higher and the charge carrier lifetime substantially shorter. For our reference sample #0, the saturation value is approximately $4.31{\times}10^{-11}$ Vs; all other diodes show a nearly linear increase to $2.716{\times}10^{-11}$ Vs, $1.976{\times}10^{-11}$ Vs and $8.46{\times}10^{-12}$ Vs for sample #1 to #3 at 1100 V bias voltage. At 600 V bias voltage, the average peak area for #1 is $2.131{\times}10^{-11}$ Vs, $1.437{\times}10^{-11}$ Vs for #2 and at last $5.70{\times}10^{-12}$ Vs for #3. Below 600 V bias voltage, also #0 shows the increase, the lower the bias is the stronger this parameter increases; this effect can also be seen in the curve of #1 where the linear-like increases starts at 400 V. Sample #2 exhibits this behavior as well, the start of the nearly linear rise is located at 300 V. On the other hand, #3 indicates the linear-like growth throughout the signal-observable bias range. Moreover, the average peak area is always below 10^{-11} Vs for sample #3, this value is surpassed by all other samples at at least 300 V. In these plots, the saturation effect of sample #0 of the average peak area is clearly observable. The red peak remains in the same position. On the other hand, the peaks referring to irradiated samples are shifted towards greater values the higher the bias voltage is. All peaks exhibit a Gaussian-like shape, the fits (visible in section 6 and Appendix A) follow this contour accurately.

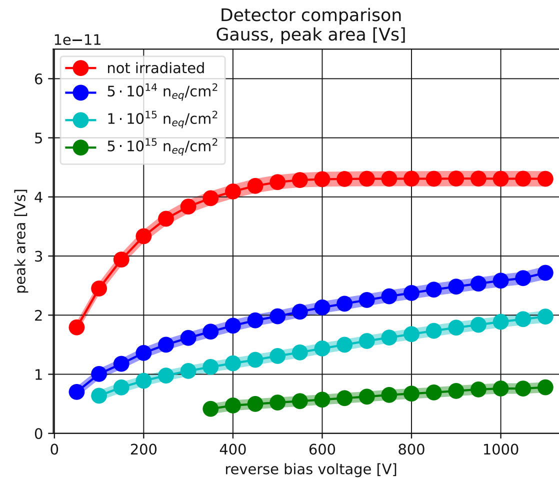

(a) The comparison of the means and standard deviations of the peak area A_{peak} after being fitted with a Gaussian distribution.

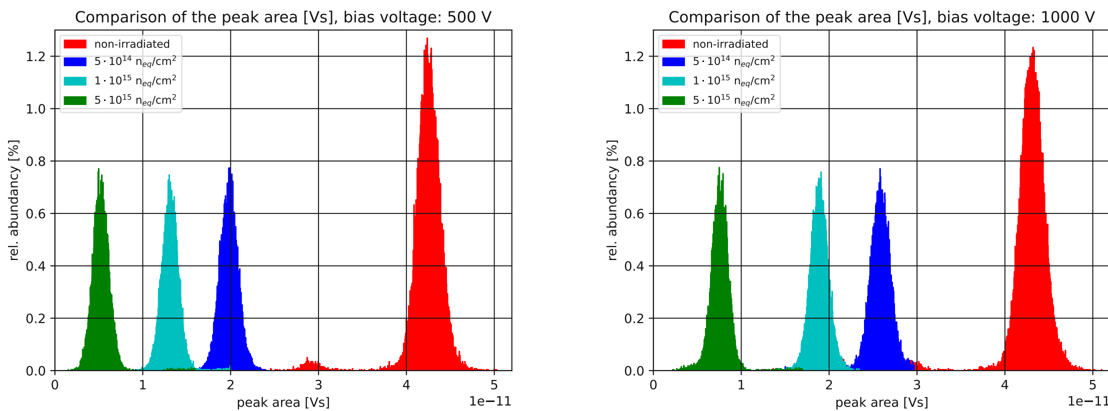

(b) The comparison of the histograms of each detector at 500 V bias voltage.

(c) The comparison of the histograms of each detector at 1000 V bias voltage.

Figure 56: The comparison of the data of the average peak maximum.

Die approbierte gedruckte Originalversion dieser Diplomarbeit ist an der TU Wien Bibliothek verfügbar
The approved original version of this thesis is available in print at TU Wien Bibliothek.
TU WIEN Bibliothek Your knowledge hub

Unlike the other parameters, the relative share regarding the non-irradiated reference sample has a specific name. As the peak area is linked to the created charge, the ratio of these parameters is called Charge Collection Efficiency and is derived by

$$CCE = \frac{A_{\text{peak}}^{\text{irr}}}{A_{\text{peak}}^{\text{ref}}} \tag{67}$$

The CCE is an often investigated characteristic parameter for detectors in high energy physics. In the case of this thesis, the trend for all samples is an increase of the CCE, as the applied bias voltage is raised. The comparison of the CCE plots for all samples is shown in Fig. 57. The most interesting bias range is above 600 V, as the average peak area of the reference sample saturates and the maximum possible created charge is observed. All maxima are located at the highest applied bias voltage of 1100 V with 63.0 %, 45.8 % and 19.6 % for sample #1 to #3 respectively. On the other end of the saturation plateau at 600 V, the CCE is 49.5 % for #1, 33.4 % for #2 and 14.9 % for the highest irradiated sample #3. Below 600 V bias voltage, the reference value changes, this does not have an effect on the trend of this parameter; The lowest charge collection efficiency is located at the least bias voltage at which a signal could be detected. This leads to a minimal CCE of 39.1 % at 50 V bias voltage for sample #1. Sample #2 has its CCE_{min} at 100 V bias voltage with a value 26.0 % and #3 at 350 V bias voltage with 11.2 %. As the peak area grows in linear-like manner, above a specific bias voltage also the CCE shows this type of increase. Thus, a loss in performance (regarding to the CCE) due to radiation damage can be compensated by higher biasing. The natural limit for compensating performance is the breakdown field E_B.

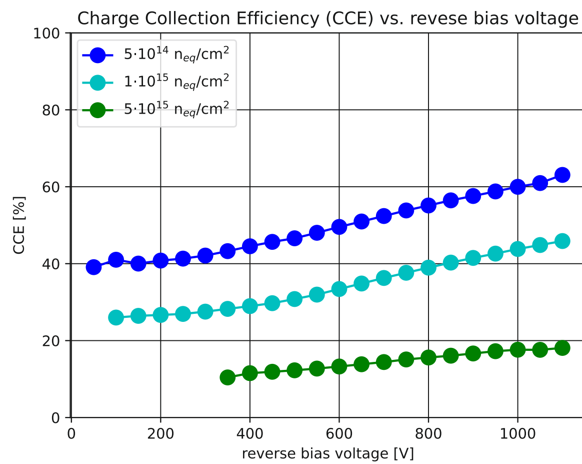

Figure 57: The charge collection efficiency based on the peak area plotted against the bias voltage.

Signal-to-Noise Ratio

The most eye-catching property of the comparison of the signal-to-noise ratio SNR is the strong similarity to the data of the time-over-threshold. The comparison of all SNR curves is presented in Fig. 58a. As the other parameter, the SNR curve exhibits a plateau-like range for the non-irradiated reference sample #0. This plateau with the maximum value of the average SNR is located at roughly 36.2 dB. This indicates a very reliable discrimination of the signal against noise. All irradiated samples show a steady increase of this parameter with a nearly linear shape above a certain bias voltage. This 'switching point' is located

Die approbierte gedruckte Originalversion dieser Diplomarbeit ist an der TU Wien Bibliothek verfügbar
The approved original version of this thesis is available in print at TU Wien Bibliothek.
TU WIEN Bibliothek Your knowledge hub

at 400 V for #1, at 200 V for #2 and at 450 V for #3. As sample #1 to #3 show a continuous increase, these diodes have the maximum average SNR located at the highest applied bias voltage of 1100 V. The values are 33.88 dB, 32.06 dB and 26.69 dB. In relative shares, these numbers are 95.4 %, 90.3 % and 75.1 % of the reference sample (35.52 dB) respectively. As sample #0 has its maximum located at 450 V, the relative shares of the irradiated are worth a closer look here. For sample #1, the percentage is 88.1 %, while it is 80.8 % for #2 and at least 66.0 % for #3.

The signal-to-noise ratio depends strongly on the voltage samples and is a pure mathematical parameter. It is based on a logarithmic function and the root main square values of the signal and the noise - see Eq. (65). As the number of samples, which are considered as signal, is small, the SNR is a parameter to be interpreted carefully. Here, especially the short time of the signal plays a role; It leads in combination with the relatively low sampling rate of the DRS4 oscilloscope to a small number of signal samples. Typically, a signal consists of three to eight samples. For these signals, the highest number of sampling points occur in the curve of the unirradiated sample #0. This is indicated through the highest average time-over-threshold. Therefore, 'faster' signals - like at the highest bias voltage for #0 - have less sampling points, which are greater than the threshold. The SNR is sensitive to the varying number of signal-samples due to the calculation of the quadratic mean. Thus, an additional sample just above the threshold affects the SNR strongly. Hence, there exist the possibility for the unexpected outcome, that signals with a higher $V_{\max}$ have a smaller SNR. This effect can be clearly seen in the histogram data of the SNR. Fig. 58b,c show the distribution of this parameter at a bias voltage of 500 V and 1000 V. Nearly every peak exhibit a double or even triple peak structure. These phenomenon is caused by the effect discussed above; the first peak of the peak structure refers to the peak with the highest number of signal samples. Consequently, the following one belongs to signal with one sample less. Only sample #3 shows a Gaussian-like shape in both plots. For all other signals, the single peaks would have to be fitted separately. This would also allow a determination of the contribution to the total area and the relative share. However, this operation was not performed in this work. Observing double peaks can be reduced or even nearly avoided. In order to do so, an analyzer with a higher sampling rate must replace the DRS4 oscilloscope in the measurement setup. Nevertheless, the SNR is still a good indicator due to values over 20 dB for reliable detection of signals for high energies, even if the diodes are heavily irradiated.

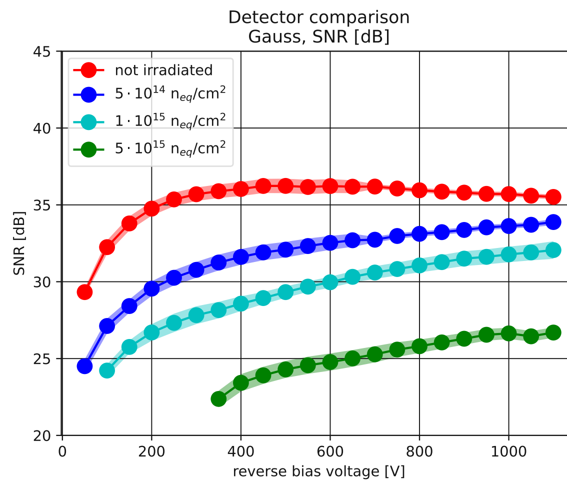

(a) The comparison of the means and standard deviations of the Signal-to-Noise ratio SNR after being fitted with a Gaussian distribution.

Die approbierte gedruckte Originalversion dieser Diplomarbeit ist an der TU Wien Bibliothek verfügbar
The approved original version of this thesis is available in print at TU Wien Bibliothek.
TU WIEN Bibliothek Your knowledge hub

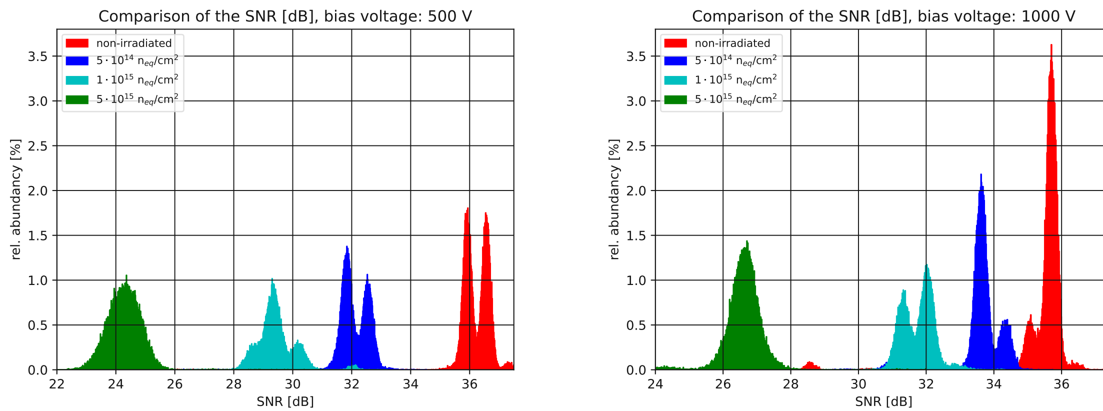

(b) The comparison of the histograms of each detector at 500 V bias voltage.

(c) The comparison of the histograms of each detector at 1000 V bias voltage.

Figure 58: The comparison of the data of the average peak maximum.

7.2 Measurements at MedAustron

The measurements at MedAustron yield quite similar results. However, comparing this experiment series directly with the UV-TCT measurements is difficult, due to principal differences in the experimental setup. First, the particles were injected into the active volume in another way, which caused a lot of uncertaities. At MedAustron the 45 µm edge of the SiC crystal was exposed to the proton beam, resulting in a 3 mm long path in the active volume. In the cleanroom, the Laser was shone onto the diode from above. On the readout board, a protection case was welded onto it. This did not affect measurements in the cleanroom, but scattered protons as they had to cross this layer of aluminum. Also, the proton beam has a spot size of 6 mm×7.5 mm (FWHM values) [30], which led to scattering of protons from all sides. They may hit the readout board itself, or at any other material like the 4H-SiC bulk underneath the active volume. Secondly, the mechanism of interaction of the injected particles with the crystal differ by nature. This causes a different distribution of the signal parameters. Hence, this complicates the comparison of the statistics of the parameters derived after the signal analysis. Next to this, the average value is not the most probable value due to the Landau-shape of the data. However, a trend for these properties could also be obtained from the average values. The signals of the same experiment with the samples #0 to #3 can still be compared internally and the shape of the plots are carefully linked to the results of the UV-TCT experiments. According to all uncertainties, this series of experiments can be seen as bare proof of principle. A lot of further systematic research is required to fully understand the performance at the detection of protons.

The average peak maximum yielded expectable results for sample #0, #1 and #2. As in the data of the TCT-measurements, the less the sensor was exposed to radiation, the higher the observed signal in general is. The comparison of all data sets is plotted in Fig. 59 below. Moreover, the increasing trend of the average peak maximum is visible in these data. Only sample #3 exhibit a not expected behavior. First, it showed higher signals, despite being irradiated for a longer time. Secondly, the values decrease, instead of the expected increase. For all investigated samples, the average peak maximum is below 8 mV. In addition to the small parameters, the standard deviations are large in comparison to the average value. For each bias data point of a detector, all other data points are located within $\mu \pm \sigma$ of this point. This is indicating a very high range of the absolute values, a result of the Landau distribution.

Die approbierte gedruckte Originalversion dieser Diplomarbeit ist an der TU Wien Bibliothek verfügbar
The approved original version of this thesis is available in print at TU Wien Bibliothek.
TU Bibliothek WIEN Your knowledge hub

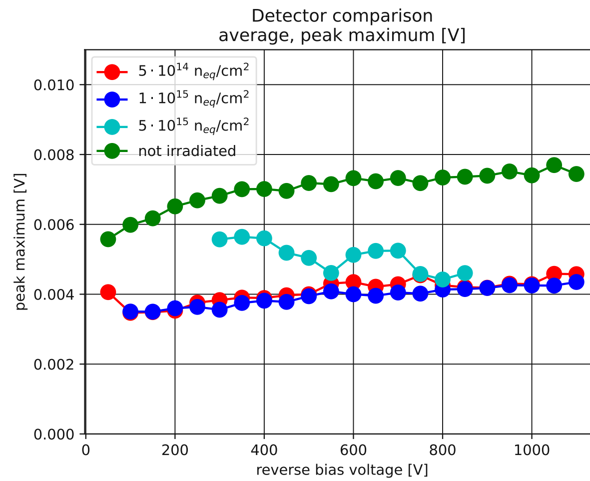

Figure 59: The comparison of the means of the average peak height V_{max}

Generally, also the comparison of the average time-over-threshold t_{ToT} yield expectable results again. With increasing fluence the samples were exposed to, the duration of the signals decreases. The biggest difference is between the reference sample #0 compared to TCT data. The comparison of the time-over-threshold curves versus the bias voltage is plotted in Fig. 60. Most noticeable, it shows a roughly 6 times longer duration of a reference sample signal in the MedAustron measurements. This is caused by settings in the analysis software and the RTP oscilloscope. The analyzer is less sensitive to noise and influence from 'outside' than the DRS4. Hence, the analysis software was configured to recognize a signal, if a voltage sample is greater than 3σ from the average voltage level. In addition, the minimal length of a signal was 0.5 ns with a sampling rate of 10 GS/s. For the cleanroom data, the signal threshold value was set to 10σ with approximately half the sampling rate. However, similar trends have been observed; #0 shows an increasing trend, until it reaches a maximum and decreases again. The irradiated samples #1 and #2 also show the increasing values with an increasing bias voltage. Their parameter values are in the same order of magnitude as in the TCT-measurements, around 1 ns or slighlty below. Only sample #3 does match the expectancy, here values tend to decrease, while staying around 1 ns as well.

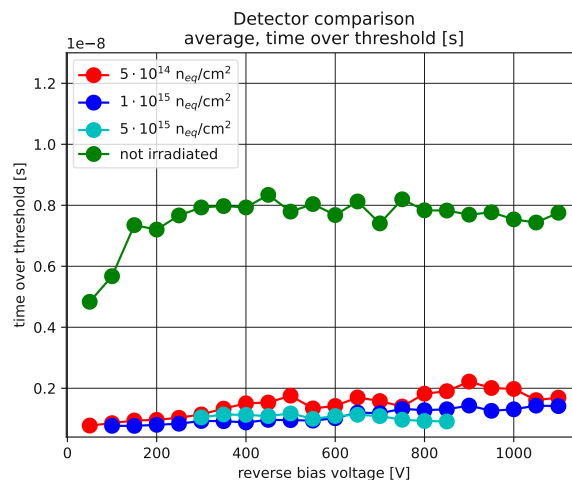

Figure 60: The comparison of the means of the average time-over-threshold t_{ToT}

Die approbierte gedruckte Originalversion dieser Diplomarbeit ist an der TU Wien Bibliothek verfügbar
The approved original version of this thesis is available in print at TU Wien Bibliothek.
TU WIEN Bibliothek Your knowledge hub

The average peak area A_{peak} shows similar results compared to the TCT-experiments as well. Plots of the average peak area as well as the charge collection efficiency are presented in Fig. 61a and 61b. For the reference sample, the saturation behavior can be observed for a bias voltage of 400 V and higher with a value of approximately 2.55×10^{-11} Vs. This value is just above half the saturation value of the TCT-measurement ($\approx 4.25 \times 10^{-11}$ Vs). For sample #1 and #2, the increase of A_{peak} is visible throughout the whole bias voltage range with higher values for #1 as expected. All irradiated sensors showed average peak areas below 1×10^{-11} Vs, indicating less excited charge than in the cleanroom with the UV-Laser setup. Sample #3 shows a decreasing trend, which is completely contrary to the expectancy and other irradiated samples. For bias voltages below 600 V, A_{peak} is greater than the values of sample #2 and vice versa. In terms of the charge collection efficiency CCE, also an increasing trend is obtainable for bias voltages higher than 200 V. At the beginning of the saturation area at 400 V bias voltage, the CCE is 12.2 % for sample #1, 9.8 % for sample #2 and 10.7 % for sample #3. These values change to 12.2 %, 9.2 % and 10.6 % at 600 V bias voltage for sample #1, #2 and #3 respectively. #1 and #2 finally reach 15.5 % and 12.3 % at the highest applied bias voltage (1100 V). Due to a lack of data no CCE for #3 can be presented here. Interestingly, these values would have been thought to be similar to the ones derived after TCT-measurements. However, there is a big difference in this parameter for each sensor. According to the TCT data, sample #1 reaches more than 60 % at the highest applies bias voltage while it is roughly 45 % for sample #2. Even #3 shows a better CCE for Laser-induced charge than #1 for proton induced charge. This may be caused by the geometry of the setup, with all at its uncertainties and less deposited energy.

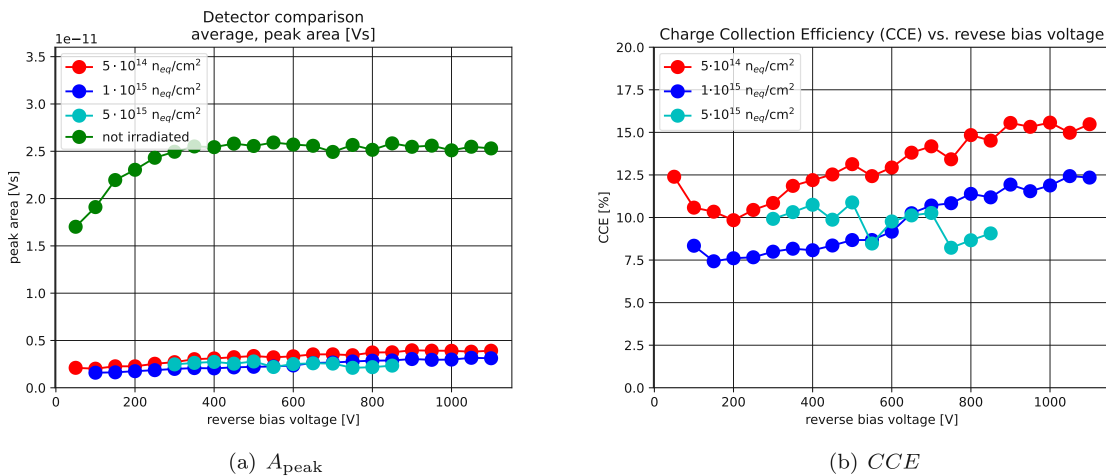

(a) A_{peak} (b) CCE

Figure 61: The comparison of the means of the average peak area A_{peak} and charge collection efficiency CCE

The last parameter to be compared is the average signal-to-noise ratio SNR. One could expect that the higher the signal is ($V_{\max}$) the better this ratio is. However, in this measurements the completely opposite case was observed. A comparison of the SNR curve is plotted in Fig. 62. With increasing exposure to radiation (fluence), also the SNR increases. This result is contrary to the one derived from the Laser-TCT experiments. In this study, the signal-to-noise ratio decreased with higher fluence exposure. This may be caused by the different geometric setup and the analysis parameters in the peak analysis software. In this case, the lower threshold for detecting a signal in combination with longer signals results in a larger number of samples just above the threshold. Hence, the SNR is calculated via the RMS value of the

Die approbierte gedruckte Originalversion dieser Diplomarbeit ist an der TU Wien Bibliothek verfügbar
The approved original version of this thesis is available in print at TU Wien Bibliothek.
TU WIEN Bibliothek Your knowledge hub

signal. A higher number of voltage samples of approximately the height of the threshold in comparison to the number of samples in the range just below the maximum, lead to a lower RMS value of the signal. This mainly effects the reference sample #0, as it showed the longest signal duration; Sample #1 and #2 have a minor number of voltages sample above the threshold, leading to a better average SNR. According to this, the reference sample #0 reached a maximum value of above 14 dB, while #1 and #2 reached an average of approximately 16 dB. Also the shape of the curves per sensor is different to the ones of the Laser-TCT. Sample #0 showed an increase and decrease in the TCT-data. For this series, it saturates at about 14 dB in the MedAustron measurements. The less irradiated samples showed a steady increase at the TCT-experiments with incresasing bias voltage. In the MedAustron data, they possess the saturation behavior above 400 V bias voltage as well, especially #2 at 16 dB. However, the saturation is indicated for sample #1 below 16 dB. The highest irradiated investigated sample #3 shows a not expected curve again. The value of the SNR decreases in the observed bias voltage range. Moreover, it shows the highest SNR (> 17 dB) in the MedAustron measurements.

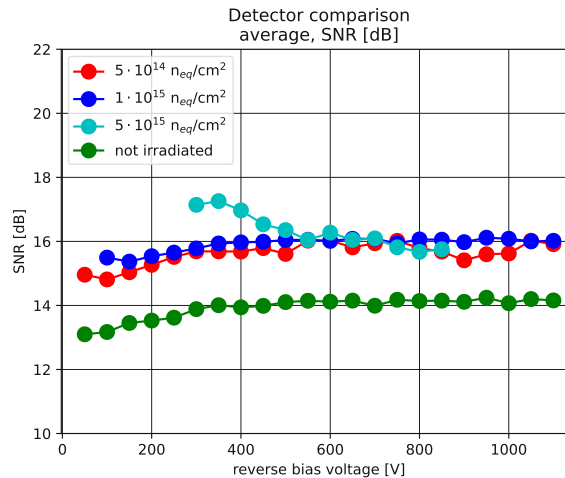

Figure 62: The comparison of the means of the average signal-to-noise-ratio SNR

Both series of experiments demonstrated the ability of 4H silicon carbide to work reliably as particle detector material. Exposure to radiation does have an effect onto the signal; especially on the peak height, the signal duration and the peak area. The named parameters decrease with the fluence the sensor was exposed to, at a constant bias voltage. These effects have been observed in both the Laser-TCT and MedAustron measurements with the proton beam. Next to the peak parameters, also the leakage current is affected. However, even the highest irradiated sensor exhibited a very low dark current in the nA range, which is a few orders of magnitude lower than for sensors made of pure silicon [15]. Next to this, the quality of the signals, based on the signal-to-noise ratio SNR, reached sufficiently high values. For the high-energy deposition (13.5 MeV) with the Laser-TCT setup, an $SNR > 22$ dB for the highest irradiated investigated sample was observed. The SNR of diode #3 decreased to 15 dB for the low-flux setting for 252.7 MeV protons at MedAustron. Unfortunately, the data of sample #3 of the MedAustron measurements show many contrary results, compared to #1 and #2. These data is considered as unreliable. As tests have been conducted at the lowest flux setting, the detection of particles is presumably easier for a higher flux and better focus. The charge collection efficiency CCE for the fluence of 5×10^{14} $\mathrm{n_{eq}/cm^2}$ is roughly 60 % at 1 kV bias voltage and is also still sufficient up to 1×10^{15} $\mathrm{n_{eq}/cm^2}$ (42 %). For a higher fluence of 5×10^{15} $\mathrm{n_{eq}/cm^2}$, the CCE drops to 18 %. However,

Die approbierte gedruckte Originalversion dieser Diplomarbeit ist an der TU Wien Bibliothek verfügbar
The approved original version of this thesis is available in print at TU Wien Bibliothek.
TU WIEN Bibliothek Your knowledge hub

the CCE can be increased by applying even higher bias voltages, it compensates loss of performance due to radiation damage. This holds for all samples irrespectively. In this thesis, only experiments for discrimination whether there is a (particle) beam focused onto the detector were conducted. In addition, the deposited energy has been held constant. According to this, no spectroscopic tests with variation of the energy were conducted on the irradiated samples. All in all, 4H-SiC diodes proved their property of high radiation hardness, as signals were detectable for highly irradiated samples with high sampling rate devices. This knowledge recommends 4H-SiC as a material for future detector technologies once again. In case of the HiBPM project, [34] 4H-SiC shall be pursued as the investigated semiconductor for sensor applications.

TU Bibliothek WIEN Your knowledge hub
Die approbierte gedruckte Originalversion dieser Diplomarbeit ist an der TU Wien Bibliothek verfügbar
The approved original version of this thesis is available in print at TU Wien Bibliothek.

8 Summary and Outlook

8.1 Summary

The aim of this work is to investigate the radiation hardness and reliability of irradiated single-pixel 4H-SiC detectors. Silicon carbide - especially the 4H crystal lattice configuration - is believed to be a revolutionary material for high energy physics detector technology. It shows promising properties which makes 4H-SiC a perfect candidate for applications in harsh environments [16, 24, 63]. One of these properties is the wide band gap ($E_{g,SiC} = 3.26\,eV$) compared to pure silicon ($E_{g,Si} = 1.14\,eV$) which promises a very low dark current [72]. Also, excitation cannot happen due to simple exposure to visible light. Moreover, a high atomic displacement ($E_D = 20$ - $35\,eV$) energy indicates radiation hardness, which raises interest to operate SiC sensor in radiation environments [21]. Unfortunately, SiC processing technology was not capable of producing reliable and ultra-pure single crystals for years until the mid 1990s [22]. Now, this has changed and SiC in all its crystal lattice configurations are a subject of intensive research. It reaches from detector technology to fundamental properties studies to processing techniques [23]. In this FFG-founded project named HiBPM (Hi-Precision Beam Position and Intensity Monitor for Accurate Cancer Treatment with Ions [34]) with MedAustron [3] silicon carbide is investigated how it is capable of being applied as particle detector for beam monitoring in the synchrotron. This thesis is part of the of the first phase of this project. Tests on 4H-SiC diodes in a newly developed Laser-TCT test facility were conducted at the Institute of High Energy Physics in Vienna.

The samples themselves are 4H-SiC p-on-n diodes provided by CNM (Centro Nacional de Microelectronica, Barcelona, Spain [71]) and have an active volume of $3\,mm \times 3\,mm \times 45\,\mu m$. The active volume is placed on top of a $350\,\mu m$ thick bulk, which makes a up a total thickness of roughly $500\,\mu m$ with all additional metallization and passivation layers [72]. As a first step, the 4H-SiC single-pad diodes were irradiated at the reactor of the Atominstitut of the Vienna University of Technology and exposed to known fluences in the range of 5×10^{14} to 1×10^{16} n_{eq}/cm^2. Irradiation took place in the reactor core. Those irradiated samples were bonded onto single-channel UCSC boards [86] which are operated as a trans-impedance amplifier with a transistor. Thus, it sends voltage samples to an output channel where an oscilloscope is connected [85]. To induce signals in the detector, a top-TCT setup was used. A pulsed UV-Laser (PiL037-FC [77]) was shot into the detector with a repetition rate of 500 Hz and deposited its energy inside the material. The UV-Laser had a wavelength of 370 nm which is equal to an energy of 3.35 eV. In the used setting, the full Laser intensity was applied in each pulse. Therefore, with each pulse an amount of 13.4 MeV is transferred into the crystal. The detector was placed underneath the Laser optics on a testing stage with further capabilities. The stage is able to heat and cool devices via a Peltier element and designed for UCSC-Boards specifically. This energy of each photon is just greater than the bandgap E_g of 4H-SiC. Therefore each photon creates one electron-hole-pair.

Data acquisition was performed with a simple and compact DRS4 evaluation board which is distributed by the Paul-Scherrer-Institute in Switzerland [2]. Hence, it works like four-channel digital oscilloscope. It has a bandwidth of 700 MHz and a maximum sample rate of 5.12 GS/s. This refers to a time resolution of 195 ps [88]. The necessary trigger signal was provided externally by the Laser driver and guaranteed the recording of a possible signal after each Laser pulse. The recorded data were analyzed afterwards by autonomous software based on Python3, developed by the Institute of High Energy Physics. The software finds and characterizes each peak with the following parameters: the peak maximum V_{max}, the

Die approbierte gedruckte Originalversion dieser Diplomarbeit ist an der TU Wien Bibliothek verfügbar
The approved original version of this thesis is available in print at TU Wien Bibliothek.
TU WIEN Bibliothek Your knowledge hub

peak area A_{peak}, the time-over-threshold t_{ToT} and the signal-to-noise ratio SNR. Once these data were collected, statistics were calculated (the mean and the standard deviation) as well as a Gaussian fit can be applied. Thus, fitting allowed to obtain more precise parameter values for μ and σ. Moreover, it reduced the influence of noise peaks which are caused by the setup and the DRS4 evaluation board.

For each irradiated sensor and the reference sample, the four previously named parameters were derived for different bias voltages of the sensors. The leakage current was also measured up to 500 V reverse bias voltage when no signals were induced. These experiments showed that also for highly irradiated SiC sensors the leakage current stays relatively low, compared to other semiconductor detectors. IV-measurements yielded that only current in the sub- µA appears, for the least irradiated diode no significant difference to the the reference sample was observed. As expected by the NIEL hypothesis, the leakage current increased, the longer the samples was irradiated. To derive reliable statistics for the characteristic parameters (V_{max}, t_{ToT}, A_{peak}, SNR), 25 000 peaks were recorded for each sample and bias. The voltage ramp started at 50 V and increased up to 1100 V in 50 V steps. Not every sample delivered a detectable signal for each bias voltage; the higher the radiation exposure was, the higher is the necessary bias voltage to detect a signal. For a exposure to $1{\times}10^{15}\,\text{n}_{\text{eq}}/\text{cm}^2$ and $5{\times}10^{15}\,\text{n}_{\text{eq}}/\text{cm}^2$ at least 100 V and 350 V bias voltage had to be applied to detect signals reliably, respectively. For the higher irradiated sample ($1{\times}10^{16}\,\text{n}_{\text{eq}}/\text{cm}$) no signals could be recorded.

On the first sight, the expected results were observed; the lower the fluence is which the sensor was exposed to, the higher is the observed signal. This holds for all parameters, especially for the average peak maximum, the average signal-to-noise ratio and the average peak area. The peak area in dependency of the bias voltage showed for an non-irradiated sample a saturation effect, due to a maximum number of created charge carriers. This property did not appear in any irradiated sample which was investigated in the observed bias voltage range. It indicated, that no irradiated sample was fully depleted at 1100 V bias voltage. The charge collection efficiency CCE was derived from the peak area data. It exhibited 63 %, 45.8 % and 19.6 % of the maximum created charge carriers for the least to higher irradiated sample at their maximum, which is located at the maximum applied bias voltage. An easily noticeable difference occured in the data regarding the average time-over-threshold. In comparison to the reference sample, which showed a maximum in the region of the full depletion voltage (296 V [73]), the irradiated diodes showed a permanent increase of this parameter.

A related series of experiments of was performed at MedAustron [3] with a low flux beam (1 kHz) of 252.7 MeV protons [30]. According to the Bethe-Bloch-equation, each particle deposited 1.4 MeV in the detector. The results have been close to the ones of the TCT-measurements; similar trends were observed. Again, with increasing exposure to neutron radiation the average signal height (V_{max}), the average time-over-threshold and the average peak area decreased. However, an unexpected trend for the signal-to-noise ratio was found, which is completely contrary to the cleanroom experiments. In this case, the SNR increased with the fluence. This is likely caused by parameter settings in the signal analysis software, as signals were longer for the reference sample and significantly lower. As at MedAustron many uncertainties cropped up - like injecting protons at the small edge of the crystal or no shielding against scattered protons - this series was considered as proof of principle, as it yielded similar results. It is highly recommended to repeat this experiments in a better controlled environment.

Die approbierte gedruckte Originalversion dieser Diplomarbeit ist an der TU Wien Bibliothek verfügbar
The approved original version of this thesis is available in print at TU Wien Bibliothek.
TU WIEN Bibliothek Your knowledge hub

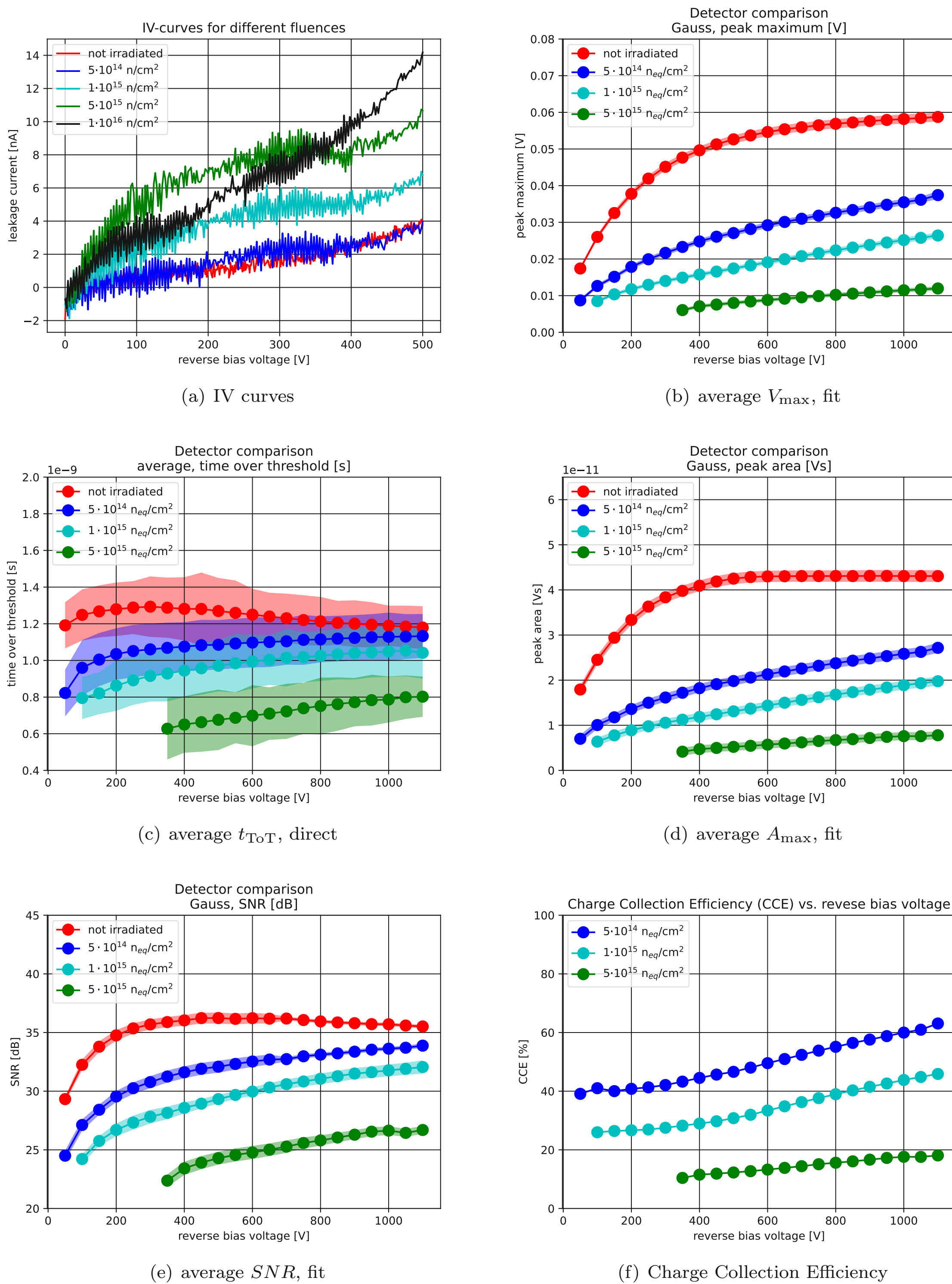

(a) IV curves

(b) average $V_{\max}$, fit

(c) average t_{ToT}, direct

(d) average $A_{\max}$, fit

(e) average SNR, fit

(f) Charge Collection Efficiency

Figure 63: The comparison plots for the investigated parameters (peak maximum, peak area, time-over-threshold, SNR) of all irradiated sensors

Die approbierte gedruckte Originalversion dieser Diplomarbeit ist an der TU Wien Bibliothek verfügbar
The approved original version of this thesis is available in print at TU Wien Bibliothek.
TU WIEN Bibliothek Your knowledge hub

8.2 Outlook

For future theses and projects, there are a numerous way to conduct studies on irradiated 4H-SiC detectors. In case of signal detection, many approaches for studies are possible. For example, diodes could be tested on their performance for spectroscopic devices. For this particular experiment the TCT-Laser method is a perfectly designed setup as simply the intensity must be reduced. Hence, less energy is deposited inside the detector and this data can be used to calibrate 4H-SiC sensors exposed to variuos fluences. Another study may be the simulation of MIP particles due to the energy deposition with less intensity. Besides varying the intensity, there is the possibility to lower and raise the temperature of the environment. For this purpose, the cold-chuck is installed inside the test box which is capable of reducing the temperature to approximately -30°C and raise it +50°C. Aim of a temperature change are studies on the dark current - which is also temperature-dependent - of the sensors as well as a possible influences on the signals. Another approach for future research are detectors based on silicon carbide with spatial resolution. This can either be a classical strip detector with implants or pixel detectors. Pixel detectors may be easier to be tested first as they consist of multiple diodes arranged in a specific array. Within the development of detectors with spatial resolution also readout systems should undergo tests with respect to their use on this specific sensor system. Of course, a complete new development of a readout chip or board might also be possible. This is also part of the HiBPM project. Against this background, there are multiple ways to extend the knowledge and understanding of devices based on silicon carbide technology. All this approaches can and will be part of research carried out by future scientists.

Die approbierte gedruckte Originalversion dieser Diplomarbeit ist an der TU Wien Bibliothek verfügbar
The approved original version of this thesis is available in print at TU Wien Bibliothek.
TU WIEN Bibliothek Your knowledge hub

APPENDIX

Die approbierte gedruckte Originalversion dieser Diplomarbeit ist an der TU Wien Bibliothek verfügbar
The approved original version of this thesis is available in print at TU Wien Bibliothek.
TU WIEN Bibliothek Your knowledge hub

A Tables and Histograms of Experimental Data (UV-Laser-TCT)

A.1 Non-irradiated SiC-Sensor

bias voltage [V]	Peak area [10^{-11} Vs]	Peak maximum [mV]	ToT [10^{-9} s]	SNR [dB]
50	1.816 ± 0.185	18.102 ± 5.304	1.191 ± 0.126	29.48 ± 1.33
100	2.450 ± 0.146	26.325 ± 4.344	1.248 ± 0.139	32.32 ± 0.94
150	2.926 ± 0.168	32.636 ± 4.031	1.268 ± 0.142	33.85 ± 0.82
200	3.304 ± 0.221	37.538 ± 3.850	1.279 ± 0.146	34.77 ± 0.79
250	3.594 ± 0.258	41.555 ± 3.828	1.288 ± 0.144	35.37 ± 0.78
300	3.794 ± 0.287	44.620 ± 3.906	1.293 ± 0.165	35.68 ± 0.81
350	3.928 ± 0.319	47.011 ± 4.270	1.288 ± 0.164	35.86 ± 0.86
400	4.408 ± 0.339	48.897 ± 4.387	1.281 ± 0.173	35.97 ± 0.89
450	4.131 ± 0.346	50.507 ± 4.390	1.281 ± 0.198	36.16 ± 0.91
500	4.191 ± 0.365	51.743 ± 4.735	1.270 ± 0.181	36.12 ± 0.95
550	4.222 ± 0.375	52.741 ± 4.941	1.259 ± 0.177	36.02 ± 0.99
600	4.240 ± 0.369	53.685 ± 4.817	1.250 ± 0.141	36.07 ± 0.95
650	4.246 ± 0.368	54.362 ± 4.883	1.239 ± 0.130	35.99 ± 0.94
700	4.248 ± 0.371	54.898 ± 4.996	1.230 ± 0.134	35.86 ± 0.98
750	4.249 ± 0.370	55.383 ± 5.117	1.220 ± 0.136	35.76 ± 0.99
800	4.250 ± 0.370	55.788 ± 5.135	1.213 ± 0.133	35.67 ± 1.00
850	4.249 ± 0.372	56.118 ± 5.228	1.205 ± 0.120	35.60 ± 0.99
900	4.250 ± 0.376	56.452 ± 5.283	1.200 ± 0.128	35.55 ± 1.01
950	4.252 ± 0.374	56.756 ± 5.279	1.195 ± 0.123	35.49 ± 1.01
1000	4.245 ± 0.381	56.984 ± 5.354	1.189 ± 0.110	35.49 ± 1.01
1050	4.250 ± 0.370	57.262 ± 5.301	1.184 ± 0.114	35.41 ± 1.00
1100	4.245 ± 0.386	57.536 ± 5.357	1.179 ± 0.117	35.35 ± 1.01

Table 4: The directly measured average values for the peak area, peak maximum, time over threshold and signal-to-noise ratio with their empirical standard deviation

bias voltage [V]	Peak area [10^{-11} Vs]	Peak maximum [mV]	ToT [10^{-9} s]	SNR [dB]
50	1.793 ± 0.094	17.414 ± 0.570	1.203 ± 0.089	29.32 ± 0.26
100	2.451 ± 0.100	26.021 ± 0.699	1.258 ± 0.080	32.25 ± 0.44
150	2.940 ± 0.105	32.541 ± 0.800	1.271 ± 0.095	33.79 ± 0.46
200	3.335 ± 0.107	37.769 ± 0.888	1.280 ± 0.101	34.75 ± 0.46
250	3.631 ± 0.112	41.928 ± 0.957	1.290 ± 0.105	35.36 ± 0.44
300	3.837 ± 0.116	45.145 ± 1.017	1.292 ± 0.106	35.69 ± 0.44
350	3.979 ± 0.119	47.660 ± 1.066	1.288 ± 0.104	35.89 ± 0.44
400	4.092 ± 0.119	49.639 ± 1.087	1.281 ± 0.100	36.03 ± 0.46
450	4.186 ± 0.121	51.275 ± 1.112	1.277 ± 0.096	36.23 ± 0.46
500	4.250 ± 0.122	52.637 ± 1.132	1.269 ± 0.089	36.23 ± 0.47
550	4.285 ± 0.123	53.707 ± 1.159	1.263 ± 0.083	36.16 ± 0.47
600	4.300 ± 0.126	54.648 ± 1.159	1.259 ± 0.081	36.22 ± 0.45
650	4.304 ± 0.126	55.374 ± 1.170	1.254 ± 0.077	36.18 ± 0.42
700	4.308 ± 0.126	55.943 ± 1.214	1.247 ± 0.076	36.19 ± 0.16
750	4.307 ± 0.127	56.470 ± 1.215	1.240 ± 0.076	36.06 ± 0.16
800	4.309 ± 0.127	56.874 ± 1.255	1.234 ± 0.074	35.95 ± 0.16
850	4.307 ± 0.129	57.242 ± 1.234	1.227 ± 0.078	35.86 ± 0.16
900	4.311 ± 0.130	57.623 ± 1.233	1.220 ± 0.079	35.80 ± 0.15
950	4.310 ± 0.130	57.920 ± 1.244	1.213 ± 0.080	35.71 ± 0.15
1000	4.307 ± 0.131	58.178 ± 1.258	1.208 ± 0.080	35.70 ± 0.15
1050	4.308 ± 0.131	58.456 ± 1.268	1.200 ± 0.081	35.60 ± 0.15
1100	4.306 ± 0.130	58.742 ± 1.220	1.191 ± 0.082	35.52 ± 0.15

Table 5: The average values for the peak area, peak maximum, time over threshold and signal-to-noise ratio after fitting with a Gaussian distribution.

Die approbierte gedruckte Originalversion dieser Diplomarbeit ist an der TU Wien Bibliothek verfügbar
The approved original version of this thesis is available in print at TU Wien Bibliothek.
TU WIEN Bibliothek Your knowledge hub

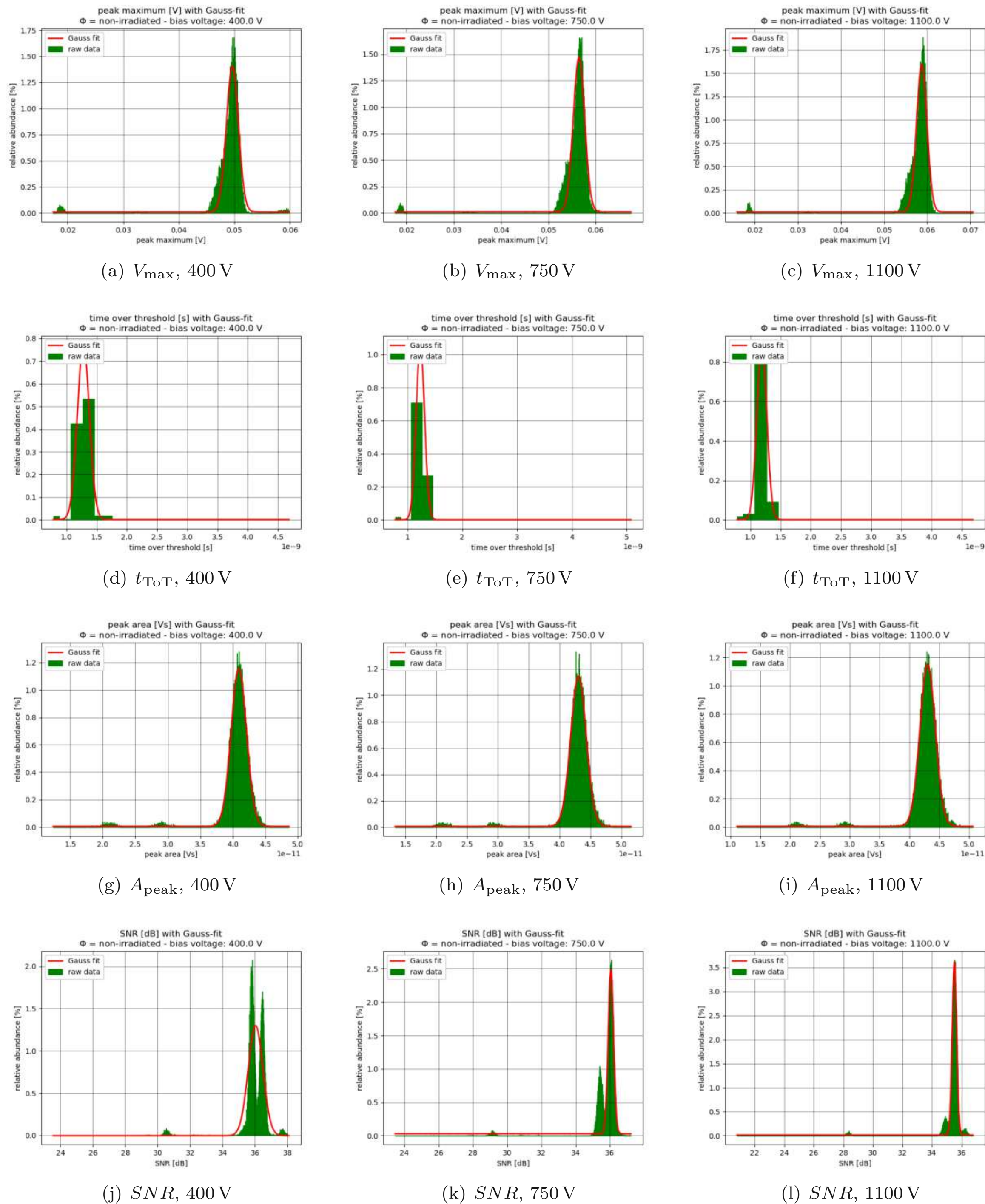

(a) $V_{\max}$, 400 V (b) $V_{\max}$, 750 V (c) $V_{\max}$, 1100 V

(d) t_{ToT}, 400 V (e) t_{ToT}, 750 V (f) t_{ToT}, 1100 V

(g) A_{peak}, 400 V (h) A_{peak}, 750 V (i) A_{peak}, 1100 V

(j) SNR, 400 V (k) SNR, 750 V (l) SNR, 1100 V

Figure 64: Exemplary histogram plots for the peak parameters V_{max}, t_{ToT}, A_{peak}, SNR at 400 V, 750 V and 1100 V reverse bias voltage.

Die approbierte gedruckte Originalversion dieser Diplomarbeit ist an der TU Wien Bibliothek verfügbar
The approved original version of this thesis is available in print at TU Wien Bibliothek.
TU WIEN Bibliothek Your knowledge hub

A.2 SiC-Sensor exposed to $5 \times 10^{14}\, \mathbf{n_{eq}/cm^2}$

bias voltage [V]	Peak area [10^{-11} Vs]	Peak maximum [mV]	ToT [10^{-9} s]	SNR [dB]
50	0.770 ± 0.371	9.907 ± 7.114	0.822 ± 0.128	24.92 ± 2.31
100	1.057 ± 0.304	13.582 ± 6.197	0.960 ± 0.151	27.48 ± 1.79
150	1.223 ± 0.278	15.970 ± 5.825	1.005 ± 0.145	28.68 ± 1.57
200	1.402 ± 0.254	18.601 ± 5.631	1.035 ± 0.141	29.75 ± 1.40
250	1.537 ± 0.236	20.609 ± 5.435	1.051 ± 0.143	30.43 ± 1.28
300	1.648 ± 0.224	22.287 ± 5.268	1.060 ± 0.141	30.93 ± 1.19
350	1.748 ± 0.198	23.745 ± 4.870	1.069 ± 0.138	31.38 ± 1.09
400	1.846 ± 0.190	25.187 ± 4.757	1.075 ± 0.134	31.75 ± 1.03
450	1.932 ± 0.184	26.419 ± 4.569	1.083 ± 0.139	32.06 ± 0.97
500	1.997 ± 0.168	27.316 ± 4.427	1.086 ± 0.135	32.23 ± 0.93
550	2.072 ± 0.159	28.319 ± 4.066	1.092 ± 0.135	32.45 ± 0.86
600	2.144 ± 0.154	29.355 ± 4.156	1.097 ± 0.136	32.68 ± 0.85
650	2.206 ± 0.154	30.217 ± 4.168	1.100 ± 0.137	32.86 ± 0.86
700	2.268 ± 0.150	31.095 ± 4.216	1.104 ± 0.128	33.02 ± 0.85
750	2.328 ± 0.150	31.868 ± 4.060	1.112 ± 0.136	32.23 ± 0.81
800	2.380 ± 0.145	32.584 ± 4.022	1.115 ± 0.125	33.35 ± 0.80
850	2.433 ± 0.142	33.260 ± 3.860	1.119 ± 0.125	33.43 ± 0.77
900	2.484 ± 0.146	34.018 ± 3.975	1.123 ± 0.125	33.56 ± 0.79
950	2.690 ± 0.147	34.723 ± 3.931	1.127 ± 0.126	33.72 ± 0.78
1000	2.580 ± 0.160	35.355 ± 4.002	1.129 ± 0.132	33.78 ± 0.79
1050	2.621 ± 0.150	35.984 ± 3.841	1.130 ± 0.123	33.86 ± 0.76
1100	2.707 ± 0.158	37.242 ± 3.833	1.133 ± 0.120	34.00 ± 0.76

Table 6: The directly measured average values for the peak area, peak maximum, time over threshold and signal-to-noise ratio

bias voltage [V]	Peak area [10^{-11} Vs]	Peak maximum [mV]	ToT [10^{-9} s]	SNR [dB]
50	0.701 ± 0.088	8.713 ± 0.487	0.412 ± 0.237	24.50 ± 0.45
100	1.005 ± 0.088	12.641 ± 0.539	0.955 ± 0.124	27.12 ± 0.48
150	1.177 ± 0.089	15.142 ± 0.570	1.004 ± 0.124	28.42 ± 0.43
200	1.361 ± 0.090	17.853 ± 0.627	1.037 ± 0.118	29.55 ± 0.48
250	1.500 ± 0.093	19.918 ± 0.673	1.054 ± 0.113	30.26 ± 0.50
300	1.615 ± 0.094	21.671 ± 0.668	1.065 ± 0.109	30.77 ± 0.52
350	1.721 ± 0.096	23.280 ± 0.703	1.069 ± 0.138	31.25 ± 0.52
400	1.822 ± 0.097	24.780 ± 0.720	1.079 ± 0.099	31.63 ± 0.51
450	1.912 ± 0.098	26.077 ± 0.736	1.085 ± 0.093	31.91 ± 0.51
500	1.981 ± 0.098	27.065 ± 0.755	1.087 ± 0.091	32.09 ± 0.51
550	2.058 ± 0.099	28.182 ± 0.774	1.090 ± 0.085	32.32 ± 0.49
600	2.131 ± 0.100	29.218 ± 0.787	1.093 ± 0.083	32.53 ± 0.45
650	2.193 ± 0.103	30.103 ± 0.800	1.095 ± 0.082	32.70 ± 0.43
700	2.257 ± 0.101	30.973 ± 0.814	1.098 ± 0.080	32.73 ± 0.19
750	2.319 ± 0.103	31.812 ± 0.825	1.102 ± 0.079	32.98 ± 0.18
800	2.375 ± 0.103	32.607 ± 0.829	1.104 ± 0.078	33.12 ± 0.18
850	2.432 ± 0.104	33.358 ± 0.850	1.106 ± 0.076	33.23 ± 0.18
900	2.483 ± 0.105	34.077 ± 0.857	1.110 ± 0.078	33.37 ± 0.18
950	2.534 ± 0.103	34.798 ± 0.872	1.114 ± 0.078	33.54 ± 0.17
1000	2.583 ± 0.105	35.477 ± 0.900	1.116 ± 0.078	33.63 ± 0.17
1050	2.626 ± 0.106	36.151 ± 0.870	1.118 ± 0.079	33.70 ± 0.17
1100	2.716 ± 0.112	37.427 ± 1.060	1.122 ± 0.080	33.88 ± 0.20

Table 7: The average values for the peak area, peak maximum, time over threshold and signal-to-noise ratio after fitting with a Gaussian distribution.

Die approbierte gedruckte Originalversion dieser Diplomarbeit ist an der TU Wien Bibliothek verfügbar
The approved original version of this thesis is available in print at TU Wien Bibliothek.
TU WIEN Bibliothek Your knowledge hub

Die approbierte gedruckte Originalversion dieser Diplomarbeit ist an der TU Wien Bibliothek verfügbar
The approved original version of this thesis is available in print at TU Wien Bibliothek.
TU WIEN Bibliothek Your knowledge hub

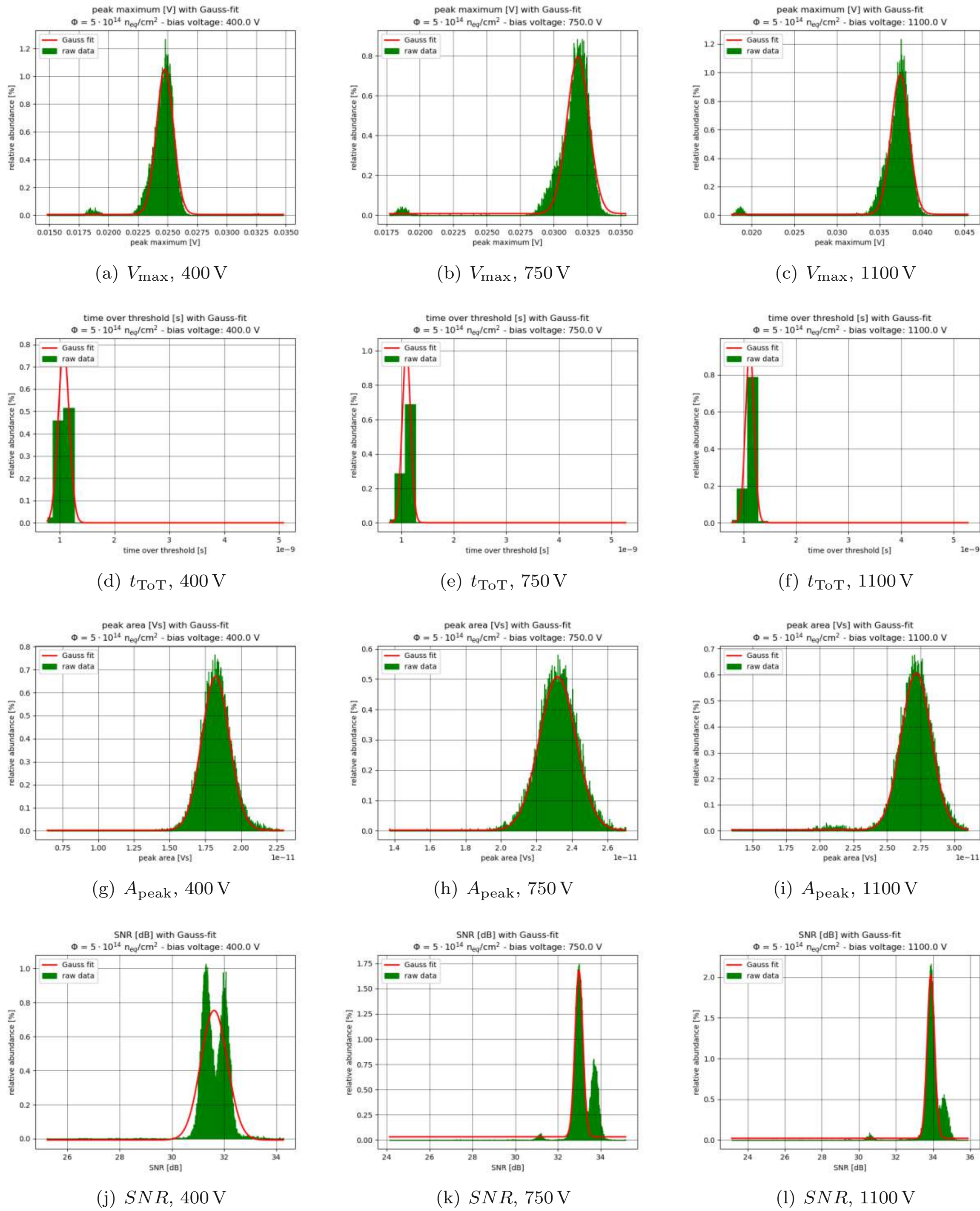

(a) $V_{\max}$, 400 V (b) $V_{\max}$, 750 V (c) $V_{\max}$, 1100 V

(d) t_{ToT}, 400 V (e) t_{ToT}, 750 V (f) t_{ToT}, 1100 V

(g) A_{peak}, 400 V (h) A_{peak}, 750 V (i) A_{peak}, 1100 V

(j) SNR, 400 V (k) SNR, 750 V (l) SNR, 1100 V

Figure 65: Exemplary histogram plots for the peak parameters V_{max}, t_{ToT}, A_{peak}, SNR at 400 V, 750 V and 1100 V reverse bias voltage.

A.3 SiC-Sensor exposed to 1×10^{15} n_{eq}/cm^2

bias voltage [V]	Peak area [10^{-11} Vs]	Peak maximum [mV]	ToT [10^{-9} s]	SNR [dB]
50	-	-	-	-
100	0.725 ± 0.415	9.973 ± 7.482	0.795 ± 0.115	24.73 ± 2.59
150	0.839 ± 0.346	11.395 ± 6.575	0.821 ± 0.114	26.08 ± 2.02
200	0.951 ± 0.335	12.799 ± 6.581	0.862 ± 0.138	27.00 ± 1.92
250	1.030 ± 0.301	13.850 ± 6.065	0.892 ± 0.134	27.63 ± 1.74
300	1.109 ± 0.301	14.936 ± 6.230	0.915 ± 0.140	28.16 ± 1.72
350	1.171 ± 0.286	15.716 ± 5.853	0.929 ± 0.153	28.48 ± 1.58
400	1.233 ± 0.278	16.580 ± 5.891	0.944 ± 0.145	28.91 ± 1.55
450	1.289 ± 0.265	17.326 ± 5.728	0.957 ± 0.144	29.26 ± 1.48
500	1.352 ± 0.260	18.154 ± 5.656	0.971 ± 0.140	29.61 ± 1.44
550	1.413 ± 0.260	18.967 ± 5.640	0.985 ± 0.160	29.92 ± 1.39
600	1.473 ± 0.238	19.732 ± 5.282	0.994 ± 0.147	30.16 ± 1.30
650	1.534 ± 0.227	20.529 ± 5.130	1.003 ± 0.136	30.47 ± 1.24
700	1.598 ± 0.228	21.370 ± 5.224	1.015 ± 0.157	30.73 ± 1.23
750	1.651 ± 0.204	22.071 ± 4.857	1.018 ± 0.138	30.93 ± 1.14
800	1.708 ± 0.201	22.821 ± 4.837	1.025 ± 0.137	31.15 ± 1.11
850	1.763 ± 0.204	23.564 ± 4.879	1.033 ± 0.136	31.36 ± 1.09
900	1.813 ± 0.191	24.240 ± 4.804	1.040 ± 0.144	31.59 ± 1.07
950	1.861 ± 0.186	24.864 ± 4.673	1.044 ± 0.137	31.70 ± 1.03
1000	1.909 ± 0.184	25.509 ± 4.705	1.049 ± 0.139	31.87 ± 1.02
1050	1.950 ± 0.175	26.066 ± 4.459	1.053 ± 0.140	31.99 ± 0.96
1100	1.878 ± 0.290	25.161 ± 5.551	1.042 ± 0.141	31.70 ± 1.45

Table 8: The directly measured average values for the peak area, peak maximum, time over threshold and signal-to-noise ratio

bias voltage [V]	Peak area [10^{-11} Vs]	Peak maximum [mV]	ToT [10^{-9} s]	SNR [dB]
50	-	-	-	-
100	0.637 ± 0.088	8.499 ± 0.514	0.795 ± 0.115	24.22 ± 0.40
150	0.777 ± 0.089	10.360 ± 0.530	0.409 ± 0.237	25.76 ± 0.42
200	0.890 ± 0.088	11.765 ± 0.542	0.835 ± 0.126	26.70 ± 0.55
250	0.978 ± 0.088	12.961 ± 0.558	0.881 ± 0.117	27.32 ± 0.60
300	1.056 ± 0.089	14.005 ± 0.572	0.907 ± 0.119	27.82 ± 0.58
350	1.124 ± 0.089	14.903 ± 0.590	0.921 ± 0.119	28.15 ± 0.54
400	1.185 ± 0.090	15.757 ± 0.601	0.938 ± 0.123	28.57 ± 0.48
450	1.125 ± 0.090	16.561 ± 0.613	0.952 ± 0.124	28.94 ± 0.40
500	1.309 ± 0.091	17.418 ± 0.642	0.968 ± 0.126	29.32 ± 0.37
550	1.369 ± 0.092	18.253 ± 0.642	0.981 ± 0.125	29.68 ± 0.34
600	1.437 ± 0.091	19.100 ± 0.650	0.992 ± 0.124	29.96 ± 0.36
650	1.499 ± 0.092	19.944 ± 0.677	1.003 ± 0.123	30.31 ± 0.37
700	1.563 ± 0.093	20.784 ± 0.679	1.014 ± 0.121	30.60 ± 0.41
750	1.621 ± 0.094	21.594 ± 0.699	1.109 ± 0.119	30.83 ± 0.42
800	1.679 ± 0.094	22.355 ± 0.710	1.026 ± 0.118	31.06 ± 0.45
850	1.735 ± 0.096	23.114 ± 0.703	1.034 ± 0.115	31.28 ± 0.47
900	1.789 ± 0.096	23.824 ± 0.717	1.042 ± 0.114	31.50 ± 0.48
950	1.837 ± 0.096	24.493 ± 0.725	1.047 ± 0.113	31.61 ± 0.49
1000	1.887 ± 0.097	25.149 ± 0.750	1.051 ± 0.112	31.78 ± 0.51
1050	1.932 ± 0.099	25.763 ± 0.753	1.056 ± 0.110	31.91 ± 0.52
1100	1.976 ± 0.126	26.411 ± 0.803	1.048 ± 0.122	32.06 ± 0.57

Table 9: The average values for the peak area, peak maximum, time over threshold and signal-to-noise ratio after fitting with a Gaussian distribution.

Die approbierte gedruckte Originalversion dieser Diplomarbeit ist an der TU Wien Bibliothek verfügbar
The approved original version of this thesis is available in print at TU Wien Bibliothek.
TU WIEN Bibliothek Your knowledge hub

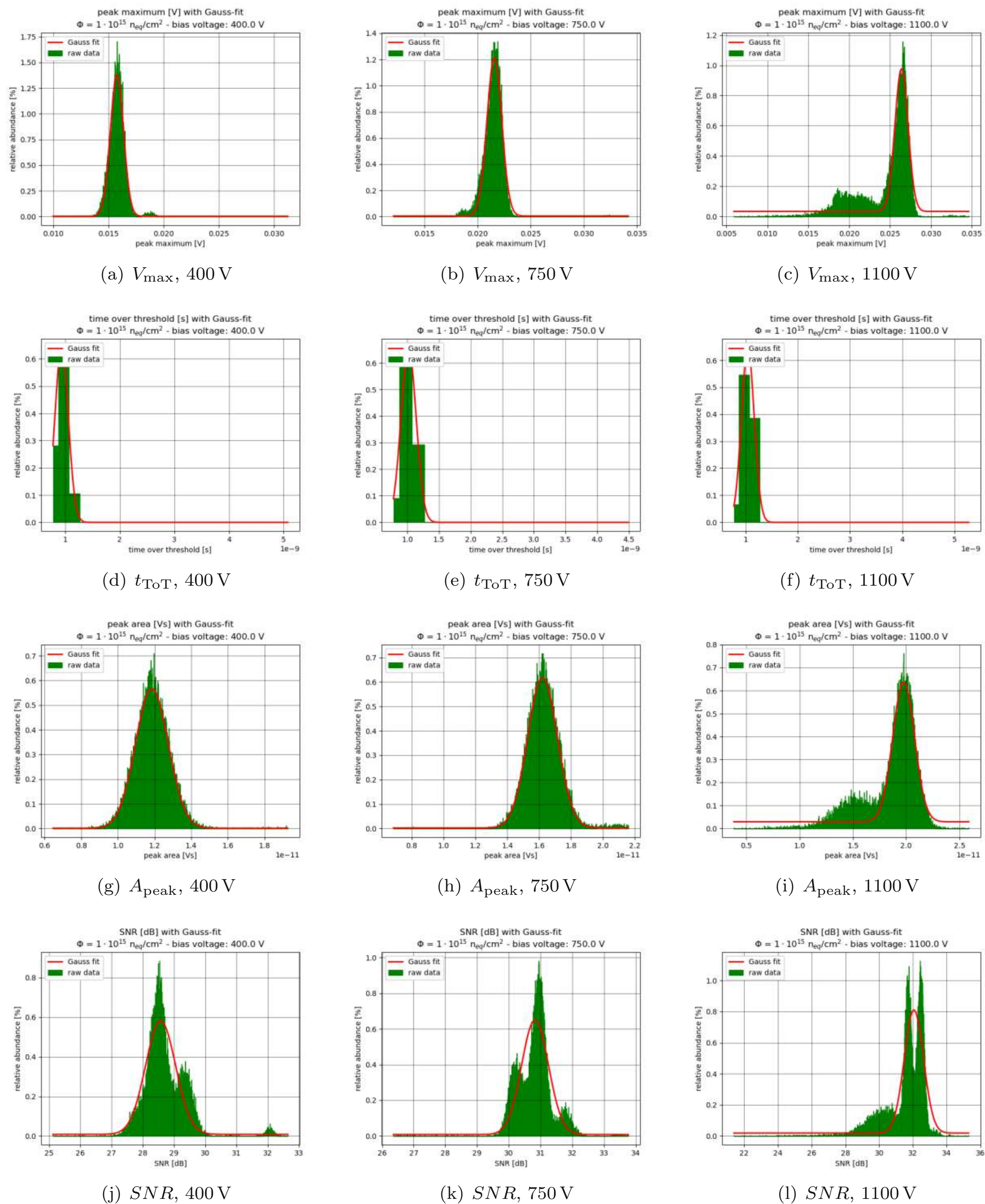

(a) V_{max}, 400 V (b) V_{max}, 750 V (c) V_{max}, 1100 V

(d) t_{ToT}, 400 V (e) t_{ToT}, 750 V (f) t_{ToT}, 1100 V

(g) A_{peak}, 400 V (h) A_{peak}, 750 V (i) A_{peak}, 1100 V

(j) SNR, 400 V (k) SNR, 750 V (l) SNR, 1100 V

Figure 66: Exemplary histogram plots for the peak parameters V_{max}, t_{ToT}, A_{peak}, SNR at 400 V, 750 V and 1100 V reverse bias voltage.

Die approbierte gedruckte Originalversion dieser Diplomarbeit ist an der TU Wien Bibliothek verfügbar
The approved original version of this thesis is available in print at TU Wien Bibliothek.
TU WIEN Bibliothek Your knowledge hub

A.4 SiC-Sensor exposed to 5×10^{15} n_{eq}/cm^2

bias voltage [V]	Peak area [10^{-11} Vs]	Peak maximum [mV]	ToT [10^{-9} s]	SNR [dB]
50	-	-	-	-
100	-	-	-	-
150	-	-	-	-
200	-	-	-	-
250	-	-	-	-
300	-	-	-	-
350	0.539 ± 0.509	8.331 ± 9.521	0.627 ± 0.168	23.34 ± 3.58
400	0.562 ± 0.428	8.617 ± 7.876	0.650 ± 0.154	24.00 ± 2.28
450	0.578 ± 0.410	8.973 ± 7.626	0.663 ± 0.161	24.41 ± 2.64
500	0.599 ± 0.398	9.350 ± 7.497	0.676 ± 0.165	24.76 ± 2.54
550	0.623 ± 0.394	9.738 ± 7.383	0.687 ± 0.139	25.05 ± 2.48
600	0.644 ± 0.388	10.077 ± 7.240	0.698 ± 0.167	25.24 ± 2.38
650	0.667 ± 0.375	10.342 ± 6.891	0.710 ± 0.143	25.46 ± 2.27
700	0.691 ± 0.374	10.722 ± 7.003	0.722 ± 0.150	25.73 ± 2.25
750	0.718 ± 0.370	11.042 ± 6.914	0.739 ± 0.139	26.03 ± 2.19
800	0.740 ± 0.374	11.376 ± 6.890	0.751 ± 0.155	26.25 ± 2.16
850	0.760 ± 0.366	11.690 ± 6.885	0.762 ± 0.146	26.47 ± 2.14
900	0.784 ± 0.368	12.020 ± 6.960	0.772 ± 0.132	26.70 ± 2.13
950	0.807 ± 0.357	12.329 ± 6.990	0.783 ± 0.138	26.92 ± 2.12
1000	0.819 ± 0.350	12.525 ± 6.682	0.787 ± 0.126	26.97 ± 2.01
1050	0.831 ± 0.378	12.853 ± 7.035	0.799 ± 0.119	26.81 ± 2.01
1100	0.846 ± 0.359	13.011 ± 6.648	0.802 ± 0.110	27.01 ± 1.90

Table 10: The directly measured average values for the peak area, peak maximum, time over threshold and signal-to-noise ratio

bias voltage [V]	Peak area [10^{-11} Vs]	Peak maximum [mV]	ToT [10^{-9} s]	SNR [dB]
50	-	-	-	-
100	-	-	-	-
150	-	-	-	-
200	-	-	-	-
250	-	-	-	-
300	-	-	-	-
350	0.445 ± 0.089	6.059 ± 0.466	0.451 ± 0.148	22.37 ± 0.54
400	0.472 ± 0.088	7.095 ± 0.495	0.642 ± 0.087	23.42 ± 0.57
450	0.498 ± 0.088	7.570 ± 0.508	0.655 ± 0.088	23.91 ± 0.56
500	0.522 ± 0.089	8.019 ± 0.512	0.670 ± 0.082	24.29 ± 0.55
550	0.545 ± 0.088	8.421 ± 0.516	0.678 ± 0.083	24.56 ± 0.56
600	0.570 ± 0.087	8.810 ± 0.516	0.685 ± 0.081	24.78 ± 0.56
650	0.596 ± 0.089	9.171 ± 0.512	0.694 ± 0.080	25.01 ± 0.54
700	0.621 ± 0.089	9.534 ± 0.532	0.702 ± 0.080	25.28 ± 0.53
750	0.650 ± 0.089	9.892 ± 0.544	0.717 ± 0.082	25.58 ± 0.48
800	0.672 ± 0.088	10.220 ± 0.550	0.728 ± 0.084	25.80 ± 0.44
850	0.692 ± 0.089	10.545 ± 0.548	0.742 ± 0.086	26.05 ± 0.41
900	0.718 ± 0.089	10.869 ± 0.548	0.756 ± 0.087	26.29 ± 0.39
950	0.743 ± 0.089	11.172 ± 0.564	0.771 ± 0.088	26.55 ± 0.38
1000	0.759 ± 0.089	11.469 ± 0.558	0.777 ± 0.087	26.64 ± 0.37
1050	0.758 ± 0.090	11.687 ± 0.582	0.799 ± 0.119	26.45 ± 0.34
1100	0.779 ± 0.087	11.961 ± 0.585	0.802 ± 0.110	26.69 ± 0.34

Table 11: The average values for the peak area, peak maximum, time over threshold and signal-to-noise ratio after fitting with a Gaussian distribution.

Die approbierte gedruckte Originalversion dieser Diplomarbeit ist an der TU Wien Bibliothek verfügbar
The approved original version of this thesis is available in print at TU Wien Bibliothek.
TU WIEN Bibliothek Your knowledge hub

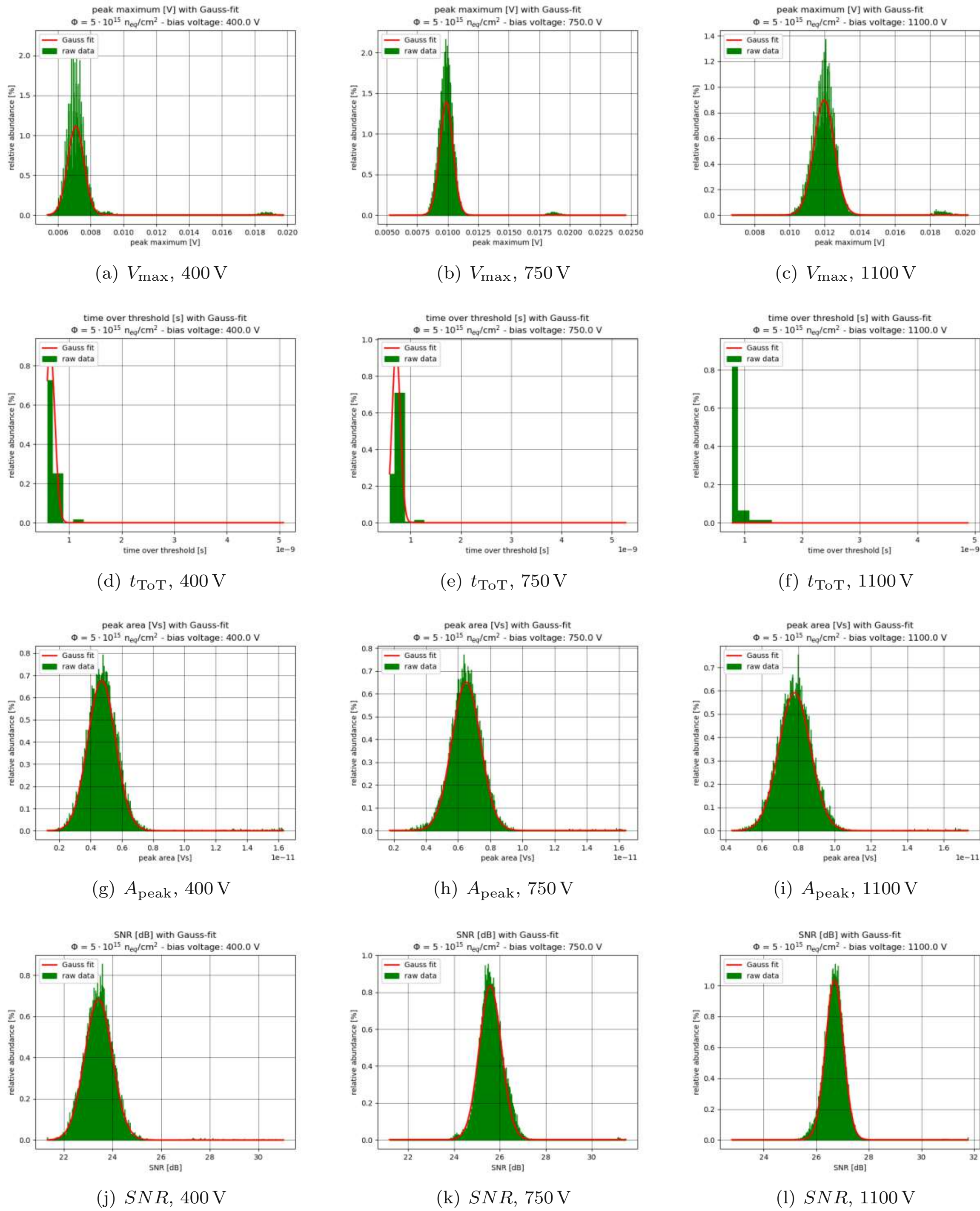

(a) V_{max}, 400 V
(b) V_{max}, 750 V
(c) V_{max}, 1100 V
(d) t_{ToT}, 400 V
(e) t_{ToT}, 750 V
(f) t_{ToT}, 1100 V
(g) A_{peak}, 400 V
(h) A_{peak}, 750 V
(i) A_{peak}, 1100 V
(j) SNR, 400 V
(k) SNR, 750 V
(l) SNR, 1100 V

Figure 67: Exemplary histogram plots for the peak parameters V_{max}, t_{ToT}, A_{peak}, SNR at 400 V, 750 V and 1100 V reverse bias voltage.

Die approbierte gedruckte Originalversion dieser Diplomarbeit ist an der TU Wien Bibliothek verfügbar
The approved original version of this thesis is available in print at TU Wien Bibliothek.
TU WIEN Bibliothek Your knowledge hub

B Tables and Histograms of Experimental Data (MedAustron)

B.1 Non-irradiated SiC-Sensor

bias voltage [V]	Peak area [10^{-11} Vs]	Peak maximum [mV]	ToT [10^{-9} s]	SNR [dB]
50	1.702 ± 2.069	5.575 ± 4.528	4.836 ± 4.482	13.098 ± 3.638
100	1.910 ± 1.963	5.986 ± 5.349	5.675 ± 4.658	13.170 ± 4.026
150	2.196 ± 2.160	6.173 ± 6.046	7.349 ± 5.596	13.453 ± 4.329
200	2.304 ± 2.168	6.515 ± 6.229	7.203 ± 5.263	13.527 ± 4.377
250	2.431 ± 2.314	6.688 ± 6.628	7.667 ± 5.518	13.617 ± 4.464
300	2.495 ± 2.387	6.817 ± 6.888	7.929 ± 5.747	13.884 ± 4.518
350	2.551 ± 2.497	7.007 ± 7.035	7.974 ± 5.768	14.007 ± 4.592
400	2.544 ± 2.411	7.012 ± 6.986	7.929 ± 5.787	13.940 ± 4.599
450	2.581 ± 2.369	6.958 ± 7.044	8.342 ± 5.951	13.987 ± 4.608
500	2.556 ± 2.612	7.184 ± 7.177	7.792 ± 5.624	14.104 ± 4.650
550	2.593 ± 2.472	7.151 ± 7.282	8.039 ± 5.793	14.146 ± 4.583
600	2.571 ± 2.643	7.323 ± 7.406	7.680 ± 5.561	14.117 ± 4.659
650	2.558 ± 2.140	7.234 ± 7.682	8.125 ± 5.783	14.150 ± 4.714
700	2.493 ± 2.196	7.327 ± 7.054	7.406 ± 5.353	13.990 ± 4.614
750	2.567 ± 2.371	7.181 ± 7.270	8.196 ± 5.952	14.176 ± 4.684
800	2.515 ± 2.168	7.341 ± 7.640	7.835 ± 5.592	14.138 ± 4.694
850	2.584 ± 2.535	7.364 ± 7.685	7.828 ± 5.735	14.149 ± 4.683
900	2.547 ± 2.557	7.392 ± 8.036	7.691 ± 5.567	14.113 ± 4.670
950	2.559 ± 2.629	7.514 ± 8.494	7.771 ± 5.660	14.241 ± 4.733
1000	2.510 ± 2.414	7.403 ± 7.488	7.537 ± 5.550	14.070 ± 4.642
1050	2.548 ± 2.414	7.697 ± 9.025	7.434 ± 5.358	14.199 ± 4.714
1100	2.530 ± 2.249	7.442 ± 8.016	7.755 ± 5.628	14.156 ± 4.697

Table 12: The average values and standard deviations for A_{peak}, V_{max}, t_{ToT} and SNR

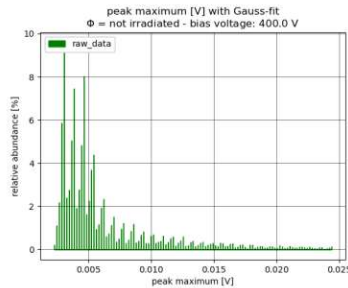

(a) V_{max}, 400 V

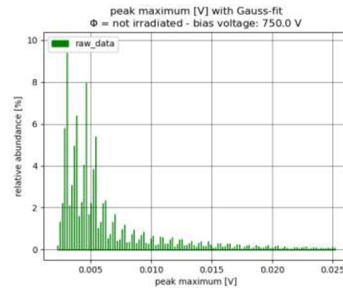

(b) V_{max}, 750 V

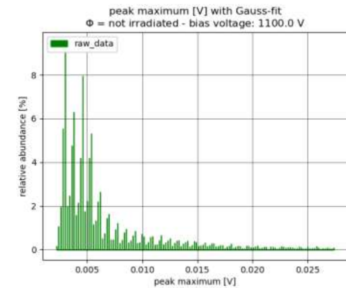

(c) V_{max}, 1100 V

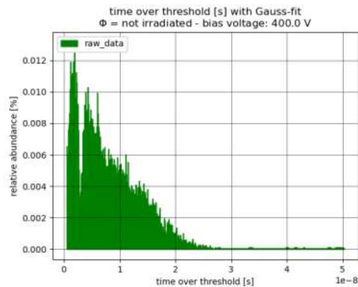

(d) t_{ToT}, 400 V

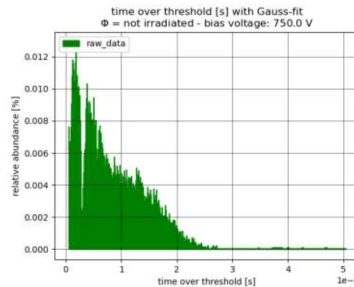

(e) t_{ToT}, 750 V

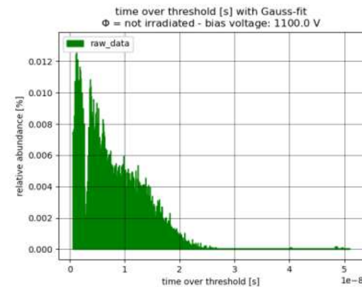

(f) t_{ToT}, 1100 V

Die approbierte gedruckte Originalversion dieser Diplomarbeit ist an der TU Wien Bibliothek verfügbar
The approved original version of this thesis is available in print at TU Wien Bibliothek.
TU WIEN Bibliothek Your knowledge hub

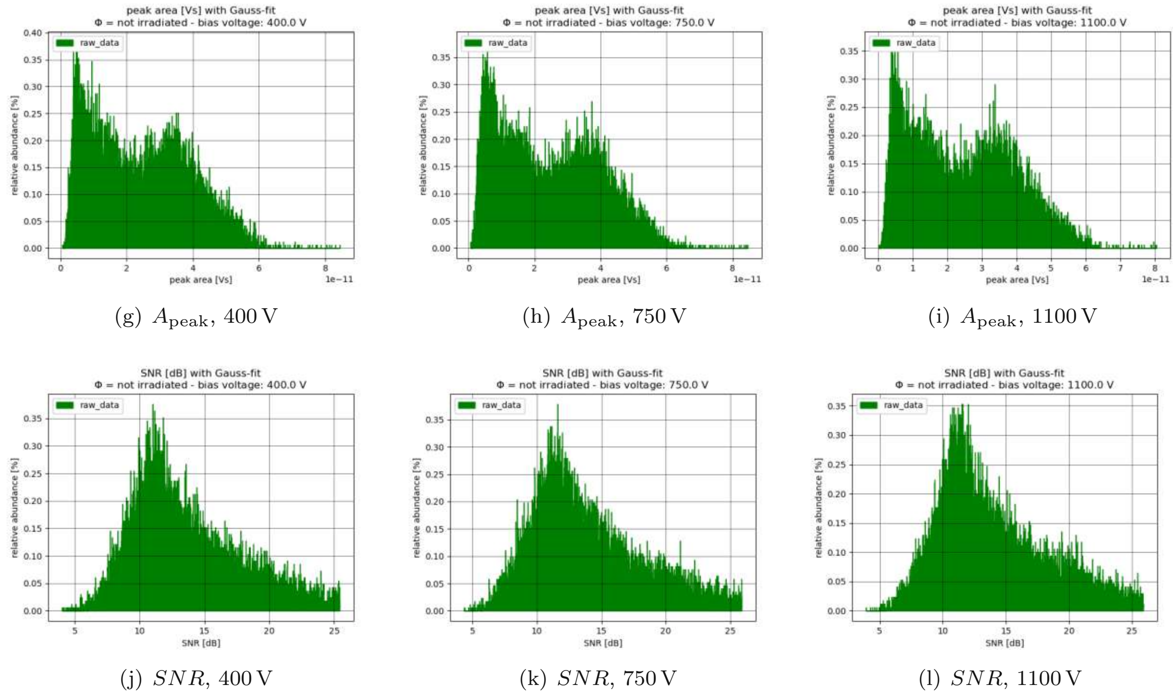

(g) A_{peak}, 400 V (h) A_{peak}, 750 V (i) A_{peak}, 1100 V

(j) SNR, 400 V (k) SNR, 750 V (l) SNR, 1100 V

Figure 68: Exemplary histogram plots for the peak parameters V_{max}, t_{ToT}, A_{peak}, SNR at 400 V, 750 V and 1100 V reverse bias voltage.

B.2 SiC-Sensor exposed to $5 \times 10^{14}\,\mathbf{n_{eq}/cm^2}$

bias voltage [V]	Peak area [10^{-12} Vs]	Peak maximum [mV]	ToT [10^{-9} s]	SNR [dB]
50	2.109 ± 2.151	4.060 ± 2.517	0.775 ± 0.515	14.959 ± 2.886
100	2.021 ± 2.308	3.468 ± 2.351	0.855 ± 0.771	14.812 ± 2.625
150	2.270 ± 2.703	3.487 ± 2.557	0.943 ± 0.915	15.036 ± 2.702
200	2.268 ± 2.560	3.529 ± 2.519	0.963 ± 0.956	15.269 ± 2.754
250	2.539 ± 3.343	3.759 ± 2.679	1.031 ± 1.206	15.515 ± 2.906
300	2.707 ± 3.273	3.832 ± 2.945	1.142 ± 1.326	15.688 ± 3.056
350	3.025 ± 3.696	3.903 ± 3.187	1.332 ± 1.660	15.689 ± 3.210
400	3.102 ± 3.257	3.892 ± 3.158	1.505 ± 1.715	15.682 ± 3.359
450	3.234 ± 3.875	3.970 ± 3.092	1.532 ± 1.854	15.791 ± 3.405
500	3.357 ± 4.201	4.000 ± 3.326	1.757 ± 2.212	15.609 ± 3.569
550	3.223 ± 4.008	4.307 ± 3.514	1.339 ± 1.669	16.024 ± 3.411
600	3.326 ± 4.280	4.348 ± 3.779	1.419 ± 1.694	16.025 ± 3.466
650	3.531 ± 4.212	4.215 ± 3.597	1.699 ± 2.059	15.814 ± 3.612
700	3.535 ± 4.317	4.286 ± 3.689	1.580 ± 1.874	15.942 ± 3.536
750	3.444 ± 4.335	4.543 ± 3.959	1.399 ± 1.545	16.018 ± 3.546
800	3.733 ± 4.750	4.257 ± 3.856	1.821 ± 2.246	15.787 ± 3.664
850	3.750 ± 4.123	4.200 ± 3.280	1.904 ± 2.260	15.682 ± 3.732
900	3.962 ± 4.863	4.186 ± 3.561	2.218 ± 2.712	15.409 ± 3.872
950	3.922 ± 5.280	4.301 ± 3.747	2.008 ± 2.643	15.598 ± 3.780
1000	3.908 ± 4.734	4.288 ± 3.583	1.978 ± 2.464	15.623 ± 3.765
1050	3.816 ± 4.793	4.584 ± 4.116	1.610 ± 1.967	16.023 ± 3.632
1100	3.917 ± 5.472	4.575 ± 4.367	1.692 ± 2.038	15.913 ± 3.714

Table 13: The average values and standard deviations for A_{peak}, V_{max}, t_{ToT} and SNR

Die approbierte gedruckte Originalversion dieser Diplomarbeit ist an der TU Wien Bibliothek verfügbar
The approved original version of this thesis is available in print at TU Wien Bibliothek.
TU WIEN Bibliothek Your knowledge hub

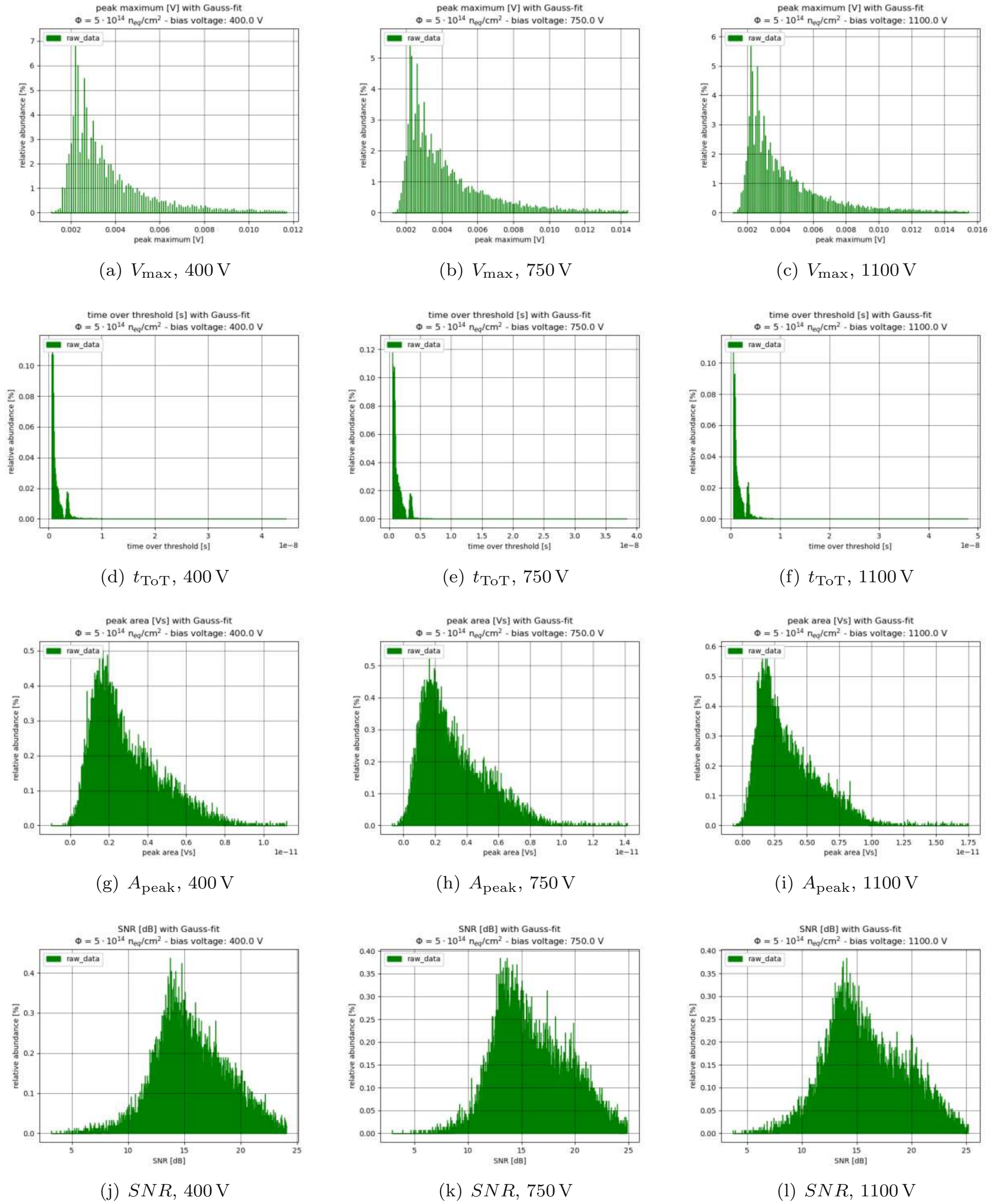

(a) V_{max}, 400 V (b) V_{max}, 750 V (c) V_{max}, 1100 V

(d) t_{ToT}, 400 V (e) t_{ToT}, 750 V (f) t_{ToT}, 1100 V

(g) A_{peak}, 400 V (h) A_{peak}, 750 V (i) A_{peak}, 1100 V

(j) SNR, 400 V (k) SNR, 750 V (l) SNR, 1100 V

Figure 69: Exemplary histogram plots for the peak parameters V_{max}, t_{ToT}, A_{peak}, SNR at 400 V, 750 V and 1100 V reverse bias voltage.

Die approbierte gedruckte Originalversion dieser Diplomarbeit ist an der TU Wien Bibliothek verfügbar
The approved original version of this thesis is available in print at TU Wien Bibliothek.
TU WIEN Bibliothek Your knowledge hub

B.3 SiC-Sensor exposed to $1 \times 10^{15}\,\mathbf{n_{eq}/cm^2}$

bias voltage [V]	Peak area $[10^{-12}$ Vs]	Peak maximum [mV]	ToT $[10^{-9}$ s]	SNR [dB]
50	-	-	-	-
100	1.593 ± 1.770	3.504 ± 2.408	0.768 ± 0.757	15.494 ± 2.600
150	1.631 ± 1.914	3.501 ± 2.487	0.766 ± 0.708	15.368 ± 2.612
200	1.753 ± 2.273	3.598 ± 2.890	0.801 ± 0.872	15.538 ± 2.653
250	1.863 ± 2.397	3.637 ± 2.928	0.837 ± 0.871	15.650 ± 2.722
300	1.994 ± 2.285	3.556 ± 2.621	0.926 ± 1.056	15.780 ± 2.738
350	2.083 ± 2.630	3.751 ± 3.083	0.921 ± 1.136	15.935 ± 2.854
400	2.055 ± 2.433	3.815 ± 2.969	0.878 ± 0.905	15.968 ± 2.811
450	2.157 ± 2.643	3.781 ± 3.106	0.962 ± 1.183	15.989 ± 2.919
500	2.218 ± 2.792	3.943 ± 3.133	0.954 ± 1.096	16.042 ± 2.968
550	2.250 ± 2.987	4.082 ± 3.465	0.938 ± 1.140	16.052 ± 2.991
600	2.357 ± 2.827	3.999 ± 2.937	1.017 ± 1.199	16.016 ± 3.074
650	2.622 ± 3.246	3.956 ± 3.324	1.203 ± 1.531	16.081 ± 3.202
700	2.668 ± 3.552	4.049 ± 3.437	1.180 ± 1.631	16.081 ± 3.207
750	2.782 ± 3.542	4.018 ± 3.424	1.324 ± 1.751	15.941 ± 3.297
800	2.864 ± 3.941	4.134 ± 3.572	1.280 ± 1.724	16.062 ± 3.283
850	2.890 ± 3.904	4.148 ± 3.529	1.311 ± 1.629	16.053 ± 3.320
900	3.039 ± 4.332	4.178 ± 3.877	1.432 ± 2.098	15.976 ± 3.436
950	2.955 ± 4.016	4.259 ± 3.925	1.260 ± 1.674	16.115 ± 3.352
1000	2.982 ± 3.964	4.251 ± 3.591	1.309 ± 1.669	16.082 ± 3.342
1050	3.167 ± 4.545	4.247 ± 3.635	1.430 ± 1.906	16.001 ± 3.407
1100	3.123 ± 4.059	4.350 ± 3.869	1.415 ± 1.874	16.018 ± 3.462

Table 14: The average values and standard deviations for A_{peak}, V_{max}, t_{ToT} and SNR

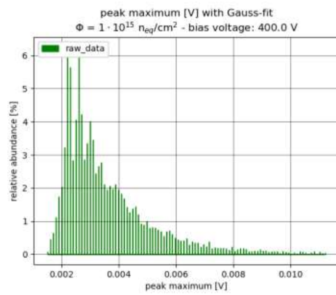

(a) V_{max}, 400 V

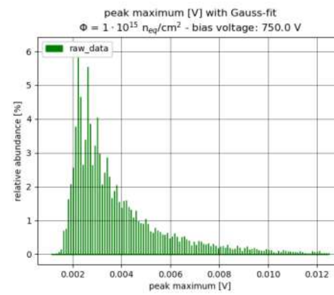

(b) V_{max}, 750 V

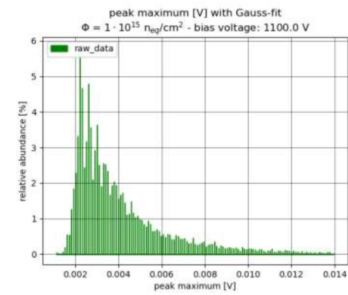

(c) V_{max}, 1100 V

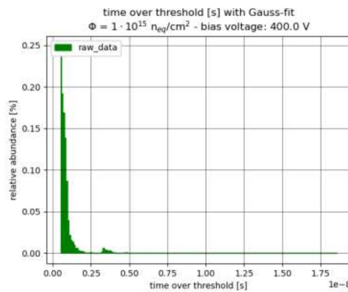

(d) t_{ToT}, 400 V

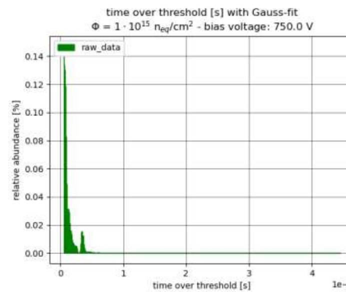

(e) t_{ToT}, 750 V

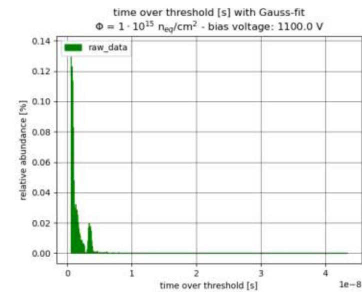

(f) t_{ToT}, 1100 V

Die approbierte gedruckte Originalversion dieser Diplomarbeit ist an der TU Wien Bibliothek verfügbar
The approved original version of this thesis is available in print at TU Wien Bibliothek.
TU Bibliothek WIEN Your knowledge hub

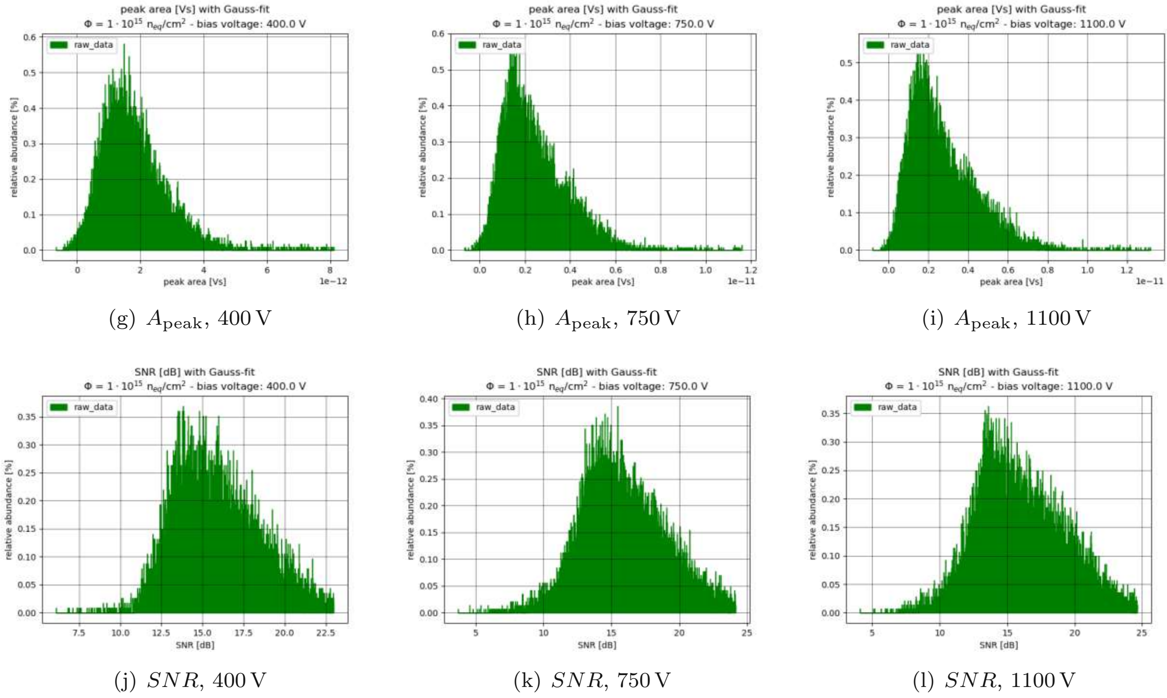

(g) A_{peak}, 400 V (h) A_{peak}, 750 V (i) A_{peak}, 1100 V

(j) SNR, 400 V (k) SNR, 750 V (l) SNR, 1100 V

Figure 70: Exemplary histogram plots for the peak parameters V_{max}, t_{ToT}, A_{peak}, SNR at 400 V, 750 V and 1100 V reverse bias voltage.

B.4 SiC-Sensor exposed to 5×10^{15} $\mathbf{n_{eq}/cm^2}$

bias voltage [V]	Peak area [10^{-12} Vs]	Peak maximum [mV]	ToT [10^{-9} s]	SNR [dB]
50	-	-	-	-
100	-	-	-	-
150	-	-	-	-
200	-	-	-	-
250	-	-	-	-
300	2.475 ± 2.076	5.571 ± 3.781	1.044 ± 1.029	17.142 ± 3.381
350	2.632 ± 2.506	5.643 ± 3.855	1.139 ± 1.715	17.258 ± 3.423
400	2.734 ± 2.372	5.600 ± 4.251	1.126 ± 1.053	16.969 ± 3.560
450	2.548 ± 2.394	5.187 ± 3.956	1.088 ± 1.053	16.534 ± 3.494
500	2.782 ± 6.115	5.040 ± 4.179	1.175 ± 1.790	16.354 ± 3.487
550	2.197 ± 2.451	4.609 ± 4.334	0.997 ± 0.997	16.043 ± 3.288
600	2.511 ± 2.815	5.127 ± 4.216	1.090 ± 1.154	16.274 ± 3.343
650	2.589 ± 2.887	5.240 ± 4.482	1.131 ± 1.232	16.048 ± 3.462
700	2.559 ± 3.422	5.247 ± 5.021	1.086 ± 1.153	16.093 ± 3.439
750	2.111 ± 2.811	4.580 ± 4.173	0.967 ± 1.112	15.814 ± 3.033
800	2.179 ± 7.384	4.422 ± 4.609	0.926 ± 1.174	15.673 ± 3.037
850	2.343 ± 9.764	4.606 ± 4.676	0.910 ± 1.088	15.756 ± 3.070
900	-	-	-	-
950	-	-	-	-
1000	-	-	-	-
1050	-	-	-	-
1100	-	-	-	-

Table 15: The average values and standard deviations for A_{peak}, V_{max}, t_{ToT} and SNR

Die approbierte gedruckte Originalversion dieser Diplomarbeit ist an der TU Wien Bibliothek verfügbar
The approved original version of this thesis is available in print at TU Wien Bibliothek.
TU Bibliothek WIEN Your knowledge hub

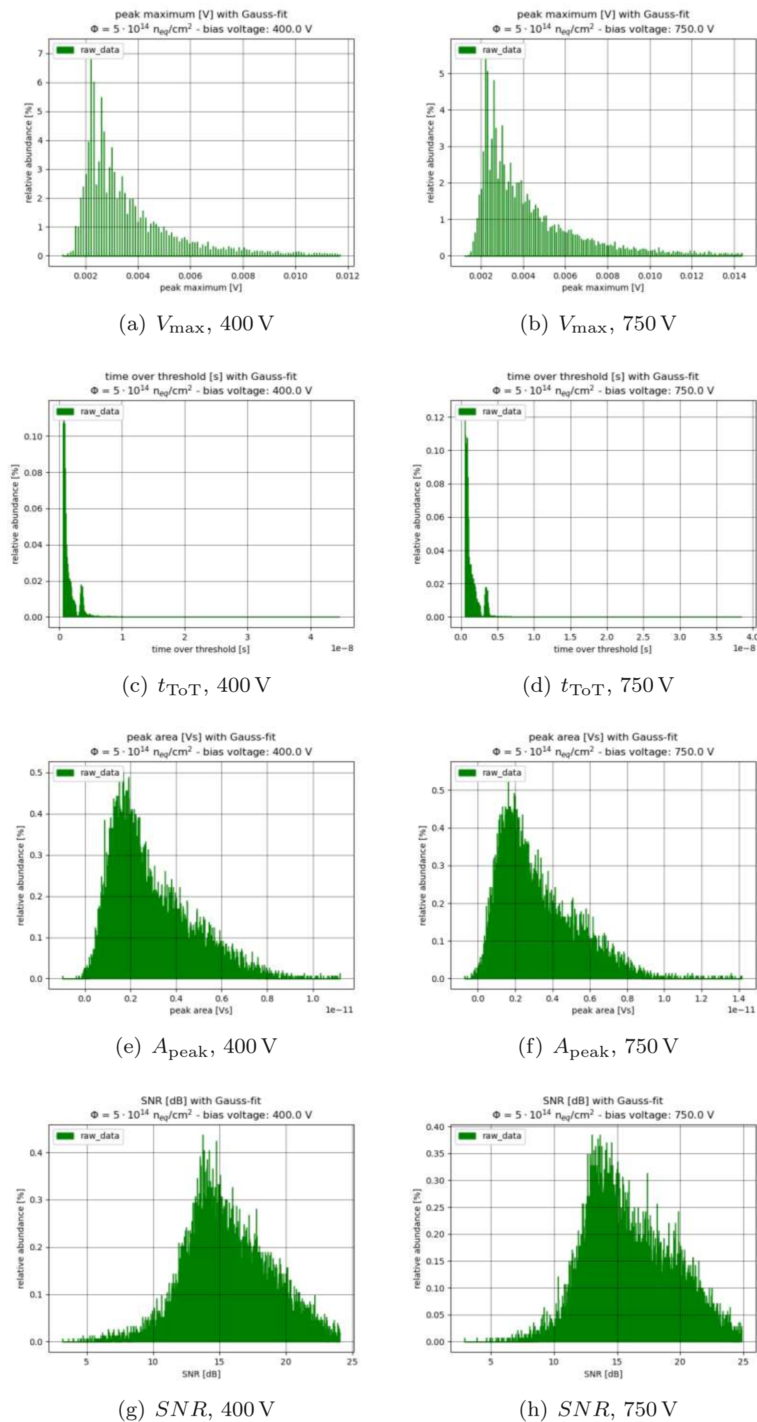

(a) V_{max}, 400 V

(b) V_{max}, 750 V

(c) t_{ToT}, 400 V

(d) t_{ToT}, 750 V

(e) A_{peak}, 400 V

(f) A_{peak}, 750 V

(g) SNR, 400 V

(h) SNR, 750 V

Figure 71: Exemplary histogram plots for the peak parameters V_{max}, t_{ToT}, A_{peak}, SNR at 400 V, 750 V and 1100 V reverse bias voltage.

Die approbierte gedruckte Originalversion dieser Diplomarbeit ist an der TU Wien Bibliothek verfügbar
The approved original version of this thesis is available in print at TU Wien Bibliothek.
TU WIEN Bibliothek Your knowledge hub

TU Bibliothek Your knowledge hub WIEN
Die approbierte gedruckte Originalversion dieser Diplomarbeit ist an der TU Wien Bibliothek verfügbar
The approved original version of this thesis is available in print at TU Wien Bibliothek.

C Testing Report of the UV-Laser

PiLas DX Test Report:

Date: July 21, 2021

by: epsc
checked: bokh

Laser Class: 3B
IEC 60825-1:2014
see manual for laser
warning label
reproduction

Item:	Characteristics:	
Head (PN)	PIL1-037-40FC	
Serial number:	1041	
Controller (PN)	EGI-D2-40	max. PRF 40MHz, FW:V1.1AEd
Serial number:	Lab Unit	
Laserdiode	WT2048	
Wavelength:	370.0nm	(measured at 40MHz)
Spectral width (FWHM):	1.1nm	(measured at 40MHz)
Optics		
Laserdiode Collimator	50CL-A4.5-01	
Focal length:	4.5mm (asphere)	
Numerical aperture:	0.55	
Beam diameter ($1/e^2$):	2.9mm x 1.1mm @ 0.5m	
Beam divergence* ($1/e^2$):	0.08mrad x 0.21mrad	
** half angle*		
Fiber Coupler	60SMS-1-4-A11-01 (FC/APC)	
Focal length:	11 mm	
Numerical aperture:	0.25	
Fiber	P3-305A-FC	
type:	SM300, 1m length, 0.9mm tube (Custom)	
core / MFD:	unknown / 2.0 - 2.4 μm @ 350 nm	
NA:	0.12-0.14	
Connectors:	2x FC/APC	
LD TEC	On	
Thermistor:	NTC 10 kΩ at 25°C	
Temp-SP:	1.25V (23°C)	

A.L.S. GmbH, www.alsgmbh.com, Germany   Page 1 / 3   Hephy_PIL1-037-40FC_1041

TU WIEN Bibliothek Your knowledge hub
Die approbierte gedruckte Originalversion dieser Diplomarbeit ist an der TU Wien Bibliothek verfügbar
The approved original version of this thesis is available in print at TU Wien Bibliothek.

Test measurements:

Setup:
Warm-up time of the entire running system is 10 min, ambient temperature 25 °C. Ambient temperature changes may influence output power.

Optical power measurement:
average power: a) 1936-R power meter + 918D-UV/918D-ST-IR optical heads b) PM100USB power meter + S150C/S154C optial heads
Measurement at collimated free space output respectively at fiber output
The peak power is calculated (pulse energy/pulse width multiplied by pulse shape factor).

Spectral measurements:
Wavelength and spectral width are measured with OSA Q8381A.

Dynamic measurement:
Optical setup: Collimated or fiber coupled laser light is coupled to the New Focus mod1024 detector.
Photodetector: New Focus mod1024 detector
Oscilloscope: 86100A + 83484A / HP54750A + 54752B, (50 GHz channel, Agilent)

1. Frequency scan with oscilloscope, photodetector and optical power meter:

				after SM fiber	after SM fiber	after SM fiber
Frequency (MHz)	Tune value (%)	FWHM (ps)	RMS - Jitter (ps)	Av. power (µW)	Energy (pJ)	Peak power (mW)
0.001	35	45	2.9	0.008	8	110
0.1	37	44	2.9	0.8	8	115
1	39	44	2.9	8	8	125
10	67	44	2.9	80	8	130
20	73	44	2.9	160	8	135
30	62	44	2.9	240	8	145
40	30	44	2.9	330	8	150

A.L.S. GmbH, www.alsgmbh.com, Germany   Page 2 / 3   Hephy_PIL1-037-40FC_1041

Die approbierte gedruckte Originalversion dieser Diplomarbeit ist an der TU Wien Bibliothek verfügbar
The approved original version of this thesis is available in print at TU Wien Bibliothek.

2. Tune scan with oscilloscope, photodetector and optical power meter at selected frequency:

Device: Oscilloscope

Frequency	Tune value (%)	FWHM (ps)	relative to norm pulse	after SM fiber Av. power (µW)	after SM fiber Energy (pJ)	after SM fiber Peak power (mW)
40 MHz	45	58	below	165	4	70
40 MHz	30	44	Norm pulse	330	8	150
40 MHz	10	39	above	495	12	220

3. Enclosed Views:

Pulse development with oscilloscope: Rep.-rate: 40MHz: Tuning rates 45, 30 and 10% with pulse data.
Pulse measurements with oscilloscope and photodetector: Rep.-rate: 40MHz, tune 30%. time base 50ps.
Jitter measurements with oscilloscope and photodetector: Rep.-rate: 40MHz, tune 30%. time base 50ps.
Optical spectrum at 40MHz Tune 30%.

4. Remarks:

TUNE values can be changed only when TUNE mode is set to "manual".
Changing frequency may require additional time for power stabilization.
For external triggering the appropriate trigger mode must be selected (ext. TTL or ext. Adj.).
For external triggering start with TTL Trigger input. If no triggering is possible use +5/-5V Trigger input and set trigger threshold and edge.
The average power at external triggering should correspond to average power at nearest internal frequency.
Do NOT apply higher frequencies than maximum ordered one (see purchase information).

5. Autotune list

PRF (Hz)	1k	100k	1M	10M	20M	22M	23M	24M	25M	26M	27M	28M	29M	30M	31M	32M	33M	34M	35M	36M	37M	38M	39M	40M
TUNE (%)	35	37	39	67	73	72	71	71	69	69	67	65	64	62	60	58	56	53	51	46	43	39	35	30

A.L.S. GmbH, www.alsgmbh.com, Germany Page 3 / 3 Hephy_PIL1-037-40FC_1041

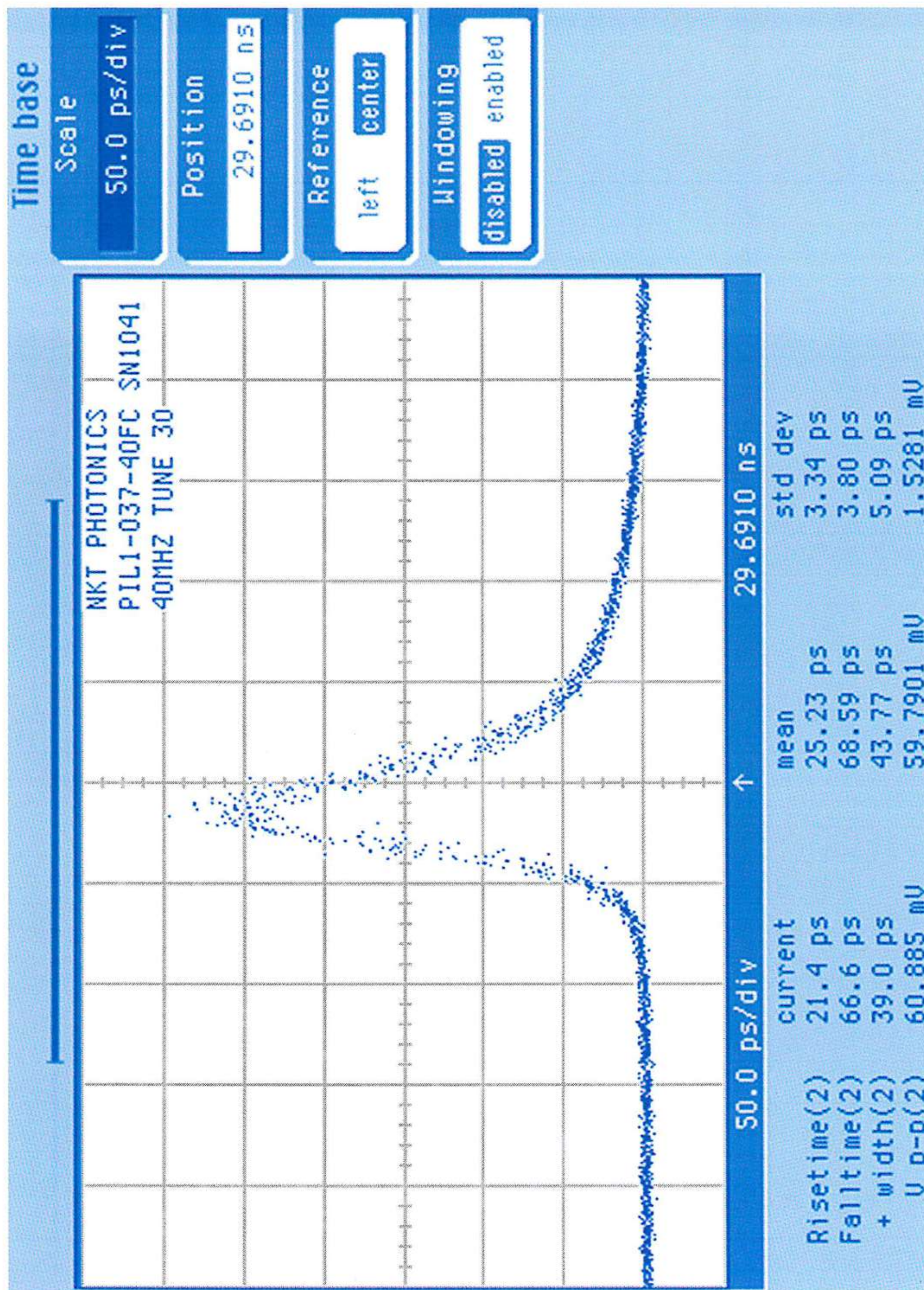

TU WIEN Bibliothek Your knowledge hub
Die approbierte gedruckte Originalversion dieser Diplomarbeit ist an der TU Wien Bibliothek verfügbar
The approved original version of this thesis is available in print at TU Wien Bibliothek.

TU WIEN Bibliothek Your knowledge hub
Die approbierte gedruckte Originalversion dieser Diplomarbeit ist an der TU Wien Bibliothek verfügbar
The approved original version of this thesis is available in print at TU Wien Bibliothek.

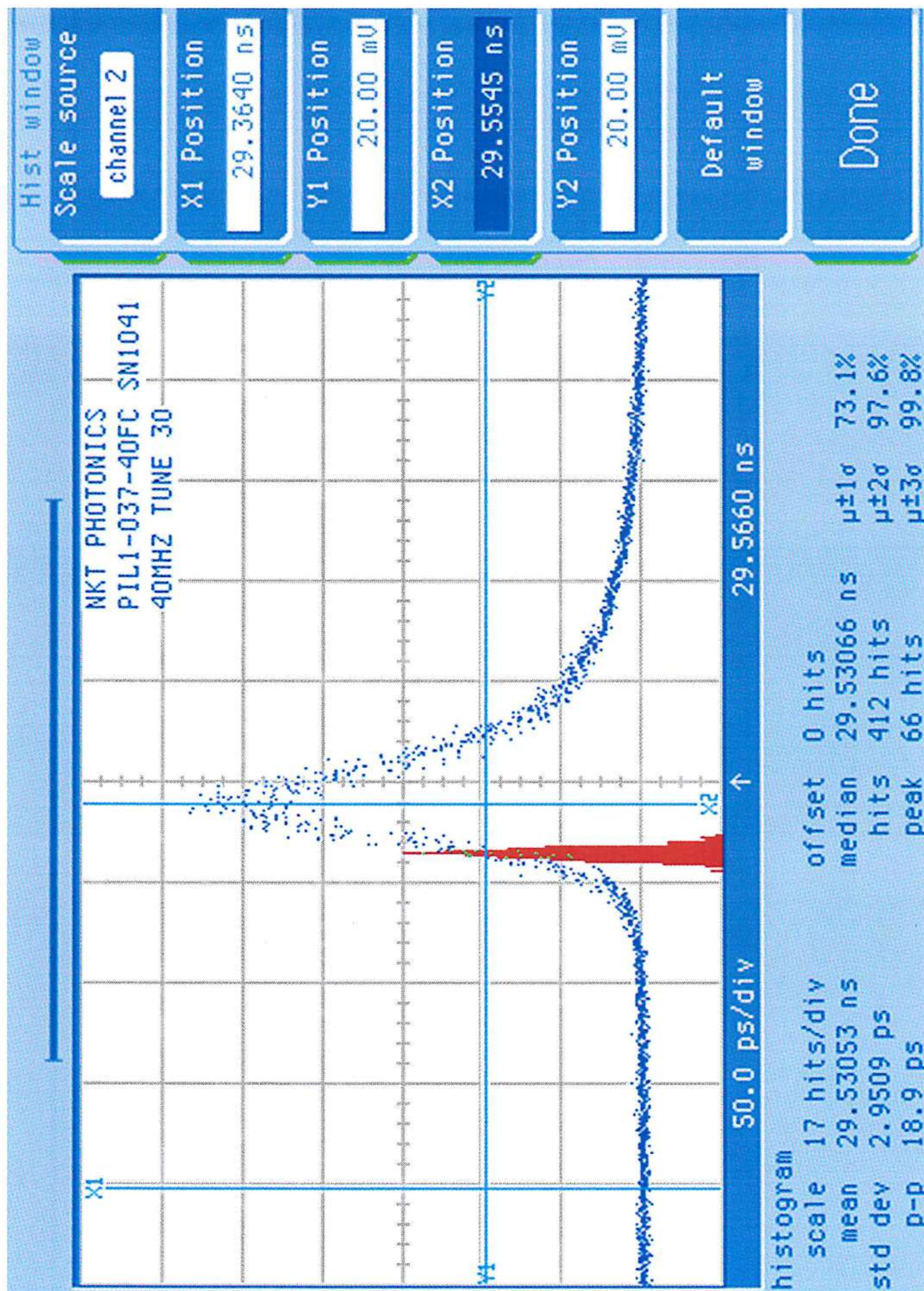

Die approbierte gedruckte Originalversion dieser Diplomarbeit ist an der TU Wien Bibliothek verfügbar
The approved original version of this thesis is available in print at TU Wien Bibliothek.
TU WIEN Bibliothek Your knowledge hub

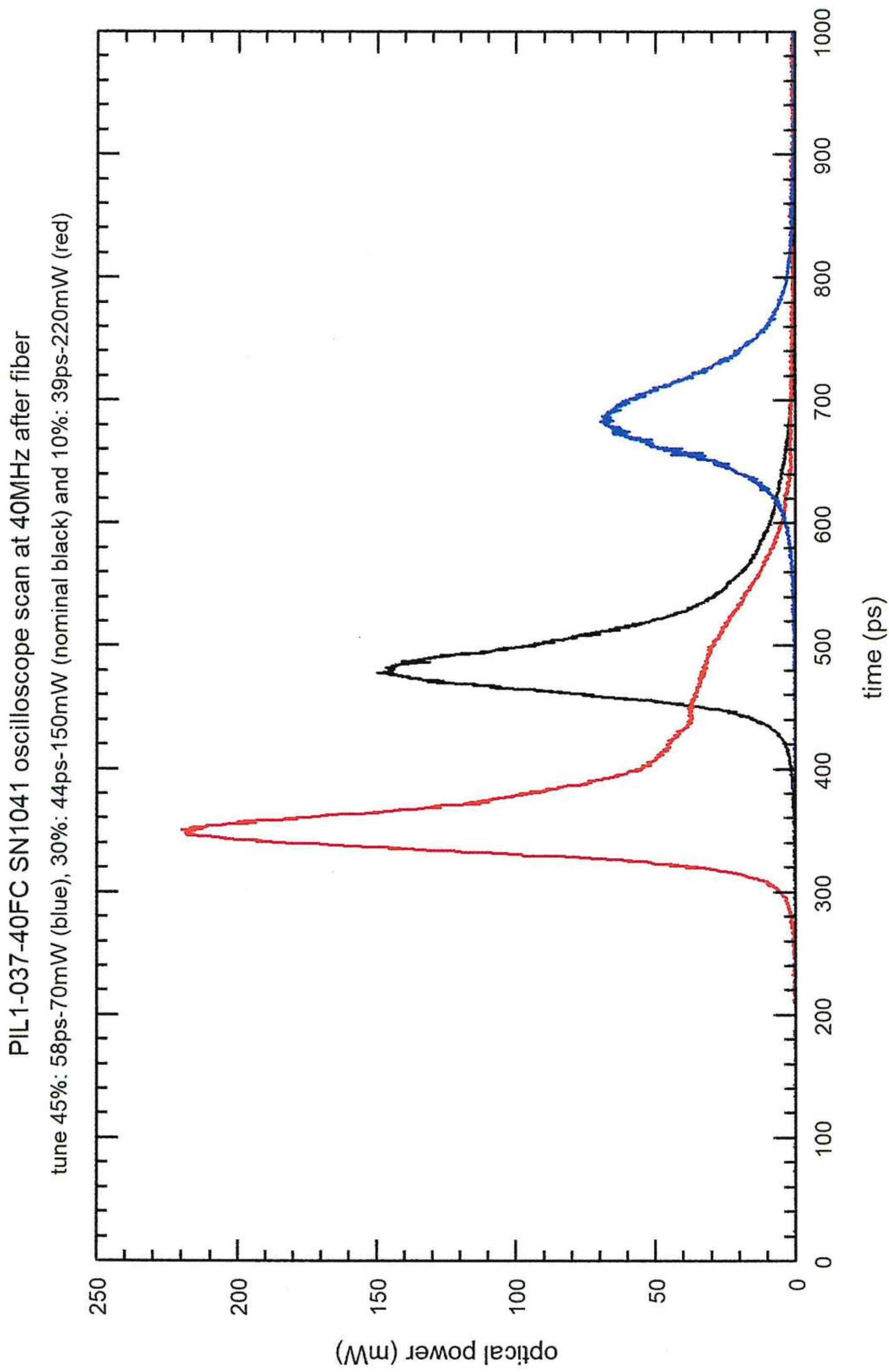

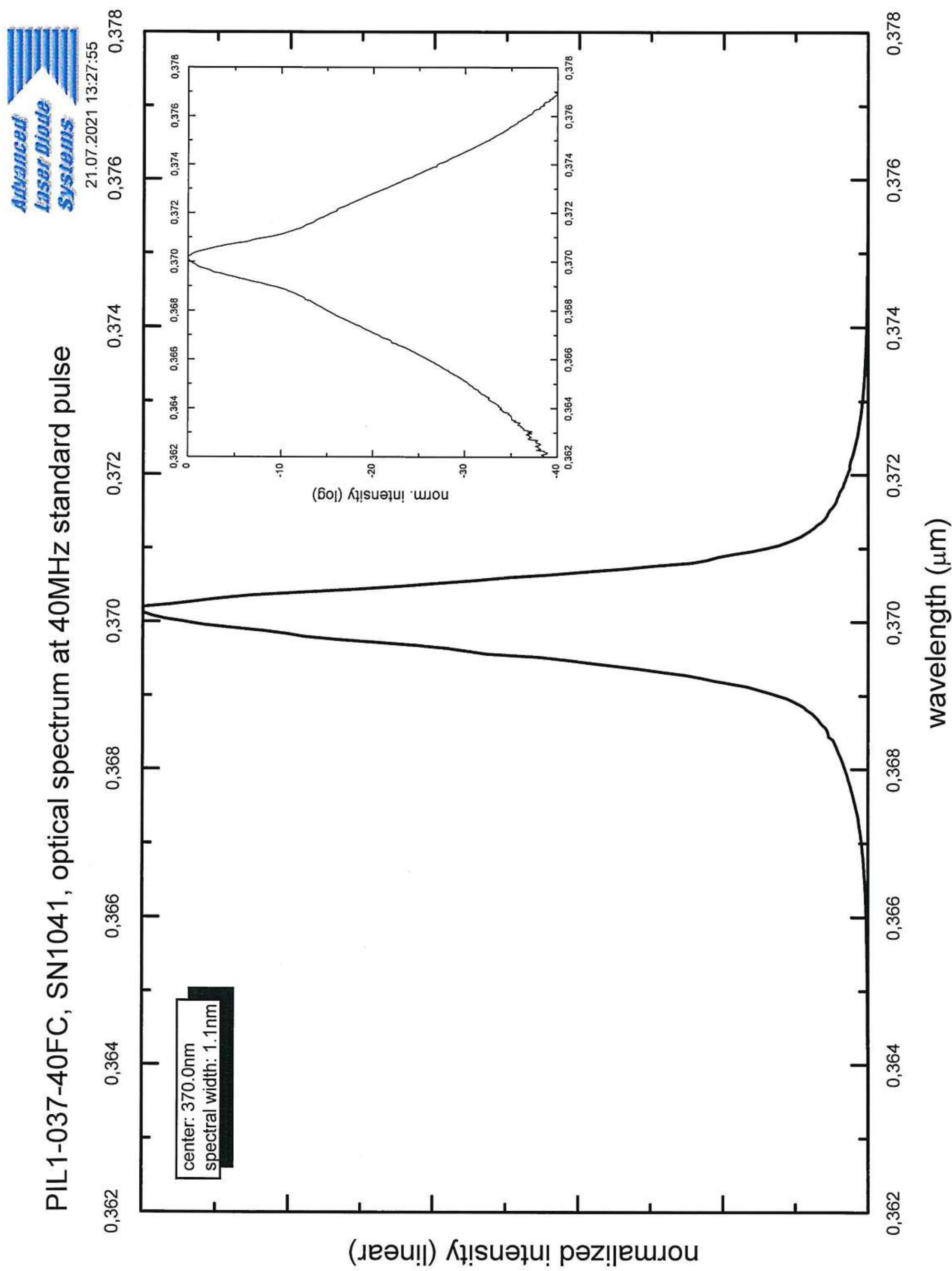

Die approbierte gedruckte Originalversion dieser Diplomarbeit ist an der TU Wien Bibliothek verfügbar
The approved original version of this thesis is available in print at TU Wien Bibliothek.
TU WIEN Bibliothek Your knowledge hub

D References

[1] *Technische Daten*. https://www.tuwien.at/trigacenter/trigareaktor/technische-daten. [Online; accessed 01.04.2022].

[2] P. S. Institut. *DRS Chip Home Page*. https://www.psi.ch/de/drs. [Online; accessed 19.05.2022].

[3] M. Benedikt and A. Wrulich. „MedAustron-Project overview and status“. en. In: *The European Physical Journal Plus* 126.7 (July 2011), p. 69. DOI: 10.1140/epjp/i2011-11069-9.

[4] H. Becquerel. *Nobel Lecture: On Radioactivity, a New Property of Matter*. https://www.nobelprize.org/prizes/physics/1903/becquerel/lecture/. [Online; accessed 19.05.2022]. Dec. 1903.

[5] V. F. Hess. *Nobel Lecture: Unsolved Problems in Physics: Tasks for the Immediate Future in Cosmic Ray Studies*. https://www.nobelprize.org/prizes/physics/1936/hess/lecture/. [Online; accessed 19.05.2022]. Dec. 1936.

[6] E. R. F.R.S. „LXXIX. The scattering of α and β particles by matter and the structure of the atom“. In: *The London, Edinburgh, and Dublin Philosophical Magazine and Journal of Science* 21.125 (1911), pp. 669–688. DOI: 10.1080/14786440508637080. eprint: https://doi.org/10.1080/14786440508637080.

[7] C. T. R. Wilson. „On a method of making visible the paths of ionising particles through a gas“. In: *Proceedings of the Royal Society of London. Series A, Containing Papers of a Mathematical and Physical Character* 85.578 (June 1911). Publisher: Royal Society, pp. 285–288. DOI: 10.1098/rspa.1911.0041.

[8] D. A. Glaser. *Nobel Lecture: Elementary Particles and Bubble Chambers*. https://www.nobelprize.org/uploads/2017/05/glaser-lecture.pdf. [Online; accessed 19.05.2022]. Dec. 1960.

[9] H. Kolanoski and N. Wermes. „Wechselwirkung von Teilchen mit Materie“. de. In: *Teilchendetektoren*. Berlin, Heidelberg: Springer Berlin Heidelberg, 2016. Chap. 3. DOI: 10.1007/978-3-662-45350-6.

[10] H. Geiger and W. Müller. „Elektronenzählrohr zur Messung schwächster Aktivitäten“. de. In: *Naturwissenschaften* 16.31 (Aug. 1928), pp. 617–618. DOI: 10.1007/BF01494093.

[11] G. Charpak, J. Derré, A. Giganon, Y. Giomataris, D. Jourde, C. Kochowski, S. Loucatos, G. Puill, P. Rebourgeard, and J. P. Robert. „First beam test results with Micromegas, a high-rate, high-resolution detector“. en. In: *Nuclear Instruments and Methods in Physics Research Section A: Accelerators, Spectrometers, Detectors and Associated Equipment* 412.1 (June 1998), pp. 47–60. DOI: 10.1016/S0168-9002(98)00311-8.

[12] J. Bortfeldt, F. Brunbauer, C. David, D. Desforge, G. Fanourakis, J. Franchi, M. Gallinaro, I. Giomataris, D. González-Díaz, T. Gustavsson, C. Guyot, F. J. Iguaz, M. Kebbiri, P. Legou, J. Liu, M. Lupberger, O. Maillard, I. Manthos, H. Müller, V. Niaouris, E. Oliveri, T. Papaevangelou, K. Paraschou, M. Pomorski, B. Qi, F. Resnati, L. Ropelewski, D. Sampsonidis, T. Schneider, P. Schwemling, L. Sohl, M. v. Stenis, P. Thuiner, Y. Tsipolitis, S. E. Tzamarias, R. Veenhof, X. Wang, S. White, Z. Zhang, and Y. Zhou. „PICOSEC: Charged particle timing at sub-25 picosecond precision with a Micromegas based detector“. en. In: *Nuclear Instruments and Methods in Physics Research Section A: Accelerators, Spectrometers, Detectors and Associated Equipment* 903 (Sept. 2018), pp. 317–325. DOI: 10.1016/j.nima.2018.04.033.

TU WIEN Bibliothek Your knowledge hub
Die approbierte gedruckte Originalversion dieser Diplomarbeit ist an der TU Wien Bibliothek verfügbar
The approved original version of this thesis is available in print at TU Wien Bibliothek.

[13] F. Hartmann. „First Steps with Silicon Sensors: NA11 (Proof of Principle)“. In: *Evolution of Silicon Sensor Technology in Particle Physics*. Vol. 275. Springer Tracts in Modern Physics. Cham: Springer International Publishing, 2017. Chap. 3. DOI: 10.1007/978-3-319-64436-3.

[14] F. Hartmann. „Basic Principles of a Silicon Detector“. In: *Evolution of Silicon Sensor Technology in Particle Physics*. Vol. 275. Springer Tracts in Modern Physics. Cham: Springer International Publishing, 2017. Chap. 1. DOI: 10.1007/978-3-319-64436-3.

[15] G. Lindström. „Radiation damage in silicon detectors“. en. In: *Nuclear Instruments and Methods in Physics Research Section A: Accelerators, Spectrometers, Detectors and Associated Equipment*. Proceedings of the 9th European Symposium on Semiconductor Detectors: New Developments on Radiation Detectors 512.1 (Oct. 2003), pp. 30–43. DOI: 10.1016/S0168-9002(03)01874-6.

[16] S. Metzger, H. Henschel, O. Kohn, and W. Lennartz. „Silicon carbide radiation detector for harsh environments“. In: *IEEE Transactions on Nuclear Science* 49.3 (June 2002). Conference Name: IEEE Transactions on Nuclear Science, pp. 1351–1355. DOI: 10.1109/TNS.2002.1039666.

[17] V. A. Izhevskyi, L. A. Genova, J. C. Bressiani, and A. H. A. Bressiani. „Review article: silicon carbide. Structure, properties and processing“. en. In: *Cerâmica* 46 (Mar. 2000). Publisher: Associação Brasileira de Cerâmica, pp. 4–13. DOI: 10.1590/S0366-69132000000100002.

[18] R. Babcock and H. Chang. „Silicon carbide neutron detectors for high-temperature operation“. In: *Reactor Dosimetry* 1 (1963).

[19] R. R. Ferber and G. N. Hamilton. „Silicon Carbide High-Temperature Neutron Detectors for Reactor Instrumentation“. In: *Nuclear Applications* 2.3 (1966), pp. 246–251. DOI: 10.13182/NT66-A27595. eprint: https://doi.org/10.13182/NT66-A27595.

[20] F. Franceschini and F. H. „Silicon Carbide Neutron Detectors“. en. In: *Properties and Applications of Silicon Carbide*. Ed. by R. Gerhardt. InTech, Apr. 2011. DOI: 10.5772/15666.

[21] P. J. Sellin and J. Vaitkus. „New materials for radiation hard semiconductor dectectors“. en. In: *Nuclear Instruments and Methods in Physics Research Section A: Accelerators, Spectrometers, Detectors and Associated Equipment* 557.2 (Feb. 2006), pp. 479–489. DOI: 10.1016/j.nima.2005.10.128.

[22] D. Brown, E. Downey, M. Ghezzo, J. Kretchmer, R. Saia, Y. Liu, J. Edmond, G. Gati, J. Pimbley, and W. Schneider. „Silicon carbide UV photodiodes“. In: *IEEE Transactions on Electron Devices* 40.2 (Feb. 1993). Conference Name: IEEE Transactions on Electron Devices, pp. 325–333. DOI: 10.1109/16.182509.

[23] M. Iwami. „Silicon carbide: fundamentals“. en. In: *Nuclear Instruments and Methods in Physics Research Section A: Accelerators, Spectrometers, Detectors and Associated Equipment*. 4th Int. Symp. on Development and Application of Semiconductor Tracking Detectors 466.2 (July 2001), pp. 406–411. DOI: 10.1016/S0168-9002(01)00601-5.

[24] J. B. Casady and R. W. Johnson. „Status of silicon carbide (SiC) as a wide-bandgap semiconductor for high-temperature applications: A review“. en. In: *Solid-State Electronics* 39.10 (Oct. 1996), pp. 1409–1422. DOI: 10.1016/0038-1101(96)00045-7.

TU WIEN Bibliothek Your knowledge hub
Die approbierte gedruckte Originalversion dieser Diplomarbeit ist an der TU Wien Bibliothek verfügbar
The approved original version of this thesis is available in print at TU Wien Bibliothek.

[25] J. Grant, W. Cunningham, A. Blue, V. O'Shea, J. Vaitkus, E. Gaubas, and M. Rahman. „Wide bandgap semiconductor detectors for harsh radiation environments". en. In: *Nuclear Instruments and Methods in Physics Research Section A: Accelerators, Spectrometers, Detectors and Associated Equipment*. Proceedings of the 6th International Workshop on Radiation Imaging Detectors 546.1 (July 2005), pp. 213–217. DOI: 10.1016/j.nima.2005.03.038.

[26] F. H. Ruddy, L. Ottaviani, A. Lyoussi, C. Destouches, O. Palais, and C. Reynard-Carette. „Silicon Carbide Neutron Detectors for Harsh Nuclear Environments: A Review of the State of the Art". In: *IEEE Transactions on Nuclear Science* 69.4 (2022), pp. 792–803. DOI: 10.1109/TNS.2022.3144125.

[27] J. Rafí, G. Pellegrini, P. Godignon, D. Quirion, S. Hidalgo, O. Matilla, A. Fontserè, B. Molas, K. Takakura, I. Tsunoda, M. Yoneoka, D. Pothin, and P. Fajardo. „Four-quadrant silicon and silicon carbide photodiodes for beam position monitor applications: electrical characterization and electron irradiation effects". In: *Journal of Instrumentation* 13.01 (Jan. 2018), pp. C01045–C01045. DOI: 10.1088/1748-0221/13/01/C01045.

[28] D. Schardt, T. Elsässer, and D. Schulz-Ertner. „Heavy-ion tumor therapy: Physical and radiobiological benefits". In: *Reviews of Modern Physics* 82.1 (Feb. 2010). Publisher: American Physical Society, pp. 383–425. DOI: 10.1103/RevModPhys.82.383.

[29] H. X. Q. Norman, A. F. Steinberg, R. B. Appleby, H. L. Owen, E. Benedetto, M. Sapinski, and S. L. Sheehy. „Review of Technologies for Ion Therapy Accelerators". en. In: *arXiv:2105.08103 [physics]* (May 2021). arXiv: 2105.08103.

[30] F. Ulrich-Pur, L. Adler, T. Bergauer, A. Burker, A. De Franco, G. Guidoboni, A. Hirtl, C. Irmler, S. Kaser, S. Nowak, F. Pitters, M. Pivi, D. Prokopovich, C. Schmitzer, and A. Wastl. „Commissioning of low particle flux for proton beams at MedAustron". en. In: *Nuclear Instruments and Methods in Physics Research Section A: Accelerators, Spectrometers, Detectors and Associated Equipment* 1010 (Sept. 2021), p. 165570. DOI: 10.1016/j.nima.2021.165570.

[31] W. Donahue, W. D. Newhauser, and J. F. Ziegler. „Analytical model for ion stopping power and range in the therapeutic energy interval for beams of hydrogen and heavier ions". en. In: *Physics in Medicine and Biology* 61.17 (Aug. 2016). Publisher: IOP Publishing, pp. 6570–6584. DOI: 10.1088/0031-9155/61/17/6570.

[32] O. Jäkel, G. Kraft, and C. P. Karger. „The history of ion beam therapy in Germany". en. In: *Zeitschrift für Medizinische Physik*. Special Issue: Ion Beam Therapy, Part II 32.1 (Feb. 2022), pp. 6–22. DOI: 10.1016/j.zemedi.2021.11.003.

[33] M. Pivi, A. De Franco, F. Farinon, M. Kronberger, T. Kulenkampff, C. Kurfürst, S. Myalski, S. Nowak, F. Osmić, L. Penescu, C. Schmitzer, P. UrschÃ¼tz, and A. Wastl. „Overview and Status of the MedAustron Ion Therapy Center Accelerator". en. In: JACOW, Geneva, Switzerland, May 2017, pp. 4627–4630. DOI: 10.18429/JACoW-IPAC2017-THPVA076.

[34] HEPHY and MedAustron. *HiBPM. Hi-Precision Beam Position and Intensity Monitor for Accurate Cancer Treatment with Ions*. https://projekte.ffg.at/projekt/3968838. [Online; accessed 15.04.2022].

[35] M. Christanell, M. Tomaschek, and T. Bergauer. „4H-silicon carbide as particle detector for high-intensity ion beams". en. In: *Journal of Instrumentation* 17.01 (Jan. 2022). Publisher: IOP Publishing, p. C01060. DOI: 10.1088/1748-0221/17/01/C01060.

TU Bibliothek WIEN Your knowledge hub
Die approbierte gedruckte Originalversion dieser Diplomarbeit ist an der TU Wien Bibliothek verfügbar
The approved original version of this thesis is available in print at TU Wien Bibliothek.

[36] H. Ibach and H. Lüth. „„Freie“ Elektronen im Festkörper“. de. In: *Festkörperphysik*. Springer-Lehrbuch. ISSN: 0937-7433. Berlin, Heidelberg: Springer Berlin Heidelberg, 2009. Chap. 6. DOI: 10.1007/978-3-540-85795-2.

[37] W. Demtröder. „Grundlagen der Quantenmechanik“. de. In: *Experimentalphysik 3*. Springer-Lehrbuch. Berlin, Heidelberg: Springer Berlin Heidelberg, 2010. Chap. 4. DOI: 10.1007/978-3-642-03911-9.

[38] W. Demtröder. „Atome mit mehreren Elektronen“. de. In: *Experimentalphysik 3*. Springer-Lehrbuch. Berlin, Heidelberg: Springer Berlin Heidelberg, 2010. Chap. 6. DOI: 10.1007/978-3-642-03911-9.

[39] H. Ibach and H. Lüth. „Elektronische Bänder in Festkörpern“. de. In: *Festkörperphysik*. Springer-Lehrbuch. ISSN: 0937-7433. Berlin, Heidelberg: Springer Berlin Heidelberg, 2009. Chap. 7. DOI: 10.1007/978-3-540-85795-2.

[40] W. Demtröder. de. In: *Experimentalphysik 3*. Springer-Lehrbuch. Berlin, Heidelberg: Springer Berlin Heidelberg, 2010. Chap. 13. DOI: 10.1007/978-3-642-03911-9.

[41] M. Gruber. „Electronic and magnetic properties of hybrid interfaces : from single molecules to ultra-thin molecular films on metallic substrates“. fr. PhD thesis. Universite de Strasbourg, Nov. 2014.

[42] G. R. Choppin, J.-O. Liljenzin, and J. Rydberg. „Absorption of Nuclear Radiation“. en. In: *Radiochemistry and Nuclear Chemistry*. Ed. by G. R. Choppin, J.-O. Liljenzin, and J. Rydberg. Third. Woburn: Butterworth-Heinemann, Jan. 2002. Chap. 6, pp. 123–165. DOI: 10.1016/B978-075067463-8/50006-6.

[43] A. Einstein. „Über einen die Erzeugung und Verwandlung des Lichtes betreffenden heuristischen Gesichtspunkt“. In: *Annalen der Physik* 322.6 (1905), pp. 132–148. DOI: https://doi.org/10.1002/andp.19053220607. eprint: https://onlinelibrary.wiley.com/doi/pdf/10.1002/andp.19053220607.

[44] A. H. Compton. „A Quantum Theory of the Scattering of X-rays by Light Elements“. In: *Phys. Rev.* 21 (5 May 1923), pp. 483–502. DOI: 10.1103/PhysRev.21.483.

[45] H. Bethe, W. Heitler, and P. A. M. Dirac. „On the stopping of fast particles and on the creation of positive electrons“. In: *Proceedings of the Royal Society of London. Series A, Containing Papers of a Mathematical and Physical Character* 146.856 (1934), pp. 83–112. DOI: 10.1098/rspa.1934.0140. eprint: https://royalsocietypublishing.org/doi/pdf/10.1098/rspa.1934.0140.

[46] W. Demtröder. „Emission und Absorption elektromagnetischer Strahlung durch Atome“. de. In: *Experimentalphysik 3*. Springer-Lehrbuch. Berlin, Heidelberg: Springer Berlin Heidelberg, 2010. Chap. 7. DOI: 10.1007/978-3-642-03911-9.

[47] H. Bethe. „Zur Theorie des Durchgangs schneller Korpuskularstrahlen durch Materie“. en. In: *Annalen der Physik* 397.3 (1930). _eprint: https://onlinelibrary.wiley.com/doi/pdf/10.1002/andp.19303970303, pp. 325–400. DOI: 10.1002/andp.19303970303.

[48] H. Kolanoski and N. Wermes. „Überblick“. de. In: *Teilchendetektoren*. Berlin, Heidelberg: Springer Berlin Heidelberg, 2016. Chap. 2. DOI: 10.1007/978-3-662-45350-6.

[49] P. Zyla and P. D. Group. „Passage of Particles Through Matter“. en. In: *Progress of Theoretical and Experimental Physics* (2020). DOI: 10.1093/ptep/ptaa104.

Die approbierte gedruckte Originalversion dieser Diplomarbeit ist an der TU Wien Bibliothek verfügbar
The approved original version of this thesis is available in print at TU Wien Bibliothek.
TU WIEN Bibliothek Your knowledge hub

[50] H. Ibach and H. Lüth. „Die Struktur von Festkörpern“. de. In: *Festkörperphysik*. Springer-Lehrbuch. ISSN: 0937-7433. Berlin, Heidelberg: Springer Berlin Heidelberg, 2009. Chap. 2. DOI: 10.1007/978-3-540-85795-2.

[51] M. Moll. „Displacement Damage in Silicon Detectors for High Energy Physics“. In: *IEEE Transactions on Nuclear Science* 65.8 (Aug. 2018). Conference Name: IEEE Transactions on Nuclear Science, pp. 1561–1582. DOI: 10.1109/TNS.2018.2819506.

[52] M. Bruzzi. „Radiation damage in silicon detectors for high-energy physics experiments“. In: *IEEE Transactions on Nuclear Science* 48.4 (Aug. 2001). Conference Name: IEEE Transactions on Nuclear Science, pp. 960–971. DOI: 10.1109/23.958706.

[53] H. Ibach and H. Lüth. „Halbleiter“. de. In: *Festkörperphysik*. Springer-Lehrbuch. ISSN: 0937-7433. Berlin, Heidelberg: Springer Berlin Heidelberg, 2009. Chap. 12. DOI: 10.1007/978-3-540-85795-2.

[54] H. Kolanoski and N. Wermes. „Halbleiterdetektoren“. de. In: *Teilchendetektoren*. Berlin, Heidelberg: Springer Berlin Heidelberg, 2016. Chap. 8. DOI: 10.1007/978-3-662-45350-6.

[55] S. Ramo. „Currents Induced by Electron Motion“. In: *Proceedings of the IRE* 27.9 (Sept. 1939). Conference Name: Proceedings of the IRE, pp. 584–585. DOI: 10.1109/JRPROC.1939.228757.

[56] Z. He. „Review of the Shockley-Ramo theorem and its application in semiconductor gamma-ray detectors“. In: *Nuclear Instruments and Methods in Physics Research Section A: Accelerators, Spectrometers, Detectors and Associated Equipment* 463 (May 2001), pp. 250–267. DOI: 10.1016/S0168-9002(01)00223-6.

[57] H. Kolanoski and N. Wermes. „Bewegung von Ladungsträgern in elektrischen und magnetischen Feldern“. de. In: *Teilchendetektoren*. Berlin, Heidelberg: Springer Berlin Heidelberg, 2016. Chap. 4. DOI: 10.1007/978-3-662-45350-6.

[58] P. Drude. „Zur Elektronentheorie der Metalle“. en. In: *Annalen der Physik* 306.3 (1900). _eprint: https://onlinelibrary.wiley.com/doi/pdf/10.1002/andp.19003060312, pp. 566–613. DOI: 10.1002/andp.19003060312.

[59] G. Kramberger. „Advanced Transient Current Technique Systems“. en. In: *Proceedings of Science* (Sept. 2014), p. 11.

[60] I. Mandic, V. Cindro, A. Gorisek, G. Kramberger, M. Mikuz, M. Milovanovic, and M. Zavrtanik. „TCT measurements of irradiated strip detectors with a focused laser beam“. en. In: *Journal of Instrumentation* 8.04 (Apr. 2013), P04016–P04016. DOI: 10.1088/1748-0221/8/04/P04016.

[61] J. Coutinho, V. J. B. Torres, I. Capan, T. Brodar, Z. Ereš, R. Bernat, V. Radulović, K. Ambrožič, L. Snoj, Ž. Pastuović, A. Sarbutt, T. Ohshima, Y. Yamazaki, and T. Makino. „Silicon carbide diodes for neutron detection“. en. In: *Nuclear Instruments and Methods in Physics Research Section A: Accelerators, Spectrometers, Detectors and Associated Equipment* 986 (Jan. 2021), p. 164793. DOI: 10.1016/j.nima.2020.164793.

[62] P. Krishna, R. C. Marshall, and C. E. Ryan. „The discovery of a 2H-3C solid state transformation in silicon carbide single crystals“. en. In: *Journal of Crystal Growth* 8.1 (Jan. 1971), pp. 129–131. DOI: 10.1016/0022-0248(71)90033-9.

[63] F. Nava, G. Bertuccio, A. Cavallini, and E. Vittone. „Silicon carbide and its use as a radiation detector material“. en. In: *Measurement Science and Technology* 19.10 (Oct. 2008), p. 102001. DOI: 10.1088/0957-0233/19/10/102001.

TU Bibliothek WIEN Your knowledge hub
Die approbierte gedruckte Originalversion dieser Diplomarbeit ist an der TU Wien Bibliothek verfügbar
The approved original version of this thesis is available in print at TU Wien Bibliothek.

[64] W. Y. Ching, Y.-N. Xu, P. Rulis, and L. Ouyang. „The electronic structure and spectroscopic properties of 3C, 2H, 4H, 6H, 15R and 21R polymorphs of SiC“. en. In: *Materials Science and Engineering: A*. NANOAM 422.1 (Apr. 2006), pp. 147–156. DOI: 10.1016/j.msea.2006.01.007.

[65] G. Rescher. „Behavior of SiC-MOSFETs under temperature and voltage stress“. PhD thesis. Wien: Technsiche Universtät Wien, 2018.

[66] A. V. Sinelnik and A. V. Semenov. „Theoretical study of the band structure of 2H-SiC and 4H-SiC of silicon carbide polytypes“. en. In: *Condensed Matter Physics* 24.2 (2021). arXiv: 2106.13626, p. 23705. DOI: 10.5488/CMP.24.23705.

[67] S. K. Chaudhuri, K. J. Zavalla, and K. C. Mandal. „Experimental determination of electron-hole pair creation energy in 4H-SiC epitaxial layer: An absolute calibration approach“. en. In: *Applied Physics Letters* 102.3 (Jan. 2013), p. 031109. DOI: 10.1063/1.4776703.

[68] F. Moscatelli, A. Scorzoni, A. Poggi, M. Bruzzi, S. Sciortino, S. Lagomarsino, G. Wagner, I. Mandic, and R. Nipoti. „Radiation hardness after very high neutron irradiation of minimum ionizing particle detectors based on 4H-SiC p/sup +/n junctions“. en. In: *IEEE Transactions on Nuclear Science* 53.3 (June 2006), pp. 1557–1563. DOI: 10.1109/TNS.2006.872202.

[69] J. L. Vasconcelos, C. G. Rodrigues, and R. Luzzi. „Anisotropic hole drift velocity in 4H-SiC“. en. In: *Materials Science and Engineering: B* 249 (Oct. 2019), p. 114426. DOI: 10.1016/j.mseb.2019.114426.

[70] P.-C. Chen, W.-C. Miao, T. Ahmed, Y.-Y. Pan, C.-L. Lin, S.-C. Chen, H.-C. Kuo, B.-Y. Tsui, and D.-H. Lien. „Defect Inspection Techniques in SiC“. In: *Nanoscale Research Letters* 17.1 (Mar. 2022), p. 30. DOI: 10.1186/s11671-022-03672-w.

[71] *Centro Nacional de Micróelectronica*. http://www.cnm.es/. [Online; accessed 01.04.2022].

[72] J. M. Rafí, G. Pellegrini, P. Godignon, S. O. Ugobono, G. Rius, I. Tsunoda, M. Yoneoka, K. Takakura, G. Kramberger, and M. Moll. „Electron, Neutron, and Proton Irradiation Effects on SiC Radiation Detectors“. en. In: *IEEE TRANSACTIONS ON NUCLEAR SCIENCE* 67.12 (2020), p. 9.

[73] M. Christanell. „4H-Silicon carbide as real time monitor for high-intensity ion beams“. eng. MA thesis. Wien: Technische Unviversität Wien, 2021.

[74] H. Böck and M. Villa. *Practical course on reactor physics and reactor kinetics*. eng. Technische Universität Wien Atominstitut, 2009.

[75] R. Khan. „Neutronics analysis of the TRIGA Mark II reactor core and its experimental facilities“. en. Accepted: 2020-06-30T20:42:20Z. Thesis. Technische Universität Wien, 2010.

[76] P. Salajka. „Irradiation of Silicon detectors for HEP experiments in the Triga Mark II reactor of ATI“. MA thesis. Technische Universität Wien, 2021.

[77] NKT Photonics. *PILAS DX. Picosecond pulsed diode lasers*. https://contentnktphotonics.s3.eu-central-1.amazonaws.com/PILAS/ALS%20Pilas%20Datasheet.pdf. [Online; accessed 01.04.2022].

[78] Tektronix. *Keithley 2470 Graphical SourceMeter SMU*. https://www.tek.com/de/datasheet/2470-graphical-sourcemeter-smu-instrument-datasheet. [Online; accessed 01.04.2022].

[79] Edmund Optics. *20X, UV-VIS Vega Broadband Beam Expander*. https://www.edmundoptics.com/p/20x-uv-vis-da-beam-expander/40661/. [Online; accessed 13.05.2022].

TU Wien Bibliothek Your knowledge hub
Die approbierte gedruckte Originalversion dieser Diplomarbeit ist an der TU Wien Bibliothek verfügbar
The approved original version of this thesis is available in print at TU Wien Bibliothek.

[80] Thorlabs. *Mounted N-BK7 Plano-Convex Lenses (AR Coating: 350 - 700 nm)*. https://www.thorlabs.de/newgrouppage9.cfm?objectgroup_id=6277&pn=LA1050-A-ML. [Online; accessed 13.05.2022].

[81] M. E. GmbH. *User Manual - TEC Controller*. Meerstetter Engineering GmbH. Rubigen, Switzerland, July 2020.

[82] P. H. K. AG. *Huber Ministat 240*. https://www.huber-online.com/de/product_datasheet.aspx?no=2016.0005.01. [Online; accessed 29.08.2022].

[83] Thorlabs. *PM100USB - Power and Energy Meter Interface with USB Operation*. https://www.thorlabs.de/thorproduct.cfm?partnumber=PM100USB. [Online; accessed 29.08.2022].

[84] U. of California Santa Cruz. *UC Santa Cruz*. https://www.ucsc.edu/. [Online; accessed 19.05.2022].

[85] N. Cartiglia, A. Staiano, V. Sola, R. Arcidiacono, R. Cirio, F. Cenna, M. Ferrero, V. Monaco, R. Mulargia, M. Obertino, F. Ravera, R. Sacchi, A. Bellora, S. Durando, M. Mandurrino, N. Minafra, V. Fadeyev, P. Freeman, Z. Galloway, E. Gkougkousis, H. Grabas, B. Gruey, C. A. Labitan, R. Losakul, Z. Luce, F. McKinney-Martinez, H. F. .-. Sadrozinski, A. Seiden, E. Spencer, M. Wilder, N. Woods, A. Zatserklyaniy, G. Pellegrini, S. Hidalgo, M. Carulla, D. Flores, A. Merlos, D. Quirion, V. Cindro, G. Kramberger, I. Mandić, M. Mikuž, and M. Zavrtanik. „Beam test results of a 16ps timing system based on ultra-fast silicon detectors". en. In: *Nuclear Instruments and Methods in Physics Research Section A: Accelerators, Spectrometers, Detectors and Associated Equipment* 850 (Apr. 2017), pp. 83–88. DOI: 10.1016/j.nima.2017.01.021.

[86] G. Vagelis. *Description and details of the UCSC single channel board design*. https://twiki.cern.ch/twiki/bin/view/Main/UcscSingleChannel. [Online; accessed 19.05.2022].

[87] S. Ritt. *PSI DRS4 evaluation board*. https://www.psi.ch/sites/default/files/import/drs/DocumentationEN/manual_rev50.pdf. [Online; accessed 1.04.2022].

[88] S. Ritt. *9 Channel, 5 GSPS Switched Capacitor Array - DRS4*. https://www.psi.ch/sites/default/files/2020-08/DRS4_rev09_2.pdf. [Online; accessed 1.04.2022].

[89] S. Ritt. *DRS4 Evaluation Board User's Manual*. https://www.psi.ch/sites/default/files/2020-02/manual_rev51.pdf. [Online; accessed 1.04.2022].

[90] Rhode&Schwarz. *R&S RTP Oszilloskop*. https://www.rohde-schwarz.com/at/produkte/messtechnik/oszilloskope/rs-rtp-oszilloskop_63493-469056.html. [Online; accessed 26.04.2022].

[91] S. G. Sridhara, R. P. Devaty, and W. J. Choyke. „Absorption coefficient of 4H silicon carbide from 3900 to 3250 Å". In: *Journal of Applied Physics* 84.5 (Sept. 1998). Publisher: American Institute of Physics, pp. 2963–2964. DOI: 10.1063/1.368403.

Die approbierte gedruckte Originalversion dieser Diplomarbeit ist an der TU Wien Bibliothek verfügbar
The approved original version of this thesis is available in print at TU Wien Bibliothek.
TU WIEN Bibliothek Your knowledge hub